WAVE EQUATION MODELING :

DESCRIBING REALISTIC MEDIA

A DISSERTATION

SUBMITTED TO THE DEPARTMENT OF GEOPHYSICS

AND THE COMMITTEE ON GRADUATE STUDIES

OF STANFORD UNIVERSITY

IN PARTIAL FULFILLMENT OF THE REQUIREMENTS

FOR THE DEGREE OF

DOCTOR OF PHILOSOPHY

By

Pierre Vincent Samec

January 1991

I certify that I have read this dissertation and that in my opinion it is fully adequate, in scope and quality, as a dissertation for the degree of Doctor of Philosophy.

_____

Amos M. Nur (Principal Advisor)

I certify that I have read this dissertation and that in my opinion it is fully adequate, in scope and quality, as a dissertation for the degree of Doctor of Philosophy.

_____

Jon F. Claerbout (Geophysics)

I certify that I have read this dissertation and that in my opinion it is fully adequate, in scope and quality, as a dissertation for the degree of Doctor of Philosophy.

_____

Jerry M. Harris (Geophysics)

Approved for the University Committee
on Graduate Studies:

_____

Dean of Graduate studies

Abstract

Most exploration of the underground for hydrocarbon reservoirs depends on the acquisition, processing, and interpretation of seismic data. In this context, this thesis investigates the use of numerical methods for modeling wave phenomena associated with different types of exploration activities, and presents new results in three distinct domains: the understanding of wave phenomena in a cross-well geometry, the influence of rock properties such as attenuation and anisotropy on seismic interpretation, and the use of fast numerical modeling for computer aided interpretation of cross-well data. Two chapters are devoted to each of the studies. The first one examines existing numerical methods, and provides new methods for the investigation. The second one applies the numerical methods to the study of a specific problem.

Downhole source design and acquisition results. (Chapters 2 and 3)

This section introduces new numerical methods such as implicit-explicit finite element modeling, and hybrid finite-element finite-difference modeling. These numerical methods are then applied to the study of various downhole source designs and yield the following results:

- Because the length of downhole sources is often comparable to the seismic wavelength, tuning effects shape the source signal and can introduce severe source dispersion as well as frequency-dependent radiation patterns.

- Unless designed otherwise, downhole sources that are not isolated from the borehole fluid convert more than 90 % of their energy into borehole guided waves. These waves generate powerful secondary sources each time a borehole heterogeneity is encountered.

- In the case where one of the borehole guided modes is faster than the the

compressional or shear velocity of the formation, conical waves are generated by the use of downhole sources.

Rock material properties and petrophysical seismic interpretation. (Chapters 4 and 5)

Chapter 4 provides a framework for the study of anisotropic viscoelastic solids that display attenuation anisotropy. It then provides two solution algorithms for plane wave propagation and for full waveform modeling using a Fourier Pseudo-Spectral method. The full waveform modeling software was used in Chapter 5 to study the sensitivity of Amplitude Versus Offset (A.V.O.) measurements and the following results were obtained:

- Reflection coefficients which are the primary target of A.V.O. interpretation, are strongly dependent on both the viscoelastic and anisotropic properties of the rock studied.

- Both the anisotropic and viscoelastic properties of a material alter the signal during propagation, first, because of elastic energy focusing and, second, because of attenuation or dispersion.

Interactive interpretation of cross-well seismic data. (Chapters 6 and 7.)

Chapter 6 provides an extension of the finite-difference ray-tracing technique to anisotropic, anelastic solids. This method is further used in the context of an interactive interpretation system specially designed for the interpretation of cross-well data.

This interpretation first reveals that a very simplistic model composed of homogeneous layers accurately accounts for the observed first arrivals. The finite-difference raytracing method is then used in a least-square-based inversion loop to recover residual variations of layer velocities, as well as interface location. This experiment shows that this type of travel time inversion can effectively relocate interface, but does not effectively recover layer velocities. This result is related to the heterogeneity of the

ray coverage in a layered medium where most of the first arrivals that would constrain the horizontal velocities actually travel as head waves along wave paths defined by the interfaces.

Acknowledgements

The thesis that follows was greatly inspired by Amos Nur, my advisor at Stanford. I am deeply indebted to him for his patience, his confidence in my work, and above all his communicative enthusiasm. He made my stay at Stanford an enjoyable and unforgettable experience.

I thank all the Stanford faculty members who have been involved with my work these last four years. Special thanks are due to Jerry Harris for interesting discussions about downhole sources, to Jon Claerbout and Fabio Rocca for allowing me to use the Stanford Exploration Project computer facility, to Jon Harbaugh for sharing his vision of geological modeling, and to Mark Zoback for teaching me what stress is all about.

I have also appreciated Gary Mavko's physical insights in rock mechanics, Dan Moos's resourcefulness at reading unreadable tapes and deciphering impossible formats, to Lev Vernik's warm discussions with me about the elusive anisotropy.

It has been a wonderful experience to be part of the Stanford Rock Physics Project for the last four years, and I wish to thank all past and present students for their help and support. In addition, I am grateful to Diane Jizba for her patience in reviewing my early English manuscripts, to Dominique Marion for his support of my work, to Charles West for his insights in rock physics, to Brian Quinn for introducing me to the department computer system, to Reinaldo Michelena and Spyros Lazaratos for sharing their views on cross-well data interpretation. I wish to express gratitude, as well, to J.P. Blangy for his patient review of this manuscript, for his resourcefulness at finding bugs in my software, but, most of all, for sharing with me his vision of what seismic interpretation should be. Through my stay at Stanford, it has also been delightful working with students from the Stanford Exploration project, and the Sedsim project. Thanks to Clement Kostov, John Etgen, Joe Dellinger, Rick

Contents

List of Figures

Chapter 1

Introduction

As most of the giant reservoir structures in the world are likely to have already been discovered, hydrocarbon exploration, essentially based on seismic investigation, turns to new frontiers whereby new, deeper reservoirs are sought, but also old reservoirs now partially depleted are reinvestigated. Two new seismic acquisition philosophies stem from these new plays. First, high resolution seismic data aims to provide valuable petrophysical information from the target investigated. Second, new acquisition geometries such as inter- or cross-well geometries aim to provide detailed images of the targeted reservoir.

By the same token, seismic processing and interpretation largely based so far on amplitude independent algorithms are being reevaluated. Migration is not only supposed to deliver a well focussed image of the underground, but also a working velocity model for it. Deconvolution is not only seen as a tool for signal shaping, but can also be used to efficiently evaluate attenuation. Above all, seismic amplitudes are now known to contain extremely valuable information on rock petrophysical properties, and must be preserved through the seismic processing stage.

Because of the previous assessments, this thesis focuses on the interpretation of seismic data from three different points of view :

- Wave equation modeling using the finite-element method, in order to better understand high resolution cross-well data.

1

- Interpretation of Amplitude Versus Offset data and their dependence on attenuation and anisotropy.

- Structural and petrophysical interpretation, and the role of inversion in seismic interpretation.

Each of these topics is articulated in two chapters. The first provides the theoretical background for the system studied, and investigates the numerical methods that will be used for interpretation. The second applies the results of the first part to the investigation or solution of a particular geophysical problem.

1.1 Seismic downhole source control, and engineering

Some of the sources customarily used for surface seismic acquisition, such as Vibroseis or air guns, have fairly well known behaviors. This is not the case with downhole seismic sources, which have only recently been developed. Based on new families of numerical algorithms – such as implicit-explicit finite-element or hybrid, finite-element, finite-difference algorithms described in Chapter 2 – Chapter 3 addresses the theoretical investigation of the radiation of downhole sources. Three different types of sources are modeled: resonant cavity sources (Kennedy 1987) piezoelectric bender sources (Harris 1987), drill-bits used as a downhole seismic sources (Rector 1990). For each of these sources the following questions are answered :

- Does the borehole affect the performance of the downhole source, in terms of both efficiency and radiation pattern ?

- Does the borehole system affect the source signal signature ?

- Finally on the basis of data acquired with each of these sources, can we identify the modes that were recorded ?

1.2 Anisotropy and attenuation: A new frontier for interpretation

Both attenuation and anisotropy are known to strongly condition wave propagation and seismic reflections in real earth rocks. The studies by Kjartanson (1979), Bourbie (1982), Amos Nur (1969), and Terry Jones (1986), among others, indicate that attenuation is a key seismic parameter that influences both seismic wave propagation and reflections. Similarly, after Crampin (1984) and Nur (1969) discovered the pertinence of including anisotropy for the description of wave propagation in rocks, both Banik (1987) and Thomsen (1987) have stressed the influence of anisotropy on seismic reflections' attributes.

In Chapter 4, I propose a unified description of rocks that includes attenuation as well as elastic anisotropy and attenuation anisotropy. This description is followed by two solution algorithms:

- The plane wave solution in a fully anisotropic medium.

- A numerical full-waveform solution algorithm for fully anisotropic solid based on the previous work of Carcione (1987).

In Chapter 5, the full-waveform algorithm is used to investigate the sensitivity of Amplitude Versus Offset (A.V.O.) measurements on anisotropy, attenuation, and attenuation anisotropy. This study focuses not only on the sensitivity of the reflection coefficient on rock properties such as attenuation and anisotropy, but also on the study of the wave-propagation phenomena involved in A.V.O. measurements and their influence on the computed petrophysical parameters.

1.3 Fast modeling: Seimic interpretation versus inversion

The numerical methods described in Chapter 2 (finite-element) and Chapter 4

(Fourier-pseudo-spectral) are extremely accurate, but are also too slow to suite the speed requirements of an interactive interpretation environment. Faster methods like ray tracing lack the accuracy of the previous methods, and become increasingly slower as the number of seismic attributes computed increases. To alleviate this drawback, I have redesigned a very fast ray tracing method known as finite-difference ray-tracing (Vidale 1988) to include modeling capability for both anisotropic and viscoelastic solids (Chapter 6).

Finally, in Chapter 7, I present an interactive interpretation environment that allows the editing of a geological model satisfying the geophysical constraints provided by both well logs and cross-well seismic data. This last chapter proposes a new interpretation methodology for cross-well data using both classical geological interpretation techniques, and geophysical inversion techniques.

References

Banik, N., C., 1987, An effective anisotropy parameter in transversely isotropic media: Geophysics, **52**, 1654,1664.

Bourbie, T., 1982, Effect of attenuation on seismic reflections: SRB **14**

Carcione, J. M., 1987, Wave propagation in real media, Ph. D. thesis, Senate of Tel Aviv University.

Crampin S., 1984, Effective anisotropic elastic constants for Wave propagation through cracked solids: Geophys. J. R. Astr. Soc. , **76**, 135,145.

Harris, J. 1988, Cross-well seismic measurements in sedimentary rocks, S.E.G. expanded abstracts,**1**, 147, 150.

Jones, T., T., 1986, Pore fluids and frequency-dependent wave propagation in rocks: Geophysics, **51**, 1939,1953.

Kennedy W., Wiggins W., Aronstam P., 1988 Swept-frequency borehole source for inverse VSP and cross-borehole surveying, S.E.G. expanded abstracts,**1**, 158, 160.

Kjartanson, E., 1979, Constant Q-Wave propagation and attenuation: J.G.R., **84**, 4737,4748.

Nur A. and Simmons, G., 1969, Stress induced velocity anisotropy in rock; an experimental study: J. G. R., **74**, 6667,6674.

Rector, J. Phd Thesis, Stanford University, 1990,

Thomsen, L., 1986, Weak elastic anisotropy: Geophysics, **51**, 1954,1966.

Van Trier J., 1989, Finite-difference computation of travel times: Stanford Exploration project report, **57**, .

Vidale J., 1989, Finite-difference computation of travel times: Bulletin of the Seismological Society of America, **78**, 2062-2076.

Chapter 2

Numerical Methods for the Investigation of Wave Phenomena around the Borehole

Abstract

This chapter compares three numerical methods based on the finite-element and finite-difference methods for the purpose of modeling elastic wave phenomena generated by downhole seismic sources. These three methods are: an explicit finite-element method, a hybrid implicit-explicit finite-element method, and finally a hybrid finite-element finite-difference method. The large difference in scale between the diameter, and the length of the borehole, as well as the necessity to accurately model fluid-solid boundary conditions at the borehole wall, makes the finite-element method the preferred modeling method in the borehole region. The numerical discretization of the elastodynamic wave equation using the finite-element method yields the canonic linear system of equations,

$$M\frac{\partial \ddot{u}_n}{\partial t} = K u_n + f_n \tag{2.1}$$

where M is the mass matrix, K the impedance matrix, u_n the discretized displacement field, and f_n the discretized vector of external forces. Unfortunately, the large size of geophysical models (20,000 elements) makes it impossible to use classical solutions

of the finite-element equations that would require prohibitively long computer run times.

Therefore, I investigated two different implementation of FEM aimed at reducing the amount of computation by profiting by the special geometry of our problem and obtained the following results:

- the finite-element discretization of the elastodynamic wave equation on a triangular grid yields a mass matrix with predominant diagonal terms (Sword 1986). The inversion of this matrix using a Taylor expansion yields a very computer-efficient algorithm, but a poor dispersion relation, especially for very low wavenumbers.

- the implicit-explicit (Hughes 1984) partition of the grid between the borehole-source region, and the far-field region provides an efficient numerical algorithm with a good control of both numerical dispersion and anisotropy.

These finite-element methods, however, are less efficient than the finite-difference method to model the inter-well region, because of both their numerical dispersion, and computer implementation. Therefore, recognizing the superiority of the finite-element method in the borehole region, I have devised a hybrid finite-element finite-difference algorithm that yields both very accurate modeling of the effects related to the presence of the borehole, and a more efficient way of propagating the radiated field away from the borehole region.

2.1 Introduction

Multiple solutions of the elastodynamic wave equation are available for the case of downhole sonic logging tools where frequencies range from 1000 to 20000 Hz and therefore span over multiple frequency transition effects (Cheng 1981). Some of these solutions are analytical for the simplest geometries. For most complex geometries

however, only numerical solutions were devised using mostly algorithms based on the finite-difference method.

Similarly, for frequencies lower than $1000Hz$, analytical solutions have been found in simple cases such as a point source in a fluid-filled borehole drilled in a homogeneous isotropic medium, (White 1973). The last class of solutions for signal frequencies ranging from 10 to 1000 Hz is the one of interest for our problem since, with the current state of technology, actual downhole seismic sources only deliver useful seismic information below $1000Hz$, (Harris 1987, Paulson 1987). These solutions to the elastodynamic wave equation are generally referred to as low frequency solutions (White 1973) that is frequencies for which the wavelength of the energy in the borehole fluid is much larger than the borehole diameter. This approximation, however, does not imply that the effect of the borehole on the radiated field can be neglected altogether, as is often assumed. Some of the effects of the borehole presence on the 'low frequency' radiated field are described by White (1973), who uses dimensional analysis to investigate conversions from borehole guided waves to body waves at solid interfaces.

My goal in this chapter is to investigate numerical methods that allow the careful study of downhole seismic sources no matter how complex the source design and setup may be. Because of the discrepancy between the borehole diameter ($10cm$) and the volume investigated which is generally of the order of 100 to 1000 cubic meters, the finite-element method is ideally suited in that it can accommodate large geometrical scales differences. This chapter compares three different implementations of the finite-element method:

- A simple implementation where the domain investigated is gridded using triangular elements, and a simple explicit solution algorithm is used.

- A more complete implementation that allows for easier description of the volume investigated as well as better control of both numerical dispersion and

anisotropy using an implicit-explicit algorithm.

- Finally, a hybrid finite-element finite-difference method that provides faster numerical computations, as well as a complete reusable sampling of the borehole radiated field.

2.2 A simple, efficient implementation of the finite-element method

This first part focuses on a rapid description of the finite-element method, its advantages, and drawbacks when applied to a geophysical problem.

2.2.1 The Lagrangian approach toward the finite-element solution of the wave equation

The finite-element solution of the wave equation is based on its integral formulation. The next part, shows that there are multiple ways of reaching such a formulation and the easiest is probably the Lagrangian formulation of the wave equation. For our problem, the elastodynamic wave equation can be cast as the following mixed boundary problem,

$$\rho u_{i,tt} = \sigma_{ij,j} + f_i \quad \text{on} \quad \Omega \times]0,T] \tag{2.2}$$

$$u_i = g_i \quad \text{on} \quad \Gamma_{g_i} \times]0,T] \tag{2.3}$$

$$\sigma_{ij}n_j = h_i \quad \text{on} \quad \Gamma_{h_i} \times]0,T] \tag{2.4}$$

$$u_i(x,0) = u_{0i}(x) \quad \text{on} \quad \Omega \tag{2.5}$$

$$\dot{u}_i(x,0) = \dot{u}_{0i}(x) \quad \text{on} \quad \Omega \tag{2.6}$$

where, Γ_{g_i} is the domain at the surface of our system where the ith component of the displacement field is defined as g_i. n_j is the normal pointing outward the bounding

surface Γ of the system investigated. Similarly, Γ_{h_i} is the domain where the ith component of the stress field is defined by h_i. The union of Γ_{g_i} and Γ_{h_i} for each component is Γ. The boundary conditions (equations 2.3 and 2.4) are defined for the system studied, as well as for each subsystem of interest such as layers or the borehole itself.

Solving equation 2.2 with the boundary conditions described by equation 2.3 and 2.4, and the initial conditions in equation 2.5 and 2.6 is equivalent to solving the following equation under the same conditions (Morse and Feshbach, 1953):

$$\frac{d}{dt}\left[\frac{\partial L}{\partial \dot{u}_j}\right] = \frac{\partial L}{\partial u_j} \tag{2.7}$$

where L is the Lagrangian of the system defined by the difference between the kinetic (KE) and potential (PE) energy density of the system:

$$L = KE - PE = \frac{1}{2}\rho \dot{u}^2 - c_{ijkl}e_{ij}e_{kl} \tag{2.8}$$

Similar formulations can be adopted for compressible fluids leading to developments similar to the one that follows in this part for an elastic solid.

2.2.2 finite-element discretization of the elastodynamic wave equation for a triangular mesh

Discretization of equation 2.7 is performed in three steps following the computation by Sword (1986):

First, the continuum domain of investigation Ω is discretized with triangular elements ω_e as shown in figure 2.1). In this process, the number of degrees of freedom of the system is decreased to a finite number n_{dof} depending on the number of nodes n_{node}, the space dimensionality n_{sp}, and the displacements boundary conditions on Γ locking n_{lock} degrees of freedom. Thus for an elastic medium, for example,

$n_{ndof} = n_{node} * n_{sp} - n_{nlock}$. There is not, in general, a simple relationship between the degree of freedom index and the node index, except for some extremely simple geometries. This is why we write

$$d_k = u_j^i \quad \text{with} \quad k = f_{ind}(i, j) \tag{2.9}$$

where d_k is the displacement component for the kth degree of freedom corresponding to the jth component of the displacement field at the ith node.

Second, equation 2.7 is integrated over Ω, yielding the following equation:

$$\frac{d}{dt} \frac{\partial}{\partial \dot{d}_k} \left[\int_\Omega KE \right] = \frac{\partial}{\partial d_k} \left[\int_\Omega PE \right] \tag{2.10}$$

where d_k is the displacement component corresponding to the $k^t h$ degree of freedom of our grid.

Finally, the previous integral equation is computed numerically. For that purpose, we need to interpolate the nodal values of the displacement field within the element, in an element-independent manner. Mapping triangular elements to a single element, as shown in figure 2.2, allows such an interpolation using the following relation (Zienkiewicz 1971):

$$x(\zeta, \eta) = P_j(\zeta, \eta) x^j \tag{2.11}$$

where the physical coordinates $x(\zeta, \eta)$ are a function of the nodal coordinates x^j, and the transformed coordinates ζ, η. For a triangular element (or any other isoparametric element, as described in the next section), the same interpolation functions can be used for all nodal variables, and in particular for the displacement variables and elastic moduli. For example:

$$u_i(\zeta, \eta) = P_j(\zeta, \eta) \times u_i^j \tag{2.12}$$

where the polynomials P_j are defined in the following manner for an isoparametric triangular element:

$$P_1(\zeta, \eta) = 1 - \zeta - \eta, \, P_2(\zeta, \eta) = \eta, \, P_3(\zeta, \eta) = \zeta \tag{2.13}$$

Reducing the integration domain of equation 2.10 to one element, both sides of 2.10 can be computed very easily yielding the following equations for one of the element shown in figure 2.1:

$$\frac{d}{dt} \frac{\partial}{\partial \ddot{u}_i^0} \left[\int_{\omega_e} KE \right] = \rho \frac{A}{12} (2\ddot{u}_i^0 + u_i^1 + u_i^2) \;\; for \;\; i = 1, 2 \tag{2.14}$$

The previous equation assumes that the mass of the element is evenly distributed over its surface. Similarly, for the right side of equation 2.10, the following equation can be written:

$$\frac{\partial}{\partial u_i^0} \left[\int_{\omega_e} PE \right] = 2 \int_{\omega_e} c_{klmn} \frac{\partial e_{kl}}{\partial u_i^0} e_{mn} \tag{2.15}$$

where e_{kl} can be written as follows after discretization and integration:

$$e_{ij} = \frac{1}{2} \left(a_{j1}(-u_i^0 + u_i^2) + a_{j2}(-u_i^0 + u_i^1) + a_i 1(-u_j^0 + u_j^2) + a_i^1(-u_j^0 + u_j^1) \right) \tag{2.16}$$

In the last equation, a_{ij} is an element of the Jacobian matrix for the transform from the real world coordinate system to the elemental coordinate system. (figure 2.2). The numerical integration is performed in the elemental coordinate system and can be carried out explicitly in the case of three-noded elements, thereby speeding up the computation. After integration, equation 2.10 can be written as follows, for a single element shown in figure 2.1:

$$\ddot{m}_i^e \times d_i = k_i^e \times d_i + f_i \tag{2.17}$$

with d defined by the equation:

$$d_i = u_i^0 \, i = 1, n_{dim} \tag{2.18}$$

An equation similar to equation 2.17 can be written for each degree of freedom of the system, yielding a linear differential system of equations that must be integrated. The system of equations has the following form:

$$\mathrm{A}_{n_{element}} m^e \ddot{d} = \mathrm{A}_{n_{element}} k^e d + f \qquad (2.19)$$

where A is the assembly operator that groups the various elemental mass matrices (impedance matrices) into a single mass matrix M (impedance matrix K). The solution of equation 2.19 implies that M needs to be inverted in order to perform the time integration. It can be easily demonstrated (Zienkiewicz, 1971) that M is a positive definite matrix, and $K = \mathrm{A}_{n_{element}} k^e$ is a negative definite matrix. Following the definition of M in equations 2.14 to 2.18, we see that M is sparse, since it only has three elements per row. But as shown in figure 2.1, it cannot be a band diagonal matrix. To be band diagonal, nodes belonging to the same element must have contiguous indeces. This can only be achieved with extremely simple grids. The bandwidth of the matrix is therefore determined by the maximum distance separating the indeces of two nodes in a same element i.e. by the way the grid is indexed. To minimize the bandwidth of M, the node indices must be arranged in such a way that they minimize the indices differences for each element in the grid. This is easily achieved in the case of elongated grids, but grids that have an equal number of elements on each side tend to maximize the distance between node indices of a single element.

The distribution or weight of each element within the mass matrix however is not conditioned by the grid indexing but instead by the elements geometry and the way equation 2.14 is obtained. Two assumptions remain arbitrary in regard to the way both K and M were computed:

- The integration domain is the element itself.

- The mass distribution over the element is uniform.

Both assumptions strongly condition M and K, and therefore the way by which the finite-element problem is solved, since M will be inverted to solve equation 2.19.

For the first hypothesis, if we choose the cluster of elements that all contain node 0 as the domain of integration as shown in figure 2.1, and keep the mass distribution over the element uniform, the contribution of the cluster to equation 2.10 can be written as:

$$k^e \times d = \rho \frac{A}{12} \left(12\ddot{u}_i^0 + 2 \sum_{k=1,6} u_i^k \right) \tag{2.20}$$

thus dramatically increasing the weight of the diagonal terms. Another, yet more algebraic, interpretation is available to understand the last equation. As M is assembled, all the equations where u_i^0 appears are summed to yield one unique equation, where the mass coefficient of this displacement component is dominant. Since the same operation can be performed for all the other degrees of freedom, it does not reduce the number of equations, but just rearranges the coefficients, and significantly increases the bandwidth of M. Both interpretations are related to the linearity of the integration operator where the integral over the cluster is the sum of the integrals over the elements belonging to the cluster.

Another way of modifying the mass operator is by choosing again the element as the integration domain, and co-locating the mass of the element at its nodes. This way the mass matrix can be made diagonal, yielding the following equation:

$$k^e \times d = \rho \frac{A}{2} \left(\ddot{u}_i^0 \right) \tag{2.21}$$

this time, the mass matrix is lumped to its diagonal terms, yielding a diagonal mass matrix after assembly.

In the case of triangular elements, most of the computations for the mass and impedance matrices contributions can be made analytically. Analytical expressions
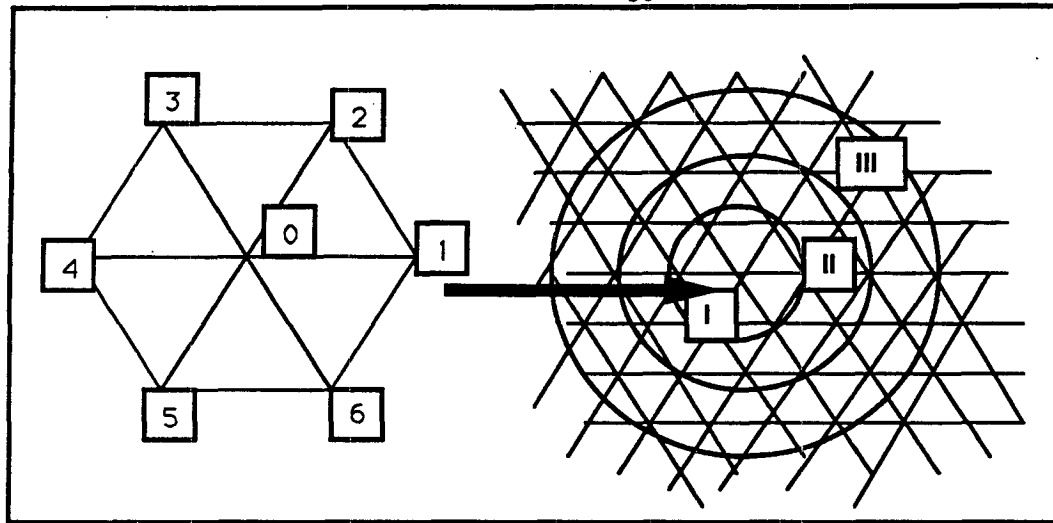
Figure 2.1: A cluster of triangular elements and its relation to the finite-element mesh. The cluster presented on the left is actually chosen as the integration domain for the finite element formulation of the wave propagation problem. On the right the neighbors of a point lie at a given element distance. The first row of neighboring points belong to the same elements as the center point.
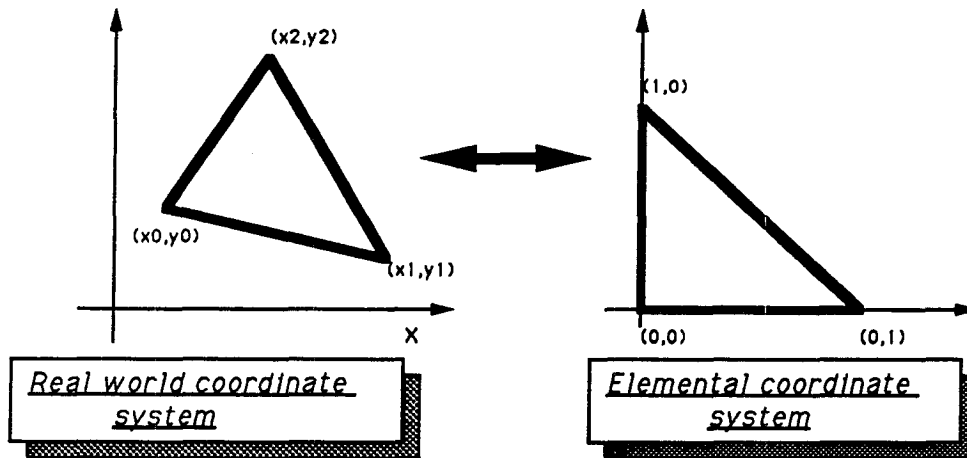
Figure 2.2: Coordinate transformation between the real world coordinate system, and the elemental coordinate system in which all the differentiation and integration required to obtain equation 2.16 are performed.

are not in general available for higher order elements, and the integration in equation 2.14 is performed numerically by Gaussian or Labatto quadrature (Hughes 1984). The choice of the weights for the quadrature depends on the function basis for which the quadrature is exact. The choice of the basis functions provides yet one more opportunity to redefine m^e, and provides further means to justify the lumping of the mass terms to a diagonal term.

Since both M and K can be arbitrarily modified, the choice for the definition of these operators resides in the optimization of the solution process. Two elements have to be taken into account: the speed at which the actual problem is solved, and the accuracy obtained for a given algorithm.

2.2.3 Numerical integration of the discretized finite-element equations.

Using a second-order central difference algorithm for time integration yields the following time stepping solution for equation 2.19 (after Sword 1986):

$$d(t + \Delta t) = \Delta t^2 M^{-1} [Kd + f] + 2u(t) - u(t - \Delta t) \qquad (2.22)$$

Since M needs to be inverted, many solutions are available, as seen in the preceding section. We can design M to be diagonal, therefore eliminating the inversion step. This option yields a simple explicit algorithm, but as section 2.2.2 shows a fairly poor numerical dispersion. But first, an approximate inversion algorithm is described in this section that provides new insights into the behavior of finite-element operators.

In equation 2.20, the diagonal terms of m^e are six times bigger than the off diagonal terms, which justifies the use of an approximate inversion of M based on a Taylor expansion of the inverse matrix. First, decomposing M in a diagonal term M_d and an off-diagonal term M_e as proposed by Sword (1986), we get

$$M^{-1} = \left[I - M_e * M_d^{-1} \right]^{-1} M_d^{-1} \qquad (2.23)$$

where I is the identity operator. Since the off-diagonal terms of M are smaller than the diagonal one, the terms of $M_e * M_d^{-1}$ are smaller than one, and therefore, the inverse can be computed with a truncated Taylor expansion as follows.

$$M^{-1} = \left[I - M_e * M_d^{-1} + (M_e * M_d^{-1})^2 - .... \right]^{-1} M_d^{-1} \qquad (2.24)$$

The inversion of M now only requires the inversion of M_d, and the multiplication of d with M_e, which only contains six terms per row. The inversion of M by this process is reduced to nN operations with $n << N$ instead of $log(N)N^2$ operations for an optimum complete inversion of M, with N being the length of d. This inversion can be interpreted in terms of the spreading of the differential operators away from the center node of the elemental cluster, as shown in figure 2.1. For a zero order inversion, $M^{-1} = M_d^{-1}$, further multiplyed by K, we see that $u_i^0(t + \Delta t)$ is a linear combination of the displacements component sampled within the cluster immediately surrounding node 0. For a first order inversion, the previous argument can be recursively implemented, showing that this time $u_i^0(t + \Delta t)$ is a now linear combination of the components sampled within ring II, shown in figure 2.1, and so on. The order of the inversion of M therefore controls the spreading of the numerical differential operators, and further controls the accuracy of our quadrature algorithm. Finally, the inversion algorithm presented here for M does not depend on the topological distribution of the nodes indices. Since M can be very large (10000 × 10000) only the non-zero terms are stored as well as the transfer function f_{ind} that relates node and component indices to degree of freedom indices. These being provided, the inversion proposed here does not depend on the distance between degrees of freedom indices of two nodes belonging to the same element.

2.2.4 Numerical dispersion and anisotropy

Since the finite-element formulation of our problems allows for multiple implemen-

tations, a mean by which the efficiency of these various algorithms can be evaluated needs to be devised. Two criteria are retained for this evaluation: numerical dispersion, and numerical anisotropy

Both can quantities can be computed by using the Fourier transform of equation 2.14 and 2.15. From equation 2.14, we can write

$$FT \left[\frac{(d(t + \Delta t) - 2d(t) + d(t - \Delta t))}{\Delta t^2} \right] = \frac{2 FT(d(t))}{\Delta t^2} e^{(i\omega t)} * (\cos(\omega \Delta t) - 1) \quad (2.25)$$

for the time stepping algorithm. Equation 2.15 then transforms as follows:

$$A \left[\begin{array}{c} FT(u_1^0) \\ FT(u_2^0) \end{array} \right] = \left[\begin{array}{cc} b_{11} & b_{12} \\ b_{21} & b_{22} \end{array} \right] \left[\begin{array}{c} FT(u_1^0) \\ FT(u_2^0) \end{array} \right] \quad (2.26)$$

Where A is defined by the following relationship:

$$A = \frac{1}{\Delta t^2} (\cos(\omega \Delta t) - 1)(6 + \sum_{i=1,6} e^{(ik_x(x^i - x^0) + ik_y(y^i - y^0)} \quad (2.27)$$

A can thus be rewritten to emphasize the origin of the previous terms, depending on whether they come from the diagonal or off diagonal terms of M:

$$A = \frac{1}{\Delta t^2} (\cos(\omega \Delta t) - 1)(A_d + A_e(k)) \quad (2.28)$$

The matrix $[b_{ij}]$ is computed numerically from equation 2.15, and is a Hermitian matrix whose eigenvalues are real and positive. A is split after Fourier transform into A_d, which is not a function of the wave number and corresponds to the diagonal part of m^e, and $A_e(k)$, which is a function of the sampled wavenumber and corresponds to the off-diagonal terms of m^e. From the previous equation, we see that A must be an eigenvalue of $[b_{ij}]$ which yields the following equation:

$$(A_d + A_e(k)) * (\cos(\omega \Delta t) - 1) = \Lambda_i(k) \quad (2.29)$$

where Λ_i is one of the two eigenvalues of $[b_{ij}]$. Equation 2.27 shows that the Fourier transform corresponding to both the mass and impedance matrices are a function of k. The computation of the numerical phase velocity $v_\phi = \frac{\omega}{k}$ can only be carried out explicitly for a regular hexagonal cluster of elements in an isotropic acoustic material (Sword 1986). For any other geometry, the solution to equation 2.29 is numerical.

Using a similar method, we can compute the group velocity using $v_g = \frac{\partial \omega}{\partial k}$. Equation 2.27 can then be reparametrized as a function of η_{el}, the number of wavelength per elements which is a direct measure of the efficiency of our algorithm: in figure 2.3, the numerical dispersion indicates that $\eta_{el} = 0.1$ to 0.15 yields 98 % accurate velocities. The effect of numerical anisotropy is not yet felt in that region. However this first estimation of η_{el} has to be revised in view of figure 2.4. The dispersions in figure 2.3 assume that the inversion of M is complete: that is, equation 2.27 can be solved as:

$$\cos(\omega\Delta t) - 1) = \frac{K(k)}{(A_d + A_e(k))} \tag{2.30}$$

which is not relevant in the case studied since the mass matrix is only inverted with the Taylor expansion of its inverse, therefore solving the equation:

$$\cos(\omega\Delta t) - 1 = K(k) * A_d^{-1} \left[1 - A_e(k) * A_d^{-1}....\right] \tag{2.31}$$

Since the convergence of the previous expansion is slow as figure 2.4 indicates, we see that the n_{el} region of investigation provided by this algorithm is extremely restricted if we want to keep a small number of iterations for the matrix inversion. For that reason, this algorithm is not suitable for our purpose. The implications of this last observation are broad. Zienkiewicz (1971), and later Hughes (1984) noticed that partial matrix inversions yield fairly poor results using the finite-element method. The main consequence of partial inversion is that low wavenumbers are poorly accounted for, leaving so called low frequency 'standing modes' trailing behind the wave fronts

and therefore including a fair amount of numerical dispersion. The method we are now going to investigate is based on the full inversion of the finite-element operators.

2.3 The implicit-explicit finite-element algorithm

2.3.1 Description of the implicit-explicit finite-element algorithm

2.3.1.1 Optimization the dispersion relation

As seen in the previous section, the computation of the mass matrix is arbitrary, and an optimum needs to be found that minimizes the dispersion and maximizes the numerical efficiency. No general theory has been found to perform a systematic optimization of this process. Sword (1986) suggests that optimization can be achieved by incorporating a new factor in equation 2.20. In the case of Sword's modeling, this coefficient is related to the thickness of the plate where the propagation takes place.

Hughes (1984) introduces a similar parameter, r which is admittedly arbitrary. He provides two tentative justifications for such a manipulation:

- the mass distribution over the element is not uniform, and r is introduced so that the mass of the element remains constant independent of the mass distribution over the element.

- the weights used for numerical integration can be modified to be consistent with different families of element interpolators.
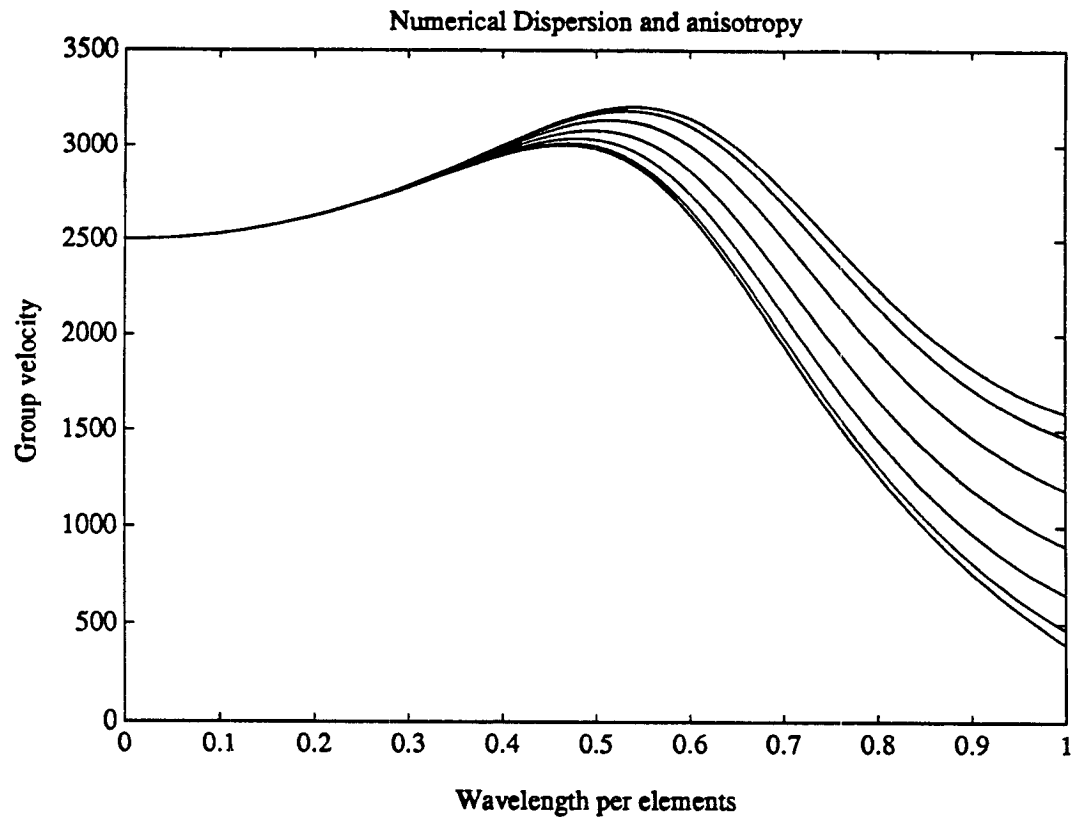
Figure 2.3: Numerical dispersion and numerical anisotropy for a cluster of triangular elements. Each of the curves plotted here is for a different propagation angle, showing the anisotropy increasing with higher number of wavelengths per elements.
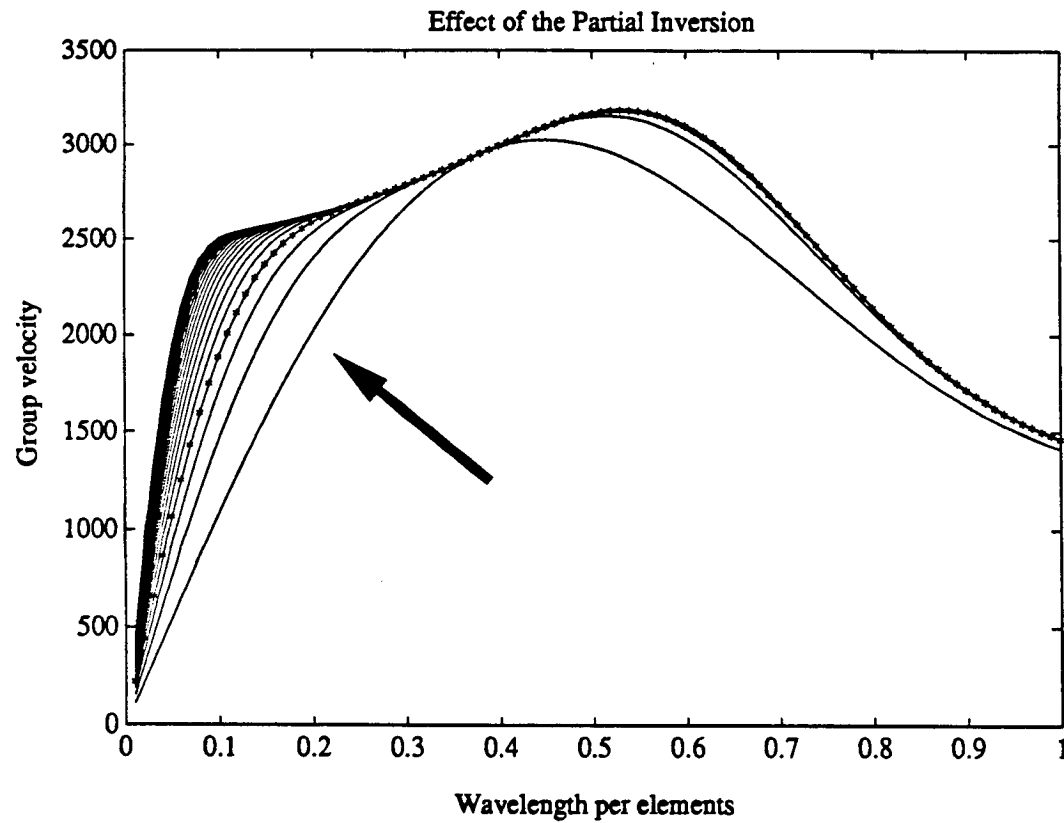
Figure 2.4: Effects of the partial inversion of the mass operator. Following
the arrow, the expansion order from equation 2.28 increases from 1 to
40. Notice that low wave numbers either do not propagate or propagate
at very low velocity, yielding a DC displacement level over the grid.

Neither justification however clearly establishes a link between the way the mass matrix is built and the performance of the overall solution algorithm. With this new parameter, equation 2.20 can be easily rewritten as:

$$m^e \times d = \rho \frac{A}{12} \left((\frac{1}{2} - r)\ddot{u}_i^0 + 2 * r \sum_{k=1,6} \ddot{u}_i^k \right) \qquad (2.32)$$

Figure 2.5 shows the various dispersion curves as r varies from 0 (the diagonal or lumped mass matrix) to $\frac{1}{6}$ which is the case we have in section 2.1 (Consistent mass matrix) to $\frac{1}{12}$ which is the optimum case (the higher order mass). Varying r actually allows the user to implement fairly controlled dispersion, or attenuation. However, when dispersion is unwanted, which is the case here, we want the dispersion curve to be as flat as possible. This is achieved with $r = \frac{1}{12}$ for a non diagonal matrix, or $r = 0$ if a diagonal mass matrix is desirable.

2.3.1.2 Matrix structure and inversion technique

The typical structure of M^* is presented in figure 2.7. As we anticipated, the large matrix bandwidth corresponds to the part of the grid where maximum accuracy is demanded, that is the borehole region. This region typically contains 20×200 elements, therefore presenting a very high contrast between the horizontal and vertical number of samples. This, we know (2.1.2) limits the bandwidth of M^*. For the major part of the grid (away from the borehole region) an explicit algorithm is used which yields the diagonal part of M^*.

The structure of M^* will be properly exploited by an inversion that neither operates nor stores the null elements of this matrix, which is extremely sparse. This is achieved by the partial inversion scheme presented in equation 2.22, which has the further advantage that it does not depend on the bandwidth of the matrix. However, the convergence of this algorithm is slow for small wave numbers which makes it unsuitable for our study.
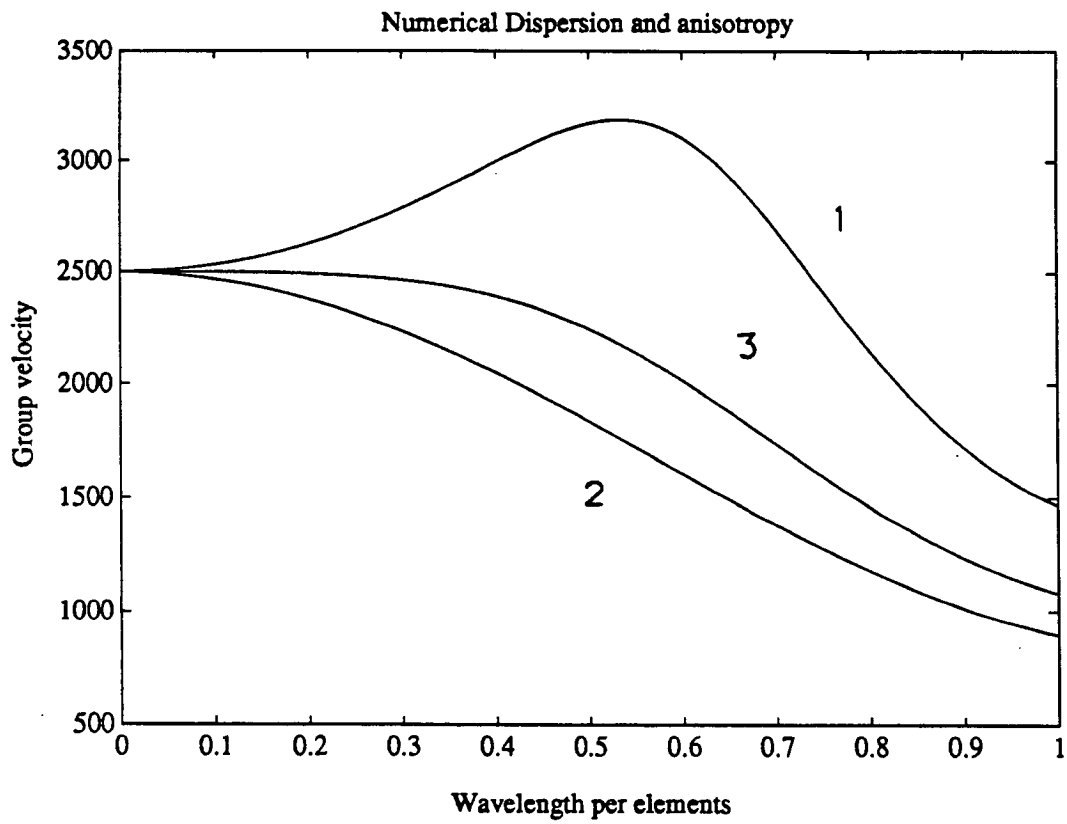
Figure 2.5: Dispersion relations for various types of mass matrices. The three curves are plotted for 1) $r = \frac{1}{6}$, 2) $r = 0$, 3) $r = \frac{1}{12}$.

The Crout elimination, which is a variation of the Gauss pivoting technique (Hughes 1984) provides a suitable inversion algorithm for the following reasons:

- it profits by the fact that M^* is diagonal in the explicit part of the computation.

- it only needs to use or store elements that are above the skyline of the matrix (figure 2.6).

- this algorithm can be completely vectorized.

However this algorithm is non-optimum since the number of operations required by the inversion depends on how close the skyline of M^* is from the diagonal, that is on how far apart are the degrees of freedom indexes within one element.(The skyline a matrix M is defined by Hughes 1984 as the difference between the diagonal index of the matrix, and the index of the last non null element away from the diagonal. This notation can only be used for diagonal matrices, which is the case here).

Nevertheless, I used the Crout algorithm for this integration, and its efficiency was found to be comparable to that of the limited inversion algorithm for very elongated grids where the bandwidth of M^* remains fairly small.

2.3.2 Boundary conditions

Besides its capability of managing geometrically complex systems, the finite-element method is also attractive because it allows the explicit handling of boundary conditions which are treated implicitly by other methods such as finite-difference. This is especially important for this study where multiple types of boundary conditions are met. The following types of boundary conditions are described in this section:

- the source boundary conditions

- the fluid-solid boundary conditions

- the solid-solid boundary conditions

- the absorbing boundary conditions

2.3.2.1 Source boundary conditions

As previously stated, this study is limited to the mechanical effects of downhole source design on their radiation patterns. However, most downhole sources are complex, coupled, electro-mechanical or hydraulic systems. This is especially true for piezoelectric fluid-coupled sources. Since such a problem is beyond the scope of this study, the source mechanical effects are modeled by equivalent sets of stress-displacement boundary conditions applied on the outer surface of the source itself. These conditions fall under two categories : the fluid-solid boundaries, and the solid-solid boundaries.

2.3.2.2 Fluid-Solid boundary conditions

As shown in figure 2.7, the boundary conditions at the fluid-solid contact can be summarized as follows:

$$\tau_{zz} = P_{fluid} \tag{2.33}$$

$$u_{z_{Rock}} = u_{z_{fluid}} \tag{2.34}$$

the first condition insures the continuity of the normal stresses across the boundary, and the second stipulates that there cannot be any cavitation effect at the fluid-solid boundary, in other words that the fluid and the solid always remain in contact.

From the finite-element point of view, the fluid and the solid are perceived as different but coupled systems. Since pressures only are computed in the fluid, τ_{zz} is computed in the solid as a linear combination of the nodal displacements, and applied to the fluid as a nodal variable at the boundary node . Conversely, the normal

displacements in the fluid can be computed as a linear combination of the pressures at the nodes surrounding the boundary nodes, and are directly applied as a nodal variable to the solid. Applying the previous equalities allows complete enforcement of the fluid solid boundary conditions.

Finally and probably most importantly, the set of boundary conditions described in equations 2.42 and 2.43 allows the fluid to slide parallel to the boundary between fluid and solid as shown in figure 2.7 finite-difference types of algorithms in general do not allow us to implement such boundary conditions, since finite-difference algorithms cannot support coupled systems.

2.3.2.3 Solid-solid boundary conditions

The grids used to model both solids are two separate coupled grids, similar to those described for fluid-solid boundary conditions. The displacements on one grid boundary are given the very same values as on the other grid boundary, since the real point that lies at the boundary has only two degrees of freedom and not four. In this case it can easily be shown that the equality of the boundary displacements on both sides also enforces the continuity of traction along the boundary (Zienkiewicz 1971).

It can be noted that node duplication along the boundary is not efficient, unless slip occurs at the boundary which is not our case. In terms of computer efficiency, duplication of nodes is not significant, since the size of the operators M and K are given by the number of degrees of freedom of the grid, which is unchanged whether or not the nodes are duplicated. The node duplication scheme was adopted because it provides a unified approach to the implementation of boundary condition algorithms, whether they are fluid-solid boundaries or solid-solid boundaries.
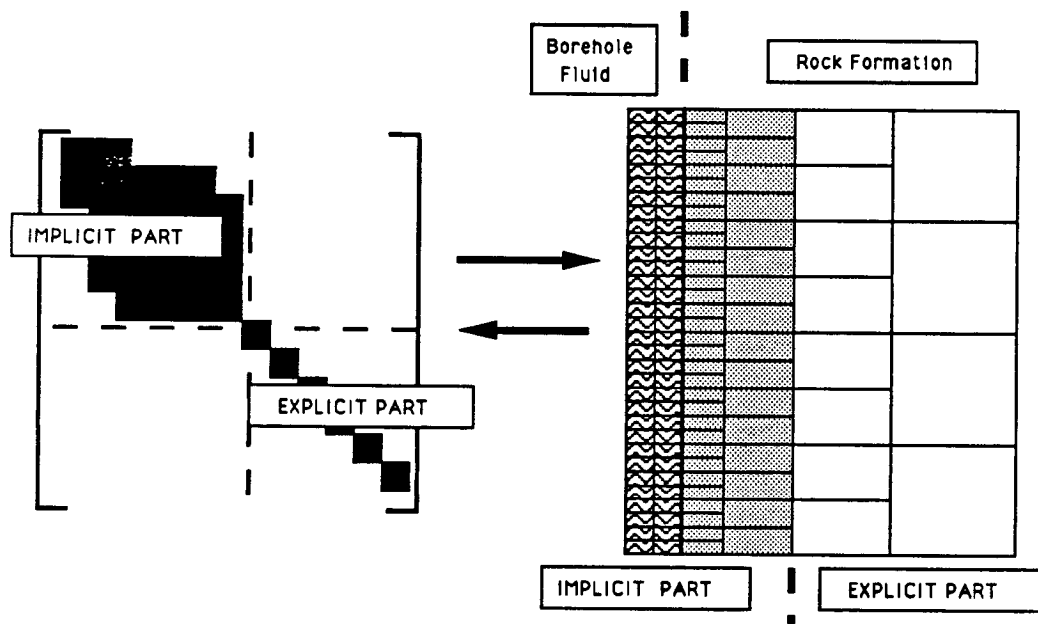
Figure 2.6 : The principle of the implicit-explicit finite-element algorithm.
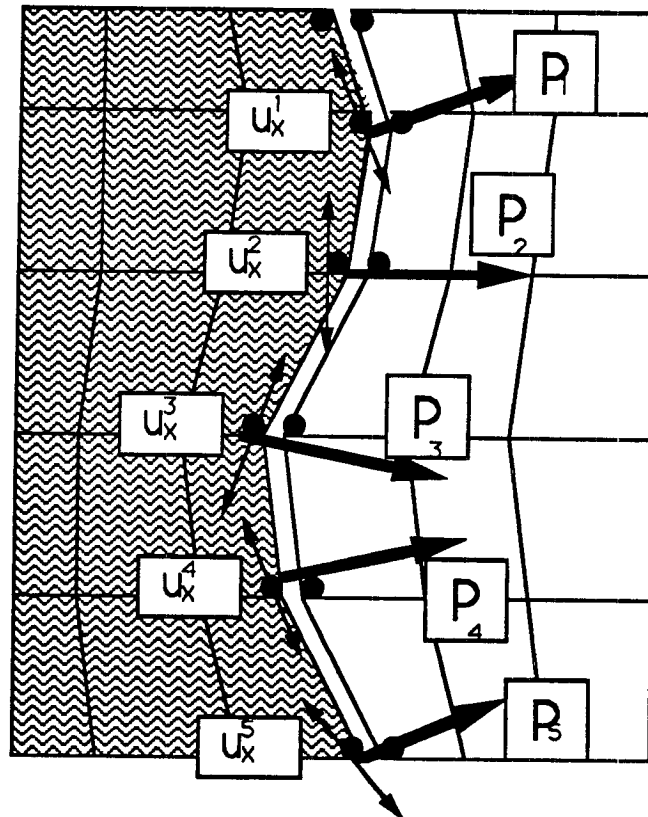
Figure 2.7 : Description of the fluid-solid boundary conditions.

2.3.2.4 Absorbing boundary conditions

Multiple methods can be used to implement absorbing boundary conditions to eliminate unwanted reflections from the edge of our model. The simplest implementation is to apply a dumping factor γ_{absorb} of the following form to each node in the grid (Kosloff 1982):

$$\gamma_{absorb} = 1. \text{ for } d_{edge} > d_{min} \tag{2.35}$$

$$\gamma_{absorb} = e^{-\frac{d_{edge}^2}{\delta^2}} \text{ for } d_{edge} =< d_{min} \tag{2.36}$$

Typically, d_{min} is equal to the average wavelength propagated, and δ is computed in such a manner that γ_{absorb} is never smaller than 0.98. The algorithm for absorbing boundary conditions was found to be extremely efficient for all modes incident on the outside boundary of our system, independent of the incidence angle.

The following algorithms to model absorbing boundary condition exist, but they are not in general numerically efficient, and do not perform well for every mode incident on the boundary:

- The use of the paraxial wave equation at the edge of our system could be implemented. This method, however, does not perform well for grazing angle incidence on the boundary, or for guided modes incident on the boundary.

- In a manner similar to that proposed in section 2.4, a hybrid finite-element boundary-element method could be implemented. Such a method would, however, require that the time integration be performed in the frequency domain as with the pseudo-spectral methods proposed in chapter 4. Another drawback of this method the need to have only homogeneous layers at the boundary between the finite-element, and the boundary-element mesh in order to be able to devise analytical solutions for the far field wave propagation.

Because of their limitations, I did not implement these two methods, preferring the absorbing buffer condition, which ensures that at least 98% of all energy incident on the outer boundaries of our system will be absorbed no matter what mode is incident.

2.3.3 Benchmark: The Heelan solution

Our implicit-explicit finite-element algorithm is benchmarked to test the algorithms that have been implemented. One case of modeling is of particular interest to us: the Heelan solution. This analytical solution for the elastodynamic wave equation solves for the far field radiated by a finite length cylindrical source in a homogeneous elastic medium. This solution is of special interest for our problem since it is often referenced for downhole source radiation patterns, despite the fact that it does not include borehole effects.

The far-field radiation of a finite-length cylinder in a homogeneous medium can be written as follows (Heelan, 1963 and White, 1973):

$$u_r = \frac{\pi a^2 d P_0}{4\pi \mu \alpha r}[1 - 2\frac{\beta^2}{\alpha^2}\sin^2 \phi]\dot{g}(t - \frac{r}{\alpha}) \qquad (2.37)$$

$$u_t = \frac{\pi a^2 d P_0 \sin \phi \cos \phi}{2\pi \mu \beta r}\dot{g}(t - \frac{r}{\beta}) \qquad (2.38)$$

where a is the radius of the source, d its length, P_0 the pressure increment of the source, α the P wave velocity, β the S wave velocity, μ the shear modulus of the rock, r the distance from the source , ϕ the angle from the horizontal, t the time, and $\dot{g}$ the first time derivative of the source time history.

The parameters selected for all the modeling cases are the following: $\alpha = 5091m/s$, $\beta = 3042m/s$ $d = 16m$, $a = 0.06m$, the density of the rock $\rho = 2700Kg/m^3$,and $P_0 = 1000Pa$. The source time history is a Ricker function with a $35Hz$ central frequency, and its spectrum spans from 10 to $70Hz$. Finally, the time sampling

Radial Displacements

Tangential Displacements
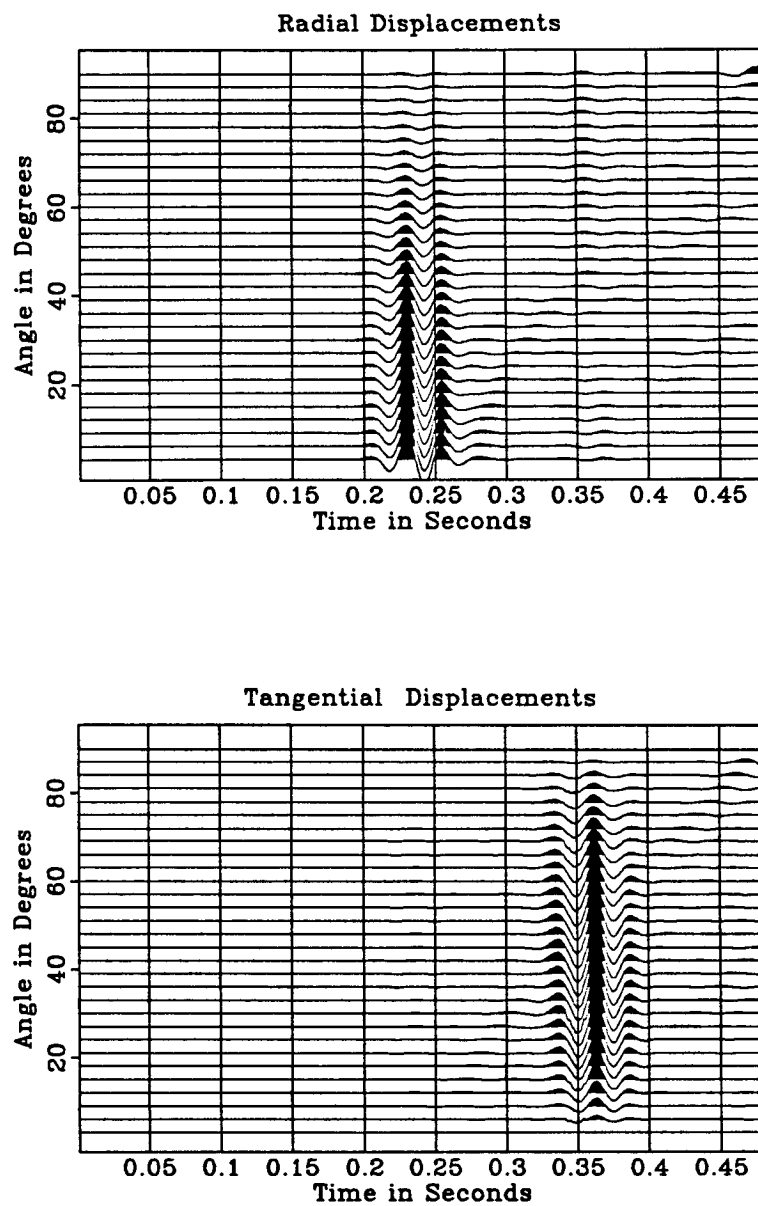
Figure 2.8: Radial and tangential components of the field radiated by a finite-length cylindrical source in a homogeneous medium. The receivers are placed around the source at $580m$ distance. Each trace is recorded for an angle θ varying from 0 along the horizontal to 90^0 along the vertical.

$\Delta t = 0.0004s$, and the spatial sampling $dx = 8m$. The computation was made using the implicit-explicit algorithm. The implicit region is located in the source neighborhood, and the rest of the grid is modeled using an explicit algorithm.

Results in figure 2.9 display the radiated field recorded on receivers placed around the source. For this acquisition geometry, and since the modeling is performed in a homogeneous isotropic solid, the compressional waves are sampled on the radial component of the field, and the shear waves on the tangential component as shown in equation 2.47 and 2.48. The compressional waves have maximum amplitude along the horizontal and decay away from the horizontal to reach a minimum at the vertical. The decay rate is directly a function of Poisson's ratio, as is the amplitude of the compressional waves along the vertical. The shear waves, on the other hand, are null along the horizontal and vertical directions, and reach their maximum at 45^0 from the horizontal. figure 2.10 compares numerical and analytical radiation patterns for both compressional and shear waves. There is a very good agreement between the two results, confirmed by the match of the detailed waveforms displayed in figure 2.11.

The only major discrepancy between numerical and theoretical results arises from the shear waves' radiation pattern. This discrepancy is not caused by numerical dispersion or anisotropy since our modeling is performed for space and time samples well below the limit where these artifacts become significant. More likely, this discrepancy is a result of the violation of one of the major assumptions that leads to the Heelan solution, that the source length must be small compared to the radiated wavelength. In our modeling case, the source length is $16m$ for an average wavelength of $86m$, and a minimum wavelength of $43m$. As shown in figure 2.12, the discrepancy for the radiation pattern of shear waves is dramatically reduced if the source length is reduced by a factor of 2. This effect can be intuitively understood as a source focusing
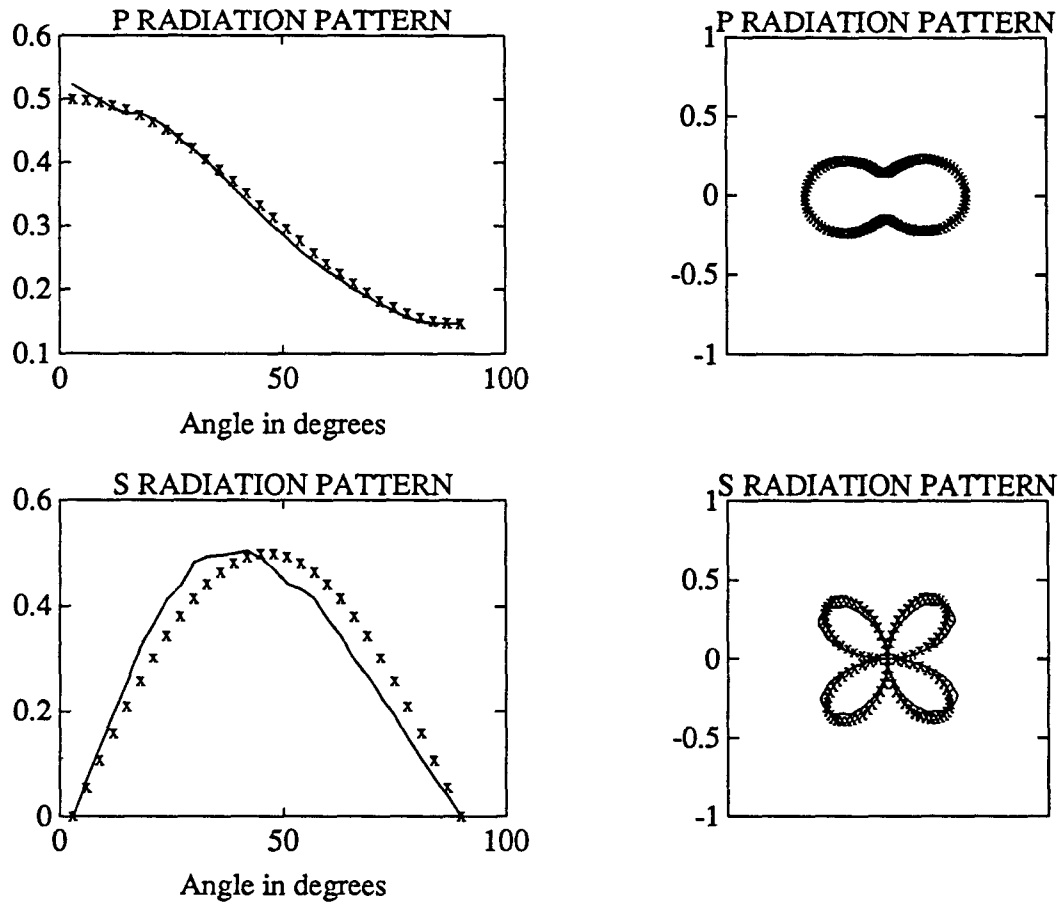
Figure 2.9: A comparison between numerical (solid line) and analytical (x line) radiation patterns: for compressional (P) waves (top) and shear (S) waves (bottom).
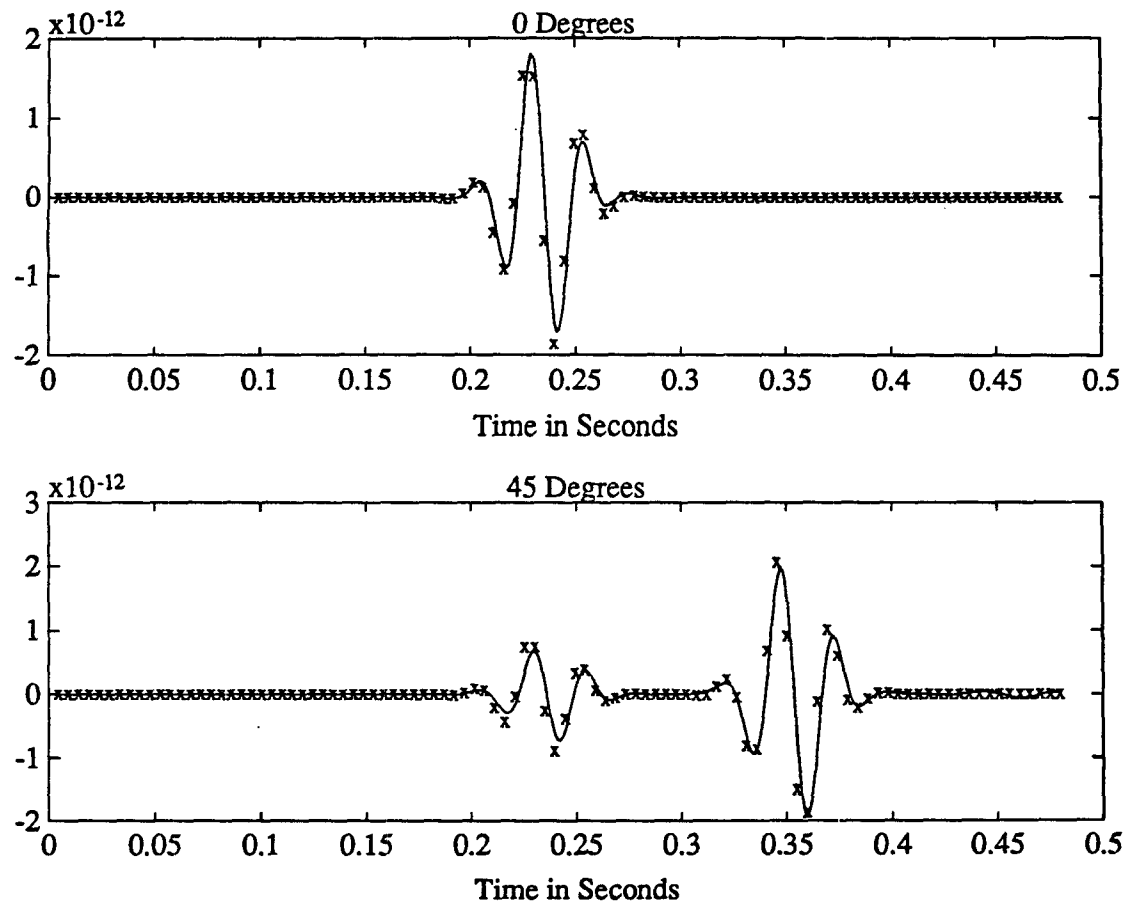
Figure 2.10: A waveform comparison of the horizontal component of the displacements at 0^0 (top), and 45^0 (bottom) for the analytical solution (x line), and the numerical solution (solid line).

effect. The longer the source compared to the wavelength, the greater the departure from the Heelan solution, since the source then tends to focus its energy along the direction orthogonal to the source axis.

The implicit-explicit finite-element algorithm performed well and efficiently in the simple case of a finite length source in a homogeneous medium. These results also indicate that the implicit explicit finite-element algorithm is adequate for studying the effects of source geometry on radiation pattern of downhole sources. However, the question remains whether this algorithm is optimum, and the answer is no. The comparison between the dispersion relations of the explicit finite-element algorithm and finite-difference algorithm clearly indicates that the explicit algorithm is not an optimum local differentiation operator. Since for a typical cross-well geometry the interwell regions can be modeled on a regular mesh, the question rises of how we can profit from the efficiency of finite-difference in the cross-well region, and adequately model the downhole-source borehole system ?

2.4 Hybrid finite-element finite-difference algorithm

To really profit by the efficiency of the finite-difference method, we need to implement long spatial operators (Dablain 1986) explicitly. This implementation is incompatible with the basic assumption of finite-element theory that long spatial operators can only be implemented implicitly through the inversion of a linear combination of the mass and impedance tensors. Furthermore, in general, finite-element computations are co-located at the nodes of the mesh. Finite-difference computations, in contrast, are staggered. To better understand what the requirements are to perform a hybrid computation let us first focus on the implementation of the finite-difference method.
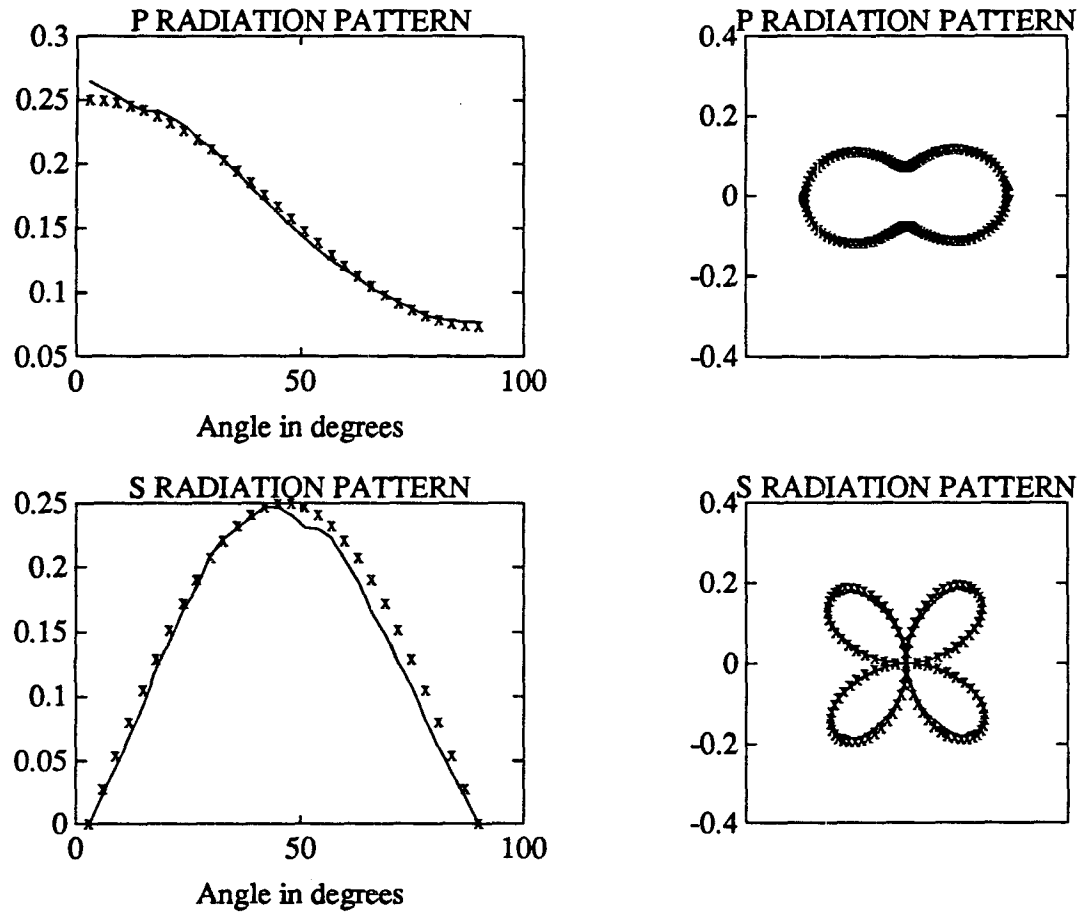
Figure 2.11 : A comparison between numerical (solid line) and analytical (x line) radiation patterns: for compressional waves (top) and shear waves (bottom). The difference between this figure and figure 2.10 is the shorter source length, which tends to eliminate the source focusing effect along the horizontal.

2.4.1 A short glimpse at finite-difference theory

Solving the elastodynamic wave equation (equation 2.2 to 2.6) by finite-difference, is performed by approximating the spatial operators by linear convolution operators of finite length. Since finite-difference is usually performed on regular grids, once we find the convolution operator, we can apply it to any part of the grid. The solution of equation 2.2 is therefore obtained by substituting the partial differential operators as follows:

$$\left(\frac{\partial v}{\partial x_i}\right)_{x_i=X} = \sum_{k=1,n_l} a^k v^k \tag{2.39}$$

where n_l is the length of the convolution operator. Muir and Dellinger (1987) proposed a way of building finite length convolution operators for filtering purposes. These operators have been selected not only because they can be used as differential operators, but also because they can be used as interpolators. Operators of half length four were selected for the rest of this part.

The central difference algorithm is preferred for time integration, despite the fact that better time integration algorithms could be used, because of the simplicity of its implementation and because it is an explicit operator. This scheme was already presented in this chapter in section 2.2 as a special case of the Newmark family of algorithms, and can be implemented easily with more sophisticated implicit algorithms as previously seen.

2.4.1.1 finite-difference implementation

Since the differential operators that we use are symmetric, the derivatives are computed between two sample points. To overcome this problem, staggered operators are generally used as shown in figure 2.13. First, e_{xx}, e_{zz}, and e_{xz} need to be computed. To assure that all the quantities in equation 2.2 are evaluated at the same location, u_x is evaluated at $x - \frac{1}{2}\Delta x, z$, and u_z is evaluated at $x, z - \frac{1}{2}\Delta z$. Then, using the

shifting property of the differential operator, σ_{xx} and σ_{zz} are evaluated at x, z, and σ_{xz} is evaluated at $x - \frac{1}{2}\Delta x, z - \frac{1}{2}\Delta z$. Thus evaluating the divergence of the stress field, we have:

$$\frac{\partial \sigma_{xx}}{\partial x}(x - \frac{1}{2}, z), \frac{\partial \sigma_{xz}}{\partial z}(x - \frac{1}{2}, z) \tag{2.40}$$

$$\frac{\partial \sigma_{zz}}{\partial z}(x, z - \frac{1}{2}\Delta z), \frac{\partial \sigma_{xz}}{\partial x}(x, z - \frac{1}{2}\Delta z) \tag{2.41}$$

which ensures that the time derivatives of the displacements are updated at the same location as the displacements themselves. This algorithm, however, differs very strongly from the finite-element algorithm in that both components of the displacements in the two dimensional case are not sampled at the same location.

2.4.1.2 Numerical dispersion: comparison with finite-element

Using a scheme similar to the one used in the first part, the numerical dispersion and anisotropy introduced by the finite-difference algorithm can be easily computed (Etgen 1988). The results for the Implicit finite-element algorithm, and the finite-difference algorithm are fairly comparable proving the superiority of the finite-difference algorithms with long spatial operators over the explicit finite-element algorithm which is equivalent to finite-difference using a central difference algorithm for spatial differentiation.

2.4.2 The hybrid principle

The principle of the hybrid finite-element finite-difference algorithm is sketched in figure 2.13. In one dimensional space first (figure 2.13), the finite-element grid provides the displacement boundary conditions on the outer edge of the finite-difference grid. These displacement values are obtained independently from the location of the
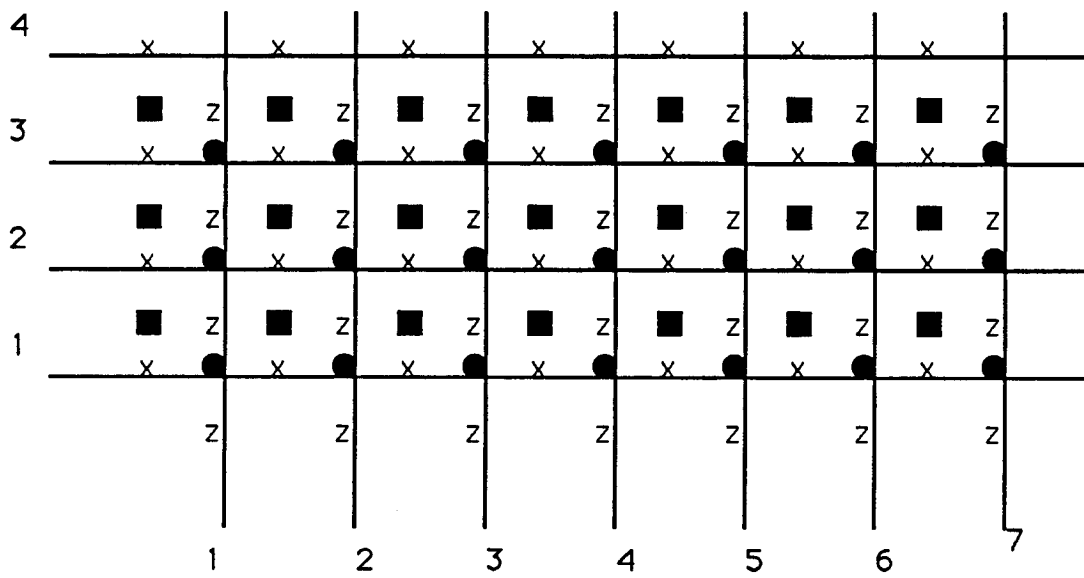
Figure 2.12: A staggered finite-difference scheme (Mora 1986).
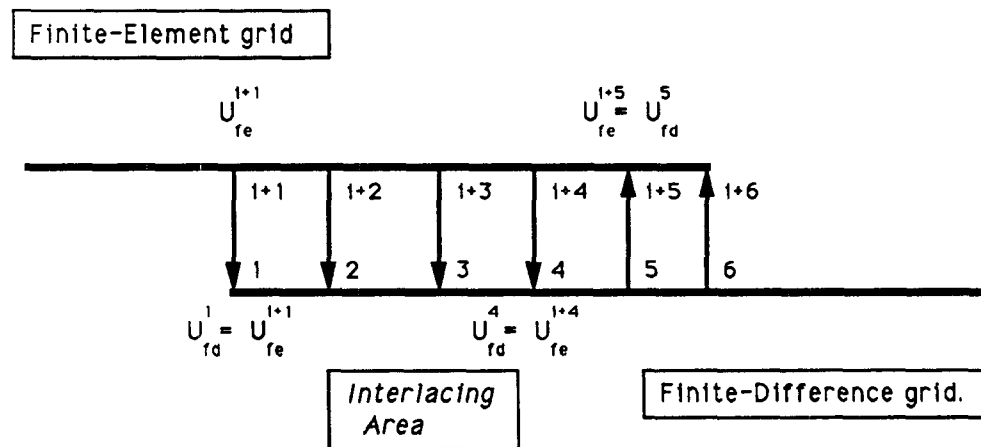
Figure 2.13 : A schematic diagram illustrating the behavior of the hybrid finite-difference finite-element algorithm.

finite-difference point provided that the element location of the point is known: the finite-difference grid's displacements are then computed by interpolation within the element and ued directly, (but not operated upon) in the finite-difference part of the computation. The region of interchange between the finite-element grid to the finite-difference grid spans the first four rows of the finite-difference grid, because the spatial operator we are using has a half length of four. Away from the displacement boundary condition zone, the finite-difference algorithm begins to compute the values of the propagated field. These values are in turn used to compute the displacement field at the nodes of the finite-element mesh. Since the nodes of the finite-element grid can be located anywhere in the finite-difference grid and the finite-difference computations are staggered, the displacements field values computed using the finite-difference method must be interpolated at the finite-element node location.

The interpolator is derived from the discrete differential operator already used. The order of the interpolator must be the same as the one of the differential operator. Not meeting the last requirement results in the instability of the numerical algorithm.

Two remarks can be made at this point about the hybrid algorithm:

- 1) The finite-difference computations are used as an 'infinite' boundary condition for the finite-element grid and vice versa. As shown in the next examples, the energy reflected both at the edge of the finite-element grid and the finite-difference grid is small. It is measured to be less than $\frac{1}{1000}$ of the incident energy on the boundary independent of the incidence angle.

- 2) The finite-element finite-difference grid boundary is transparent both ways. That is, the transmission mechanism from the finite-element grid to the finite-difference grid is the same as the reverse mechanism which ensures that this boundary is transparent independent of the incident wave.

The time integration algorithm used for the hybrid algorithm is exactly the same

as the algorithm for the implicit-explicit finite-element method. They both use an implicit Newmark algorithm for the finite-element side, and an explicit central difference algorithm on the finite-difference (explicit finite-element) side.

2.4.3 Benchmark of the hybrid solutions

The hybrid algorithm was benchmarked for the case of a horizontal point source in an isotropic homogeneous medium. As illustrated in figure 2.14, The source is placed on the finite-element part of the grid, and the radiated field propagates on from the finite-element grid to the finite-difference grid. Merging the two grids and interpolating the displacements on the finite-difference grid to match the new pixel location, provides the total field snapshots provided in figure 2.15 in which the merging limit is also outlined. No contrast at the boundary between the two grids can be detected visually. A more detailed study of the displacements amplitude along this interface showed that less than $\frac{1}{1000}$ of the energy incident on that boundary is actually diffracted. This result is confirmed by the trace by trace comparisons provided in Fig 2.16 between the hybrid modeling and a straight implicit finite-element modeling.

The advantages of the hybrid method presented here are twofold:

- First, it is faster than the implicit-explicit finite-element implementation because it takes advantage of the numerical efficiency of finite-difference over explicit finite-element, and because the computer implementation of that type of algorithm optimizes the use of vector/parallel central processor unit capabilities. In the case of the example previously shown, the speed gain is approximately a factor of ten.

- Second, it is ideally suited for the study of cross-well wave propagation. The borehole region for this kind of acquisition is in general well recognized, and has
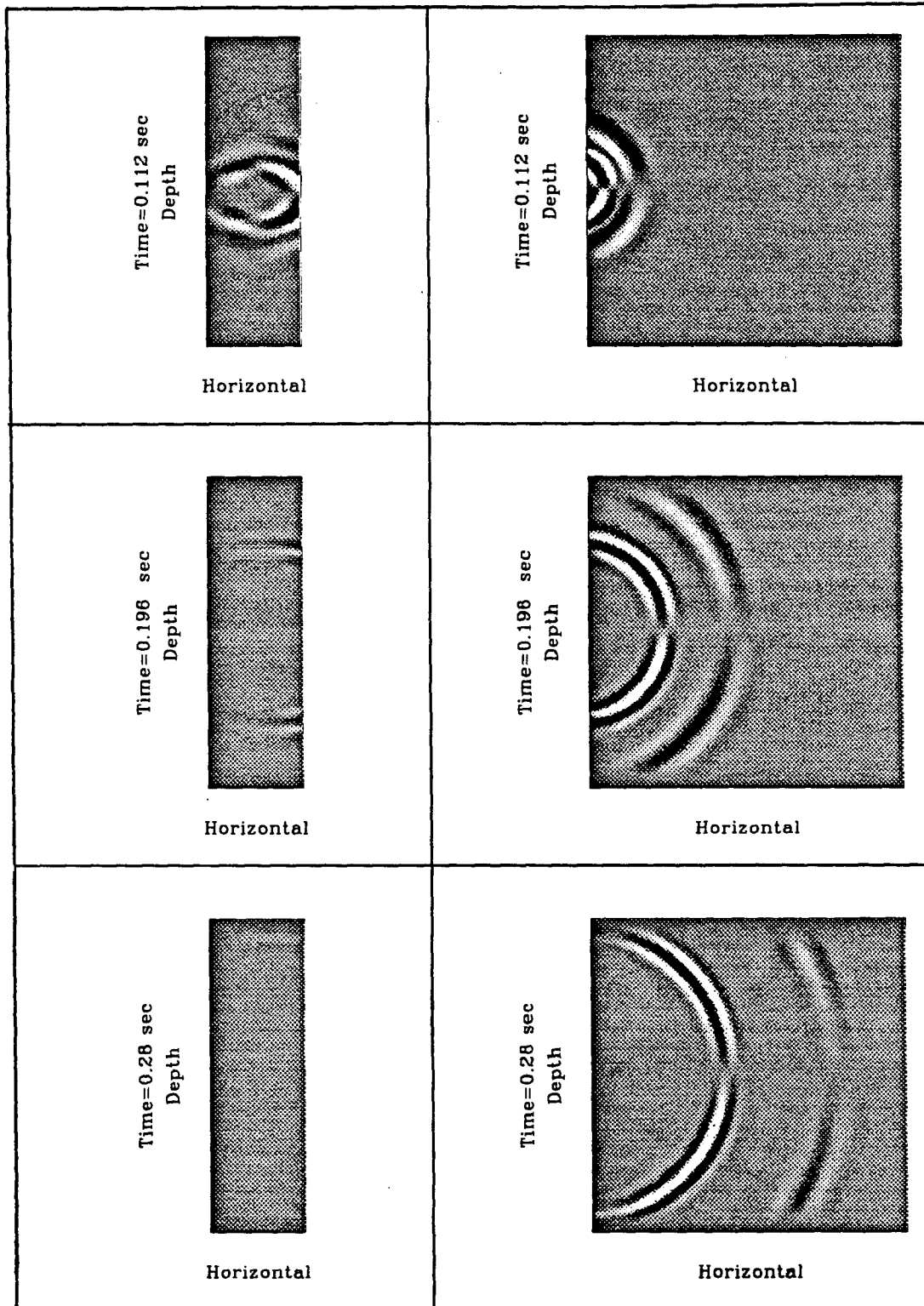
Figure 2.14: Hybrid finite-element modeling illustration. The finite-element modeling is shown on the left, and the finite-difference modeling on the right. The modeling is performed in a homogeneous medium.
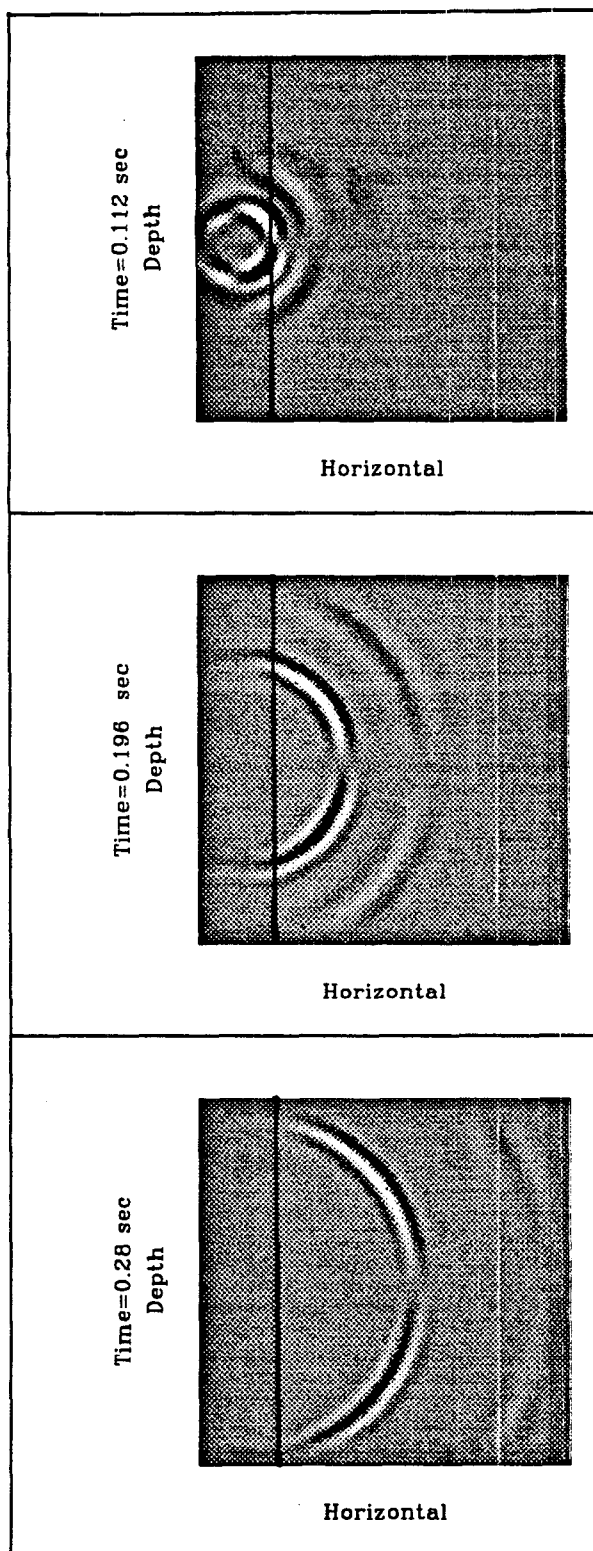
Figure 2.15: Merged finite-element finite-difference coupled results.
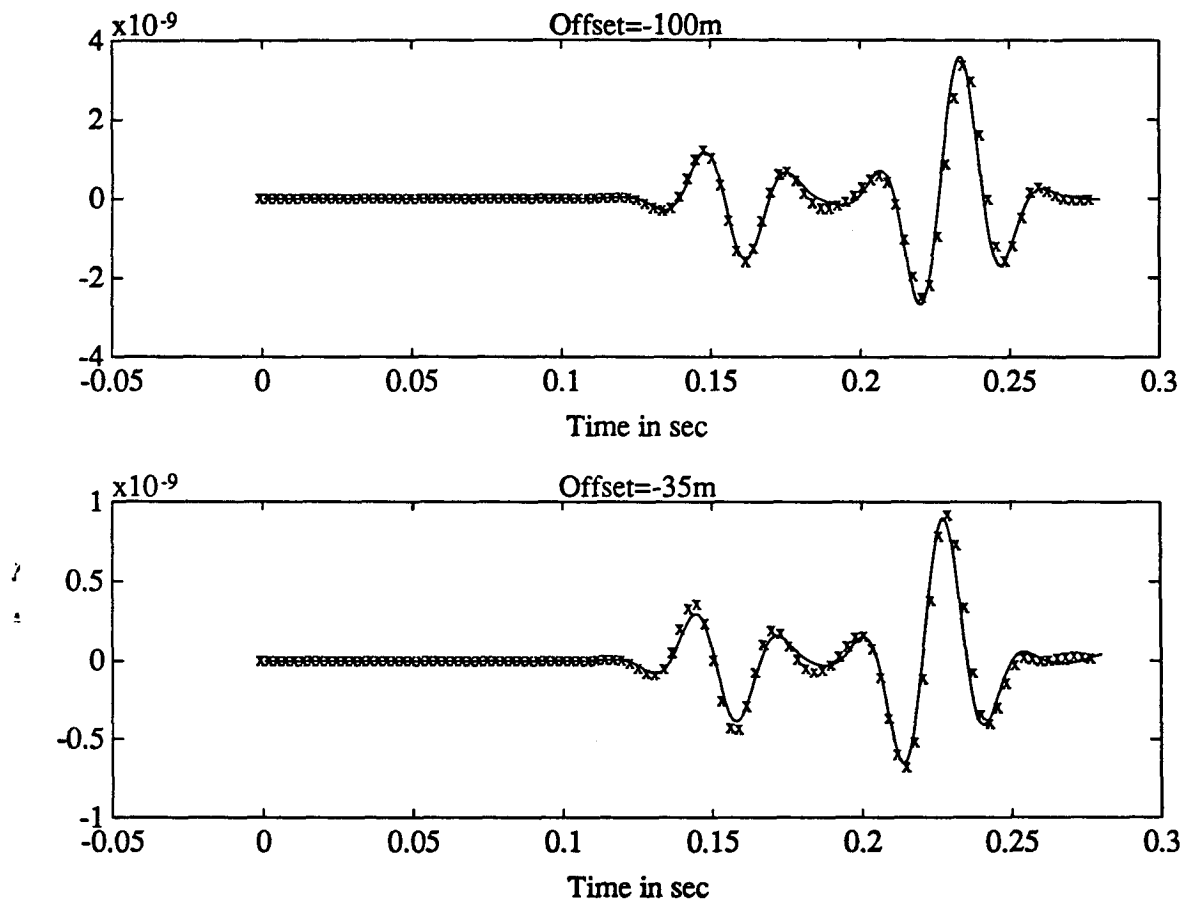
Figure 2.16 : A trace by trace comparison between the hybrid method (solid line), and the implicit finite-element method (x line). for two receiver locations.

been the object of intense investigation through the use of well logs. The cross-well region, on the other hand, is in general poorly constrained since it is the object of the cross-well investigation. For that matter, the borehole response can be computed for a given source location independently of the velocity in the cross-well region by using the implicit finite-element or the hybrid method. The borehole response sampled in the interlacing region between the two grids can then be re-used for fast finite-difference modeling only thereby increasing the efficiency of the overall scheme.

2.5 Conclusions

Three algorithms were presented to provide a numerical method capable of modeling the effect of the borehole on the radiation pattern of downhole sources.

The first algorithm, based on an approximation of the inverse mass matrix, is not adequate for our purpose, since it does not accurately model low wavenumbers, and introduces unwanted numerical dispersion.

The second family of algorithms investigated is based on the implicit-explicit finite-element algorithm. As shown in the case of the radiation by a cylindrical source in a homogeneous medium, this algorithm is very well suited for a careful investigation of the effects of both the borehole and the source design on the source radiation pattern because it provides a very controlled modeling environment in terms of both numerical dispersion and numerical anisotropy.

Finally, on the basis of results obtained with the two previous numerical experiments, a hybrid finite-element finite-difference algorithm was devised that significantly improves the computer efficiency of the implicit-explicit method. The hybrid method further provides the advantage of being able to use a single computation of the borehole field for multiple modeling of the interwell region.

The results obtained by using both the implicit-explicit finite-element algorithm

and the hybrid algorithm are shown in Chapter 3. This next chapter shows the versatility of these two methods as they are used to model three different types of downhoole sources: the resonant cavity source, the fluid-coupled source, and the drill-bit used as a downhole source.

References

Cheng, C.H., and Toksoz, M. N., 1981, Elastic wave propagation in a fluid filled borehole and synthetic acoustic logs: Journal of Geophysical Research, V. 87, p. 5477-5848.

Harris, J. M., 1988, Cross-Well Seismic Measurements in Sedimentary Rocks, S.E.G. expanded abstracts,1, 147, 150.

Heelan, P.A., 1953, Radiation from a cylindrical source of finite length: Geophysics, 18, 685, 696.

Hughes, T., 1984, The finite-element method: Prentice Hall, New York.

Kosloff, D., and Baysal, E., 1982, Forward modeling by a Fourier method: Geophysics, v. 47, p. 1402-1412.

Morse, P.M., and Feshbach, H., 1953, Methods in theoretical physics: Mc Graw Hill, New York.

Paulson B., 1988, Three-Component Downhole Seismic Vibrator, S.E.G. expanded abstracts,1, 139, 142.

Sword, C., 1986, Finite-element propagation of acoustic waves on a spherical shell: Stanford Exploration Project, V. 50

White, J. E., 1983, Underground sound: Elsevier, New York.

Zienkiewicz, O. C., 1971, The finite-element method in engineering science: McGraw-Hill, New York.

Chapter 3

Study of the behavior of downhole sources using the Finite-Element method

Abstract

Knowledge of the field radiated by a downhole seismic source is requisite for numerous seismic processing procedures, as well as for data interpretation. In the case of downhole sources, the source geometry as well as a good description of the borehole are key factors for a satisfactory modeling. This is especially true for sources whose length is comparable to the seismic wavelength emitted, and which cannot be considered as point sources. The flexibility of finite-element modeling makes it possible to incorporate the most important features of various source types as well as a proper description of the borehole. Such a level of detail in the source description makes analytical or semi-analytical solutions untractable.

In a homogeneous medium, the source-borehole assembly radiation pattern may depart significantly from the radiation pattern of a cylindrical source within the formation. (see for example Heelan 1963), depending on the source design. In general, downhole source radiation patterns cannot be adequately modeled by this analytical approximation for the following reasons :

- The source length is not small compared to the radiated wavefield.

- The source is not properly isolated from the borehole fluid.

- The source is not mechanically coupled to the rock formation, or is weakly coupled through a fluid layer.

The consequences of each of these violations of the Heelan hypotheses can be listed as follows :

- Long sources create signal filtering and may also deliver frequency-dependent radiation patterns.

- A strong coupling between the downhole source and the borehole fluid results in very energetic borehole-guided waves that, in turn, can convert into body waves at borehole heterogeneities. The energy associated with these conversions is of the same order as the source's initial radiated field.

- Finally a poor source-formation coupling results in a dramatic source performance degradation, because the energy provided by the source is actually 'stolen' by the borehole fluid if the source is not decoupled.

These observations can be directly applied to the study of the drill-bit used as a downhole seismic source. In this case, the borehole wave propagation problem is further complicated by the presence of the drill-string and casing. Modeling the behavior of the drill-bit as a seismic source allows us to isolate conical waves (equivalent to refracted waves in two-dimensional space) generated by the drill-string, as well as the associated drill-string guided waves.

In most cases, the borehole related effects cannot be neglected when downhole sources are modeled, unless special care was initially given to a special design of the

downhole source that inhibits the propagation of borehole guided modes.

3.1 Introduction

Unlike seismic sources used for surface seismic investigation, the development of downhole seismic sources is still in its infancy (Harris 1987, Paulson 1987, Kennedy 1987), and their use remains experimental to date. The diversity of design and implementation of downhole sources probably stems from their recent development, and renders both the processing and interpretation of the data acquired with these sources fairly difficult.

My purpose in this chapter is to use the numerical methods developed in Chapter II to investigate the impact of the source design and implementation on the understanding and interpretation of cross-well seismic data. To that end I have chosen three source types that illustrate most of the working principals of downhole sources:

- the resonant cavity source (Kennedy, 1988)

- the fluid-coupled source (Harris, 1988)

- the drill-bit used as a downhole seismic source (Rector ,1990)

Other types of sources currently existing such as the weight drop source or the downhole vibrator have not been modeled in this chapter because the results obtained for the three sources listed are directly applicable to these source types. These results focus on the following issues for the sources studied:

- coupling of the source with the borehole fluid and the rock formation.

- modes and mode conversions in a cross-well geometry.

- control over the seismic signal signature.

3.2 Resonant cavity downhole sources

3.2.1 Principle of operation, and modeling setup

Resonant cavity sources were initially implemented to provide high levels of downhole seismic energy from a weak energy source, thereby allowing users to profit by the resonance effect that builds up the cavity energy from weak exciters. To create a cavity in the borehole, an entire section of the well is isolated from the rest of the well by a very low impedance material (gas, for example). As illustrated in Fig. 3.1, two gas bladders isolate the fluid filled cavity from the rest of the well. A mechanical exciter provides the energy to the cavity, and drives the cavity to resonance. This mechanical implementation was used by Downhole Seismic Services for their downhole source.

This source is modeled using the implicit-explicit finite-element scheme described in Chapter 2. The source itself is modeled by isolating the source part of the borehole fluid from the rest of the fluid, using a helium-filled bladder. The mechanical apparatus of the exciter as well as the source' stem pipes are not taken into account, and the source pressure distribution on the borehole wall is modeled by a cosine pressure distribution within the source cavity. Since the source is axisymmetric, and the median axis of the source is also a plane of symmetry, only half the source is actually modeled as figure 3.1 illustrates. The source time history remains the same throughout this chapter and is a Ricker wavelet (see figure 3.2).

The borehole diameter for this modeling is $18cm$, the source length is inferred directly from the fluid velocity ($1500m/s$), and the signal central frequency ($70Hz$), so that the source length is exactly half the wavelength in the fluid. The length of the helium bladders is $2.1m$. The rock formation compressional wave velocity is $2600m/s$, the shear wave velocity $1700m/s$, the rock density $2700Kg/m^3$, and the maximum

pressure amplitude applied to the cavity is $1KPa$. The time step chosen for modeling

is $0.0004s$, and the average grid sampling away from the borehole region is $2.5m$.
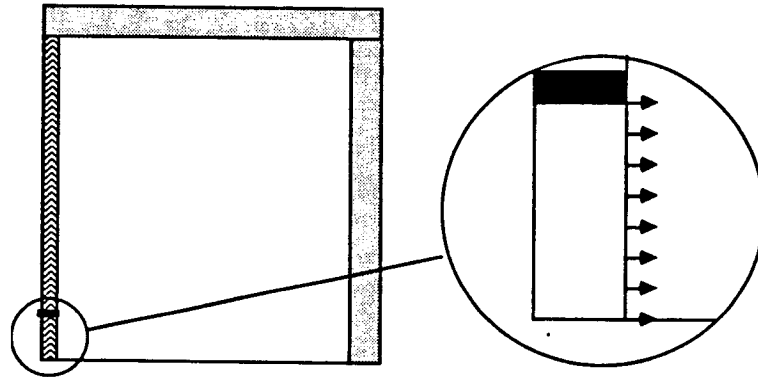
SOURCE TYPE 1 :
The source applies a pressure to the borehole fluid

Figure 3.1: Principle of operation of the resonant cavity downhole source
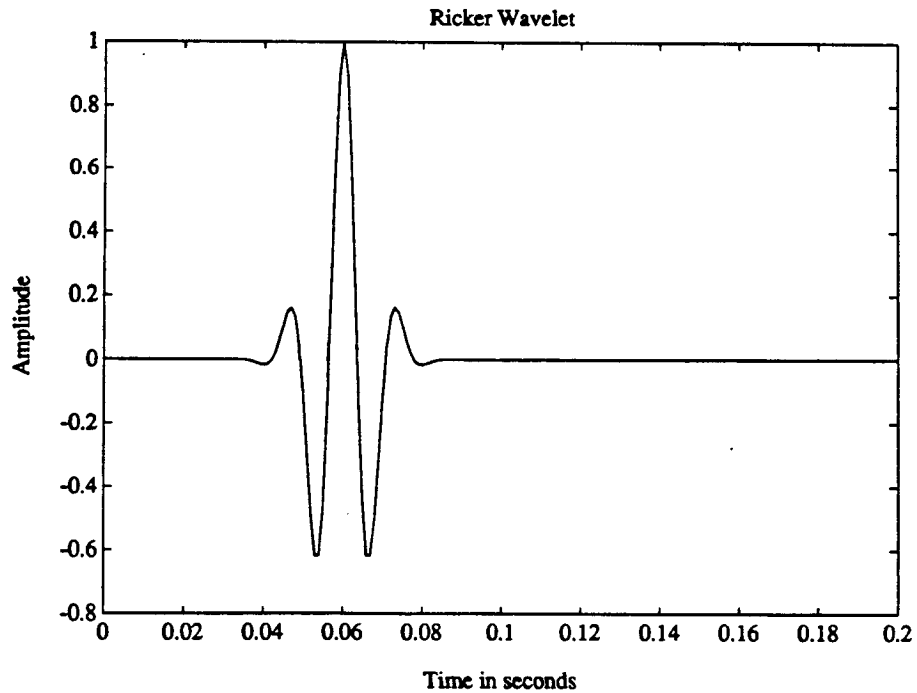
Figure 3.2: Source time history.

3.2.2 Finite-element modeling in a homogeneous isotropic solid

The computed signal at the receivers is monochromatic, as can be seen in figure 3.3, and 3.8. The actual computation of the traces' spectrum indicates that the signal central frequency is exactly $70Hz$, which corresponds to the resonance frequency of the source. Furthermore, more than 95 % of the wavelet energy is between 65 and $75Hz$. Though this result may appear surprising considering the input time function shown in figure 3.2, it only indicates that the finite-element computation acts as a simple linear filter which is applied to the initial signal. Another more mechanical interpretation is that the cavity tunes the input energy so that the output energy corresponds exactly to the resonance energy.

Comparing the results obtained in Chapter 2 for the radiation of a cylindrical source in a homogeneous medium, and the results obtained by modeling the resonant cavity downhole source in the borehole provides the results displayed in figure 3.4 and 3.5. The energy output of the resonant cavity source placed in the borehole is slightly smaller than the energy of the same source embedded in a homogeneous elastic medium and once again, the radiation pattern computed with the finite-element method very closely matches that predicted by Heelan, as shown in figure 3.4.

The energy drop between the radiation in a homogeneous background, and the radiation computed when the source is placed in a borehole can be explained by the existence of a weak borehole-guided mode. Evidence for the existence of this mode is shown in figure 3.3 and 3.5. In figure 3.3, the trace at 90^0 from the source, the trace closest to the borehole displays an outburst of energy around $0.25s$. Such an energy also appears in figure 3.5, for a high emergence angle from the source. This energy is associated with a borehole-guided mode traveling up the well at $1390m/s$. This mode is elliptically polarized, and its major axis is horizontal. The mode is similar in all aspects to a Stoneley wave (Cheng 1981). It is generated at the source-borehole fluid interface through the gas bladders. A simplistic one -dimensional transmission
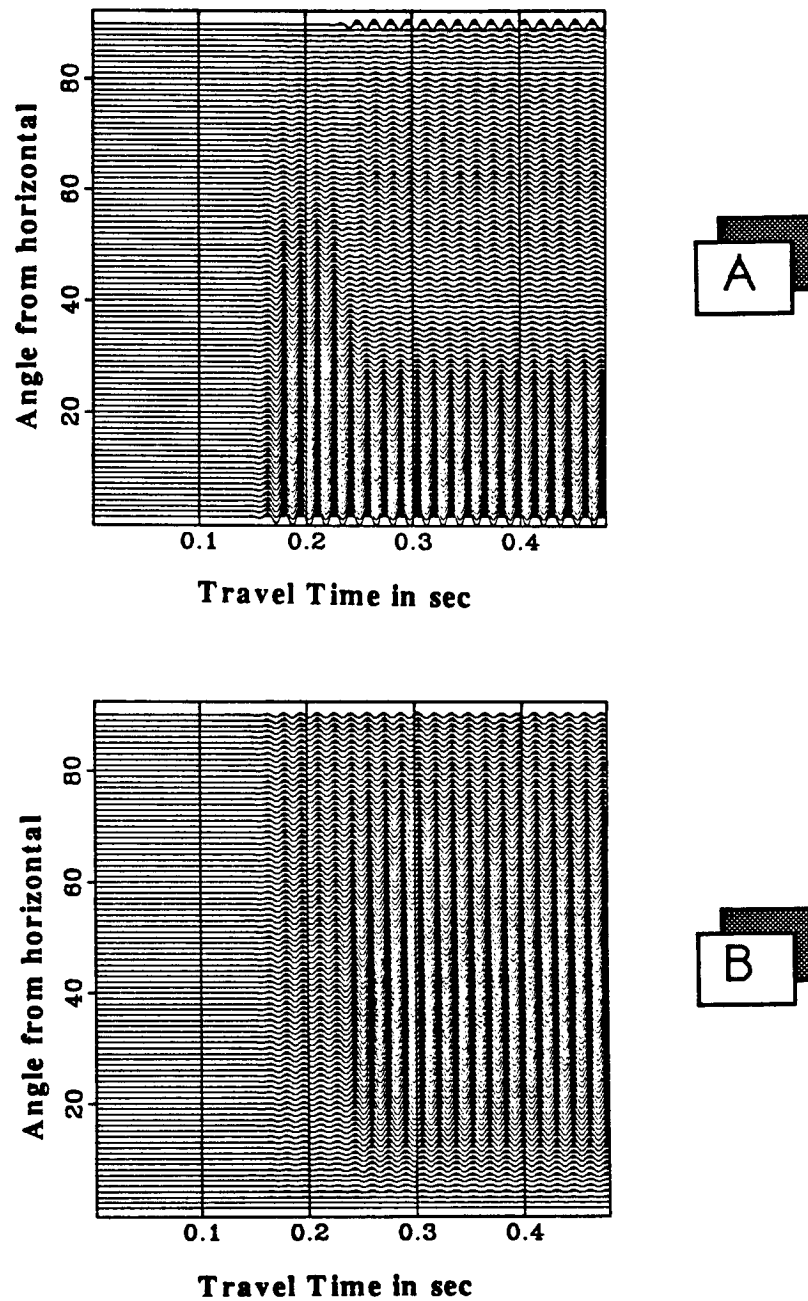
Figure 3.3: The radiated field for the resonant cavity downhole source. The receivers are placed around the source, and the receiver locations are displayed as a function of the angle from the horizontal. A) Horizontal component, B) Vertical component.
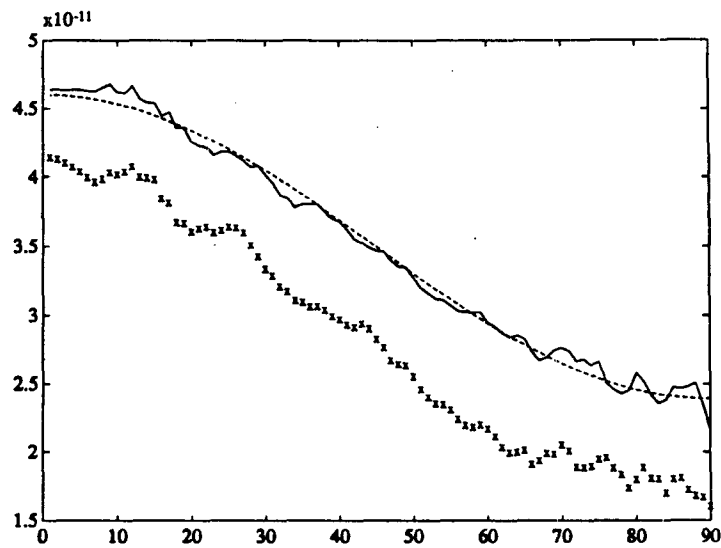
Figure 3.4: Measurement of the compressional waves amplitudes as a function of the angle of emergence from the source. The following computations are displayed: Analytical radiation pattern for the Heelan solution (dashed lines). Numerical solution for the Heelan geometry (solid line). Numerical solution for the resonant cavity source (x line).
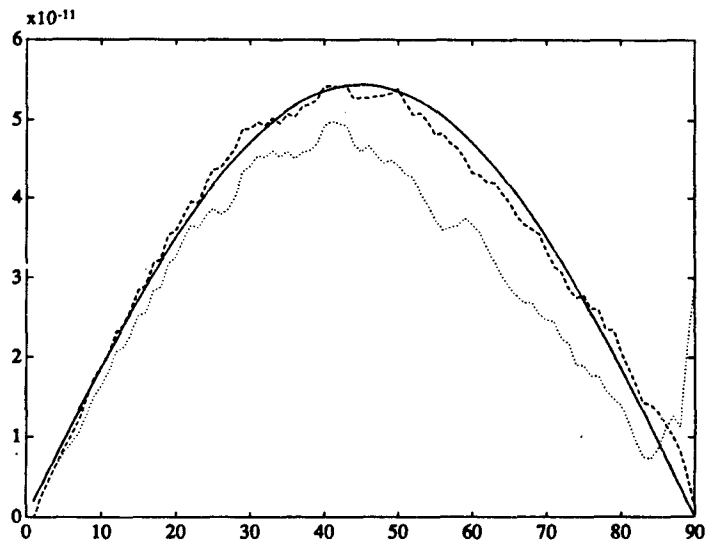
Figure 3.5: Measurement of the shear waves amplitudes as a function of the angle of emergence from the source. The following computations are displayed: The analytical radiation pattern for the Heelan solution (solid line), the numerical solution for the Heelan geometry (dashed lines), and the numerical solution for the resonant cavity source (dotted line).

model indicates that 5% of the cavity's energy leaks through the bladders; estimate is very close to the amplitude drop observed in figures 3.4 and 3.5. Finally, the source length (10.7m) is small compared to the wavelength of compressional waves in the rock formation (38.5m), but closer to the wavelength of shear waves (24.3m). figure 3.5 shows that the shear wave radiation pattern is slightly offset from the predicted radiation pattern. As shown in Chapter 2, this effects results from a preferential source-focusing effect along the direction orthogonal to the source axis.

Overall, the behavior of the resonant cavity source is very close to that of a source placed in a homogeneous medium. The source is mechanically isolated from the borehole fluid, and fully coupled with the rock formation because the cavity fluid is directly in contact with the borehole wall. However, since the source is not a point source, significant wavelet filtering effects are introduced by the source which are not predicted by Heelan (1953) or White (1983).

3.2.3 Frequency dependent radiation pattern

The resonant cavity source operates in such a way that the mechanical exciter only delivers the frequency tuned to the source length. When the source is shortened, the exciter's frequency increases by a proportional amount. For other sources that are not designed to be resonant cavity sources, the seismic energy source is placed between two buffers for the sole purpose of decoupling the source from the borehole fluid in order to eliminate borehole guided waves. In such a case, the mechanical exciter's frequency is not tuned to the source length for all possible frequencies. This situation is modeled numerically by using the previous source setup but for a source length double that of the one previously chosen. In this case, the source length is no longer tuned to the exciter's central frequency.

The results of this computation appear in figure 3.6 to 3.8. The traces recorded at the receivers (figure 3.6) clearly display lower amplitude zones between 40^0 and

Radial Displacements

Tangential Displacements
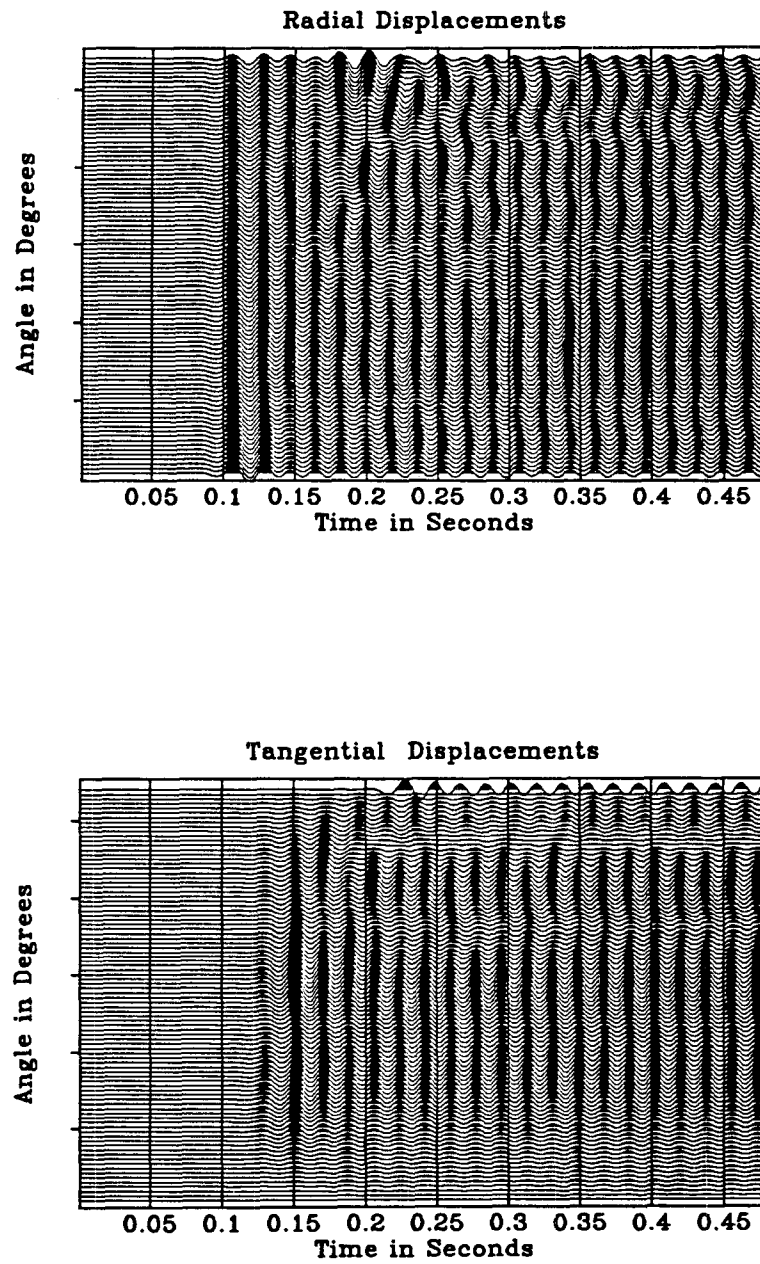
Figure 3.6: The radiated field for the resonant cavity downhole source operated out of tune.

x10⁻²¹   **P wave Radiation Pattern**
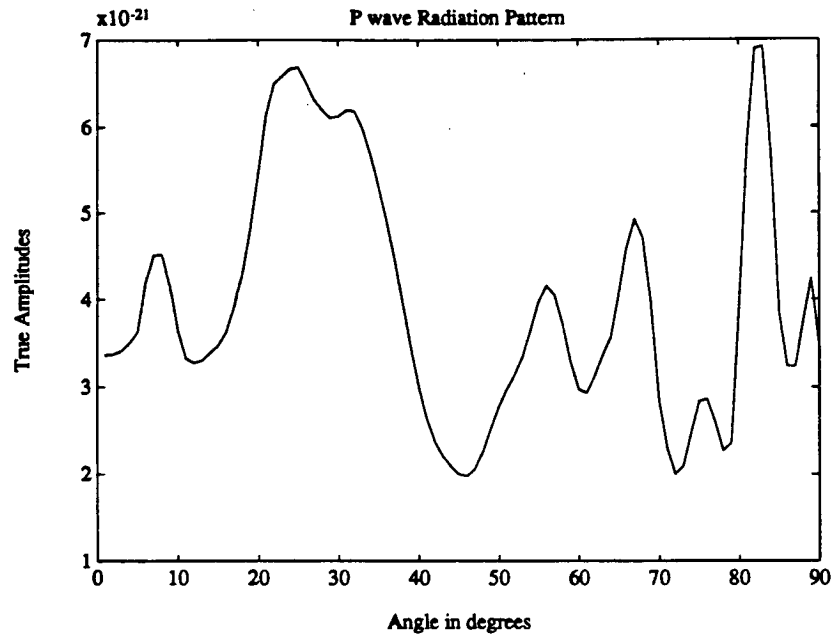
Figure 3.7: The compressional wave radiation pattern. This radiation pattern can be explained as a superimposition of two different radiation patterns for two different source harmonic behavior shown in figure 3.8.

x10⁻²¹
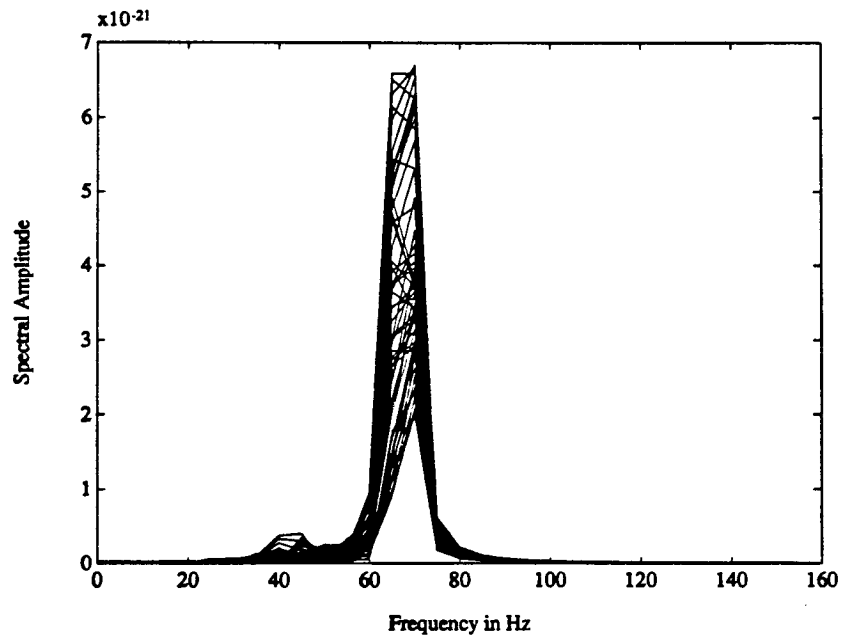
Figure 3.8: The receiver spectrum for each traces from 0^0 to 90^0 from the horizontal direction. The peak spectrum shift appears at 50^0.

60°. Over the complete record, the arrival structure does not display the typical compressional and shear waves pattern observed in figure 3.3. The absence of clear compressional and shear waves arrival structure in figure 3.6 is explained in figure 3.7 by the radiation pattern of the compressional waves. This radiation pattern, measured from the maximum Fourier component of the signal, does not show the decaying behavior shown in figure 3.4. The frequency spectrum for each trace in figure 3.8 explains the radical change of behavior of the source. Two lobes are apparent in figure 3.8: The dominant mode at $70Hz$ corresponds to the central frequency of the input ricker wavelet. This frequency excites the second harmonic of the source and for that frequency band, the source acts as a dipole. The second lobe, centered around $40Hz$ corresponds to the source first harmonic. For this second frequency band, the source acts as a monopole.

These results show that the signal displayed in figure 3.6 can be interpreted as a superposition of two distinct radiation patterns for the source first harmonic, which corresponds to the resonance mode, and the source second harmonic, where the source actually acts as a dipole for the higher frequencies. Thus the waveform emitted by downhole sources can significantly diverge from the waveform predicted by the Heelan solution. The two main reasons for the departure of the received signal from the analytical prediction from Heelan are:

- A tuning of the signal to the source structure

- A destruction of the radiation pattern due to the presence of the various source harmonics.

3.2.4 Effect of the casing: The existence of conical waves

The field radiated by the resonant downhole source is computed when the source is placed in a cased well. The general setup is illustrated in figure 3.9. The borehole

casing is modeled by a steel pipe $4mm$ thick. The steel compressional wave velocity is $5141m/s$, the shear wave velocity is $3109m/s$, and the steel density is $7860kg/m^3$. Steel is modeled as an isotropic elastic solid. The cement bonding the casing to the rock formation has the following properties: a compressional wave velocity of $1400m/s$, a shear wave velocity of $900m/s$, and a density of $1630kg/m^3$. For the rock formation, source geometry, and input signal, the parameters are the same as those described in section 3.2.1.

The modeling results are displayed in figure 3.10. Once again, the received signal is quasi-monochromatic, and the arrival of both the compressional (P) and shear (S) waves is clearly visible. Two other modes, however, can be isolated. First a mode oblique to all previous arrivals (H) then the Stoneley waves (St) with their late arrival. A careful study of the first oblique arrival shows that it has a plane wave move-out, and propagates at the compressional velocity in the rock formation. The polarization of this mode also indicates that it is a compressional wave. This last mode is interpreted as a conical wave (White, 1973). A conical wave is the three-dimensional, axisymmetric space equivalent of a two dimensional space refracted wave (also called a head-wave). This mode ensures the displacement continuity condition at the casing-formation boundary, and matches the displacements of a compressional wave propagating in the steel parallel to the borehole axis. This mode will be studied in greater detail in the last part of this chapter which focuses on the study of the drill-bit radiation pattern.

Figure 3.11 displays both the compressional and the shear wave radiation pattern. The compressional waves are not obtained this time by simply separating the radial and tangential components of the displacements because the conical waves are interfering strongly with the rest of the signal. Instead the components of the compressional waves A_P and shear waves A_S are obtained as follows (Etgen, 1988):

■	Downhole source
▨	Borehole fluid
■	Steel casing
☐	Cement filling
☐	Rock formation
▬ ▬ ▪	Axis of symetry
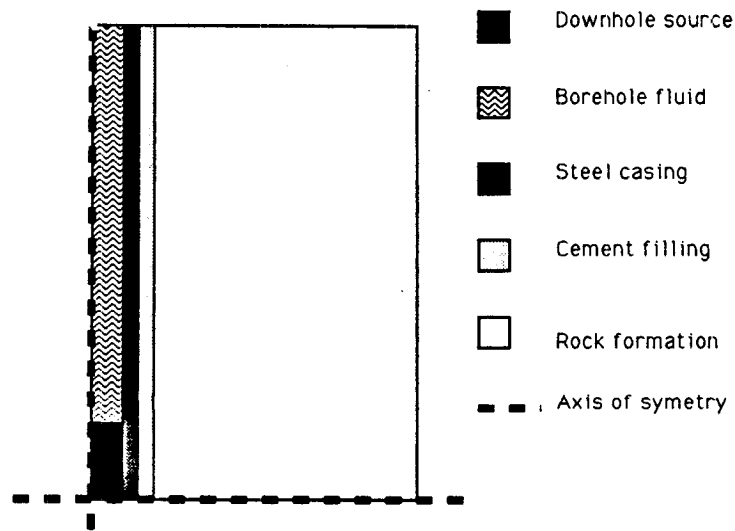
Figure 3.9: The setup of the resonant cavity source in a cased well.
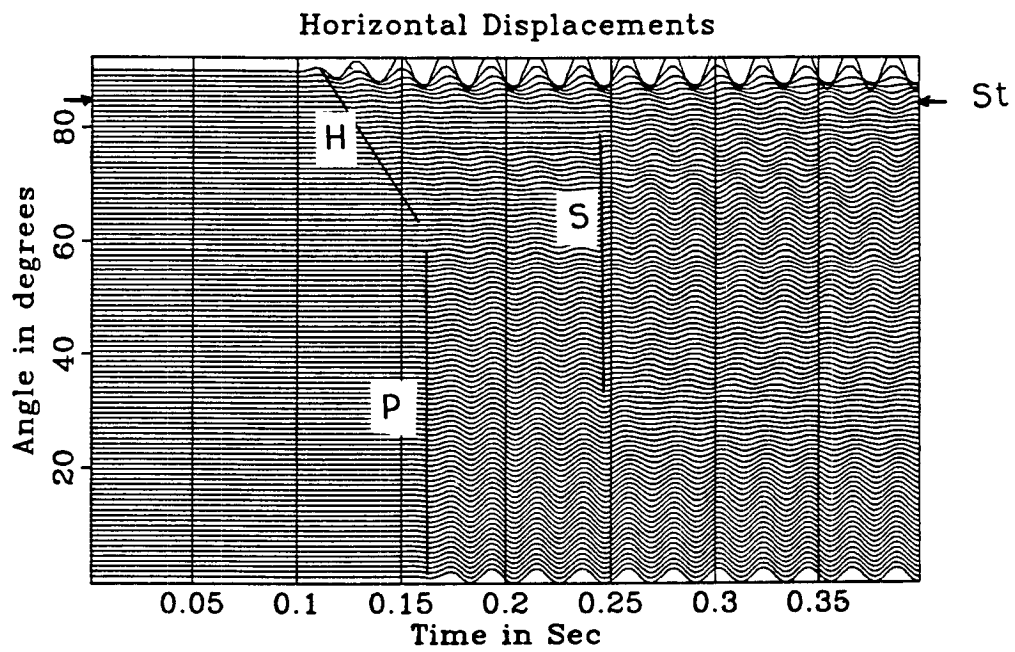
Figure 3.10: The horizontal component of the displacement field radiated field by the resonant cavity source in a steel cased well. Four modes are clearly visible: (H) the conical waves, (P) the Compressional waves, (S) the shear waves and (St) the Stoneley waves.

$$A_P = \frac{\partial u_x}{\partial x} + \frac{\partial u_y}{\partial y} \qquad (3.1)$$

$$A_S = \frac{\partial u_x}{\partial y} - \frac{\partial u_y}{\partial x} \qquad (3.2)$$

where u_x and u_y are the horizontal and vertical components of the wave field. The compressional and shear waves' amplitudes are lower than those obtained for the source radiation both in a homogeneous medium, and in the borehole. (figures 3.11 and 3.12). These lower amplitudes are caused by the presence of the steel casing and cementing that attenuates the radiated field because of the higher apparent impedance of the borehole surface. Consequently, the energy difference is essentially converted into steel-casing-guided-waves propagating at approximately $5090 m/s$, and this energy is responsible for the conical waves. The angle between the conical waves and the borehole axis θ is determined by the ratio between the apparent velocity in the casing V_{casing} and the compressional velocity in the rock formation V_{rock} using the following relationship:

$$\sin(\theta) = \frac{V_{rock}}{V_{casing}} \qquad (3.3)$$

The rapid oscillations of the compressional wave radiation pattern shown in figure 3.11 from 70^0 to 90^0 is generated by the interference between true compressional waves generated by the source and conical waves also generated by the source but first traveling along the borehole casing. This interference pattern is therefore strongly frequency dependent, and serves as an illustration of the difficulties encountered when downhole sources are used in a transposed VSP configuration.

Finally, figure 3.11 displays a comparison between the radiation pattern computed for the resonant cavity source in a cased well and the theoretical radiation pattern computed by Heelan (1953) after scaling. The discrepancy, in this case, is not related to a shift between source harmonics, but instead to the partition of the pressure wave emitted by the source into body waves, casing-cementing-guided-waves, and

conical waves. As figure 3.11 shows, this partition is strongly dependent on the angle of emergence, and dramatically affects the compressional wave radiation pattern, even for fairly low angles of emergence, therefore showing the extreme sensitivity of downhole sources to their immediate borehole environment.

3.2.5 Hybrid method modeling in a layered isotropic solid

The earth model that will now be investigated is displayed in figure 3.13. The model is built up of three layers of increasing velocity with depth. The wellbore length is $380m$, and its diameter is $18cm$. The source parameters and time history specifications are the same as those described in section 3.2.1. The radiated wavefield is sampled along a line parallel to the well, $200m$ offset from the source. The receivers sample directly the wavefield computed on the numerical mesh, and do not incorporate the effects related to the presence of a second borehole.

The two principle modes generated by the source, compressional and shear waves, are clearly visible in both figure 3.13 and 3.14 despite the monochromaticity of the signal. Reflections from both formation interfaces as well as from the free surface are visible. The free surface reflections are by far the strongest, and display conversions from compressional to shear waves. Finally, the radiation patterns behaves as predicted, with decaying compressional waves away from the horizontal and shear waves maximum at 45°. Effects of the borehole-guided modes are not visible on these plots.
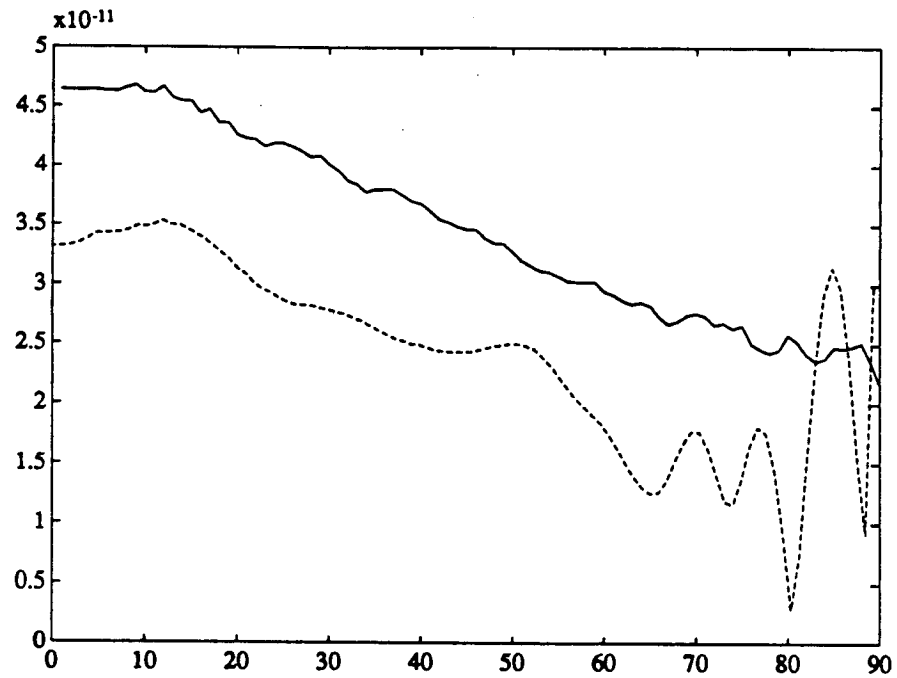
Figure 3.11: The radiation pattern of compressional waves in a cased hole. Comparison of the radiation pattern in a steel cased well (dashed line) and in an uncased well (solid line).
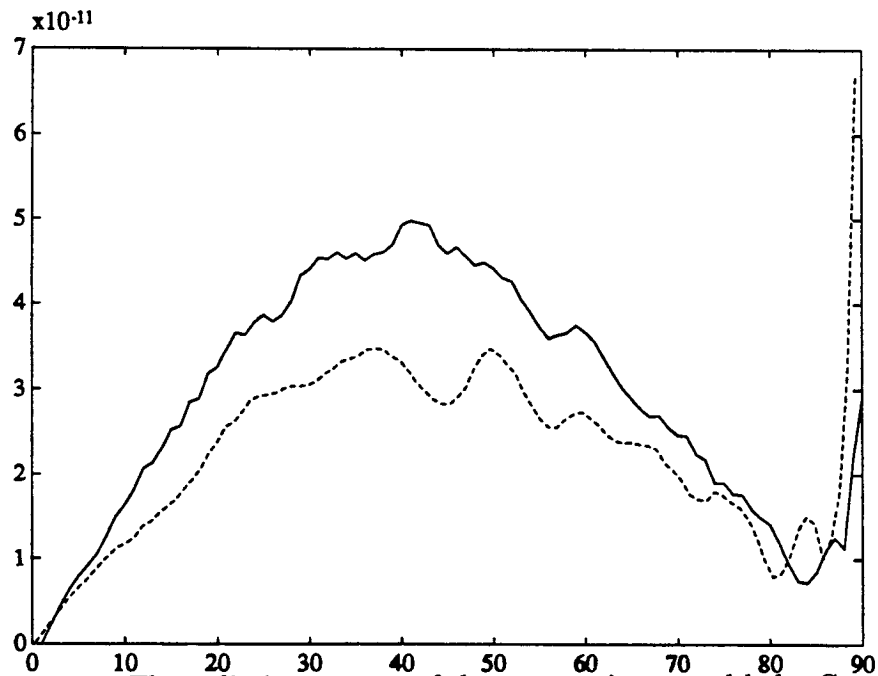
Figure 3.12: The radiation pattern of shear waves in a cased hole. Comparison between the radiation pattern in a steel cased well (dashed line) and in an uncased well (solid line).
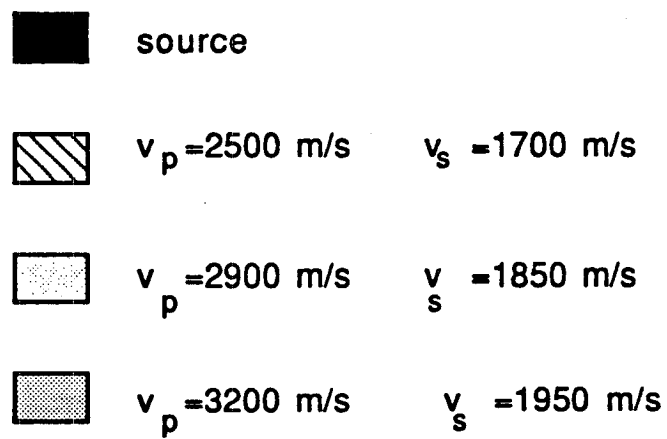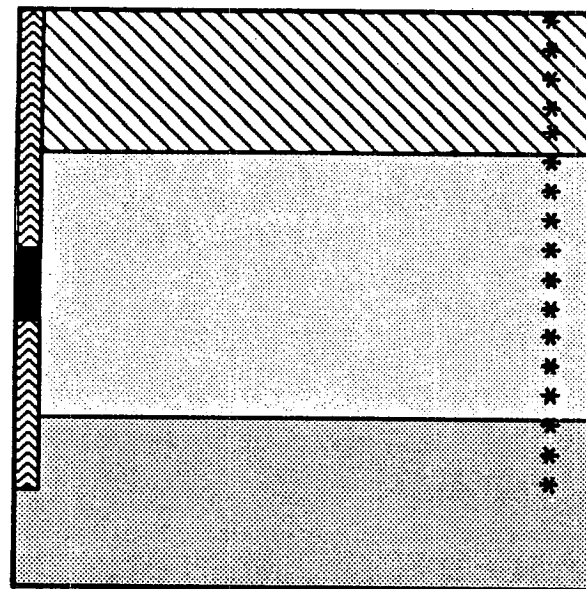
Figure 3.13: The modeling setup in a layered medium.
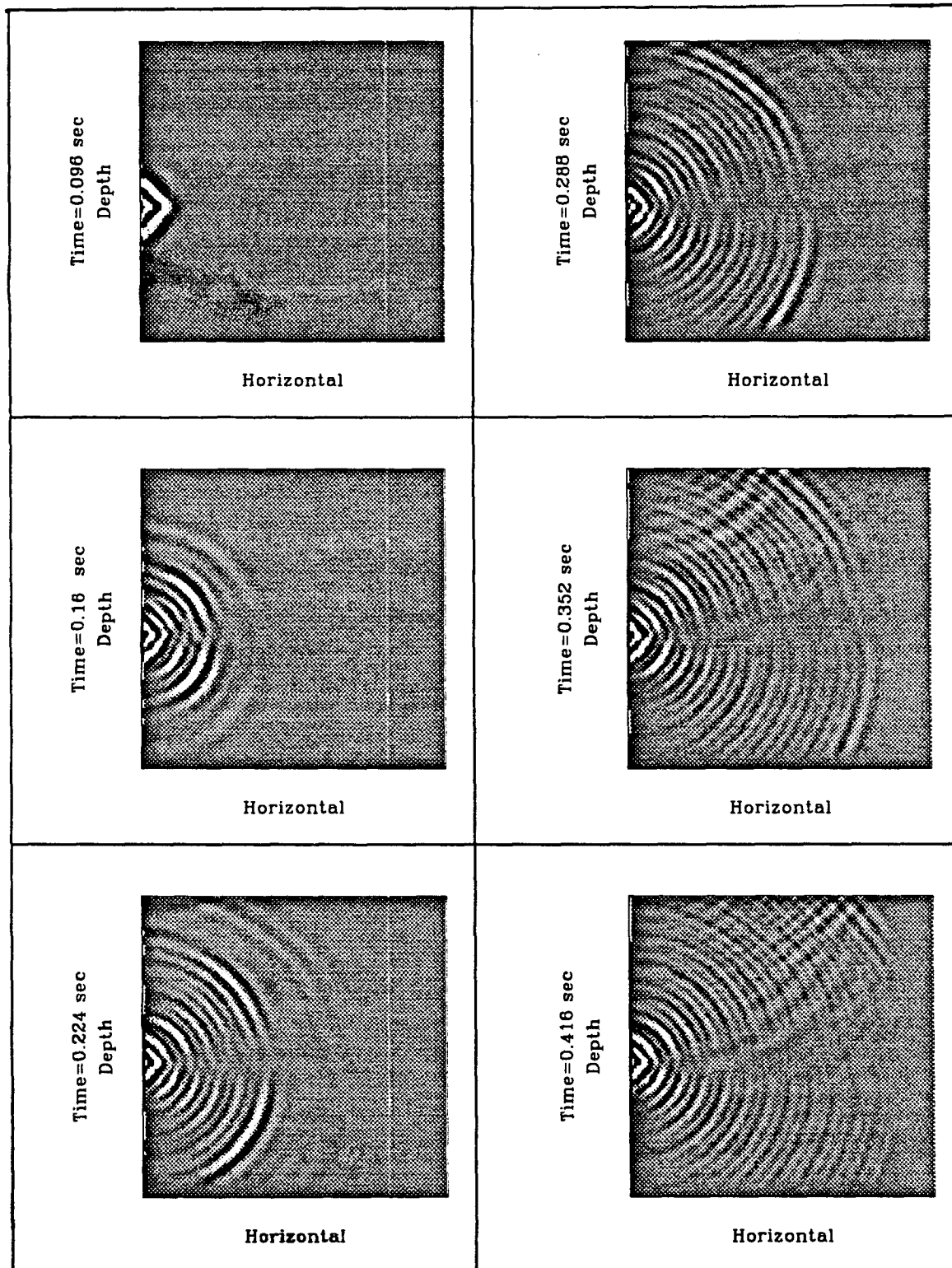
Figure 3.14: Snapshots of the field radiated by the resonant cavity source.

A comparison of our model with the data acquired by Western Geophysical (figure 3.16) shows that they display the same features: decaying compressional waves away from the horizontal, and increasing shear wave amplitudes away from the horizontal. Reflections from both the compressional and especially the shear waves are also clearly visible. The dominance of the shear wave reflections after the shear wave arrives can be easily explained by the shear wave radiation pattern. In our modeling, the shear wave amplitude at 45^0 away from the horizontal is four times higher than the compressional wave amplitude, and, for most rock arrangements, reflections can only occur for emergence angles greater than 45^0.

Beyond 45^0, body waves both compressional and shear, are likely to be critically reflected or refracted. In the case of refracted waves, the counterpart of the head wave in the low velocity medium is an interface mode with a two dimensional geometrical spreading. (Aki, 1980). The same type of interface modes also exist in the case of a low velocity layer embedded between two higher velocity materials. In that case, a layer guided mode will be generated and will once again have a two-dimensional geometrical spreading. These modes are responsible for the linear move-out arrival outlined in figure 3.16. The linear move-out suggests that this mode actually propagates within the receiving borehole at the Stoneley wave velocity. These Stoneley waves are believed to be generated by the conversion of highly energetic, elliptically polarized interface modes into borehole-guided modes.

Thus far, the following partial conclusions can be drawn from the study of resonant cavity sources.

- The behavior of the resonant cavity source is extremely close to that of an idealized cylindrical source if the downhole source is driven to resonance. The reasons for this behavior are a perfect source coupling with the rock formation, a proper isolation of the source from the borehole fluid, and a match between the input and output signal of the source at resonance.

- The failure to drive the source to resonance, whether it is accidental, or because a source that is not designed to be monochromatic is actually isolated by buffers from the borehole fluid, results in highly undesirable effects. Among them is the fact that the source radiation pattern becomes frequency dependent.

- Finally, the use of downhole sources inevitably results in a wealth of modes that are not commonly encountered in surface seismic investigations. I isolated two of them in the first part of this investigation: 1) conical waves arise from the use of downhole sources in cased wells, 2) interface waves propagating along layer interfaces that only have a two dimensional geometrical spreading, and therefore provide high energy for mode conversions, as figure 3.16 shows.

3.3 Fluid-coupled downhole sources

3.3.1 Principle of operation, and modeling setup

For fluid coupled sources, the active source element is immersed in the borehole fluid, and the source applies its energy to the borehole fluid. Then the borehole fluid transmits the source energy to the rock formation. There is in general no contact between the source active elements and the rock formation for fluid-coupled sources. The principle of the fluid-coupled downhole source is implemented by numerous downhole sources.

It is first used by piezoelectric downhole sources such as those developed by South West Research, British Petroleum, and the Stanford Tomography Project. The active element of piezoelectric sources is a large, low impedance arrangement of transducer crystals that deliver the energy level required for seismic investigation. It is also used by air guns downhole sources where, this time, the source active element is a gas bubble released by the gun.

Horizontal Displacements

Vertical Displacements

Figure 3.15: Traces computed for the resonant source in a layered medium: a)the horizontal component of the displacements, b) the vertical component of the displacements.
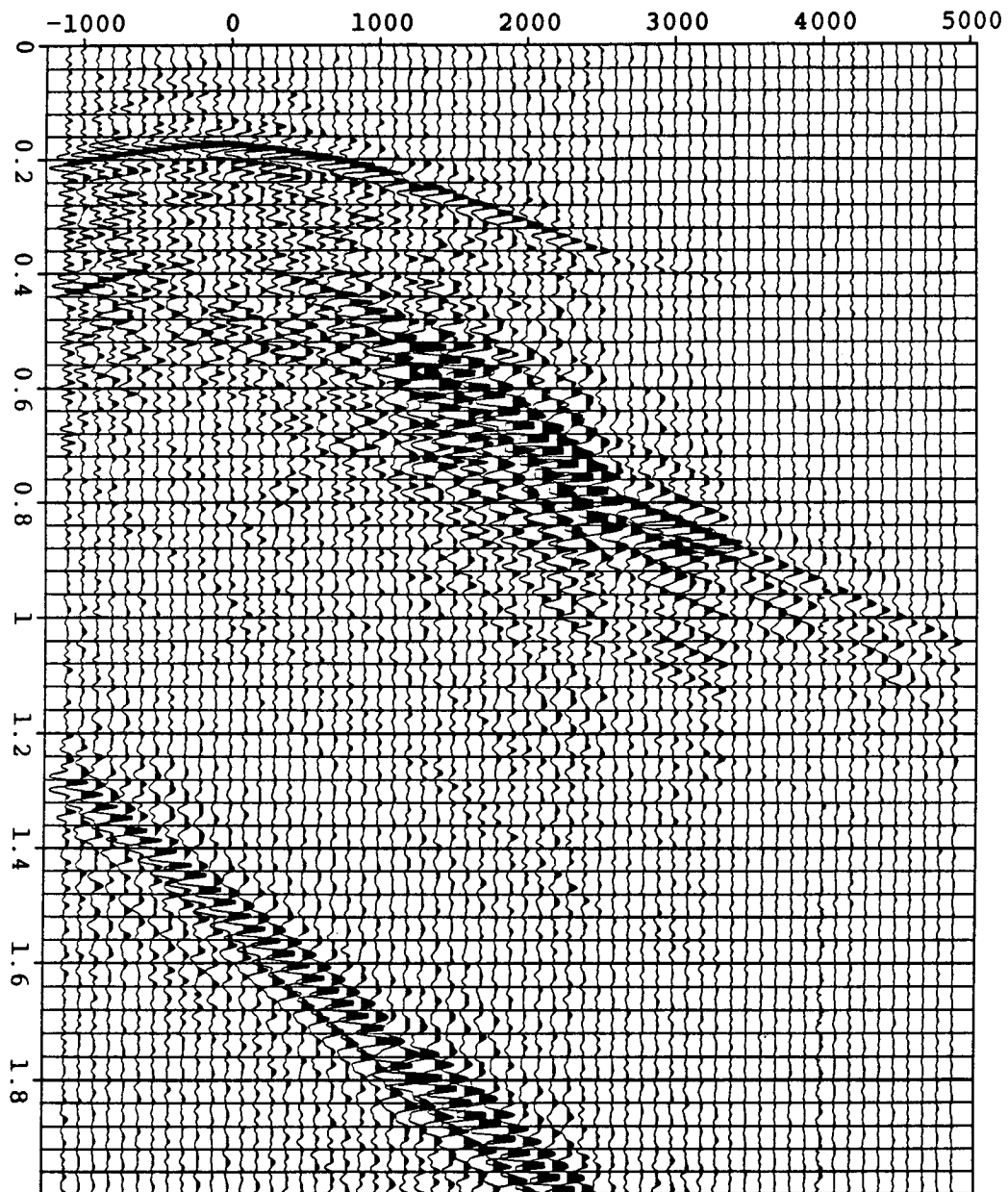
Figure 3.16: Field data obtained after correlation for the resonant cavity source. (Courtesy of Downhole Seismic Services).

My goal is not to investigate the complex, coupled, mechanical systems that deliver the seismic energy, but instead to investigate the mechanical effects involved in the radiation of seismic energy. For that reason, the force applied by the fluid-coupled source to the borehole fluid is modeled by a time and space dependent distribution of equivalent external forces. The fluid-coupled source is modeled as a cylinder with the elastic properties of aluminium, and the source is assumed to be axisymmetric.

The pressure applied by the fluid-coupled source to the borehole fluid is described as a homogeneous external pressure distribution applied at the interface between the source and the borehole fluid. There is no contact between the source and the borehole surface, the coupling between the source and the formation being achieved through the borehole fluid layer.

3.3.2 Finite-element modeling in a homogeneous isotropic solid

All the modeling parameters are exactly identical to those described in section 3.2.1, except for the source design itself. The radiated field (figure 3.18) clearly displays both the compressional and shear wave arrivals, with a now familiar amplitude behavior. The signal dispersion observed is not an effect of numerical dispersion, but instead an effect related to the interaction of the modeled source with the borehole fluid. In our modeling case, the source impedance is higher than the borehole fluid impedance, which tends to lower this dispersion effect. Should the source impedance match the fluid impedance, this dispersion or tuning of the signal with the source length is expected to be much higher, as shown in section 3.2.2 in regard to the resonant cavity source. Finally, the Stoneley waves are also present in this modeling case, as shown in figure 3.18.

The amplitudes measured for both compressional and shear waves are displayed in figure 3.19 where the effect related to the propagation of the Stoneley waves is removed. The comparison between figures 3.4 and 3.5 on one hand, and figure 3.19 on the other, shows that the computed amplitudes are smaller for the fluid-coupled
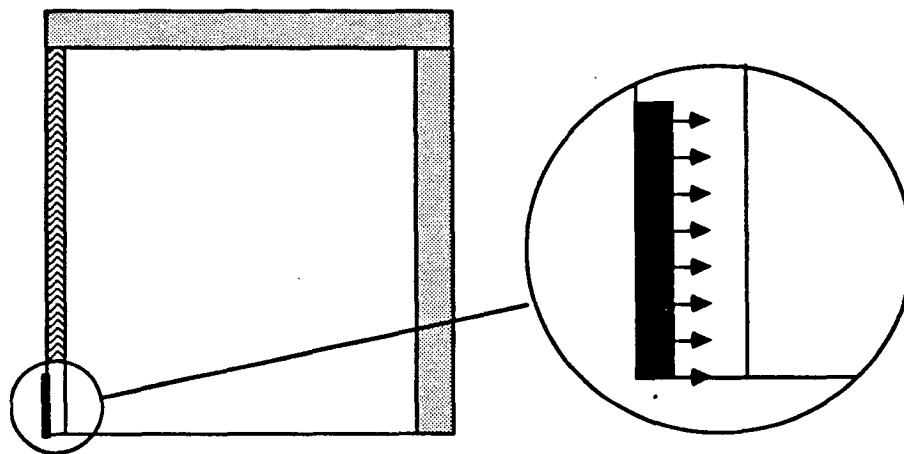
source type 2 :

The borehole fluid applies a pressure at the
borehole surface

Figure 3.17: A schematic diagram of the fluid-coupled source as used for
the Finite-Element modeling.

downhole source by a factor of 50. This low amplitude measurement is easily explained by the presence of the fluid layer between the source and the rock formation. In the case of the resonant cavity source, the borehole fluid itself was the source of seismic energy with a direct coupling of the source with the rock formation. In the case of the fluid-coupled source, the seismic energy is transmitted from the source to the borehole fluid, and then only to the rock formation. This energy transmission line is responsible for the low seismic wave amplitude output of fluid-coupled sources, since most of the source energy is actually converted into borehole-guided mode energy.

Two types of borehole-guided waves are clearly visible in figure 3.18. The first one propagates slightly under the shear velocity of the medium and arrives at $0.22sec$ in figure 3.18. The second propagates at the Stoneley wave velocity, that is slower than the fluid velocity, and arrives at $0.28sec$. The first mode is identified as an axisymmetric Rayleigh wave (White, 1973).

In summary, the behavior of the fluid-coupled downhole source does not differ significantly from the behavior of the resonant cavity downhole source as far as radiation patterns alone are concerned. However, the efficiency of the fluid-coupled source measured as the ratio between the seismic energy available for seismic investigation and the mechanical energy delivered by the source is considerably smaller than the efficiency of the resonant cavity source. This difference in efficiency is related to the perfect coupling of the fluid-coupled source with the borehole fluid and its weak coupling with the rock formation.

3.3.3 Hybrid method modeling of the fluid-coupled downhole source in a layered isotropic solid, and evidence for secondary downhole sources

As displayed in figure 3.21, the field generated by a downhole cavity and the field generated by a fluid-coupled source differ greatly, except for the first arrival travel time which is consistent from one source to the other. The differences can be attributed to two major causes:

Horizontal Displacements
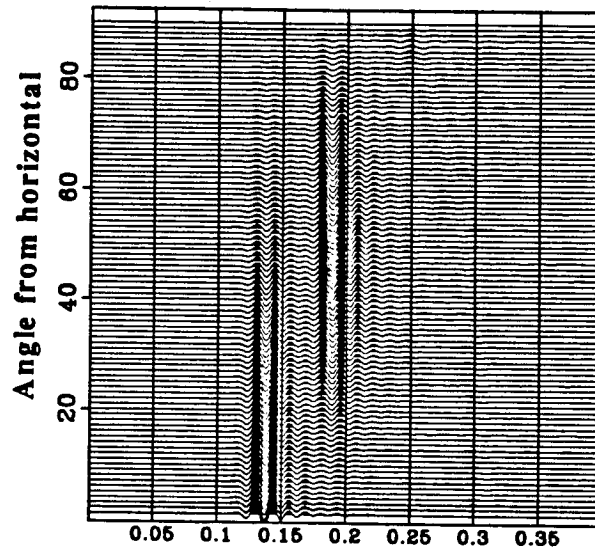
Vertical Displacements
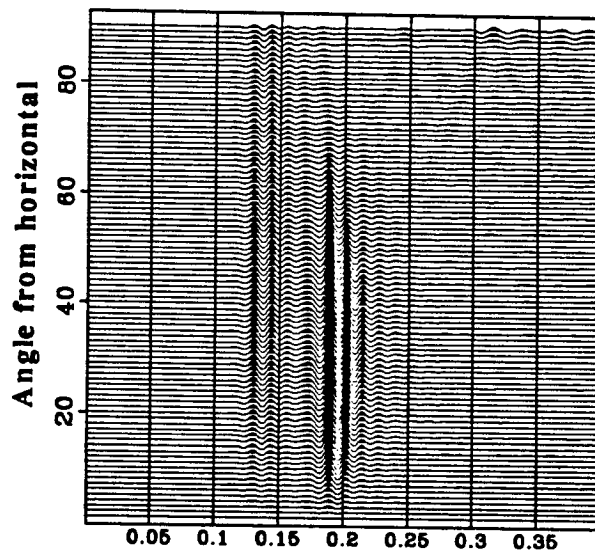
Figure 3.18: The field radiated by the fluid-coupled downhole source.
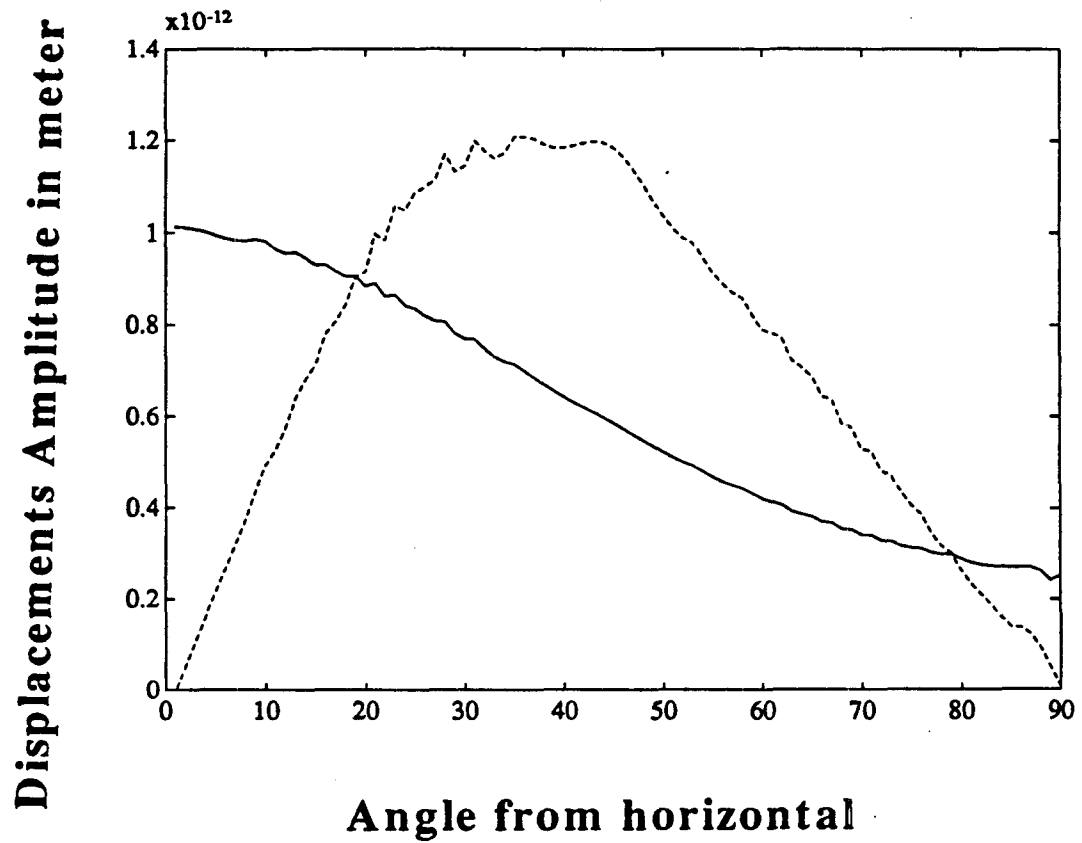
Figure 3.19: Measurement of the compressional waves' (solid line) and shear waves' (dashed line) amplitude as a function of the angle of emergence from the source.

- the signal dispersion introduced by the downhole source, described in the previous section

- the existence of secondary sources along the borehole

As shown in figure 3.20, each borehole heterogeneity, (namely the rock interfaces, the borehole top, and the borehole bottom) acts as a very strong secondary source (actually stronger in our case than the source itself). Because of the interfering arrivals, the direct shear waves cannot be clearly recognized in figure 3.21. On the other hand, the strongest secondary source radiated fields (namely the secondary sources at the top and the bottom of the well) appear very clearly in figure 3.21.

The mechanism by which these secondary sources appear was first outlined by White (1973) using dimensional analysis. Fluid-coupled sources generate powerful Stoneley waves propagating up and down the well. The velocity of these waves is a function of the fluid velocity, the rock formation velocity, and finally the borehole diameter. A change in rock formation velocity results in an equivalent change of the borehole impedance. However, the propagation of Stoneley waves along the borehole cannot be simply assimilated to a one-dimensional propagation system, since a Stoneley wave incident on a rock formation interface generates the following converted waves:

- a transmitted Stoneley wave

- a reflected Stoneley wave propagating in the borehole in the reverse direction of the incident wave

- an interface wave propagating along the rock interface within the rock formation. This interface mode is similar to that described by Auld, 1973, and are clearly visible in figure 3.20

- compressional and shear body waves propagating within the rock formation. These waves are also clearly visible in both figures 3.20 and figure 3.21.

Finally, this modeling only dealt with the case of a rock interface as a borehole heterogeneity. I expect that other types of borehole heterogeneities such as fractures intersecting the borehole, borehole caves or abrupt diameter changes, casing bottom, or cementing variations will generate similar Stoneley wave conversions.

3.3.4 Mode conversions, and more 'tube' waves

Other modes shown in real cross-well seismograms are not modeled by the software used. These are receiving-well borehole-guided waves. They are clearly apparent in figure 3.22, and interfere with most of the signal. This mode has a conical move-out characterized by two parameters: the apex of the cone, and the move-out velocity of the cone branches. For all the cases considered with both the fluid-coupled, and the resonant cavity sources, the move-out velocity is consistent with the velocity of the Stoneley waves (slightly slower than the borehole fluid velocity).

On the other hand, the apex location as well as the amplitude of these tube waves is a more elusive parameter to interpret. In general, receiving borehole guided waves are maximum, when both emitting and receiving boreholes cross a narrow low velocity zone, as shown in figure 3.22. Receiving borehole tube waves also appear immediately after the compressional waves' arrival when a strong rock interface is met. The following are possibilities that can account for the existence of this mode.

- First, the secondary sources generated within the source borehole also generate strong interface modes propagating within the rock formation along rock interfaces. Since these modes display a two-dimensional geometrical spreading, their energy is stronger at the receiving borehole, which allows for the creation of tube waves at the receiving borehole.
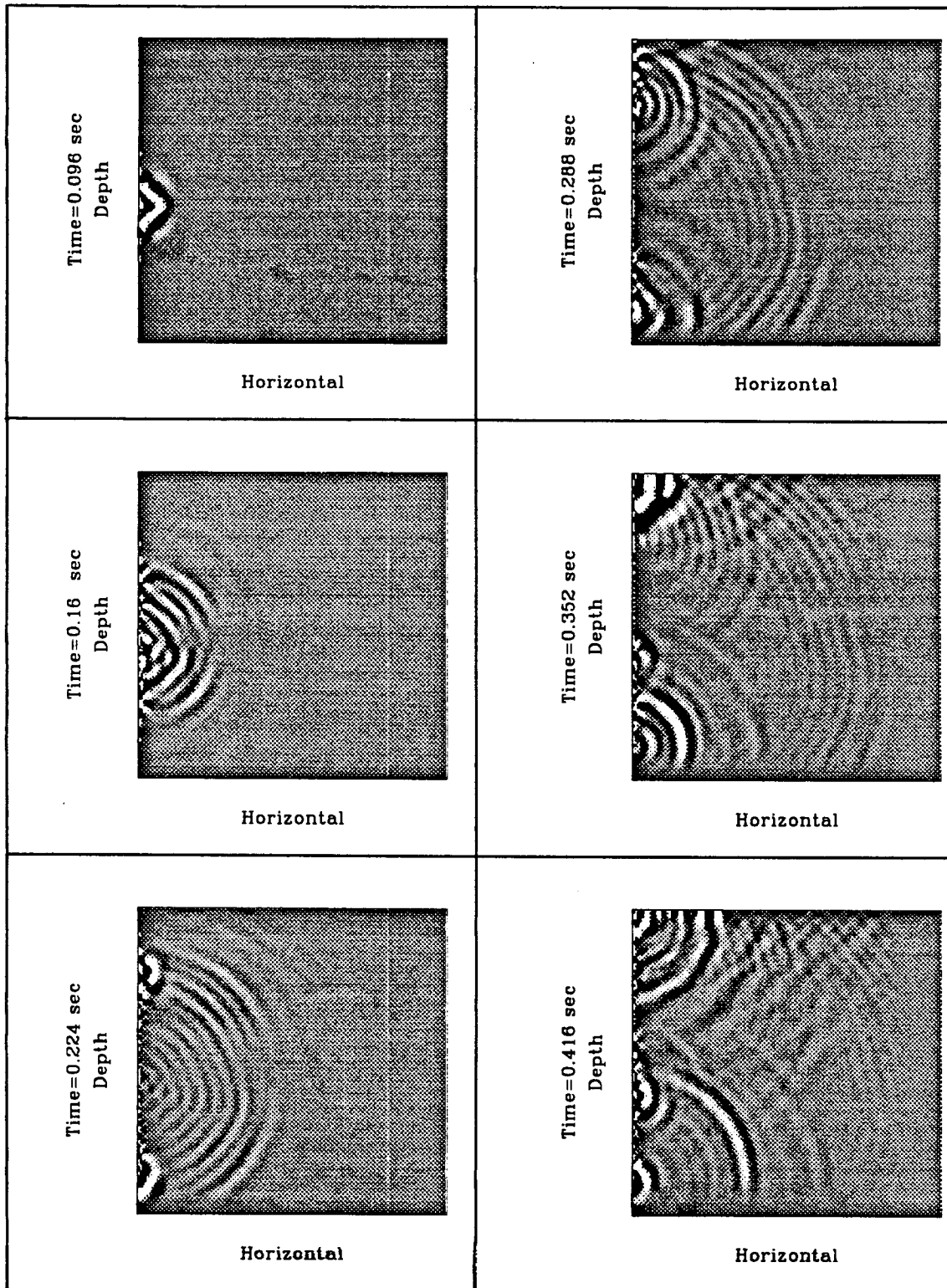
Figure 3.20: Snapshots of the field radiated by the fluid-coupled downhole source.

Horizontal Displacements
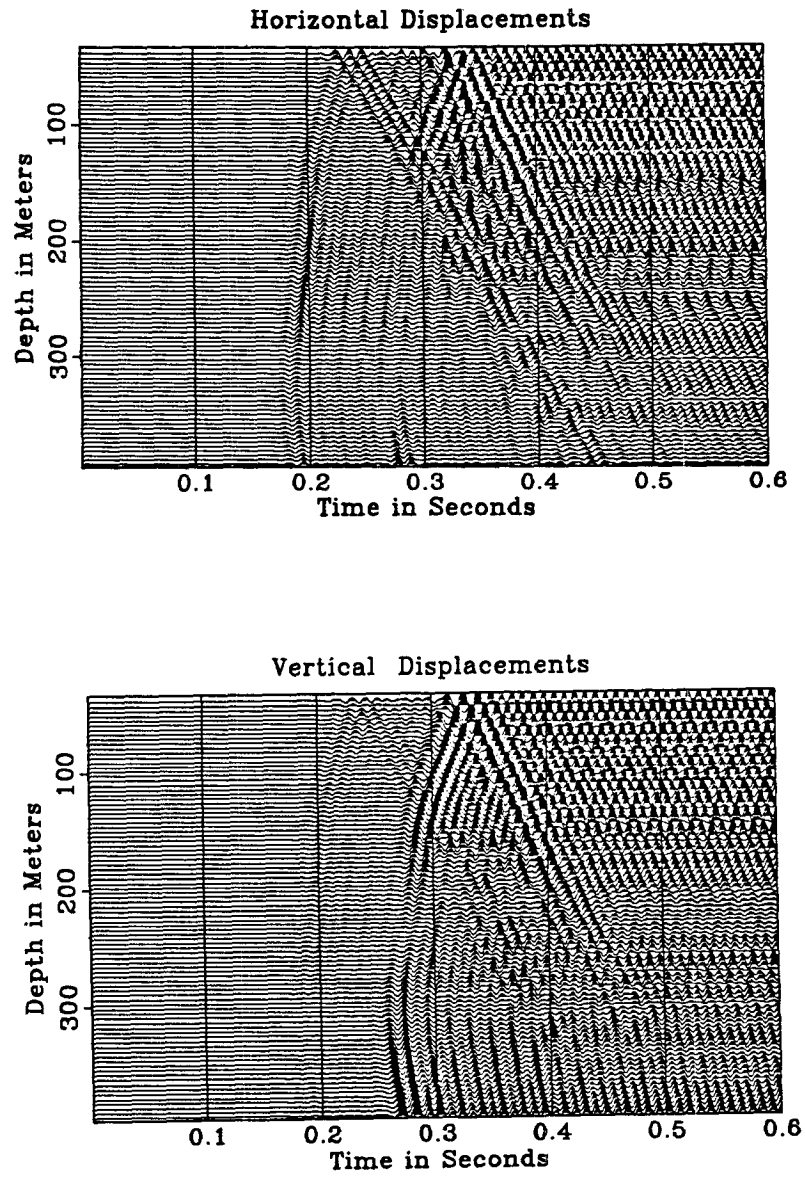

Vertical Displacements
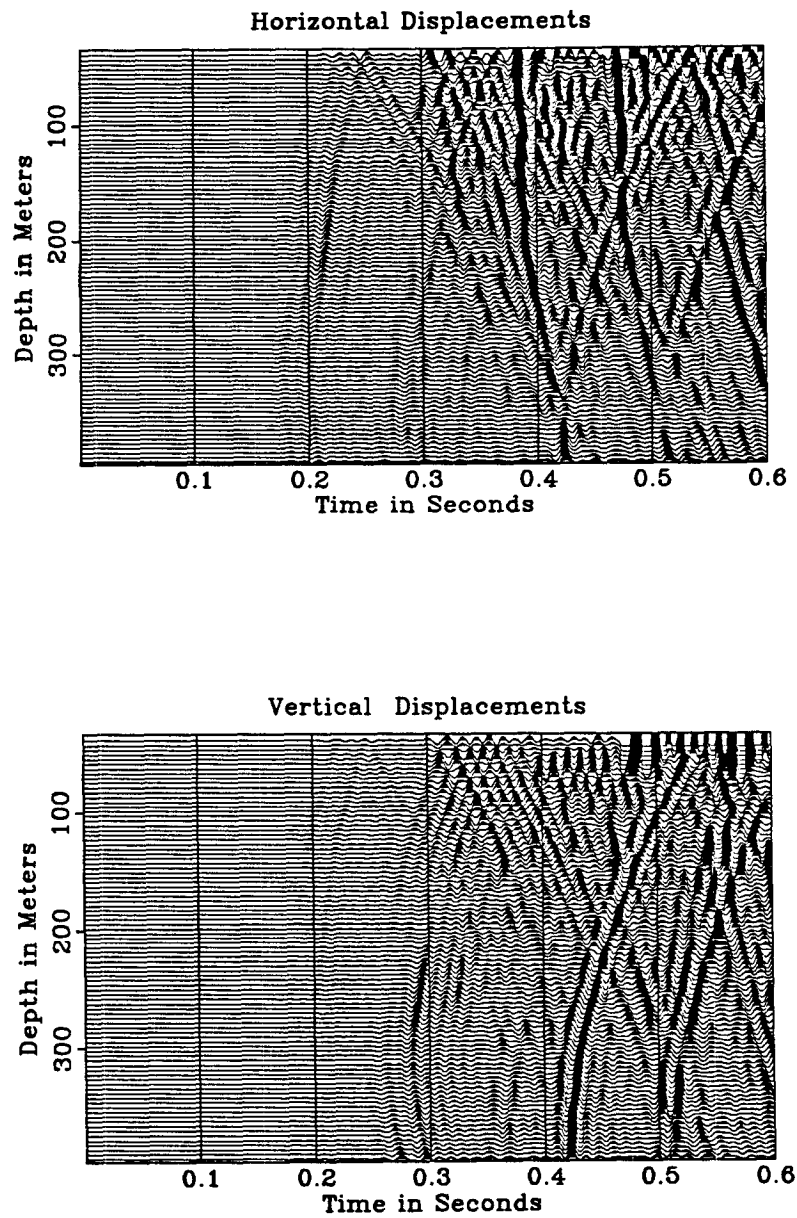
Figure 3.21: Traces computed for the fluid-coupled downhole source in a layered medium: a) the horizontal component of the displacements, b) the vertical component of the displacements.

- Second, independent of the secondary sources mechanism, if seismic energy is incident on a high-impedance contrast interface at the critical refraction angle, two new modes are created apart from the classical reflections and transmissions (Aki, 1980): 1) head waves in the slow velocity medium and 2) an exponentially decaying guided mode propagating in the fast medium. Once again, this last mode displays a two dimensional geometrical spreading, and has enough energy to create receiving borehole tube waves.

The two previous interpretations are not mutually exclusive, and both mechanisms have been encountered depending on the move-out of the apex of the receiving borehole tube waves with the source location. If the apex move-out has the Stoneley wave velocity (the rock formation velocity) the first interpretation applies (the second interpretation applies).

One last case, however, needs to be discussed. In the case where the compressional wave velocity of the rock formation is lower than the fluid velocity which occurs for soils and unconsolidated sediments, a new mode appears, the borehole conical waves. These waves first described by White (1973) are the two-dimensional axisymmetric space equivalent of head waves. With such waves incident on the receiving boreholes, a new phenomenon takes place in which the two boreholes are actually coupled through the action of these head waves. One striking manifestation of this phenomenon is the amplitude increase of the receiving-well-guided waves with time and propagation (Paternoster, 1990 oral communication).

3.4 The drill-string used as a downhole seismic source

The effects of the borehole guided waves detailed in the two preceding sections, namely their ability to generate secondary sources and conical waves, is one of the keys toward the understanding of the behavior of the drill-string used as a downhole
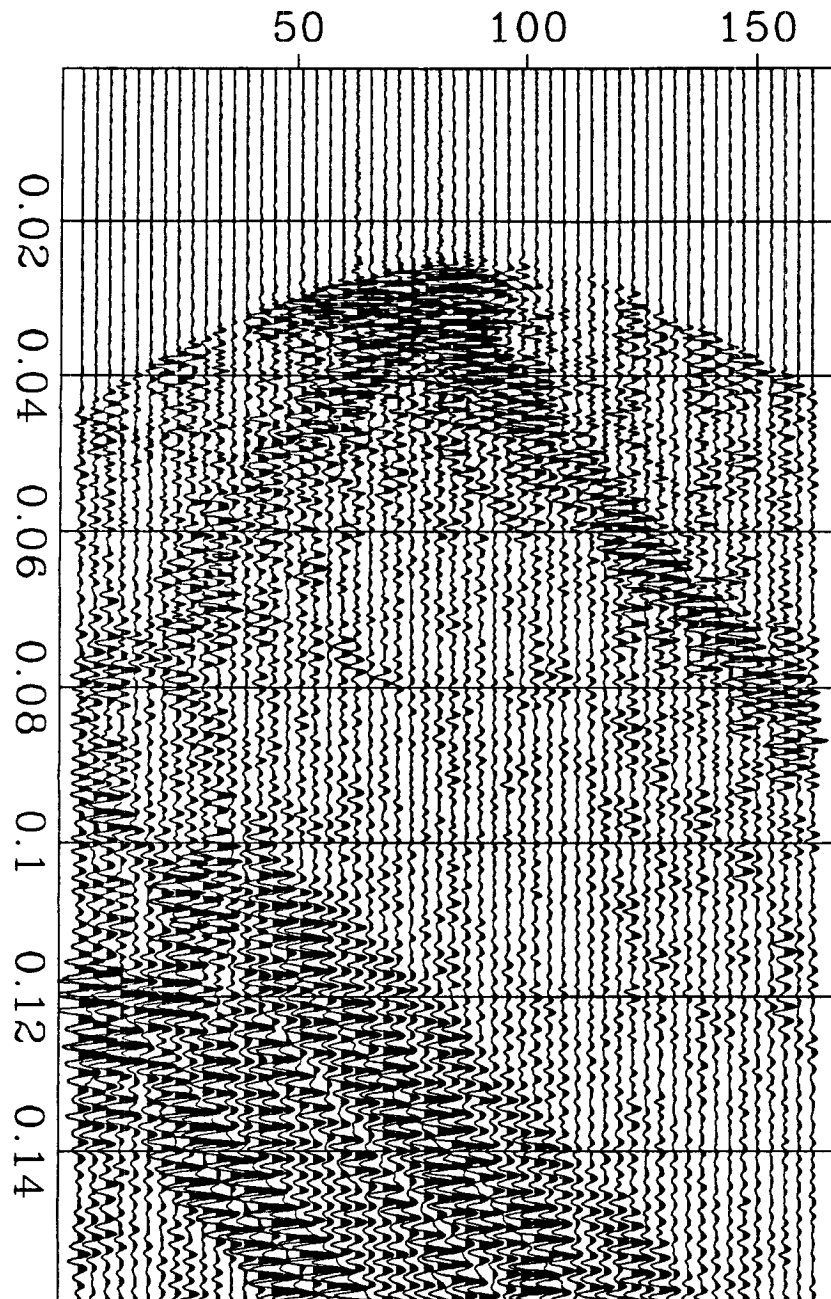
Figure 3.22:   Field data obtained after correlation for the piezoelectric downhole source (courtesy of the Stanford Tomography Project).
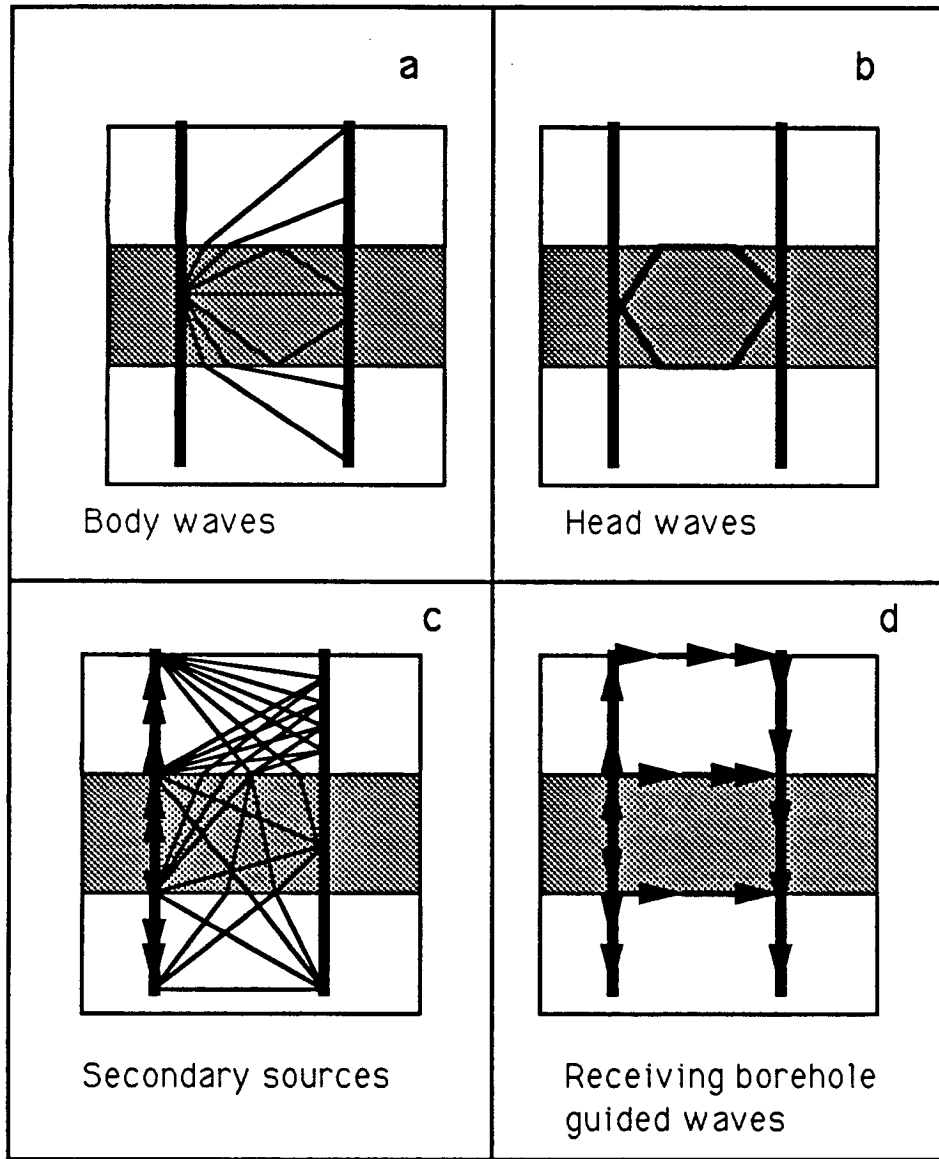
Figure 3.23: Possible paths for mode conversions in the case of the fluid-coupled downhole source. Thin line describe body waves ray paths, thick lines describe head waves paths, and arrows display borehole or interface modes paths. Each figure illustrates: a) classical body wave radiation, b) head waves radiation, c) conversion of tube waves to body waves, d) conversion of tube waves to interface modes to receiving borehole tube waves.

seismic source. A lot of effort has recently been invested in using the drill-bit noise as a seismic signal in a transposed VSP configuration (Rector 1990). Apart from the signal processing difficulties brought up by the use of this type of data, the interpretation of the processed data still remains obscured by wavefield effects that are described in the following section.

3.4.1 Principle of operation, and numerical model description

The principle of operation as well as the general setup of the drill-bit experiment are illustrated in figure 3.24. Four elements of this experiment are taken into account for the numerical modeling:

- The drill string has an interior diameter of $8.5cm$ and a thickness of $7mm$. The bottom hole assembly has an interior diameter of $8cm$ and a thickness of $18mm$. Both components of the drilling assembly are made of steel with the following physical properties: the compressional waves velocity is $5150m/s$, the shear wave velocity is $3110m/s$, and the density is $7800kg/m^3$. The drill string as well as the bottom hole assembly is modeled as a continuous homogeneous medium, and the assembly joints are not taken into account in this modeling.

- The borehole itself has two components: The upper part of the borehole is cased. In the cased part, the borehole diameter is $25cm$, the steel casing thickness is $3mm$, and the concrete cementing is $1.5cm$ thick. The steel quality of the casing is taken to be the same as the one of the drill pipe. The concrete compressional wave velocity iz $3251m/s$, and the shear wave velocity is $1861m/s$. The concrete density is $1630kg/m^3$. The bottom part of the well is not cased, and the borehole diameter is taken to be constant from the casing down to the bottom of the well. The well diameter is $10cm$ in the lower part.

- The drill-bit is assumed to apply a vertical force at the bottom of the well

directly to the rock formation (Rector 1990). The predominant drilling force is the weight of the drill-bit on the rock formation, and additional forces, such as the torque applied by the drill cone to the formation, or lateral forces at the bottom of the well are not taken into account here.

- Finally, the field seismic signal is recorded while drilling. The recording length may vary from a couple of seconds to hundreds of minutes, depending on the type of acquisition. Most of the signal processing of this data is intended to find the explosive source equivalents, that is computing the impulse response of the drill-bit, well, and rock formation system. Since it would be impractical to model very long seismic records because of computer limitations, our modeling is limited to the previously used source time history described in section 3.2.

3.4.2 Finite-element modeling of the drill-bit behavior in a homogeneous isotropic solid

Snapshots of the wavefield generated by the drill bit used as a downhole source are presented in figure 3.25, and the corresponding receiver traces for receivers placed at the surface appear in figure 3.26. Four different modes can be clearly identified in both figure 3.25 and figure 3.26.

The first two one are the compressional and shear primary body waves. Even though they are not the strongest modes, they remain the modes of choice for seimic interpretation. Figure 3.26 shows that the amplitude of the compressional waves is maximum at zero offset and decreases with offset. On the other hand, the amplitude of the shear waves is null at zero offset and increases with offset. This radiation pattern behavior is consistent with the radiation of a single vertical point force source buried in the ground. This interpretation ,however, is not coherent because single couple forces do not exist (Aki and Richards 1973). Actually, the rig drill bit system is truly a double couple system where the reaction force applied downhole is balanced by the
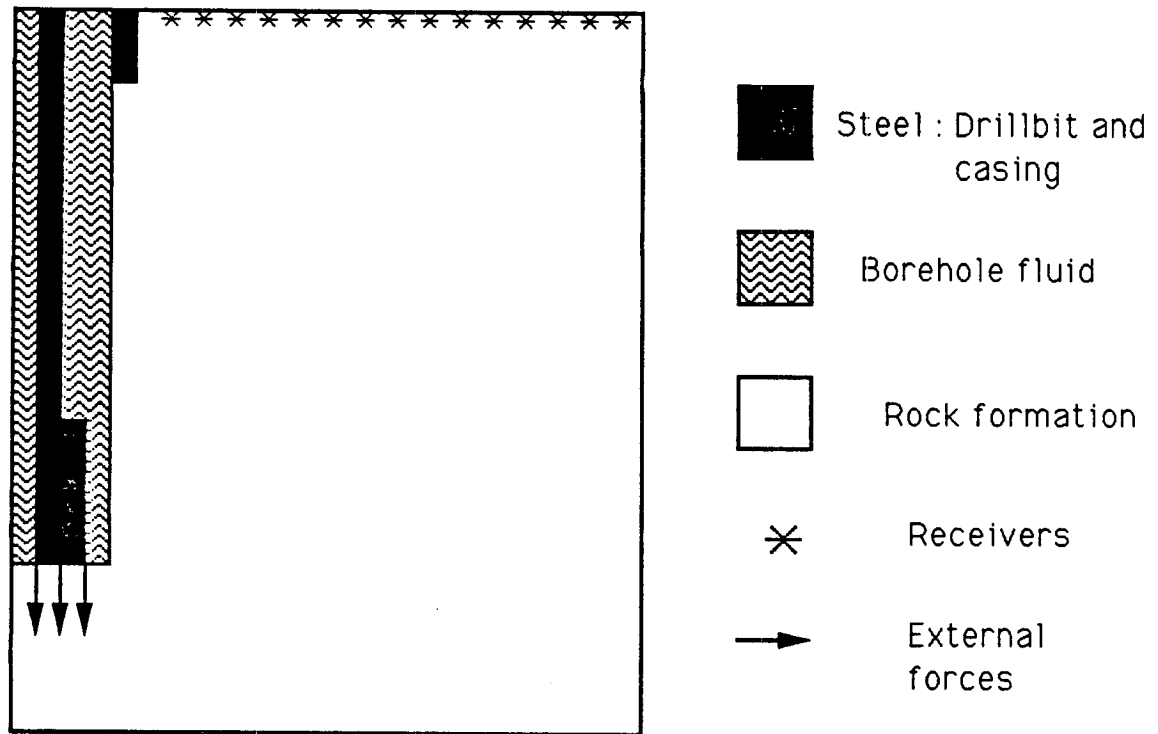
Figure 3.24:   A schematic diagram of the implementation of the drill-bit as a downhole seismic source.
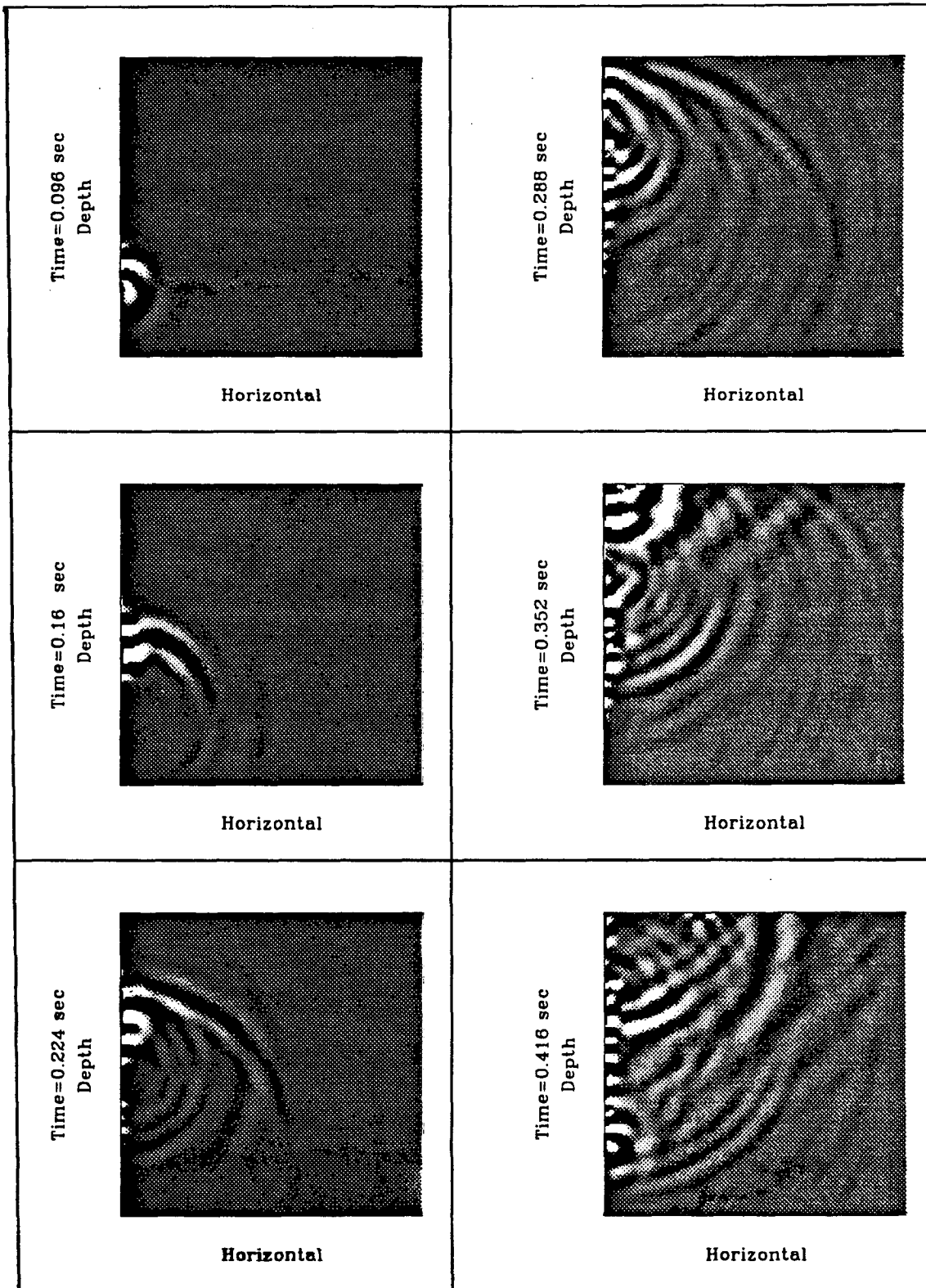
Figure 3.25: Snapshots of the field radiated by the drill-bit used as a downhole seismic source in a homogeneous medium.
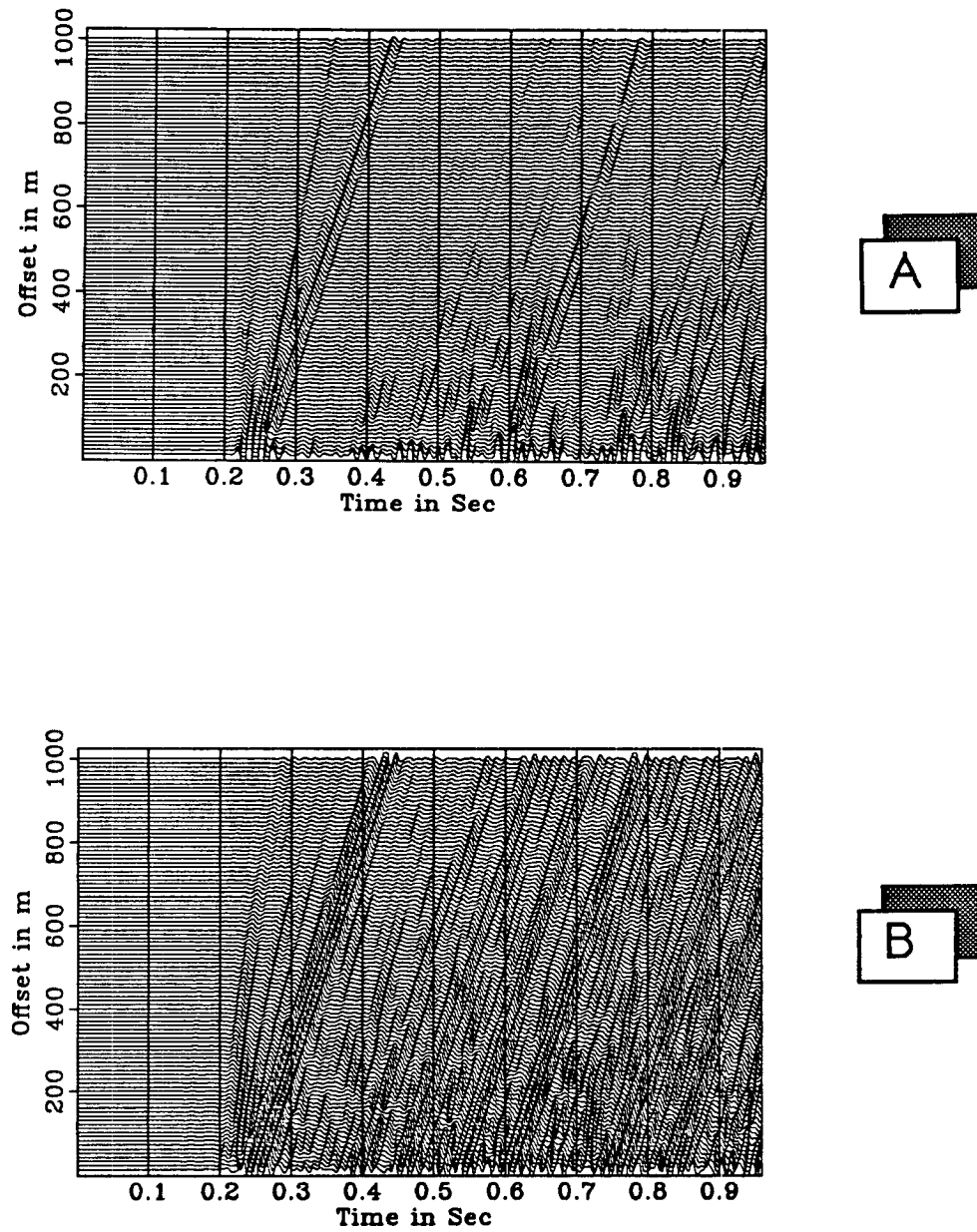
Figure 3.26: Traces computed for the drill-bit used as a downhole seismic source in a homogeneous medium: A) The horizontal component of displacements, B) The vertical component of displacements.

force applied by the rig to the ground. Thus for an ideal system the force applied downhole is also applied at the surface with a reverse direction, thereby yielding a second seismic source at the surface. This second source is of no interest to our problem except that it can dramatically affect the quality of the seismic data for two reasons:

- The surface source creates powerful surface waves that have to be filtered. This filtering is achieved by the receiving array, or at the processing stage. Furthermore, the casing bottom also generates a secondary source that is less powerful than the initial source.

- Actual seismic reflections that will not be attenuated by the receiving antenna can be generated by the surface sources. These modes however have not been identified in actual drill-bit data for the following reasons. In general the signal-to-noise ratio of processed drill-bit data is poor, and seismic reflections initiated by the rig acting as a seismic source are weaker than the seismic energy coming directly from the rig because: 1) the rig acts as a distributed source over the rig foundation surface, and 2) reflected signals are weaker than direct signals, because of the effect of the reflection coefficient.

The third mode is the borehole conical wave. The existence of this mode was initially predicted by White (1973), and was previously mentioned in this chapter (sections 3.2 and 3.3) in the case where the formation velocity is slower than the borehole fluid velocity, and in the case of the resonant cavity in a cased well. Conical waves are the axisymmetric equivalent of head waves. Let us consider the case of a fast medium in two-dimensional space with a compressional wave velocity slightly lower than the steel velocity in contact with a lower velocity medium. If a seismic source is triggered, it will generate an incident and a reflected compressional wave in the fast medium, as well as a transmitted and critically refracted wave in the slow medium. The critically refracted wave is often called a head wave ; it is a plane wave.

The angle θ between the plane wave direction and the normal to the interface is given by the following relation illustrated in figure 3.27:

$$\sin(\theta) = \frac{V_{slow}}{V_{fast}} \qquad (3.4)$$

where V_{slow} and V_{fast} are the respective velocities of the two media considered. In the axisymmetric case, the plane wave previously described is now the envelope of a cone of revolution with the same axis as the borehole. Within the borehole, the mode velocity is controlled by the steel velocity and the borehole fluid velocity. Since the steel density is so much higher than the water or mud density, the drill-pipe-guided mode velocity is very close to the steel velocity, and was measured to be $5080m/s$ for this modeling case, which is quite close to Rector's measurements (1990). The effect of the drill-pipe -guided mode is felt in the rock formation but is fairly weak because of the high impedance of the water layer between the drill-string and the rock formation for that geometry. For the drill bit modeling, both compressional and shear head waves were identified, but were an order of magnitude smaller than those previously modeled with the resonant cavity and this for the following reason. In the case of the resonant cavity source, the source is in direct contact with the casing, which itself is in direct contact with the rock formation. Because of this direct transmission line, the conical waves were strong. In the case of the drill bit, the steel string is not in direct contact with the formation. For that reason the conical waves are weak in the last case modeled.

The last mode belongs to the now familiar generic family of borehole-guided modes. Two of these modes are of particular interest for the modeling cases chosen here. First, the drill-string and the steel-casing-guided waves are responsible for the existence of the conical waves. Two other phenomena of interest can be further associated with this mode:

- The existence of drill-bit multiples: The two most powerful drill-string scatter-

ers are the drill string bottom and top (here taken to be at the free surface). These two scatterers ensure that each signal generated at the borehole bottom is echoed with a delay double the travel time of the drill string guided mode. These multiples are clearly visible at 0.2 and 0.55*sec* in figure 3.26 and are illustrated in the snapshots in figure 3.25. Since our model does not contain any intrinsic attenuation mechanism, the signal echoes up and down the well with only little absorption. In reality, it is not rare to have four to ten drill-string multiples before the amplitude of the multiple drops below the noise level.

- The existence of drill-bit sub-multiples: as with the borehole guided waves previously discussed in section 3.2.3, every variation along the drill-string acts as a scatterer. One of the dominant scatterers is the junction between the drill-string, and the bottom-hole-assembly. As the up-going drill-string guided mode meets this junction, it is converted into 1) a transmitted guided mode, 2) a reflected guided mode, and 3) a scattered packet of body waves. Then the down-going reflected guided mode impacts the drilling cone and the rock formation, it generates a further family of body waves similar to those generated with the initial source impact, and another reflected up-going guided mode assembly. This mechanism is illustrated in figures 3.28 and 3.29 where the length of the bottom hole assembly is 60*m*. The bottom-hole-assembly multiples are both clearly visible on the snapshots in figure 3.28 where the source at the bottom of the well gets fired for each multiple, as well as in the recorded seismograms shown in figure 3.29.

Other types of scatterers exist along the drill string that are not taken into account by this modeling. Among others, the drill-bit joints introduced each time a new segment of drill-string is added act as drill-string-guided waves scatterers, and contribute strongly to both the attenuation and dispersion of the drill-bit signal (Rector 1990).

Second, the equivalents of the Stoneley waves for this borehole configuration are also very powerful. Their velocity in our modeling case is still slightly slower than the fluid velocity. This mode is also responsible for the powerful emission of secondary sources as shown in figures 3.25 and 3.26.

3.4.3 Finite-element modeling of the drill-bit behavior in a layered isotropic solid

The layered medium chosen here is similar to the one previously used for the controlled downhole source modeling (sections 3.2 and 3.3). As expected from the results previously obtained, the following results are clearly visible in figure 3.30 and 3.31.

First, each layer boundary appears as the source of a very strong borehole secondary source, generated essentially by the conversion of the Stoneley waves. Other secondary sources, such as those created by the bottom hole assembly multiples, are also clearly visible.

Second, as the conical wave, described in the preceding section of this chapter, travels up the well, it enters formations with lower and lower compressional wave velocity. As illustrated in figure 3.30, as the rock velocity decreases, the angle between the borehole normal and the conical waves increases. This angle is null if the rock formation is equal to the velocity of the drill-string, and increases with slower formations. As illustrated in figure 3.27, the general increase in velocity with increasing depth is responsible for the negative curvature of the conical waves' arrival at the surface, and thereby provides an easy-to-interpret attribute of this arrival.

The events previously described in two simple modeling experiments allow for the interpretation of the data displayed in figure 3.32. This data is obtained with a transposed VSP configuration where the drill-bit is used as the source of the seismic signal. The raw data was processed, using the algorithm described in Rector (1990)
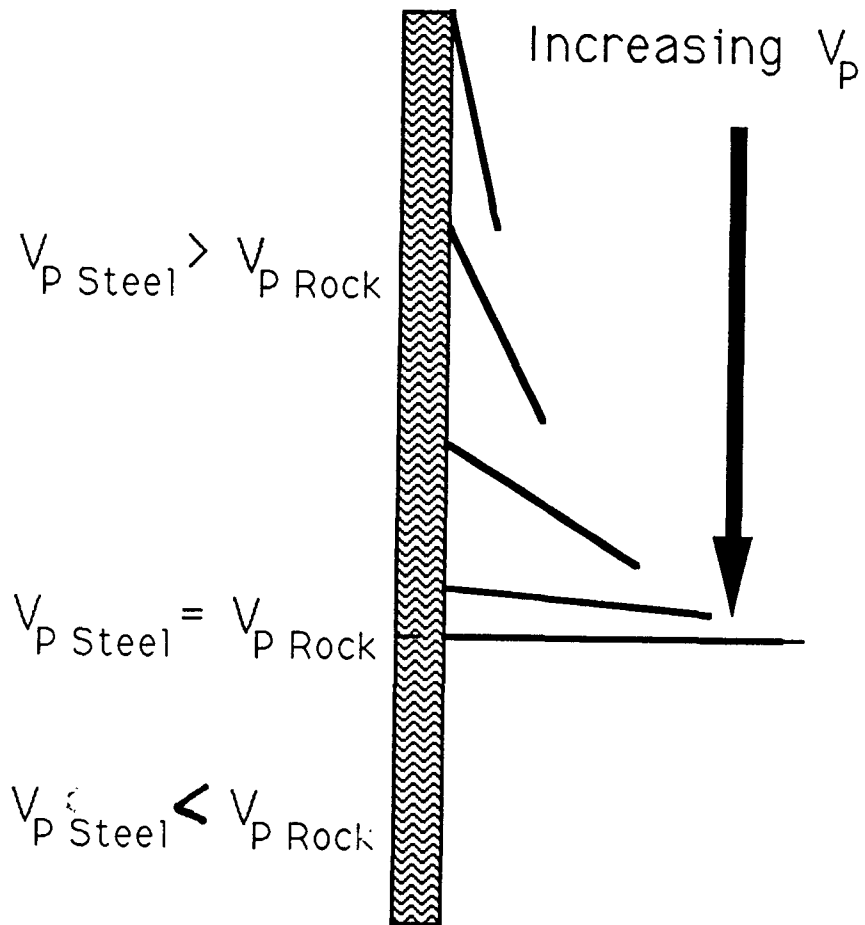
Figure 3.27: A schematic illustration of the behavior of conical waves.
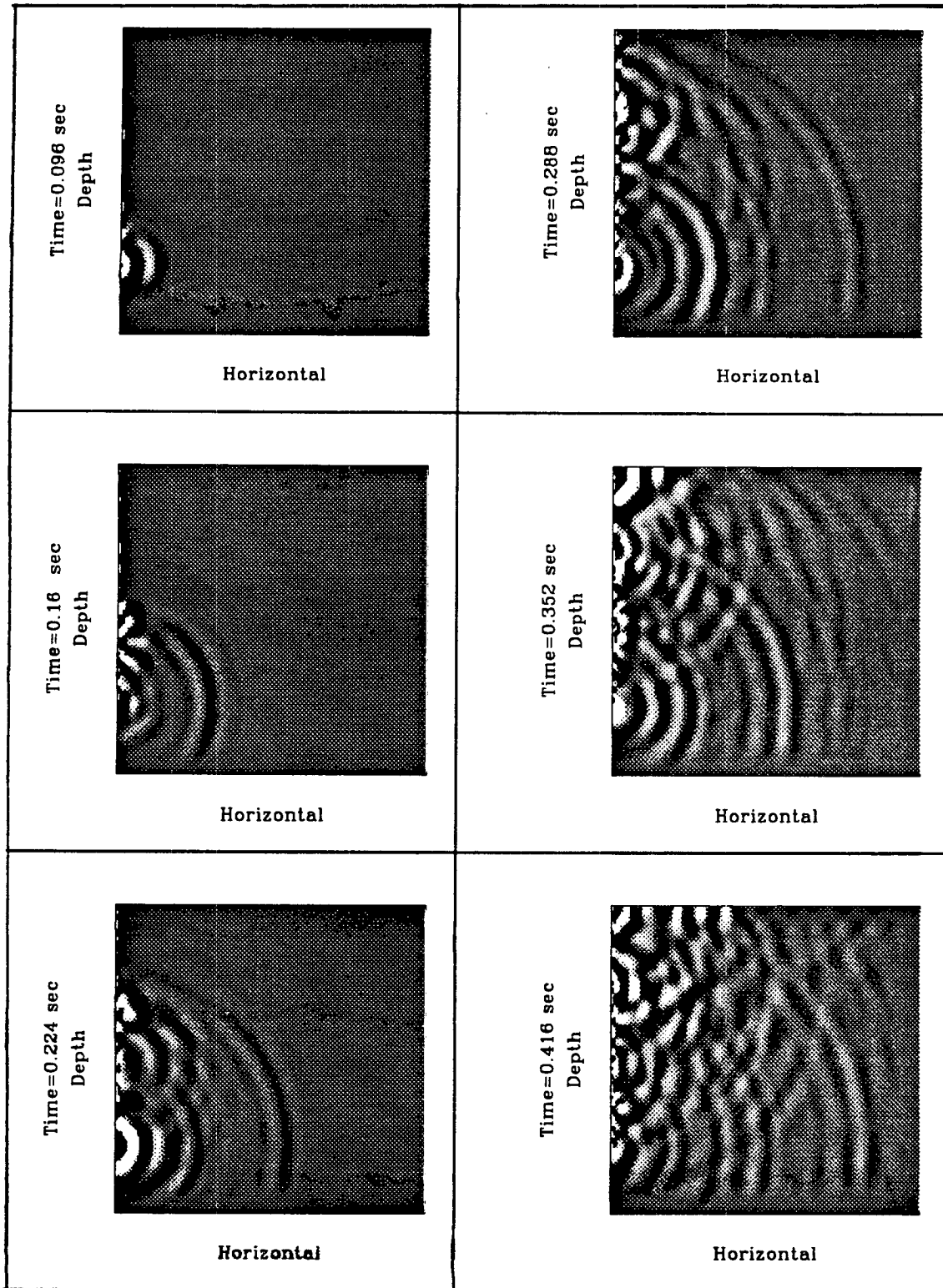
Figure 3.28: Snapshots of the field radiated by a drill-bit. This time the drill string is modeled with a bottom hole assembly.
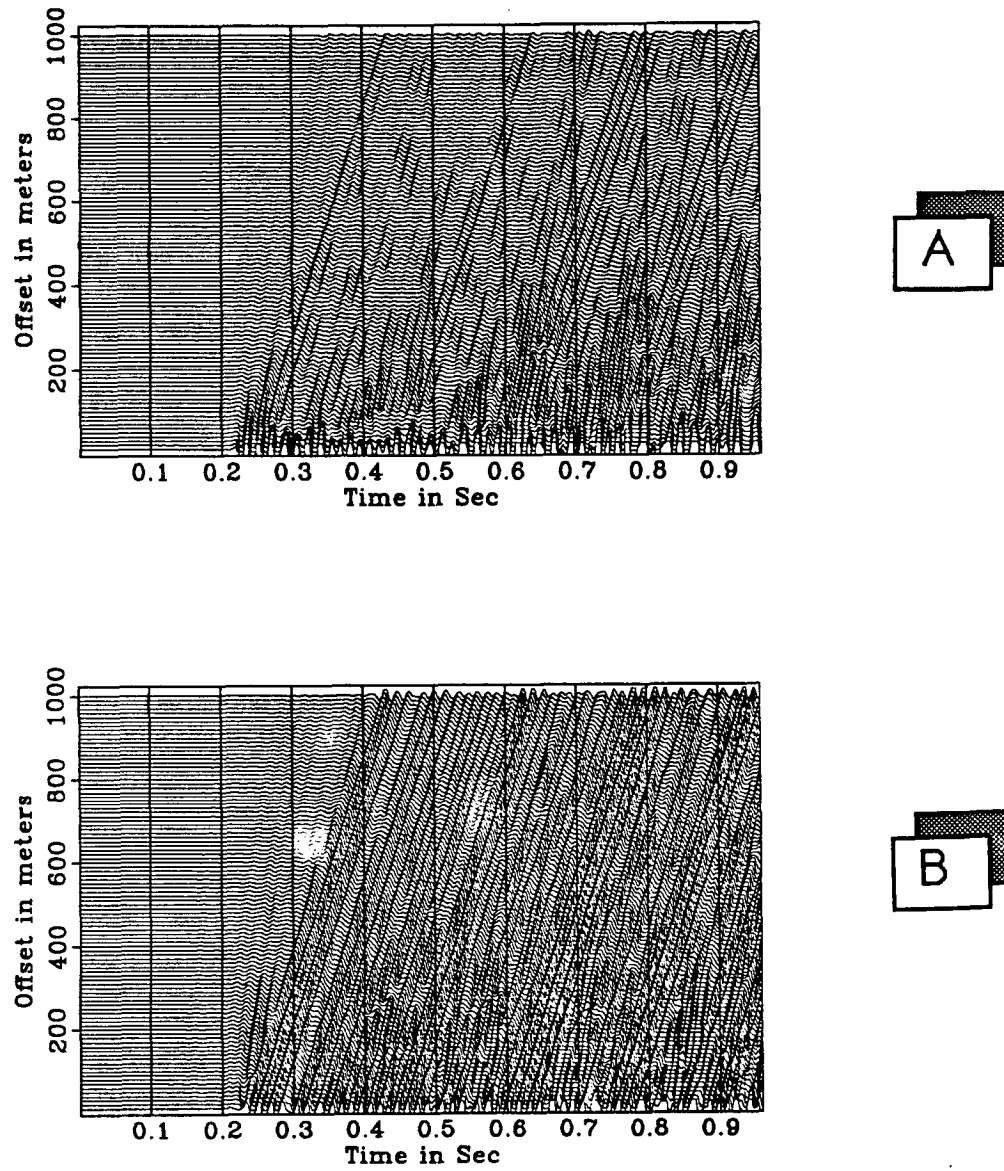
Figure 3.29: Traces computed for the drill-bit used as a downhole source. This time the drill string is modeled with a bottom hole assembly. A) The horizontal component of displacements, B) The vertical component of displacements..

to obtain the data presented here where the phase of the signal is null. Three major arrival or energy packets can be easily identified:

- 1) The first arrival is caused by the propagation of the conical waves previously described, and are easy to recognize because of their inverse curvature.

- 2) The arrival of the compressional and shear waves. These modes can be identified first because of their arrival time, but also because of their amplitude versus offset dependence. The compressional waves have a maximum amplitude for small offsets, and the amplitude decreases with offset. The shear waves exhibit the opposite behavior, their amplitude increasing with offset.

- 3) A group of arrivals similar to the one previously described is reproduced attenuated beginning at 1.15 seconds. This arrival is caused by drill-bit multiples attenuated both by the travel up and down the well, and by the deconvolution algorithm applied to the initial data.

3.5 Conclusions

This modeling of various downhole sources and the actual comparison and interpretation of the synthetic data with real data indicates that in most cases the effects related to the borehole cannot be neglected. Even though the borehole is small along the radial direction, it is an elongated object, and its effects must therefore be taken into account even for the frequencies used with downhole seismic sources. The same conclusion can be applied to the downhole sources themselves if their length is comparable to the seismic wavelength, unless special engineering features mechanically decouple the active components of the source from the remaining part of the downhole apparatus.

The main effects of the borehole can be summarized as follows:
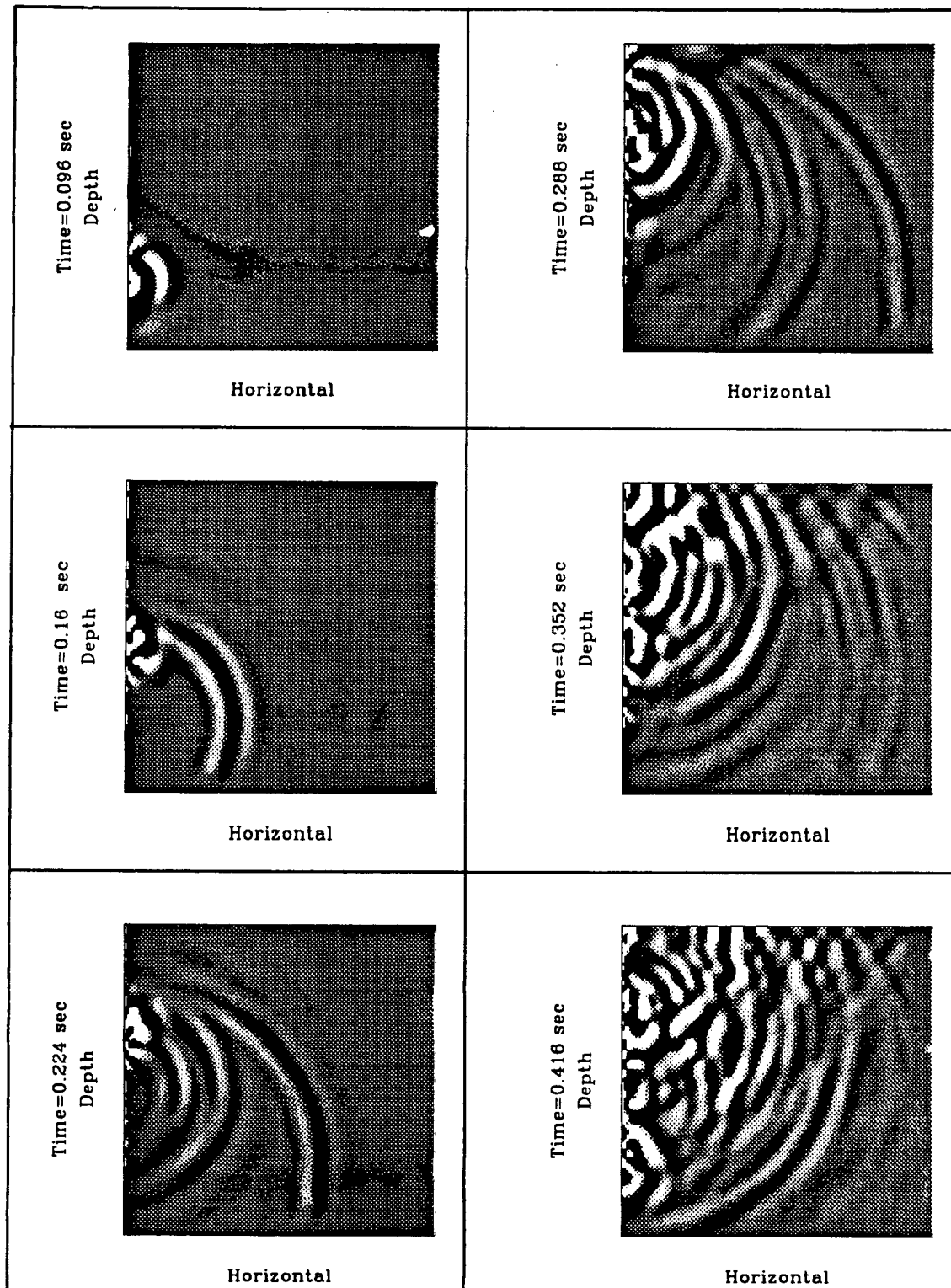
Figure 3.30: Snapshots of the field radiated by the drill-bit used as a downhole seismic source in a layered medium.
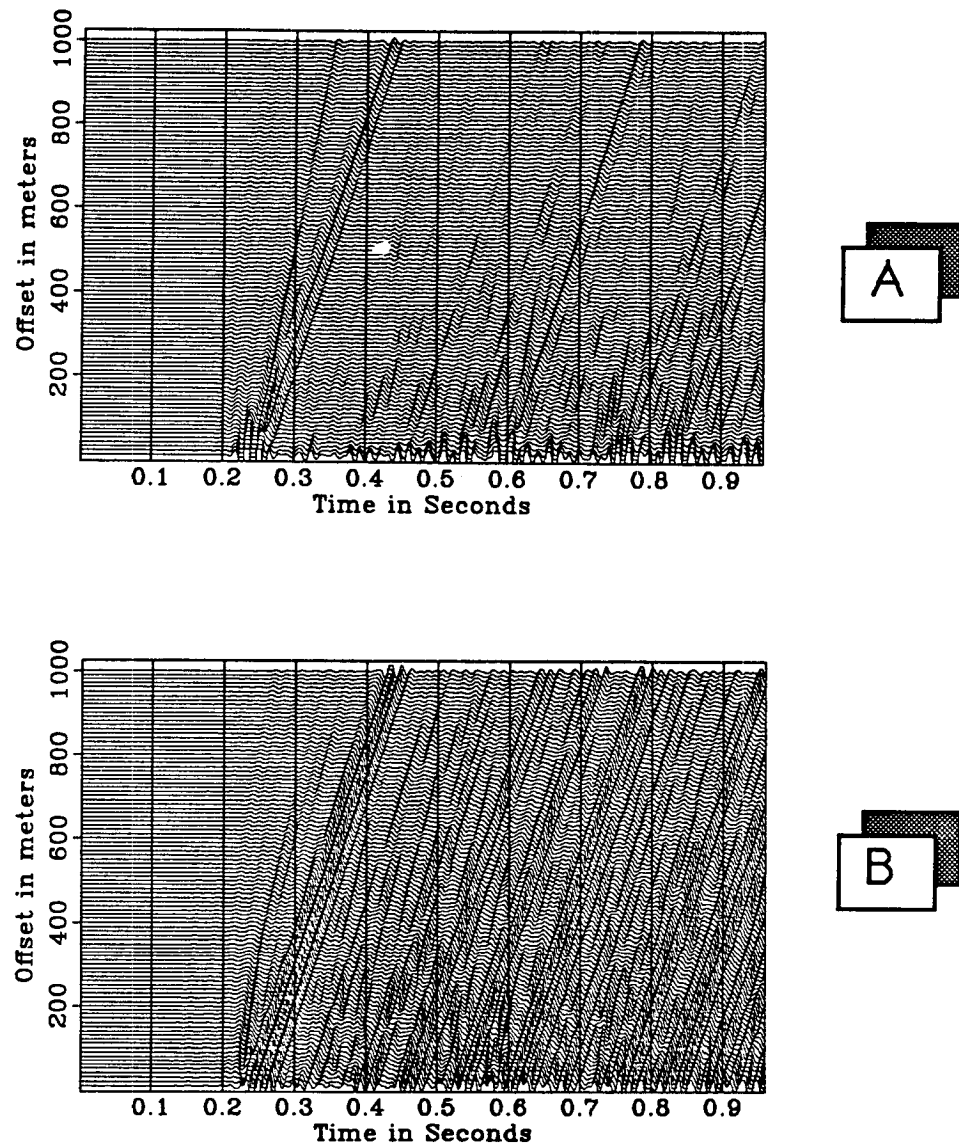
Figure 3.31: Traces computed for the drill-bit used as a downhole seismic source in a layered medium: A) the horizontal component of displacements, B) the vertical component of displacements.
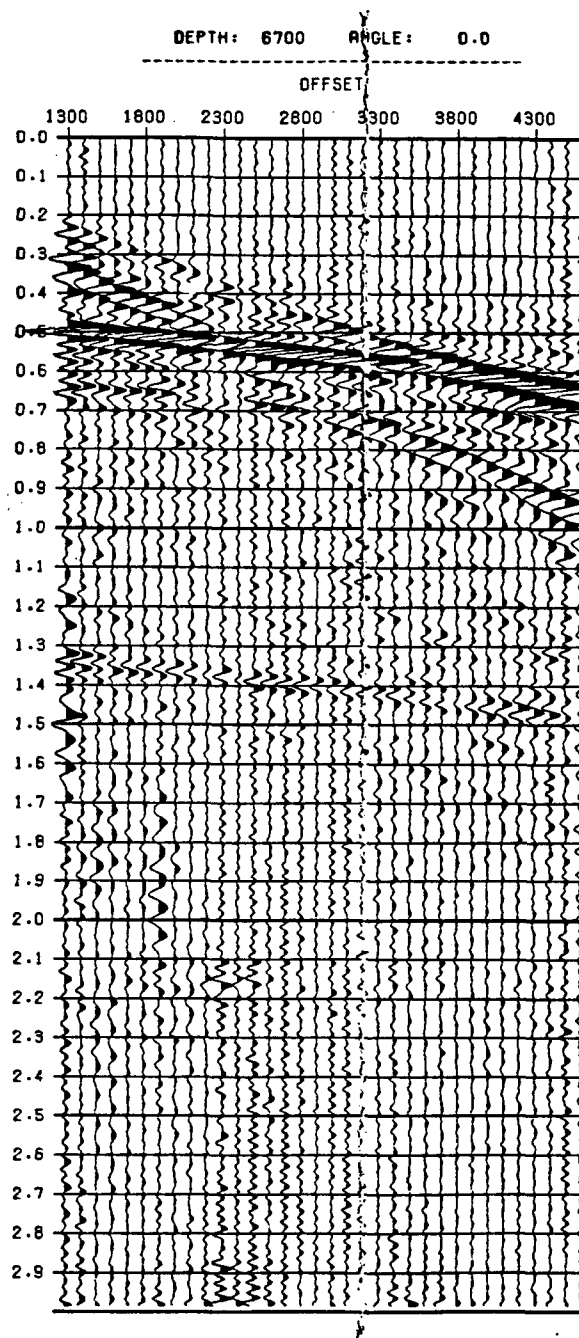
Figure 3.32: Drill-bit data after processing. The following modes are clearly visible: 1) Head waves arrival, 2) Primary compressional waves arrival, 3) Shear waves arrival, 4) multiple arrival.

- First, the failure to isolate the downhole source from the borehole fluid results in the generation of powerful tube waves that dramatically decrease the source efficiency. In the process of isolating the source from the borehole fluid, however, great care must be given to the source design in order to prevent such unwanted effects as frequency-dependent radiation patterns when the source length is comparable to the seismic wavelength in the borehole fluid.

- Second, the existence of powerful borehole-guided waves results in the generation of borehole secondary sources. For strong borehole heterogeneities such as the casing bottom, rock formation velocity contrasts, or borehole diameter changes, the amplitude of these secondary sources is comparable to the initial source amplitude.

- Third, in the receiving wells, the rock-interface-guided modes generated by the use of downhole seismic sources convert into receiving-wells-guided modes, thereby establishing a direct coupling between the emitting and receiving borehole.

- Finally, in the case where the speed of the borehole-guided modes is faster than the formation velocity, conical waves are radiated by the emitting borehole, thus providing a new mode for velocity investigation, as well as a new level of coupling between two boreholes.

References

Aki, K., and Richards, P. G.,1980, Quantitative seismology, theory and methods, W. H. Freeman and Co., San Francisco, California.

Auld B. A., 1973, Acoustic Fields and Waves in Solids, John Wiley & sons, New York.

Cheng, C. H. and Toksoz, M. N., 1981, Elastic wave propagation in a fluid filled borehole and synthetic acoustic logs: Geophysics, **46**, p. 1042-1053

Harris, J. M., 1988, Cross-Well Seismic Measurements in Sedimentary Rocks, S.E.G. expanded abstracts,**1**, 147, 150.

Heelan, P.A., 1953, Radiation from a cylindrical source of finite length: Geophysics, **18**, 685, 696.

Hughes, T., 1983, The Finite element method: Prentice Hall, New York.

Kennedy W., Wiggins W., Aronstam P., 1988 Swept-Frequency Borehole source for Inverse VSP and Cross-Borehole Surveying, S.E.G. expanded abstracts,**1**, 158, 160.

Kosloff, D. and Baysal, ER., 1982, Forward modeling by a Fourier method: Geophysics, **47**, 1402,1412.

Paulson B., 1988, Three-Component Downhole Seismic Vibrator, S.E.G. expanded abstracts,**1**, 139, 142.

Samec, P., and Kostov, C., 1988, Full Waveform Modeling of a Downhole Source Radiation Pattern Using the Finite-Element Technique, S.E.G. expanded abstracts,**1**, 143, 146.

Rector, James, 1990, Utilization of drill-bit energy as a downhole seismic source, PhD Thesis, Stanford University.

White, J. E., 1983, Underground sound: Elsevier, New York.

Zienkiewicz, O. C., 1973, The finite element method: Mac Graw Hill, London.

Chapter 4

Theoretical Investigation of Viscoelastic Anisotropic Material

Abstract

Attenuation of elastic waves in rocks has been studied extensively in the past years under the following assumptions : rocks have a linear behavior for low strains, and the attenuation mechanism is isotropic, that is independent of the wave propagation direction. Both laboratory, and field experiments recently demonstrated that these assumptions are not always valid. This is why this chapter focuses on the study of linear anelastic media with both propagation and attenuation anisotropy.

As a framework for the study of these materials, this chapter first presents an energy formulation of the wave equation, generalizing the approach followed for isotropic material. The application of this formulation to plane waves propagating in a homogeneous medium provides an adequate formulation for Q.

Second, a numerical method for the modeling of material with these properties is investigated . The benchmark modeling results indicate that the theoretical investigation, and the numerical modeling are in good agreement. The results also indicate that materials with viscoelastic anisotropic properties have great energy focusing ca-

pabilities related to both elastic focusing and direction-selective attenuation.

4.1 Introduction

The effect of anisotropy on wave propagation in rocks has recently been extensively studied with the assumption that anisotropic rocks behave in a purely elastic way. (Crampin 1980 among others). Various causes for rock anisotropy have been investigated, relating it to the constitutive crystal anisotropy (Christensen, 1970), but most often to the anisotropic distribution of the pore space within the rock mass (Nur 1969, Budiansky, 1976). The effects of pore fluid and pore shape on elastic wave attenuation in rocks have also been studied relating the fluid displacement in the pore space to energy dissipation. (Biot 1965 a,b, Nur 1969, Murphy 1982, Jones 1986).

Hudson (1981), following Garbin and Knopoff (1975), introduced an imaginary component into the description of the elastic tensor, specifying that the imaginary part of the viscoelastic tensor displays a very high degree of anisotropy. In a recent experiment, the dependence of energy dissipation on wave propagation direction (attenuation anisotropy) has been demonstrated on composites (Hosten 1987) yielding again a very high degree of attenuation anisotropy where the ratio of quality factors in different directions can range from 17 to as much as 500.

In this chapter, viscoelastic anisotropy will be described using :

- an energetic approach that generalizes the description of isotropic viscoelastic materials to anisotropic materials,

- a numerical approach that allows the actual computation of the wavefield propagating in a viscoelastic anisotropic material.

4.2 Energetic description of linear viscoelastic anisotropic material

Since most of the work in this chapter concentrates on the energy focusing capabilities of anisotropic anelastic solids, an energetic description of such solids is ideally suited in that it provides a clear accounting of the energy balance of the system studied. This is why this description is implemented in the next section of this chapter.

4.2.1 The definition of a linear, viscoelastic, anisotropic solid

A linear viscoelastic solid is defined as a medium for which there exists a relaxation function $c_{ijkl}(t)$ relating the stress tensor $\sigma_{ij}(t)$ and the strain tensor $\epsilon_{ij}(t)$ in the following way (Gurtin and Sternberg, 1962) (The notations used in this chapter are presented in the first appendix, for the most part):

$$\sigma_{ij}(t) = \int_{-\inf}^{t} c_{ijkl}(t - \tau) d\epsilon_{kl}(\tau) = \tag{4.1}$$

$$c_{ijkl}(t) \times [(1 - H(t)\epsilon_{kl}(t)] \tag{4.2}$$

summation on repeated indices is assumed here, and H is the Heavyside step function. Taking the Fourier transform of Eqn. 4.1 leads to a frequency domain stress-strain relation of the following form, where ω is the frequency:

$$\sigma_{ij}(\omega) = i\omega c_{ijkl}(\omega)\epsilon_{kl}(\omega) \tag{4.3}$$

using the mass and momentum conservation principles, equation 4.1 leads to the equation of motion for the continuum in the time domain:

$$\sigma_{ij,j} + f_i = \rho \ddot{u}_i \tag{4.4}$$

Finally, using equations 4.1 to 4.3, the equation of motion can be rewritten as follows using the method of Borcherdt (1973):

$$i\omega \frac{\partial}{\partial x_j} \left[\tilde{c}_{ijkl}(\omega) \tilde{\epsilon}_{kl}(\omega) \right] + \rho \omega^2 \mathcal{U}(\omega) = 0 \tag{4.5}$$

where $\mathcal{U}$ is the Fourier transform of the displacement field, and the tilde denotes the Fourier transform for both c_{ijkl} and ϵ_{kl}. Further proposing that $\mathcal{C}_{ijkl} = i\omega \tilde{c}_{ijkl}$, and equating both the real and imaginary part of Eqn 4.5, we obtain:

$$\frac{\partial}{\partial x_j} \left[\mathcal{C}_{ijkl}^{(R)} \epsilon_{kl}^{(R)} + \frac{1}{\omega} \mathcal{C}_{ijkl}^{(I)} \epsilon_{kl}^{(R)} \right] + \rho \omega^2 \mathcal{U}^{(R)}(\omega) = 0 \tag{4.6}$$

$$\frac{\partial}{\partial x_j} \left[\mathcal{C}_{ijkl}^{(R)} \epsilon_{kl}^{(I)} + \mathcal{C}_{ijkl}^{(I)} \epsilon_{kl}^{(R)} \right] + \rho \omega^2 \mathcal{U}^{(I)}(\omega) = 0 \tag{4.7}$$

The notations (R) and (I) respectively denote the real and imaginary parts of a complex number. From the previous equations, the most interesting quantity is: $\mathcal{V}_{ij}^{(R)} = \left[\mathcal{C}_{ijkl}^{(R)} \epsilon_{kl}^{(R)} + \frac{1}{\omega} \mathcal{C}_{ijkl}^{(I)} \epsilon_{kl}^{(R)} \right]$. Equation 4.5 can now be rewritten:

$$\nabla(\mathcal{V}^{(R)}) - \rho \ddot{u}^{(R)} = 0 \tag{4.8}$$

4.2.2 The energy conservation principle for a viscoelastic continuum

Proceeding to obtain an integral energy conservation equation is first achieved by multiplying equation 4.8 by $\dot{u}^{(R)}$ and using the relationship: $\nabla(\dot{u}^{(R)}\mathcal{V}) = \dot{u}^{(R)}\nabla\mathcal{V} + \nabla u^{(R)}\mathcal{V}$. Equation 4.8 can then be rewritten when integrated over a volume V as:

$$\int_V -\nabla(\dot{u}^{(R)})\mathcal{V}^{(R)} + \int_V \nabla\left[\dot{u}^{(R)}\mathcal{V}^{(R)}\right] + \int_V \rho \ddot{u}^{(R)} \dot{u}^{(R)} = 0 \tag{4.9}$$

For the clarity of the development the three terms in the previous equation will be dealt with separately. Each of the terms is numbered from I to III from left to right.

First, expanding the first term (I), we find that:

$$\nabla \dot{u}^{(R)} \mathcal{C}_{i}jkl^{(I)} \dot{\epsilon}_{k}l^{(I)} = \mathcal{C}_{i}jkl^{(I)} \dot{\epsilon}_{ij}^{(R)} \dot{\epsilon}_{kl}^{(I)} \tag{4.10}$$

then using the same tensor equality again, we get:

$$\nabla \dot{u}^{(R)} \mathcal{C}_{ijkl}^{(R)} \epsilon_{kl}^{(R)} = \frac{1}{2} \frac{\partial}{\partial t} \left[\mathcal{C}_{ijkl}^{(R)} \epsilon_{ij}^{(R)} \epsilon_{kl}^{(R)} \right] \tag{4.11}$$

For term II, the following integral equality is used:

$$II = \int_{V} \nabla \left[\dot{u}^{(R)} \mathcal{V}^{(R)} \right] dV = \int_{S} \left[\dot{u}^{(R)} \mathcal{V}^{(R)} \right] \vec{n} dS \tag{4.12}$$

where $\vec{n}$ is the outgoing normal to the surface S bounding the volume V. It is easy to recognize that III can be rewritten as:

$$\int_{V} \rho \ddot{u}^{(R)} \dot{u}(R) = \frac{1}{2} \frac{\partial}{\partial t} \int_{V} \rho \dot{u}^{(R)} dV \tag{4.13}$$

Finally when I II and III are regrouped, equation 4.9 can be written as:

$$\frac{\partial}{\partial t} \int_{V} \mathcal{W} dV + \int_{V} \mathcal{D} dV = \int_{S} (\vec{\phi} + \vec{C}) \vec{n} dS \tag{4.14}$$

with the following definitions:

$$\mathcal{W} = \rho (\dot{u}^{(R)})^{2} + \mathcal{C}_{ijkl}^{(R)} \epsilon_{ij}^{(R)} \epsilon_{kl}^{(R)} \tag{4.15}$$

$$\mathcal{D} = \frac{1}{\omega} \mathcal{C}_{ijkl}^{(R)} \dot{\epsilon}_{ij}^{(R)} \dot{\epsilon}_{kl}^{(I)} \tag{4.16}$$

$$\vec{\phi} = \dot{u}_{j}^{(R)} \mathcal{C}_{ijkl}^{(R)} \epsilon_{kl}^{(R)} \tag{4.17}$$

$$\vec{C} = \dot{u}_j^{(R)} C_{ijkl}^{(I)} \dot{\epsilon}_{kl}^{(R)} \qquad (4.18)$$

This separation of terms is not arbitrary because each of the previous terms can be attributed a special physical meaning: $\mathcal{W}$ is obviously the system total energy density consisting of the sum of the kinetic energy and energy, and $\mathcal{D}$ is the energy dissipation rate density within the volume investigated. Since the second law of thermodynamics requires that the amount of energy dissipated increases with time, in can be deduced from the definition of $\mathcal{D}$ that:

$$C_{ijkl}^{(R)} > 0 \qquad (4.19)$$

Finally, $\vec{\phi}$ is the work flow through the volume external boundary S, and $\vec{C}$ is the work convected through S. This interpretation allows to rephrase equation 4.14 by saying that the change of the total mechanical energy of the system is equal to the rate of mechanical energy dissipation caused by viscoelastic effects plus the energy that flowed or was convected through the system's external surface. It can be easily demonstrated that in the case of an isotropic material this equation is strictly identical to the one provided by Borcherdt (1973), and thereby constitutes a generalization of the aforementioned conservation principle.

4.2.3 Modified Christoffel equations: A steady state plane wave solution for an anisotropic viscoelastic continuum

In order to apply the energy conservation principle demonstrated in the preceding section, a solution to the viscoelastic wave equation (4.5) must be found. The easiest possible solution is a plane wave of the following form:

$$u_i(x,t) = u_j exp\left[i\left[\omega t - (\vec{K} - i\vec{A})\vec{x}\right]\right] \qquad (4.20)$$

which can also be interpreted as a damped plane wave if it is rewritten as:

$$u_i(x,t) = u_j exp(-\vec{A}.\vec{x}) exp\left(i\omega t - \vec{K}.\vec{x})\right) \qquad (4.21)$$

In the two previous equations u_j is the polarization vector, $\vec{K}$ is the propagation vector, and $\vec{A}$ is the attenuation vector. The angle between the propagation and attenuation vectors is γ. If we now combine equation 4.5 in the frequency wavenumber domain with equation 4.21, we obtain the following set of linear equations:

$$- \rho a_i = c_{ijkl}(\omega)\left(Aa_l + iKk_l\right)\left(Aa_j + iKk_l\right) a_j \qquad (4.22)$$

noting $A = \frac{|\vec{A}|}{\omega}$, and $K = \frac{|\vec{K}|}{\omega}$. In the previous equation, a_l (and k_l) is defined as $\vec{A} = a_l \vec{x}_l$ ($\vec{K} = k_l \vec{x}_l$) where $\vec{x}_l$ is the unit vector along the lth direction. The previous equation states that $-\rho$ is an eigenvalue of the matrix $[\gamma_{ij}]$ defined as

$$\gamma_{ij} = c_{ijkl}(\omega)\left(Aa_l + iKk_l\right)\left(Aa_j + iKk_l\right) \qquad (4.23)$$

This matrix is known to be the Christoffel tensor in the elastic case. (Auld 1975). To satisfy equation 4.23 the following relationship must be true:

$$det\left[\gamma_{ij} - \rho I\right] = 0 \qquad (4.24)$$

where I is the identity operator.

It is now apparent that the algebra of our problem will rapidly become untractable if no assumption is made to simplify it. The two following assumptions will therefore be made:

- $\epsilon_{ijkl} = \frac{Im(c_{ijkl})}{Re(c_{ijkl})} \ll 1$. This assumption states that the material studied is only weakly attenuating. By analogy with the isotropic case where Q is the ratio between the real and imaginary parts of the appropriate modulus, $\frac{1}{Q}$ is often assumed to be small compared to one.

- $\frac{A}{K} \ll 1$ and $\frac{A}{K} \simeq \frac{Im(c_{ijkl})}{Re(c_{ijkl})} \ll 1$. This last statement assumes the amplitude ratio of the attenuation and propagation vectors is also small compared to one, but of the same order as $\frac{1}{Q}$ which is, once again, a valid assumption for an isotropic viscoelastic medium (Borcherdt 1973).

Under these assumptions, it is shown in Appendix 3 that equation 4.24 separates into a real and an imaginary part with the following form for the real part:

$$P(K) = 0 \tag{4.25}$$

where $P(K)$ is the same polynomial that is obtained in the case of a purely elastic anisotropic solid (Auld 1975). This first computation allows us to conclude that for linear, viscoelatic, anisotropic solids with weak attenuation, the influence of viscoelasticity on the propagation phenomena is a second order effect in ϵ_{ijkl}. This last remark is particularly important since the effect of viscoelasticity does not affect anisotropic wave propagation phenomena such as those described in Thomsen (1986), and the use of the δ and ϵ parameters is still legitimate.

Once K is computed from equation 4.25, the ration A/K can be easily computed from the imaginary part of equation 4.24. The relation has the following form according to the notation adopted in Appendix 1:

$$\left[\frac{A}{K}\right] Q_1(K) + Q_2(K) = 0 \tag{4.26}$$

where $Q_1(K)$ and $Q_2(K)$ are two polynomials in K. The solution for A is therefore trivial, provided that the initial angles between the propagation and attenuation vectors are known.

4.2.4 Energetic description of a linear, viscoelastic, anisotropic material

To obtain the full solution of the equation system 4.4, for a plane wave, the direction parameters l_x for both the propagation and attenuation vectors must be

provided. These are, in general, provided by boundary conditions at the source, or by a two-point boundary condition system as for example in classical ray-tracing. These directions being provided, the previous section shows how to compute both A and K so that both the attenuation and propagation vectors are now completely known. Finally the polarization vectors are obtained by replacing the solution of equation 4.21 into equation 4.24 so that the polarization vector is actually an eigenvector of equation 4.24. The polarization vector can then be written as follows:

$$I = \frac{a_1}{\begin{bmatrix} \gamma_{22} & \gamma_{23} \\ \gamma_{32} & \gamma_{33} \end{bmatrix}} = \frac{a_2}{\begin{bmatrix} \gamma_{23} & \gamma_{21} \\ \gamma_{33} & \gamma_{31} \end{bmatrix}} = \frac{a_3}{\begin{bmatrix} \gamma_{21} & \gamma_{22} \\ \gamma_{31} & \gamma_{32} \end{bmatrix}} \qquad (4.27)$$

where I is the intensity factor of the source, once again determined by the boundary conditions at the source.

With the plane wave solution, the energy conservation principle can be used to compute wave attributes such as group velocity and attenuation (Q). Defining the group velocity as the energy propagation velocity, we can state:

$$\vec{v}_g = \frac{<\vec{\phi} + \vec{\mathcal{C}}>}{\mathcal{W}} \qquad (4.28)$$

The brackets denote time averaging. From the weak-attenuation-approximation previously stated it is reasonable to assume that $\vec{\mathcal{C}}$ is negligible compared to $\vec{\phi}$ because $\mathcal{C}_{ijkl}^{(R)} >> \mathcal{C}_{ijkl}^{(I)}$. In other words, the effect of viscoelasticity on the group velocity is a first order in $\frac{1}{Q}$, and for large Q the effect of anisotropy on velocity is dominant. For very low Q weakly anisotropic material, on the other hand, the effect of viscoelasticity is comparable in magnitude to the effect of anisotropy.

Again following Borcherdt's definitions, we can define Q^{-1} from Eqn. 4.14 as the time average of the energy dissipation over a time cycle:

$$Q^{-1} = \frac{2\pi <\mathcal{D}>}{\omega} \qquad (4.29)$$

The last quantity can be easily computed from the plane wave solution computed below. Since $\mathcal{D}$ is a function of the imaginary part of the elastic tensor, the attenuation principal directions are directed by the symmetries of the $C_{ijkl}^{(I)}$ tensor, independently from the real part of the tensor, so that viscoelastic anisotropy is decoupled from elastic anisotropy to the second order in $\frac{1}{Q}$.

4.2.5 Partial Conclusions

Thus far, three major results have been reached:

- First, an energetic formulation has been obtained for viscoelastic anisotropic solids that is consistent with the known results for isotropic viscoelastic solids. This formulation allows us to quantify the properties of the viscoelastic material studied independently of its degree of symmetry.

- Second, the solution for a plane wave propagating in an anisotropic viscoelastic solid has been found. In a first approximation, the elastic properties of such a material are affected only to the second order in $\frac{1}{Q}$. In other words, the anisotropic effects and the viscous effects are decoupled.

- Third viscoelastic anisotropic materials have two distinct energy focusing mechanisms. The first is related to the purely elastic effects and results from the possibly large discrepancy between phase and group velocity. The second is a result of preferential energy absorption, depending on the direction of propagation. Even though it seems to make little sense that a rock has different symmetries for both its elastic and anelastic properties, these two properties are in fact decoupled for materials that are weakly attenuating.

In order to both verify and illustrate the properties of viscoelastic anisotropic solids, the following section presents a numerical modeling procedure that allows the description of the above mentioned energy-focusing mechanisms.

4.3 Numerical modeling of a linear viscoelastic anisotropic solid

4.3.1 Constitutive equations: A generalized standard linear solid

Modeling the time-dependent part of the elastic tensor requires preliminary knowledge of the behavior of the solid. This knowledge is represented by the constitutive relation of the system studied. Let us assume that a viscoelastic anisotropic solid behaves microscopically like an assembly of springs and dashpots organized to yield the general behavior of a standard linear solid for which the equation was formulated by Liu (1976), and Carcione (1987). This constitutive equation can be written as follows:

$$\sum_{k=0}^{m} c_k \frac{\partial^k}{\partial t^k} \sigma_{ij} = \sum_{k=0}^{m} \frac{\partial^k}{\partial t^k} \epsilon_{ij} \tag{4.30}$$

the solid being subjected to the initial conditions:

$$\sum_{k=0}^{m} c_k \frac{\partial^{(r-k)}}{\partial t^{(r-k)}} \sigma_{ij}(0) = \sum_{k=0}^{m} \frac{\partial^{(r-k)}}{\partial t^{(r-k)}} \epsilon_{ij}(0) \tag{4.31}$$

where c_k are the coefficients describing the macroscopic properties of the material subjected to the initial conditions described in equation 4.31. Following Carcione (1987), and generalizing equation 4.30 to a general viscoelastic anisotropic solid by replacing c_k by c_{ijkl}, we can find a solution to equation 4.30, after it is transformed in the Laplace domain. This solution provides $c_{ijkl}(t)$ as a function of $c_{ijkl}(0)$ as follows:

$$c_{ijkl}(x,t) = c_{ijkl}(x,0) \left[1 - \sum_{m=1}^{L_{ijkl}} \left[1 - \frac{\tau_{\epsilon_m}^{ijkl}}{\tau_{\sigma_m}^{ijkl}} \right] e^{\frac{-t}{\tau_{\sigma_m}^{ijkl}}} \right] \tag{4.32}$$

where $\tau_{\sigma_m}^{ijkl}$ and $\tau_{\epsilon_m}^{ijkl}$ are the stress and strain relaxation times, respectively, for the mth attenuation mechanism of the $ijkl^{th}$ component of the viscoelastic tensor. We see from the previous equation that each component of the viscoelastic tensor is actually

modeled by a series assembly of L_{ijkl} Standard Linear Solids (SLS). In order to use the theoretical results obtained in the previous part, we need to compute the Fourier transform of the time dependent viscoelastic parameters. This computation yields

$$c_{ijkl}(x,0) = c_{ijkl}(x,0) \left[1 - L_{ijkl} + \sum_{m=1}^{L_{ijkl}} \frac{1 + i\omega\tau_{\epsilon_m}^{ijkl}}{1 + i\omega\tau_{\sigma_m}^{ijkl}} \right] \qquad (4.33)$$

Combining the previous definition of the frequency-dependent elastic tensor and the definition of Q, Fig. 4.1 shows that an almost constant Q can be obtained over a given frequency domain with $L_{ijkl} = 2$. In other words two relaxation mechanisms are sufficient to provide a quasi-constant band limited attenuation coefficient. Finally Carcione (1987) has demonstrated that the previous definition of the elastic tensor provides a causal attenuation mechanism.

4.3.2 Rewriting the dynamic equation for a viscoelastic anisotropic solid

To solve equation 4.4, we will substitute the form of $c_{ijkl}(x,t)$ devised in the previous section into that equation. Equation 4.4 can therefore be rewritten as:

$$\sigma_{ij}(x,t) = c_{ijkl}(x)\epsilon_{kl}(x,t) - \sum_{m=1}^{L_{ijkl}} c_{ijkl}(x)\phi_{ijkl}^m(x,t) * \epsilon_{kl}(x,t) \qquad (4.34)$$

where $\phi_{ijkl}(x,t)$ can be easily inferred from equation 4.32. From now on, our problem will be restricted to two-dimensional space, but all the further developments can be easily generalized to three-dimensional space. In two-dimensional space, the previous equation can be rewritten as:

$$\rho \ddot{u}_x = M_1 u_x + M_2 u_z + f_x + C_x \qquad (4.35)$$

$$\rho \ddot{u}_z = M_3 u_x + M_4 u_z + f_z + C_z \qquad (4.36)$$

where M_i is a partial differential operator that corresponds to the elastic part of the

propagation algorithm, C_i is also a partial differential operator that corresponds to the convolution part or viscoelastic part of equation 4.34, and f_i are the components of the external forces applied to the system studied. M_i is defined as follows in two-dimensional space:

$$M_1 = \left[\frac{\partial}{\partial x} c_{1111} \frac{\partial}{\partial x} + \frac{\partial}{\partial z} c_{1313} \frac{\partial}{\partial x} \right] \tag{4.37}$$

$$M_2 = \left[\frac{\partial}{\partial x} c_{1133} \frac{\partial}{\partial z} + \frac{\partial}{\partial z} c_{1313} \frac{\partial}{\partial x} \right] \tag{4.38}$$

$$M_3 = \left[\frac{\partial}{\partial x} c_{1313} \frac{\partial}{\partial z} + \frac{\partial}{\partial z} c_{1133} \frac{\partial}{\partial x} \right] \tag{4.39}$$

$$M_4 = \left[\frac{\partial}{\partial x} c_{1313} \frac{\partial}{\partial z} + \frac{\partial}{\partial z} c_{3333} \frac{\partial}{\partial z} \right] \tag{4.40}$$

If we now define ψ_i^m as $M_i(x)\phi_i^m(x,t)$, then the C_i coefficients can be easily rewritten as follows:

$$C_x = \frac{\partial}{\partial x} \sum_m \psi_1^m * \epsilon_{11} + \frac{\partial}{\partial x} \sum_m \psi_3^m * \epsilon_{33} + 2\frac{\partial}{\partial z} \sum_m \psi_4^m * \epsilon_{13} \tag{4.41}$$

$$C_z = 2\frac{\partial}{\partial x} \sum_m \psi_4^m * \epsilon_{13} + \frac{\partial}{\partial z} \sum_m \psi_1^m * \epsilon_{11} + \frac{\partial}{\partial z} \sum_m \psi_4^m * \epsilon_{13} \tag{4.42}$$

Then, changing variable, we define the new variable e_i^m that will be called memory variables:

$$e_1^m = \psi_1^m * \epsilon_{11} \tag{4.43}$$

$$e_2^m = \psi_2^m * \epsilon_{33} \tag{4.44}$$

$$e_3^m = \psi_4^m * \epsilon_{13} \tag{4.45}$$

$$e_4^m = \psi_2^m * \epsilon_{11} \tag{4.46}$$

$$e_5^m = \psi_3^m * \epsilon_{33} \tag{4.47}$$

On the basis of this definition, the following first order in time partial differential operator can be computed for the e_i^m. An example for such a computation for e_1^m is written as follows:

$$\frac{d}{dt}(e_1^m) = \frac{d}{dt}\left[M_1(x)\phi_1^m(x,t) * \epsilon_{11}\right] = M_1(x)\left[\phi_1(x,0)\frac{\partial u_x}{\partial x} - \frac{e_1^m}{\tau_{\sigma_1}^{m_{11}}}\right] \qquad (4.48)$$

Using this last expression, equations 4.35 and 4.36 can be written in the following matrix form:

$$\frac{d}{dt}\begin{bmatrix} u_x \\ u_z \\ \dot{u}_x \\ \dot{u}_z \\ e_i^m \end{bmatrix} = \begin{bmatrix} 0 & 0 & 1 & 0 & 0 \\ 0 & 0 & 0 & 1 & 0 \\ M_1 & M_2 & 0 & 0 & c_{ij} \\ M_3 & M_4 & 0 & 0 & d_{ij} \\ a_{ij} & b_{ij} & 0 & 0 & t_{ij} \end{bmatrix}\begin{bmatrix} u_x \\ u_z \\ \dot{u}_x \\ \dot{u}_z \\ e_i^m \end{bmatrix} + \begin{bmatrix} 0 \\ 0 \\ f_x \\ f_z \\ 0 \end{bmatrix} \qquad (4.49)$$

The previous system of equations can be written in symbolic form as follows:

$$\frac{dU}{dt} = MU + F \qquad (4.50)$$

where U is the generalized displacement vector that contains the displacement field, the first time derivative of the displacement field, and the memory variables. The matrix M is a partial differential operator in space, and F is the field of external forces acting on the system. To solve the previous equation, we must first sample it on a regular grid with $N_x \times N_z$ samples, and then we can write:

$$\dot{U}_n = M_n U_n + F_n \ with \ U_n(0) = U_n^0 \qquad (4.51)$$

where U_n, F_n, and M_n are the discrete representations of U, F, and M respectively. The length of the vector U is $L \times N_x \times N_z$ where L is the number of independent variables per node. In the case where the space dimensionality n_{space} is 2, and the number of relaxation functions n_{rel} is also two, we have
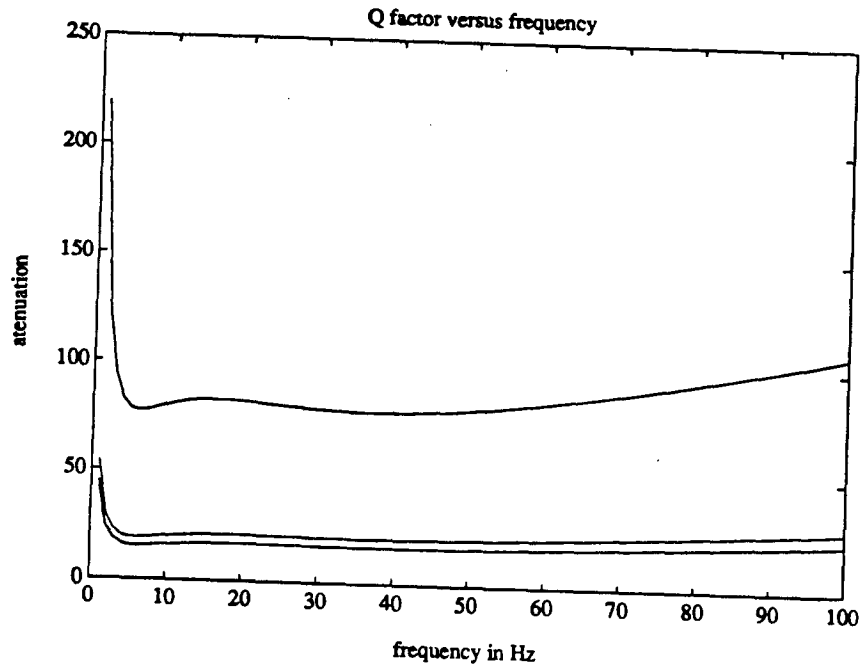
Figure 4.1: Attenuation as a function of frequency using two (2) relaxation mechanisms.
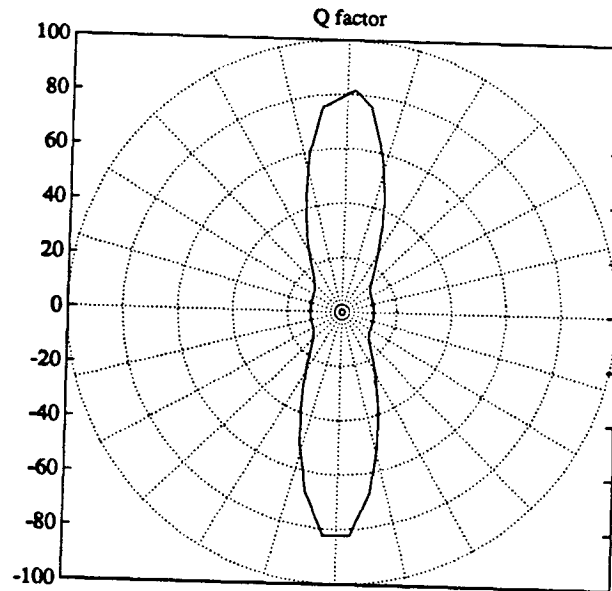
Figure 4.2: Attenuation as a function of the propagation angle for homogeneous waves.

$$L = n_{space} + 5 * n_{rel} = 14 \qquad (4.52)$$

Where the factor two comes from the fact that both u and $\dot{u}$ are sampled in the generalized displacement vector. The factor five is based on the hypothesis that the axis of symmetry of the solid studied is parallel to the axis of the sampling grid. Should this last hypothesis be removed, a factor of nine would be used instead.

The previous equation system in U_n has a unique solution of the following form:

$$U_n = e^{M_n t}U_n^0 + \int_0^t e^{M_n \tau}F_n(x, t - \tau)d\tau \qquad (4.53)$$

where U_n^0 is the starting condition at time $t = o$ for the generalized displacement vector. Further assuming that the source term F_n is separable in time and space (i.e. $F_n(x, t) = A_n(x)h(t)$) and that U_n^0 is null, the preceding equation can be written

$$U_n = \left[\sum_0^t e^{M_n \tau}h(t - \tau)d\tau \right] A_n \qquad (4.54)$$

To perform the preceding integration, we first need to compute $e^{M_n \tau}$. Carcione (1987) after Tal-Ezer (1986) suggests using the Chebycheff expansion of the operator's exponential. This expansion can be written as follows:

$$e^{M_n \tau} = \sum_{k=0}^{\inf} C_k J_k(\tau R)Q_k \left[\frac{M_n}{R} \right] \qquad (4.55)$$

where J_k is a Bessel function of the first kind k^{th} order, and R is the radius of convergence of the expansion. C_0 is defined by:

$$C_0 = 1 \ and \ C_k = 2 \ for \ k > 1 \qquad (4.56)$$

Finally the Q_k are defined by the following recursive relation:

$$Q_{k+1}\left[\frac{M_n}{R} \right] = \frac{M_n}{R}Q_k\left[\frac{M_n}{R} \right] + Q_{k-1}\left[\frac{M_n}{R} \right] \qquad (4.57)$$

with $Q_0 = I$, and $Q_1 \left[\frac{M_n}{R} \right] = \frac{M_n}{R}$. Equation 4.53 can now be completely rewritten in its final form:

$$U_n(t) = \sum_0^K C_k \alpha_k(tR) Q_k \left[\frac{M_n}{R} \right] A_n \tag{4.58}$$

$$\alpha_k(tR) = \sum_o^t J_k(\tau R) h(t - \tau) d\tau \tag{4.59}$$

Let us consider now the convergence conditions of this algorithm: The Chebycheff expansion is known to converge for eigenvalues of M_n close to the imaginary axis. (Tal-ezer 1986). The eigenvalues of M_n are purely imaginary for a purely elastic solid. The eigenvalues associated with the viscous absorption, on the contrary, are real and negative, thereby making the Q_k recursive relation (Eqn. 4.57) unstable. Nevertheless, the overall expansion of U_n remains stable (Tal-Ezer 1986) because $\alpha_n(t)$ converges to zero very rapidly as n increases, as long as $t > \frac{1}{R}$. The problem is therefore to make sure that $Q_k \left[\frac{M_n}{R} \right]$ does not exceed the dynamic range of the computer. In order to minimize the divergence of the Q_k expansion, the following relation can be used easily:

$$e^{\gamma It} U_n = \int_0^t e^{(M_n + \gamma I)\tau} e^{-\gamma I(t-\tau)} F_n(t - \tau) d\tau \tag{4.60}$$

This last relation shifts the eigenvalues of M_n by γ. In order to minimize $Q_k \left[\frac{M_n}{R} \right]$ as k increases, γ was chosen to be exactly one half of the smallest real negative eigenvalue of M_n.

To complete the computation formulated in equation 4.58, $M_n A_n$ needs to be computed. Two standard methods can be used for this computation:

- the finite-difference method

- the spectral or Fourier method

The finite difference method requires a very fine discretization of the system modeled in order to prevent numerical dispersion (Marfurt 1986, Samec 1990 this volume).

Furthermore, the method by which the derivatives are evaluated needs to be accurate down to the Nyquist sampling frequency, since the spatial source term A_n is very close to a Dirac function, as will be shown in the next section.

Since the material modeled naturally introduces dispersion owing to the causality of the attenuation mechanism, it is absolutely necessary to minimize numerical dispersion. This is why the spectral method (also called the Fourier method) has been chosen here. This method proposed by Kosloff (1987) minimizes numerical dispersion with a better numerical efficiency than the finite-difference method, and also insures that the computation of spatial derivatives is accurate up to the Nyquist spatial frequency.

Using this method, the spatial operator M_n is evaluated in the Fourier domain and multiplied by the direct Fourier transform of A_n, and the result is transformed back into the space domain yielding a very accurate computation of spatial derivatives.

4.3.4 Numerical experiment setup

The purpose of the modeling examples in this chapter is to help ascertain the results obtained in section 4.1, as well as to illustrate the energy-focusing mechanisms displayed by viscoelastic anisotropic solids. For those reasons, the source is designed as an explosive point source, therefore generating mainly compressional waves, even in an anisotropic medium. The choice of compressional waves for this investigation is motivated by their extensive use in seismic exploration, and by the fact that even though recent studies of anisotropy have focussed on shear waves, the impact of elastic and attenuation anisotropy clearly affects the results of current seismic experiences. Finally, this choice does not restrict the scope of our results which can be extended equally well to shear waves.

The spatial distribution for a compressional wave point source is:

$$A(x,y) = \frac{d}{dx}\left(\delta(x - x_0)\right) * \delta(z - z_0)\vec{u}_x + \frac{d}{dz}\left(\delta(z - z_0)\right)\delta(x - x_0)\vec{u}_z \qquad (4.61)$$

where x_0 and z_0 are the source coordinates, and δ is the Dirac function. For the numerical computation, the spatial distribution of the source is modeled by the spatial derivatives of a very narrow two-dimensional gaussian function centered at the source point. This distribution spans over three grid points along both the horizontal and vertical directions. The grid chosen here has 128×128 points. This number is limited by the large amount of nodal variables, as well as by the necessity of performing all the computations using double precision arithmetics.

The source time history is a symmetrical Ricker wavelet of the following form:

$$F(t) = e^{-\eta f_0^2 (t - t_0)^2} \cos\left(\epsilon \pi f_0 (t - t_0)\right) \qquad (4.62)$$

with $\eta = 0.5$, $\epsilon = 1.$, $t_0 = 6ms$, and finally $f_0 = 50Hz$. For the elastic case, convergence is achieved for $R > 1800 sec^{-1}$, and γ was given a value of around $200 sec^{-1}$ depending on the anelastic case modeled. Absorbing boundary conditions have been applied to prevent reflections from the edges of the model. They were implemented using the algorithm proposed by Kosloff, 1984.

4.4 Modeling results

Four cases were modeled to further investigate the impact of quality factor anisotropy on compressional waves and to compare these effects to the better known effects of velocity anisotropy. For each of the following cases, snapshots of the wavefield are displayed.

- 1: Purely elastic isotropic medium (figure 4.5).

- 2: Elastic anisotropic medium (figure 4.6).

- 3: Vicoelastic isotropic medium (figure 4.7).

- 4: Viscoelastic with isotropic elastic properties, and anisotropic attenuation (figure 4.8).
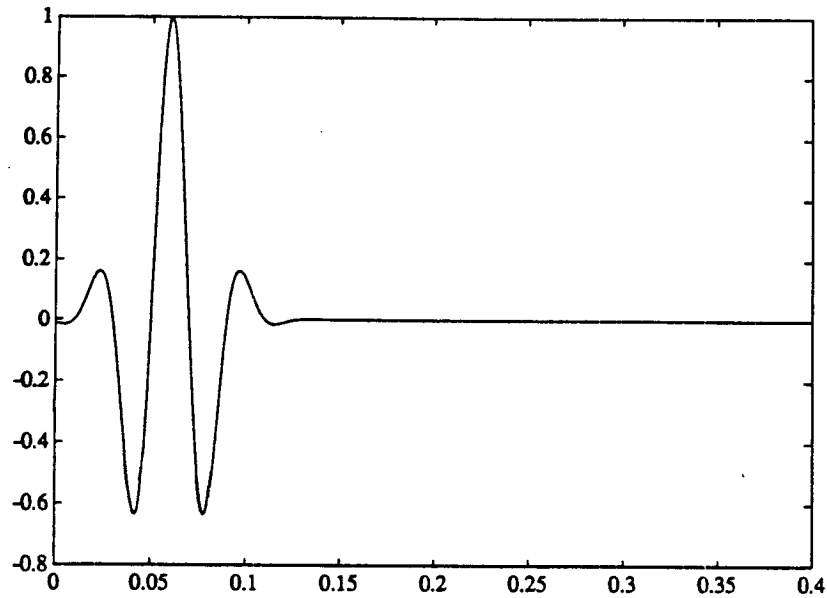
Figure 4.3: A symmetrical Ricker wavelet used for the modeling.
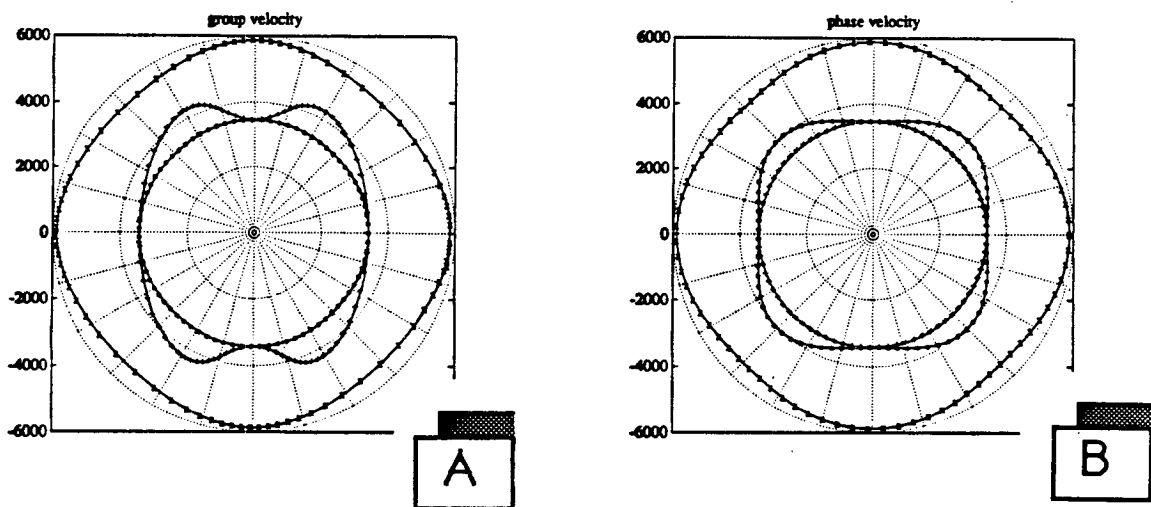
Figure 4.4: A) Group velocity and B) phase velocity used for the anisotropic elastic modeling.
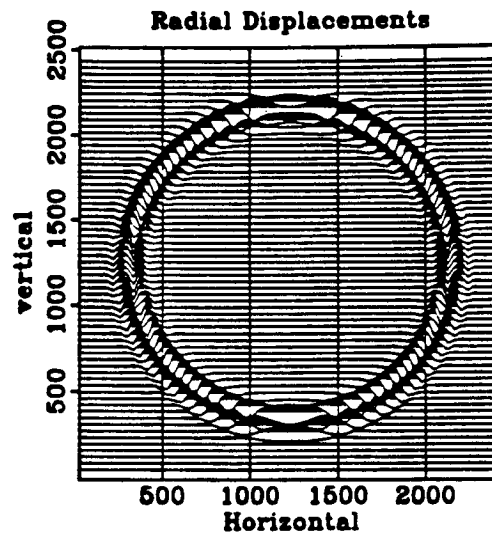
Figure 4.5: Snapshot of the wavefield generated by an explosive source in an isotropic elastic solid at time $t = .3sec$.
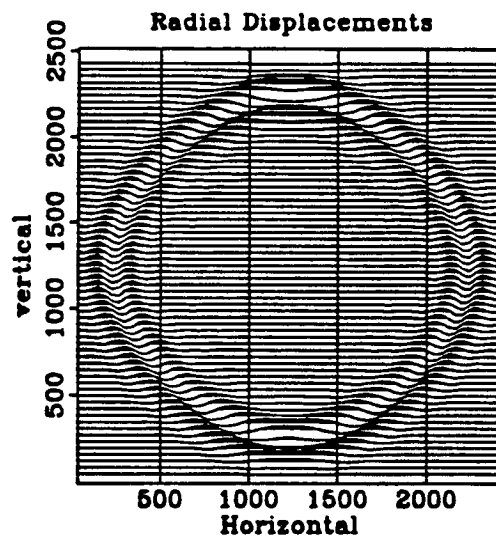
Figure 4.6: Snapshot of the wavefield generated by an explosive source in an anisotropic elastic solid at time $t = .3sec$.

Figures 4.5 and 4.6 compare the wavefield snapshots of an isotropic and an anisotropic elastic solid. They clearly display the main effects of elastic anisotropy on the wavefield.

- First, the wavefield is shaped according to the group velocity, and the phase distribution along the wavefront is conditioned by the difference between phase and group velocity.

- Second, as will be seen in Chapter 5, the energy distribution along the wavefront is inherited from two phenomena. First, elastic anisotropy introduces radiation pattern anisotropy, and, second, the energy distribution along the wavefront shifts toward the high group velocity regions as the wave propagates.

In contrast to figures 4.5 and 4.6, figures 4.7 and 4.8 illustrate the importance of quality factor anisotropy on the wavefield. The effects of attenuation anisotropy can be summarized as follows:

First the results presented with the purely isotropic, viscoelastic rock model are consistent with the analytical prediction. As shown in figure 4.9, the amplitude decay as a function of the distance from the source is consistent with the combination of a two-dimensional geometrical spreading model where the amplitude decays as a function of $\frac{1}{\sqrt{r}}$ and the attenuation model that predicts that attenuation will be of the following form:

$$A(r) = A(0) * exp\left[\frac{-\omega r}{2v\omega Q}\right] \times \frac{1}{\sqrt{r}} \tag{4.63}$$

where A is the signal amplitude as a function of the distance from the source r, ω is the signal central frequency ($25Hz$), and the attenuation Q is 34. The comparison between the isotropic and anisotropic attenuation modeling displays the two following results:

First, the energy propagated in a medium with attenuation anisotropy is clearly focussed along the minimum attenuation direction, consistently with the theoretical

predictions of the previous section as shown in figures 4.7 and 4.8. Obviously, the wave energy has been absorbed faster along the high attenuation direction, and the effect is clearly visible even for the comparatively small Q anisotropy chosen for this study.

Second, a close look at the wave fronts presented in figures 4.7 and 4.8 reveals the phase advance on the low Q direction. This is especially apparent in comparing figures 4.10 b and 4.10 c. These seismograms were obtained by recording the wavefield along a receiver line orthogonal to the maximum Q direction. The phase advance event results in a significant change in the first arrival moveout, where the moveout in the isotropic Q model remains hyperbolic, contrary to the anisotropic Q case, where the moveout is a strong function of the Q factor azimuthal distribution.

The previous results show that, realistic quality factor anisotropy yields strong energy focusing effects. This focusing effect is stronger in magnitude than the one obtained for strongly elastic anisotropic rocks. Furthermore, the phase effects associated with quality factor anisotropy are of the same order as those encountered in weakly anisotropic solids.

4.5 Conclusions

The theoretical results obtained using a unified description of both elastic and viscoelastic anisotropic materials is confirmed in the second part of this chapter by the use of a purely numerical method. These results can be summarized in three essential points:

- First, elastic anisotropic and viscoelastic effects are decoupled to the first order in $\frac{1}{Q}$. That result is justified even for Q as low as 34.

- Second, phase shifts associated with attenuation azimuthal variations can significantly perturb seismic event moveout.

Radial Displacements
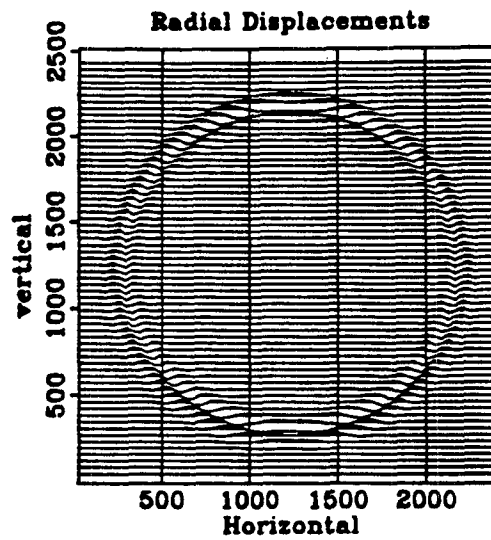
Figure 4.7: A snapshot of the wavefield generated by an explosive source in a viscoelastic isotropic solid at time $t = .3sec$. The attenuation parameter Q is: 34.

Radial Displacements
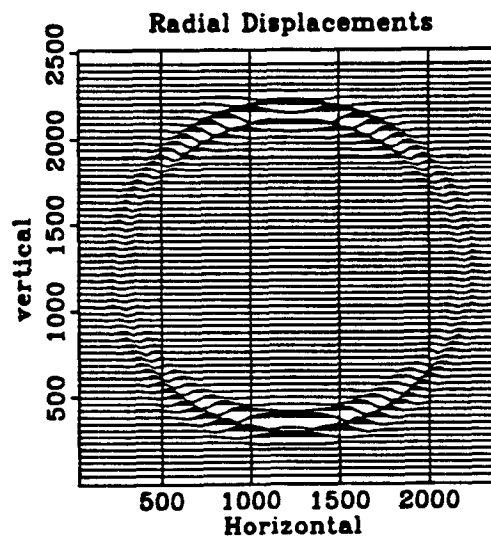
Figure 4.8: A snapshot of the wavefield generated by an explosive source in a viscoelastic anisotropic solid at time $t = .3sec$. The attenuation parameter Q is: 34 along the horizontal, and 130 along the vertical. The elastic part is isotropic, and identical to the one used in figure 4.5.
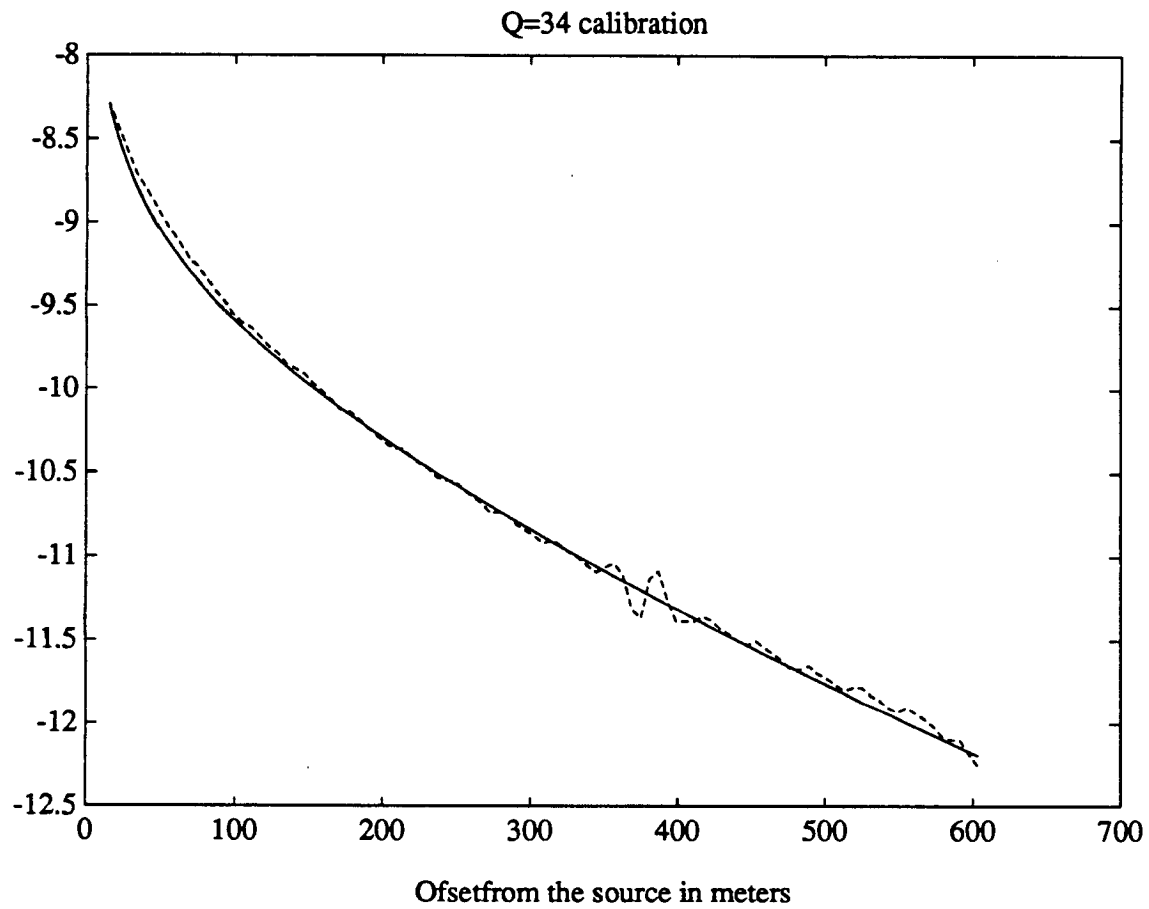
Figure 4.9: Comparison between the theoretical and numerical amplitude decay as a function of the distance from the source. The solid line represents the theoretical prediction, and the dashed line is the computed numerical decay.
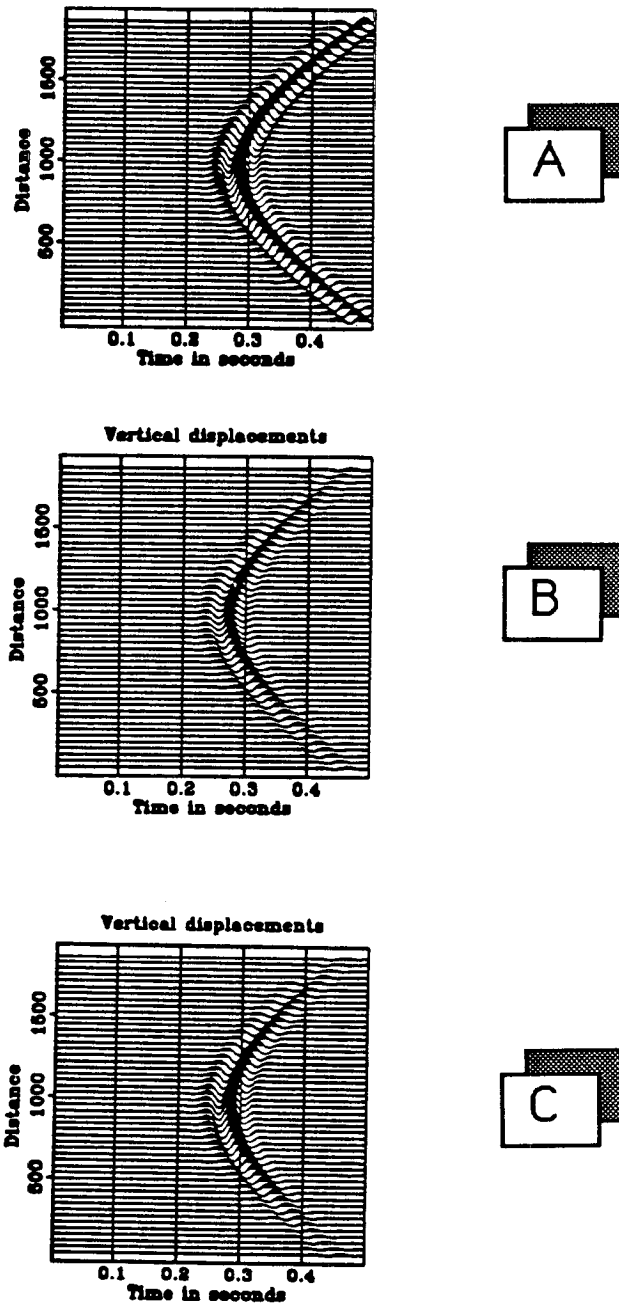
Figure 4.10 : Vertical component eismograms obtained for the modeling
cases a):1, b):3, c):4

- Finally, energy focusing effects related to elastic anisotropy only become significant for fairly large anisotropy ratios. On the other hand, attenuation anisotropy induces a comparatively high focusing along the minimum attenuation arrivals. As will be seen in the next chapter, both effects can severely affect the interpretation of Amplitude Versus Offset data.

References

Aki, K., and Richards, P. G.,1980, Quantitative seismology, theory and methods, W. H. Freeman and Co., San Francisco, California.

Auld B. A., 1973, Acoustic Fields and Waves in Solids, John Wiley & sons, New York.

Borcherdt, R., D., 1973, Energy and plane waves in linear viscoelastic media, J. Geophys. Res. **78**, 2443-2453

Biot, M. A., 1965, Theory of propagation of elastic waves in fluid saturated porous solid, I. low frequency range. II. higher frequency range. Journal of Acoust. Soc. Am., **28**, p. 168, 179.

Budiansky B., O'Conell J. R., 1976, Elastic moduli of a cracked solid, Int. Journ. Solids Structures, **12**, p. 81, 87.

Carcione J., M., 1987 Wave propagation in real media, PhD Thesis, Senate of Tel Aviv University.

Christensen N., 1971 Compressional wave velocity in metamorphic rocks at pressures up to 10 Kilobars, J. Geophys. Res., **70**, p. 6147-6164.

Christensen N., 1971 Shear wave velocity in metamorphic rocks at pressures up to 10 Kilobars, J. Geophys. Res., **71**, p. 3549-3556.

Crampin S., Mc Gonigle R., Bamford D., 1980, Estimating crack parameters from observation of P wave velocity anisotropy, Geophysics, **45**, p. 345-360.

Crampin S., 1984, Effective anisotropic elastic constants for wave propagation through cracked solids, Geophys. J. R. Astr. Soc. **76**, p. 135-145

Hosten B., Deschamps M., and Tittman B. R., 1987, Inhomogeneous waves propagating in a lossy anisotropic solid. Application to the characterization of viscoelastic composite materials, Journal Acoustical Society of America, **82**, p. 1763, 1770.

Hudson J. A., 1983, Wave speed and attenuation of elastic waves in material containing cracks, Geophys. J. R. Astr. Soc., **64**, p. 134-150

Kosloff D., and Baysal E., 1982, Forward modeling by a Fourier method. **47**, p. 1402,1412.

Liu H. P., Anderson D. L., and Kanamori H., 1976, Velocity dispersion due to anelasticity ; implication for seismology and mantle composition, Geophys. J. Roy. Astr. Soc. **47**, p. 41-58.

Marfurt K. J. 1984, Accuracy of finite-difference and finite-element modeling of the scalar and elastic wave equation, Geophysics, **49**, p. 533-549.

Morse P. M., and Feshbach H., 1953, Methods of theoretical physics, Mc Graw Hill, New-York.

Murphy W. F. III, 1982, Effect of microstructure and pore fluids on the acoustic properties of granular sedimentary materials, PhD thesis, Stanford Univ., Stanford Rock Physics Project Vol. 16.

Nur A., Simmons G., 1969, Stress induced velocity anisotropy in rock: an experimental study, J. Geophys. Res., **74**, p. 6667-6674.

Nur A., 1971, Effects of stress on velocity anisotropy in rocks with cracks, J. Geophys. Res., **76**, p. 2022-2034.

Tal-Ezer H., 1986, Spectral methods in time for hyperbolic equations, SIAM J. Numer. Anal., **23**, p. 11-26

Thomsen L., 1986, Weak elastic anisotropy, Geophysics, **51**, p. 1954-1966.

Chapter 5

Effects of Viscoelasticity and Anisotropy on Amplitude Versus Offset Data Interpretation

Abstract

The effects of attenuation, elastic anisotropy, and attenuation anisotropy on Amplitude Versus Offset measurements are investigated using a full waveform modeling algorithm.

The modeling method, based on pseudo-spectral time integration and the Fourier method for spatial differentiation, is extremely accurate and allows a careful modeling of the behavior of anisotropic viscoelastic materials as shown in Chapter 4. The accuracy of the method applied to reflection seismology is first confirmed by comparing the numerical and analytical solutions of the Amplitude Versus Offset variations of a reflected seismic event in an elastic isotropic model.

This numerical method is further used to demonstrate that the classical interpretation that relates Amplitude Versus Offset to the rock formation Poisson's ratio is only valid for isotropic elastic media. For viscoelastic anisotropic media, this simple interpretation is no longer valid for the following reasons :

- First, as shown by Thomsen (1986) and Banik (1987), reflection coefficients at an interface are strongly dependent on the elastic anisotropy of both adjacent

media. This dependency is further increased in media with anisotropic viscous properties.

- Second, the reflection coefficients along an interface are difficult to recover from surface seismic data, because the energy and phase distribution of the incident and reflected wavefronts is influenced both by elastic anisotropic energy focusing and by anisotropic dissipation. These two phenomena are of the same order of magnitude as the reflection amplitude variations, and make the amplitude evaluation of a seismic event strongly dependent on the changes in the phase of the signal, which occur continuously as the wavefront propagates.

5.1 Introduction

Recent studies by Thomsen (1986) have shown that the elastic properties of shales, chalks, and other materials can be highly anisotropic. In fact, much work (Wright, 1987, Thomsen, 1986, Banik, 1987) has been devoted to characterizing transverse isotropy in an attempt to more accurately describe the properties of shales and their effects on reflection coefficients. On the other hand, numerous investigations (Kjartansson 1979, Jones 1986, Winkler and Nur 1986, Nur 1969) among others) have concentrated on the effect of intrinsic attenuation on wave propagation. The results of Crampin (1984), and Hosten (1987) suggest that dissipation itself is an anisotropic phenomenon, and that media with anisotropic elastic properties also display quality factor or attenuation anisotropy. In fact, Crampin (1986) showed that by modeling the effect of cracks on rock anisotropy one introduces the imaginary part of the elastic tensor written in the frequency domain, and that this imaginary part has symmetry similar to that of the real part. Hosten (1987) also showed that for a composite fine-layered medium, the expected ratio of Q measured in a direction parallel to the layers to that measured perpendicularly to the layers can be as large as 30. It is therefore

logical to consider fully anisotropic media, when velocity <u>and</u> attenuation anisotropy are considered.

After reviewing the implementation of the modeling algorithm described in the preceding chapter to a seismic reflection experiment, this chapter separately examines the effects of both attenuation and anisotropy on Amplitude Versus Offset data interpretation.

5.2 Implementation of the modeling algorithm for the study of seismic reflections

5.2.1 The modeling method and a description of the parameters

The numerical modeling of the seismic experiments that are described in this chapter is achieved with the Fourier Pseudo-Spectral method outlined in the previous chapter. This method provides an adequate level of modeling accuracy for the study of the wave phenomena related to both attenuation and anisotropy. The following are the parameters used in all the modeling cases :

- The standard acquisition geometry is described in figure 5.1. This geometry was modeled using a 128×128 samples grid, with a grid spacing of $10m$. The interface studied is located $450m$ below the receiver line. The receiver line itself is built of 100 receivers with $10m$ spacing between the receivers. The entire model is enclosed within the absorbing buffers, which eliminate most of the unwanted reflections from the edge. The method is similar to that presented in Chapter 2.

- The source spatial distribution is arranged to yield an explosive symmetrical source. Since the modeling is two-dimensional, the point source used is actually a three-dimensional line source. The hypothesis that the source is isotropic is succesfully tested in figure 5.2 where the energy away from the source does not

depend on the propagation vector. The source time history is the same as the one used in chapter 4 (equation 4.61).

- Throughout the following examples, the notations defined by Thomsen (1986) are used. This parametrization is especially attractive since the compressional and shear velocities along the vertical can remain constant for all the examples, and only the δ parameter is varied in our numerical experiments to modify the anisotropy parameters. The ϵ and γ are taken null for all our modeling cases. The compressional velocity is $V_{P_1} = 2896m/s$ for the upper layer, and $V_{P_2} = 3322m/s$ for the lower one. The shear waves' velocities are, respectively, $V_{S_1} = 1402m/s$ and $V_{S_2} = 1402m/s$. The densities are the same for both layers that is $\rho = 2.25g/cc$. For the modeling of elastic anisotropic solids, δ is set to 0.1.

- Attenuation is modeled following the mechanism proposed in Chapter 4. Only two relaxation functions are used, and they allow an almost constant causal Q factor over the frequency range of investigation, as shown in figure 5.3.

As shown in figure 5.4a, $\delta = 0.1$ is a common value of anisotropy as measured on core samples and in fact can be taken as a lower bound estimate for some strongly anisotropic shales. Attenuation anisotropy which was theoretically predicted by Crampin (1984), has been experimentally measured on synthetic materials (Hosten 1988). Hosten's experimental results are shown in figure 5.4 b and report a very high level of attenuation anisotropy for a synthetic, layered medium. A similar ratio of approximately 30 between high and low attenuation was also predicted theoretically by Crampin (1984). Such a ratio was used for modeling as shown in figure 5.12 b.
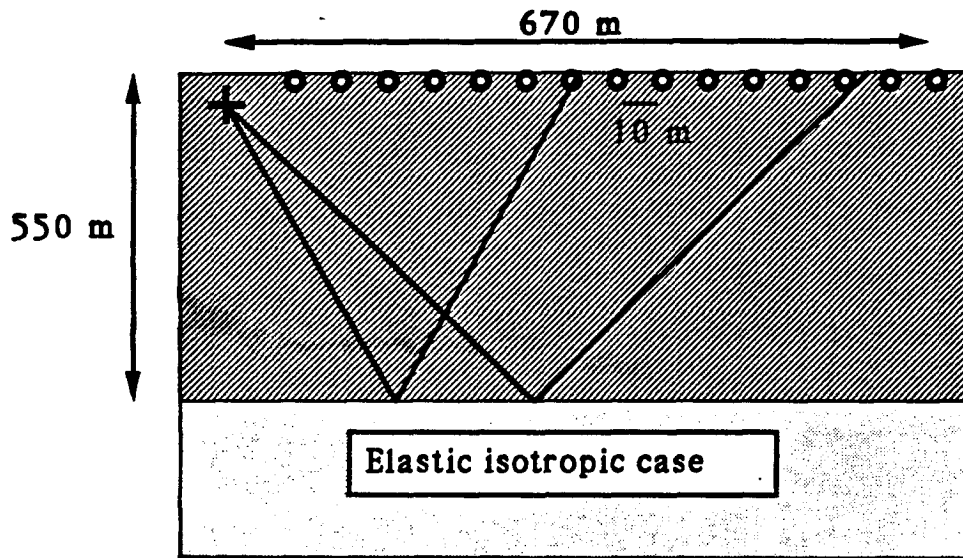
Figure 5.1: The reflection acquisition setup. The explosive (isotropic) point source + is placed in the upper left corner of the model. The receiver *o* spacing is 10*m*.
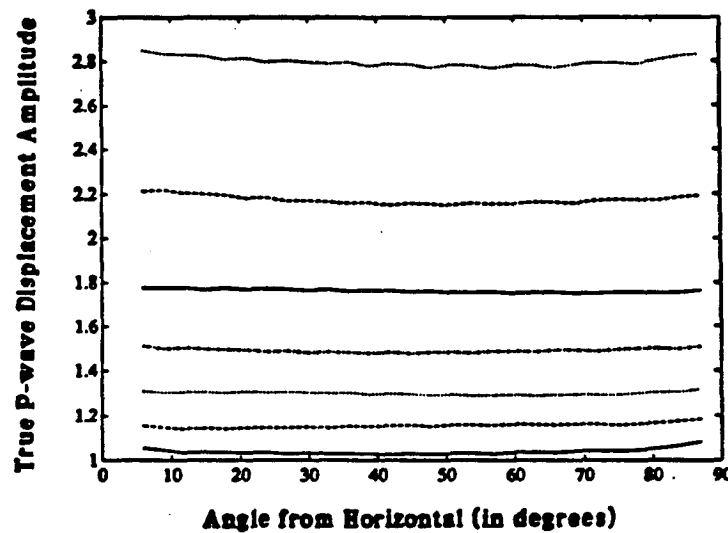
Figure 5.2: Energy radiated by the source in a homogeneous isotropic solid as a function of the propagation angle.
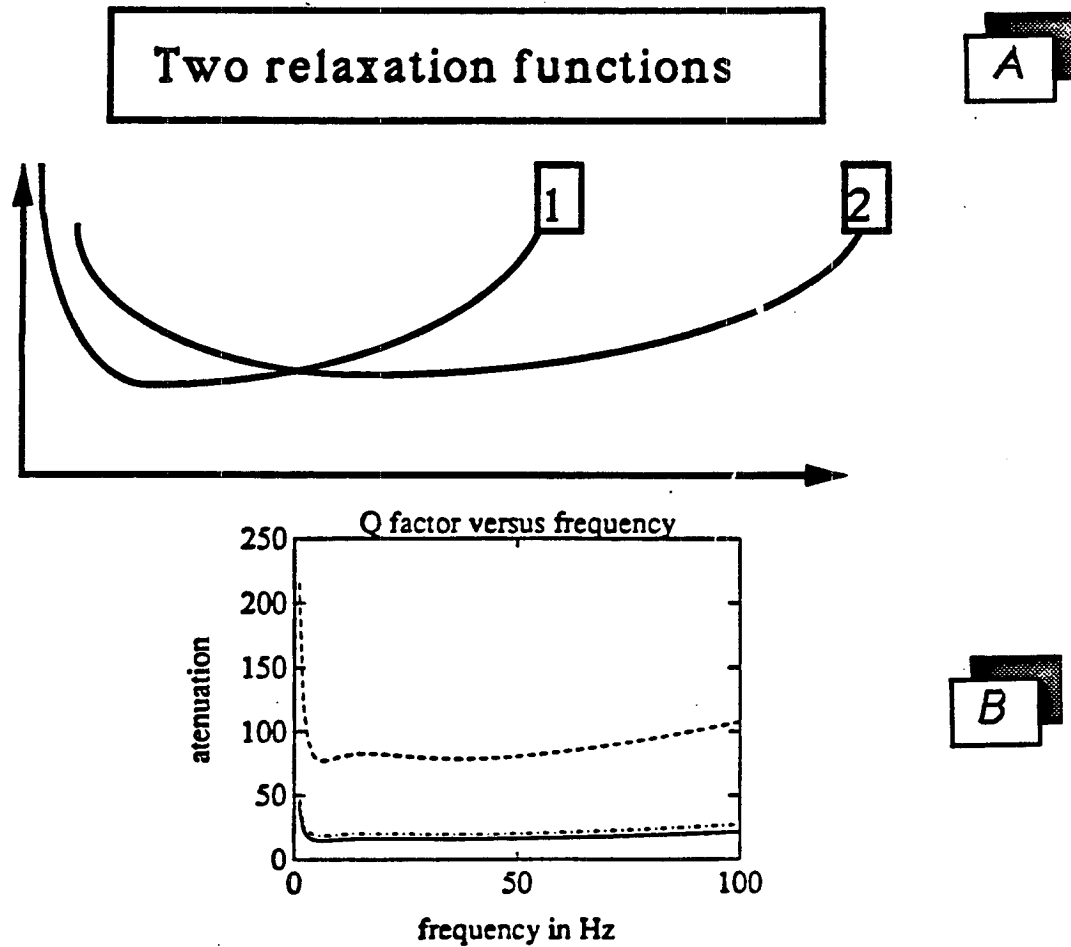
Figure 5.3: Modeling attenuation : Attenuation is modeled by assuming that the energy absorption can be modeled by two relaxation functions (a). Such a modeling results in an almost constant causal Q model over the frequency range investigated (from 5 to $100Hz$).

Typical Anisotropy Parameters
using Thomsen's 1986 notation
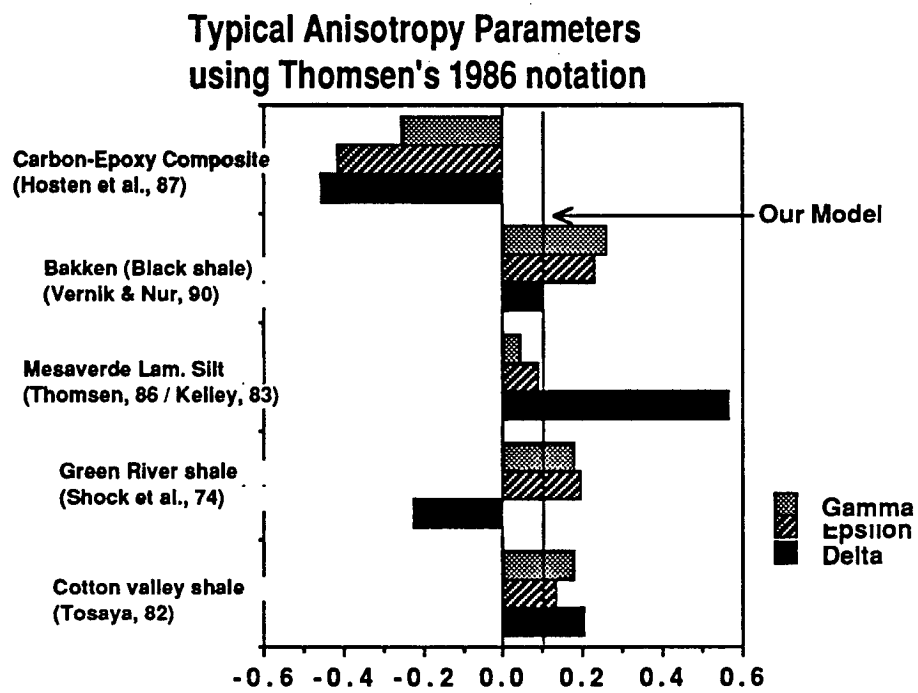
Figure 5.4: A comparative estimation of the measured anisotropic properties, and the anisotropic properties used in our modeling.
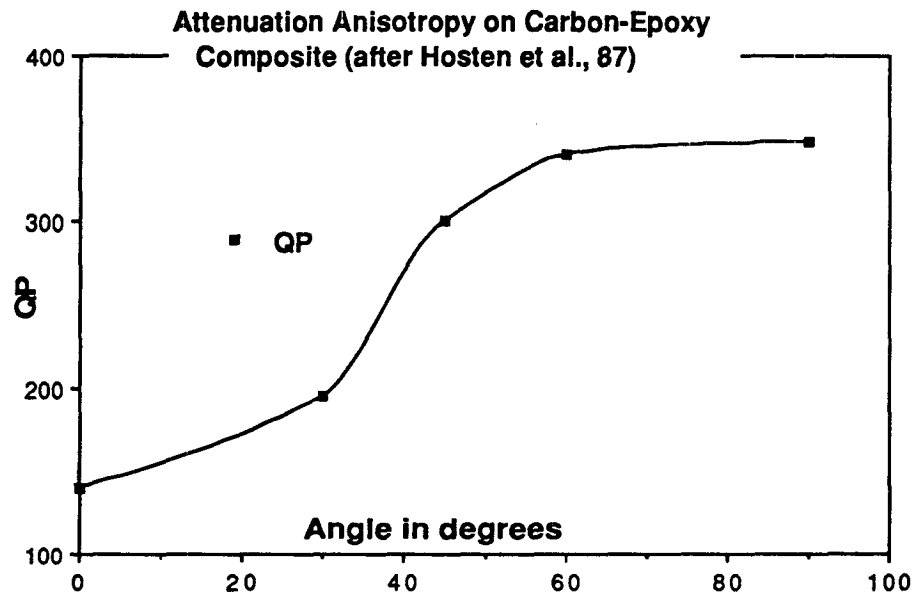
Figure 5.4: b) Experimental measurement of attenuation anisotropy in a composite material after Hosten (1987).

5.2.2 Modeling Benchmarks and reflection calibration

The following numerical experiments were conducted to evaluate the accuracy of our algorithm when used to evaluate reflected amplitudes as well as reflection coefficients. Two different methods have been implemented that yield consistent results in the evaluation of reflected amplitudes and reflection coefficients :

5.2.2.1 Direct measurement of the reflection amplitudes

For the cases where the upper layer is isotropic and purely elastic, recording the amplitude variations with offset after geometrical spreading correction is equivalent to recording the reflection coefficient. Since our modeling is only two-dimensional, the amplitude decay is proportional to $\frac{1}{\sqrt{r}}$ where r is the distance from the source (Aki and Richards i1980). Should the modeling be truly three-dimensional, the decay would be proportional to $\frac{1}{r}$. This observation is consistent with the results obtained in Chapter 4. However the previous use of the word *amplitude* is very imprecise. Amplitudes can be evaluated in multiple ways with multiple meanings attached to the measurement. Among other methods, the following were considered :

- maximum picked amplitude for the reflected event.

- root mean square average of the reflected arrival amplitude within a window.

- spectral amplitude attached to a frequency component of the reflected event.

Each of these methods yield the same results, provided that the transmission line from the source to the receivers does not introduce any signal dispersion. This can only be achieved when both the upper and lower layers of our model are purely elastic, and when the numerical method does not introduce any signal dispersion.

Should there be attenuation or anisotropy in one of the layers, the three preceding methods would yield very different results for the following reasons :

- Amplitude picks over-emphasize the effects of phase shifts because the location of the maximum amplitude on the wave train shifts with the signal's phase. Overall, the results from picks were found to be unstable and difficult to interpret when anisotropy or viscoelasticity was modeled.

- The root mean square average provides a measure of the reflected energy within a given window. (Aki and Richards 1980). This type of measurement eliminates the undesirable phase effects noticed with the picking algorithm. However, this method lumps the phase and pure energy focusing effects into one result, and does not provide us with the level of discrimination that we expect in a low signal-to-noise environment such as numerical modeling.

- The spectral amplitude method provides a perfectly calibrated measurement of the reflection amplitudes for a given frequency, and allows us to discriminate between phase distortion effects and energy focusing mechanisms. The spectral amplitude method could only be adopted in this study because of the excellent signal-to-noise quality delivered by synthetic data;

Figures 5.5 and 5.6 display the results obtained with the spectral method when the top and bottom layers are purely elastic and isotropic. The spectral amplitude data was measured at $35Hz$, and corrected for two-dimensional geometrical spreading. This data shows good agreement with the reflection coefficient data multiplied by the source amplitude at $35Hz$, and confirms that for elastic isotropic media, the measurement of amplitude variation with offset after geometrical spreading correction is the actual measure of the reflection coefficient as a function of the incidence angle. Furthermore, should the upper layer be isotropic and purely elastic, the spectral measurement previously described provides a good estimate of the reflection coefficients,

since the signal is not distorted while propagating in the upper layer.

5.2.2.2 Direct measurement of the reflection coefficient

Should the upper layer of our model be purely elastic, the spectral method previously described allows a direct computation of the reflection coefficient as a function of the incidence angle. Should the upper medium be viscoelastic or anisotropic, the transmission effects would dramatically alter the quality of both the incident and reflected waves, as will be shown later in this chapter. In such a case, numerical modeling still allows an adequate evaluation of the reflection coefficients for arbitrary media.

Figure 5.7 shows receivers that are placed along both down-going and up-going ray paths of the mode of interest. Further extracting amplitude variations along these receiver traces using the spectral method provides the data displayed in figure 5.8. The amplitude along the ray path first decays due to the effects of both geometrical spreading and attenuation until the ray reaches the interface. The sudden amplitude jump in figure 5.8 then provides a direct measurement of the reflection coefficient for each ray path selected. This method yields a direct numerical estimation of the reflection coefficient. Figure 5.9 shows the agreement between the analytical reflection coefficient and the numerical computation is excellent.
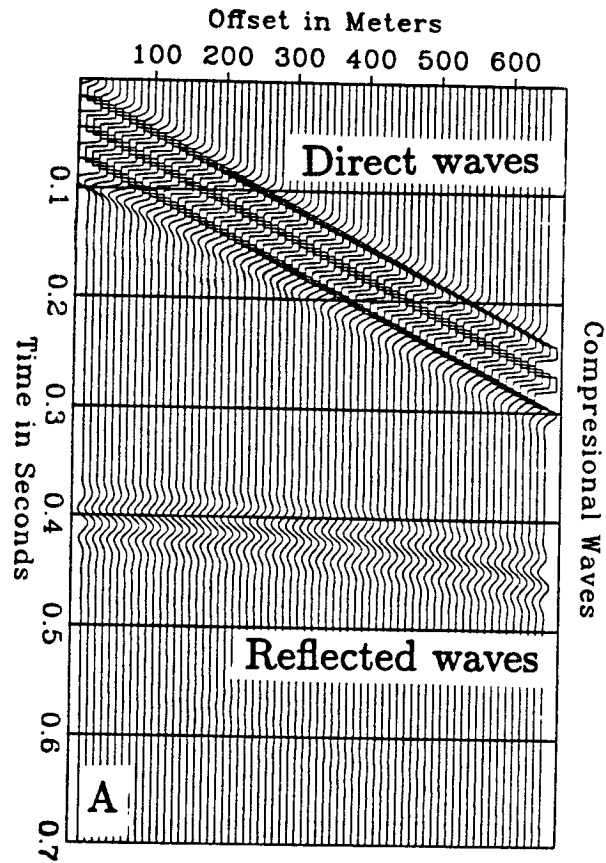
Figure 5.5: A typical record for the reflection receiver geometry. Only compressional waves are displayed on this graph, and two modes can be clearly identified, direct waves, and reflected compressional waves.
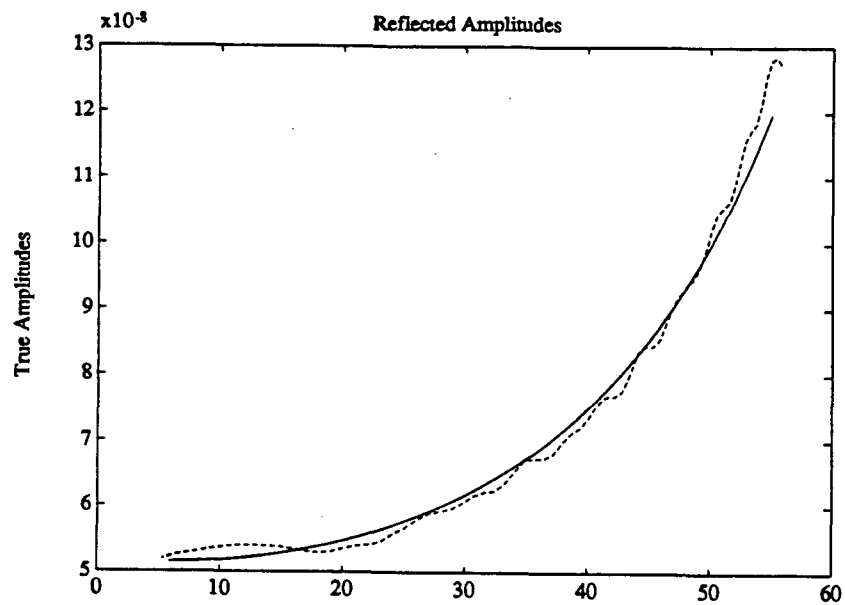
Figure 5.6: Comparison between the numerical and theoretical computation for the amplitude of the reflected compressional waves. The theoretical prediction (solid line) is obtained after multiplying the reflection coefficient by the source amplitude. The picked amplitude (dashed line) is corrected by $\frac{1}{\sqrt{r}}$ for two dimensional geometrical spreading.
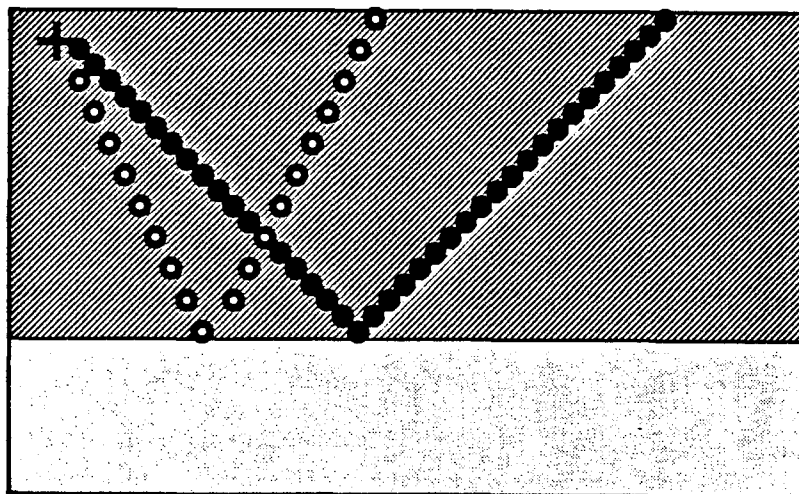
Figure 5.7: Second acquisition geometry to directly compute the reflection coefficients from the records placed along the ray paths.
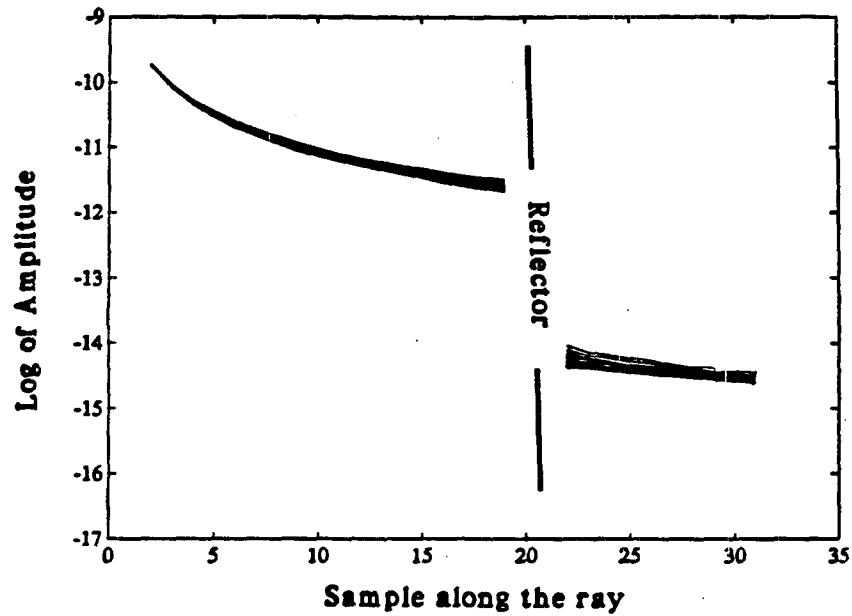
Figure 5.8: Actual amplitudes picked along the ray paths for the compressional waves as a function of the ray parametrization. The abrupt amplitude jump is caused by the reflection coefficient. Each of these curves is plotted for a different incident ray, which allows for the computation of the reflection coefficient as a function of the angle of incidence.
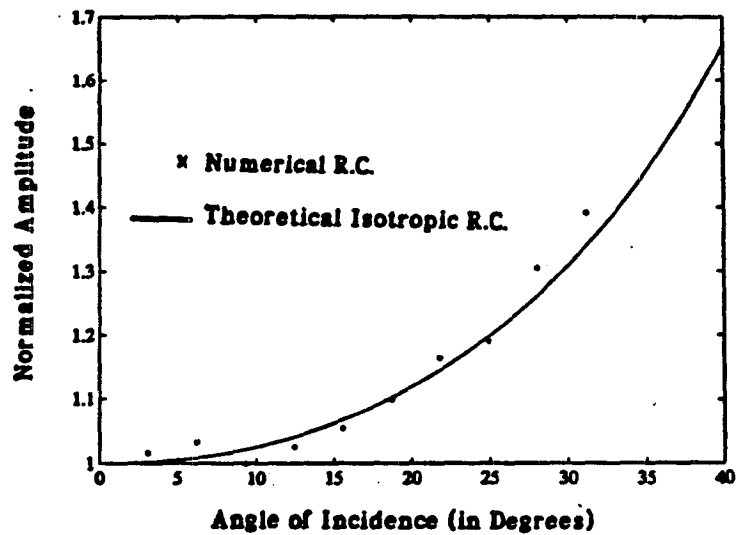
Figure 5.9: Comparison between the theoretical and numerical reflection coefficients computed with the method presented in section 5.2.2.2.

5.2.2.3 Monitoring the wave fronts

In order to understand the effects of wave propagation phenomena on the measurement of Amplitude Versus Offset for reflected signals, the effects of energy focusing and defocusing along the wave front need to be understood as well as the effects related to anisotropic attenuation. To that end, a new receiver geometry was introduced; it is similar to the one described in Chapters 1 and 2 for measuring downhole source radiation patterns. For that last configuration, the receivers are placed around the source along equal phase curves as shown in figure 5.10. The signal recorded for one of these receiver arrays is displayed in figure 5.10, where the upper layer is elastic and anisotropic. The mis-alignment of the first arrival is caused by the discrepancy between phase and group velocity in an anisotropic medium as figures 5.15 shows. Fig 5.11 clearly displays both the down-going compressional wave, and the reflected compressional wave. Since the down-going arrival is stronger than the reflected one, it is apparent that this type of plot can be used as a diagnostic tool to measure both phase distortion and energy focusing effects that affect wave propagation phenomena in anisotropic viscoelastic solids.

5.2.3 Partial conclusions

Various tools were presented in this part that allow to harness the numerical modeling of wave phenomena in viscoelastic anisotropic solids. For the rest of this chapter, we will assume that wave amplitude refers to the spectral amplitude of an isolated mode measured at $35Hz$ which is the central frequency of our signal. All amplitude displays will be in true "amplitude", and theoretical measurements will be displayed after normalization by the source amplitude. The following two parts detail a sensitivity analysis of Amplitude measurement Versus Offset with respect
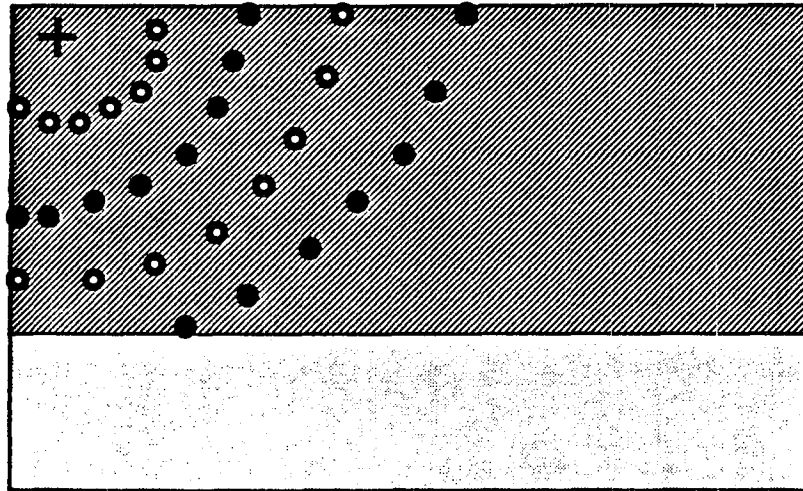
Figure 5.10: Receivers' distribution for monitoring the energy distribution along wavefronts.
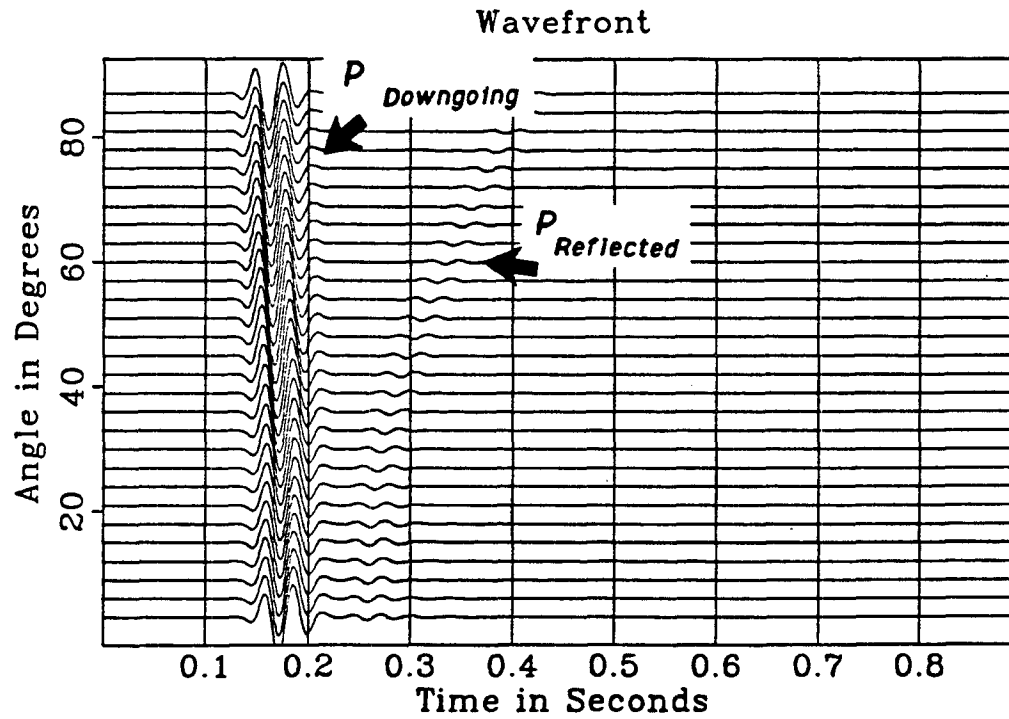
Figure 5.11: The numerical computation of the signal propagated through a receiver array placed along the wavefront in an anisotropic medium.

to both anisotropy and viscoelasticity. Due the high precision required for these measurements, direct reflection coefficient measurements will be achieved by using an isotropic elastic upper layer.

5.3 The effects of attenuation on Amplitude Versus Offset measurements

Two distinct effects of attenuation on Amplitude Versus Offset measurements will be reviewed in the following section. The first one concerns the direct effect of attenuation on the reflection coefficient, and the second concerns the effect of attenuation on the wave propagation from the source to the reflector and back to the receiver array.

5.3.1 The effects of attenuation on the reflection coefficients

For the first modeling case, the lower layer is viscoelastic, and both the elastic and attenuation parameters are isotropic. The bottom layer parameters are described in figure 5.11. The measured amplitude at the surface receivers (figure 5.13 a) for both an elastic bottom layer (solid line), and a viscoelastic bottom layer (dashed line) clearly display the effect of attenuation on the reflection coefficient : an overall increase in amplitudes with no appreciable change in the A.V.O trend. The overall amplitude jump can be easily interpreted by considering that the addition of the viscoelasticity in the bottom layer increases the apparent impedance contrast between the two layers. Our results are consistent with the one described by Bourbie (1982) both qualitatively and quantitatively.

Should the bottom layer still be attenuating but with an anisotropic attenuation parameter identical to the one in figure 5.12, the reflection coefficient curve departs from the one obtained previously as shown in figure 5.13 b where the dotted line represents the anisotropic attenuation case. This last result further illustrates the

dependence of the reflection coefficient on the attenuation parameter : At normal incidence, attenuation is the same for both isotropic and anisotropic attenuation models. As incidence angle increases, the attenuation decreases with propagation angle, thereby reducing the contrast between the upper and lower layer. This results in the relative decrease of the reflection coefficient for the anisotropic attenuation case, when compared to the isotropic case.

5.3.2 The effects of attenuation on wave propagation mechanisms

figure 5.14 displays the measured reflected amplitude where the upper layer is isotropic viscoelastic (solid line), and viscoelastic anisotropic (dashed line).

For the isotropic viscoelastic case first, the A.V.O. trend is now flat instead of strongly positive. This phenomena can be easily explained by accounting for the effect of attenuation along the ray path. The longer the ray path, the higher the attenuation, thereby destroying most of the A.V.O trend created by the reflection coefficient alone. This explanation is confirmed by considering the anisotropic attenuation case where the A.V.O trend recorded in the elastic case is amplified. As offset increases, the propagation or incidence angle also increases lowering, the attenuation effect and increasing the original A.V.O trend.

In the latter case it is important to notice that picking the reflected arrival would have not always been giving the answer found with the spectral method because it depends on the phase of the reflected event picked. In an anisotropic attenuating medium, the dispersion introduced by the difference between phase and group velocity is not uniformly spread along the wave front and therefore creates large errors in the picked measurements.
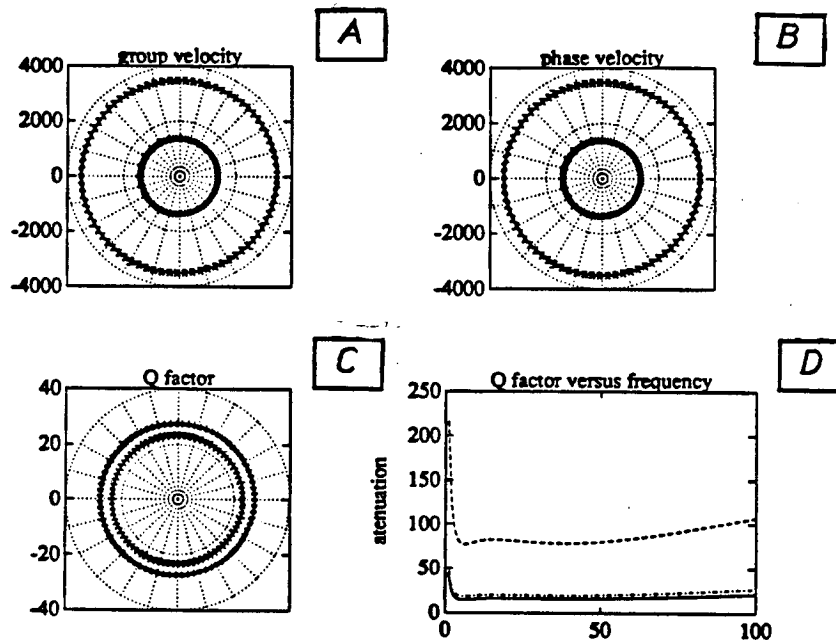
Figure 5.12 a: Description of an isotropic viscoelastic solid. Such a solid can be described by a) the group velocity, b) the phase velocity, and c) the Quality factor for both compressional (outer circles) and shear waves (inner circles). d) The dependency of the various attenuation parameters on frequency.
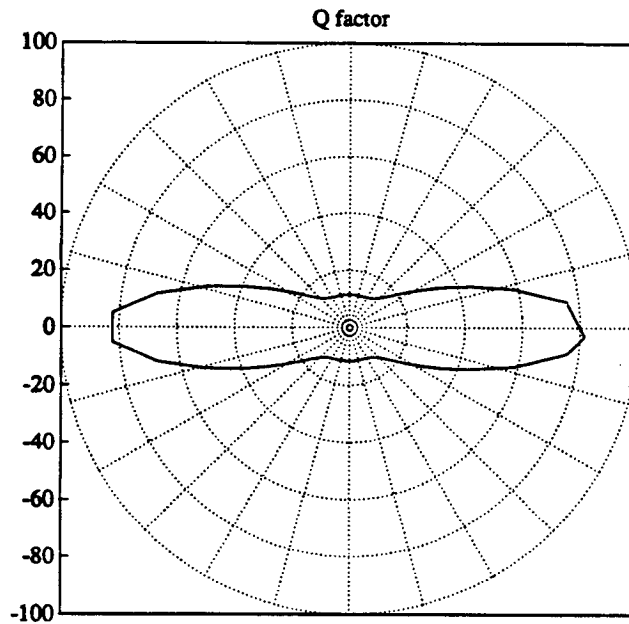
Figure 5.12b: Attenuation anisotropy properties of the material modeled.
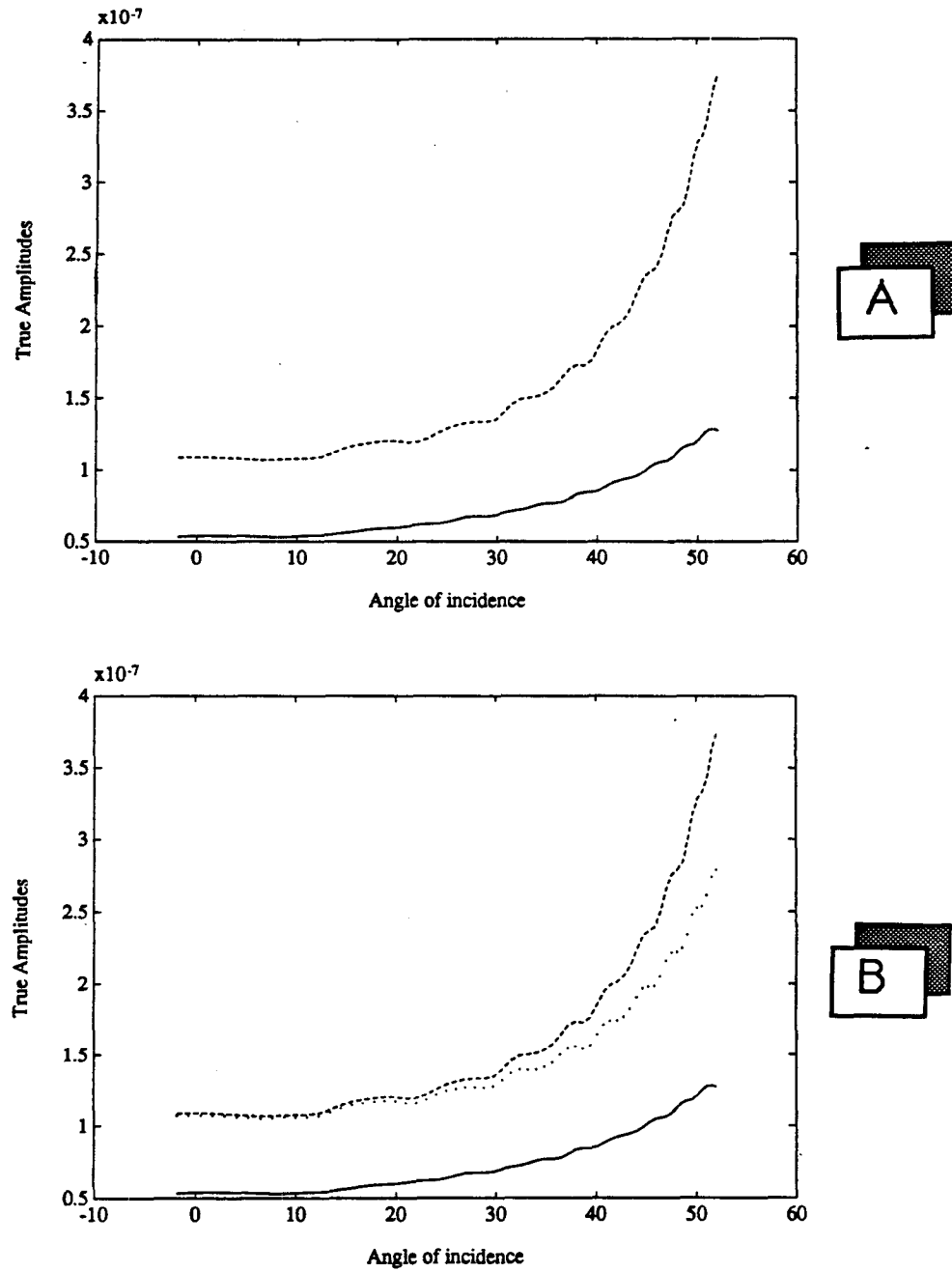
Figure 5.13: a) Comparison between the reflected compressional waves amplitude where the bottom layer is purely elastic (solid line), and viscoelastic (dashed line). b) The dotted line now shows the reflected amplitudes where the bottom layer has anisotropic viscoelastic properties.

5.3.3 Partial conclusions

Three partial conclusions can be drawn out of the previous results :

- 1) Viscoelasticity contrast is not a controlling factor of the variation of the reflection coefficient with incident angle for small incidence angles, but is certainly a controlling factor of amplitude.

- 2) For a fairly typical shallow reflector geometry, attenuation along the ray path can mask the effect of an increase in the reflection coefficient with incidence angle.

- 3) The role of viscoelastic anisotropy is more difficult to evaluate. Viscoelastic anisotropy can severely affect the variations of the reflection coefficient with the incidence angle, and is expected to yield a relative decrease. However, attenuation anisotropy has a very strong effects on propagation effect, and can actually create a positive A.V.O effect for an otherwise constant reflection coefficient.
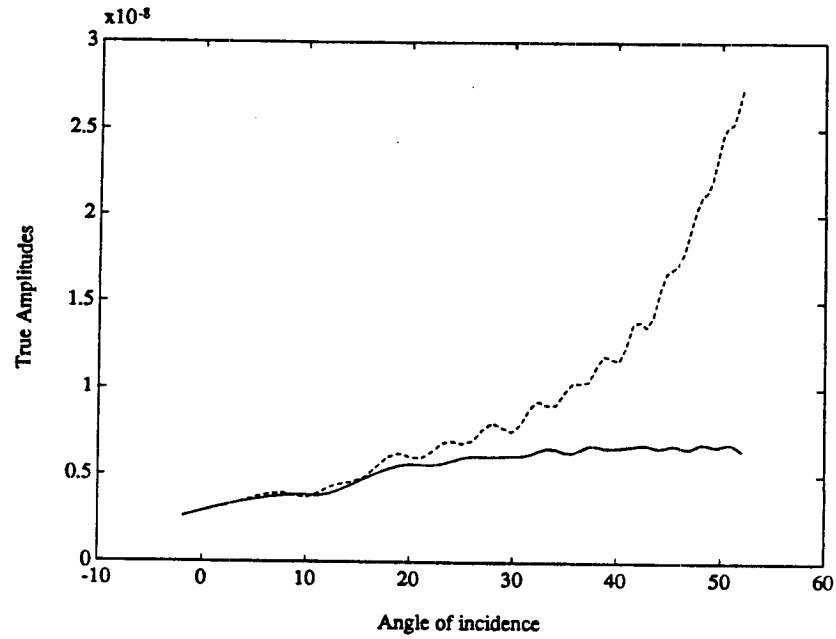
Figure 5.14: Compressional waves reflected amplitude measurement. In the first case the top layer is viscoelastic isotropic (solid line). In the second case, the top layer attenuation properties are anisotropic.
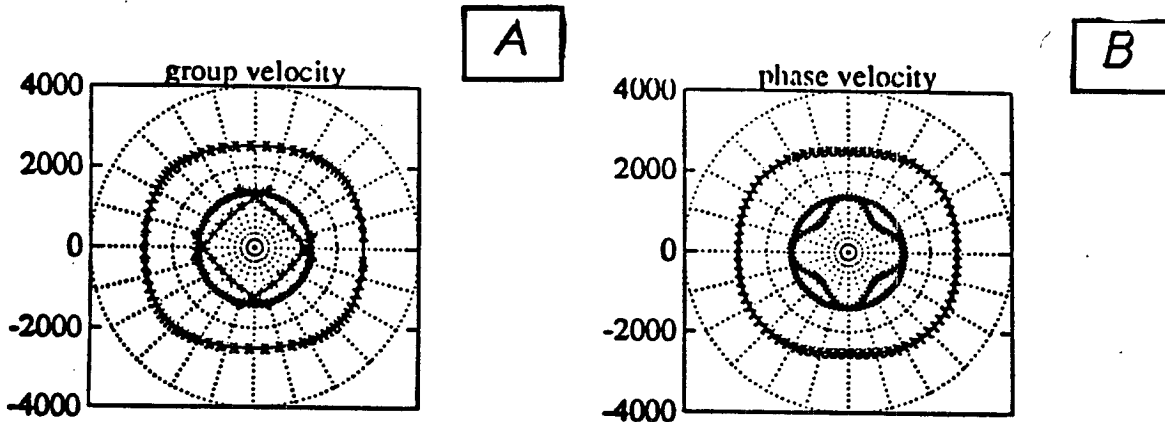
Figure 5.15: Elastic properties of the anisotropic material used for modeling : a) Group velocity, b) Phase velocity.

5.4 The effects of elastic and attenuation anisotropy on Amplitude Versus Offset measurements

For this study, the anisotropic material modeled is depicted in figure 5.15. It is obtained by using the velocities previously described, and by taking $\delta = 0.1$. Should anelastic anisotropy be considered, anelastic anisotropy is similar to the one presented in the previous part.

5.4.1 The effects of anisotropy on the reflection coefficients

The effect of elastic anisotropy on reflection coefficients was extensively described by both Banik (1987) and Thomsen (1986). Their results were reproduced with the greatest accuracy as shown in figure 5.16 where the upper layer is isotropic, and the lower layer is anisotropic. Each curve cluster presents a comparison between the analytical computation (*) and the numerical computation (solid line). As expected for the special case of anisotropy studied here, anisotropy yields a larger increase of the reflection coefficient as a function of incidence angle. However the effect related to elastic anisotropy is relatively small compared with the dramatic effects introduced by viscoelasticity.

Should a fully anisotropic medium displaying both elastic and viscoelastic anisotropy be used to model the bottom layer, the results presented in figure 5.17 display a very sharp increase in the reflection coefficient with offset, as well as an increase in the over-all reflected amplitude. This result may seem somewhat contradictory with the result previously obtained using a bottom layer material that is isotropic for the elastic behavior, and anisotropic for the viscoelastic behavior. However this last result indicates that even though elastic and viscoelastic propagation phenomena are decoupled to the first order (Chapter 4), the reflection coefficient introduces a close coupling effect

between these two material properties and explains the result previously described.
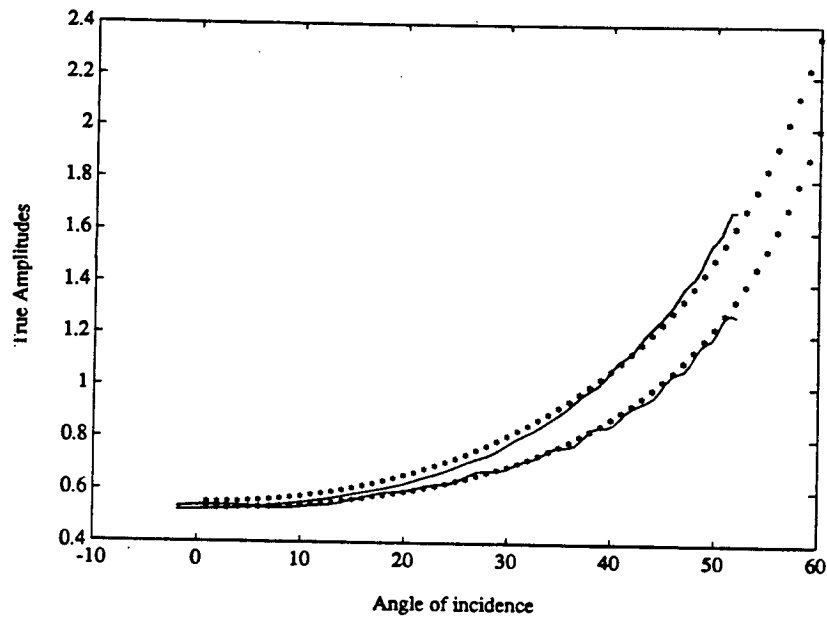
Figure 5.16 : Effect of anisotropy on the reflection coefficient. a) Where the reflecting layer is isotropic, b) the reflecting layer is anisotropic. Each curve cluster displays a comparison between the numerical (-) and analytical (*) computation.
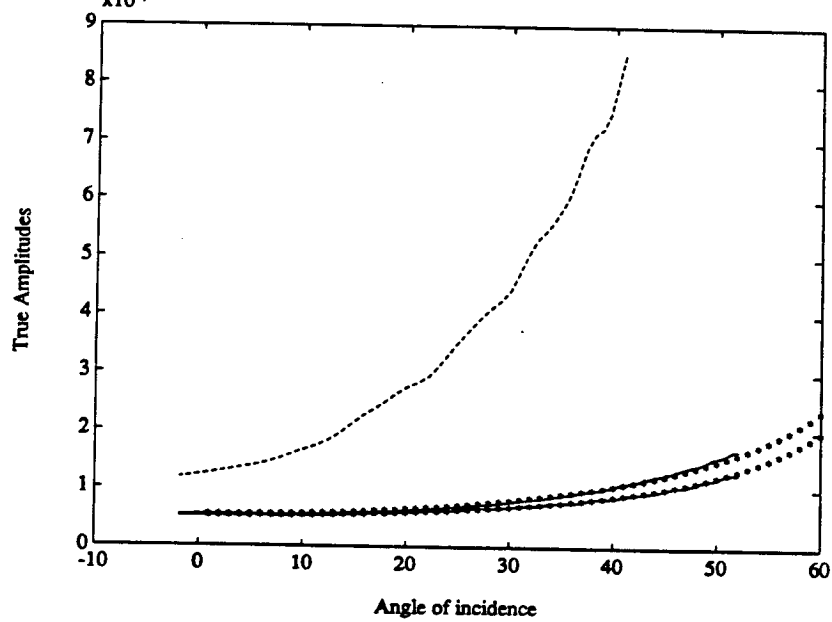
Figure 5.17 : Same as figure 5.16, but the upper curve is obtained for a both elastic and viscoelastic anisotropic bottom layer.

5.4.2 The effects of anisotropy on wave propagation mechanisms

Consider that the upper layer of our model is anisotropic with $\delta = 0.1$ as before. The reflected amplitudes after geometrical spreading correction are displayed in figure 5.18. The predicted result (*), and the actual numerical result (dashed line) differ very strongly. This discrepancy is not related to the method inaccuracy but instead is related to the wave propagation phenomena introduced by the intrinsic elastic anisotropy of the upper layer.

To verify this hypothesis, the receiver geometry described in 5.9 is used to monitor the energy distribution on the down-going compressional wave front. These results are presented in figure 5.19 for both an isotropic upper layer (a), and an anisotropic upper layer (b). As expected in the isotropic case, the source radiates energy isotropically since the amplitude as a function of the propagation direction for a given time is constant. As time increases, the amplitude on the wave front decays due to geometrical spreading. For an anisotropic upper layer however, the initial energy distribution along the wave front is not a constant as shown in figure 5.19 b. This first effect implies that elastic anisotropy introduces radiation pattern anisotropy. This is further explained by the fact that even though the source is an explosion, a significant amount of shear waves are generated by the source due to elastic anisotropy, and the compressional wave radiation pattern reflects such a partition between compressional and shear wave energy.

Furthermore, as time goes, the energy distribution along the wavefront shifts. This particularly interesting result is due to the difference between group and phase velocities that differentially focuses energy along the wavefront. This last result allows us to interpret the results displayed in figure 5.18. The discrepancy between the numerical computation, and the theoretical prediction is due to the anisotropy of

energy distribution along the wavefront.

Reflection coefficients significantly depend on the elastic anisotropic parameters of the material involved. However A.V.O. measurements do not solely reflect the effects of the reflection coefficient on the surface-recorded signal, but also of the wave propagation phenomena from the source to the reflector and back to the surface. For weakly anisotropic rocks, the impact of propagation phenomena are as large if not larger than the pure effect of anisotropy on the reflection coefficient, and should therefore be taken into account for the interpretation of A.V.O. data.

5.5 Conclusions

The translation of Amplitude Versus Offset trends into rock petrophysical properties such as Poisson's ratio can only proceed under the assumption that rocks are isotropic and elastic. As indicated by both laboratory and field studies, the last two assumptions are in general not valid, and assuming that the earth is neither isotropic nor purely elastic yields the following observations:

- Reflection coefficients, which are the primary target of A.V.O. interpretation, are strongly dependent on both the viscoelastic and the anisotropic properties of the rock studied.

- Both the anisotropic and viscoelastic properties of a material will alter the signal during propagation, first, because of energy focusing, and, second, because of attenuation or dispersion.

For these reasons, it is reasonable to assume that both viscoelastic and anisotropic parameters should be included in A.V.O. interpretation. The system considered is not only the reflecting target but rather the full wave path from the surface to the target, as well as the target itself.
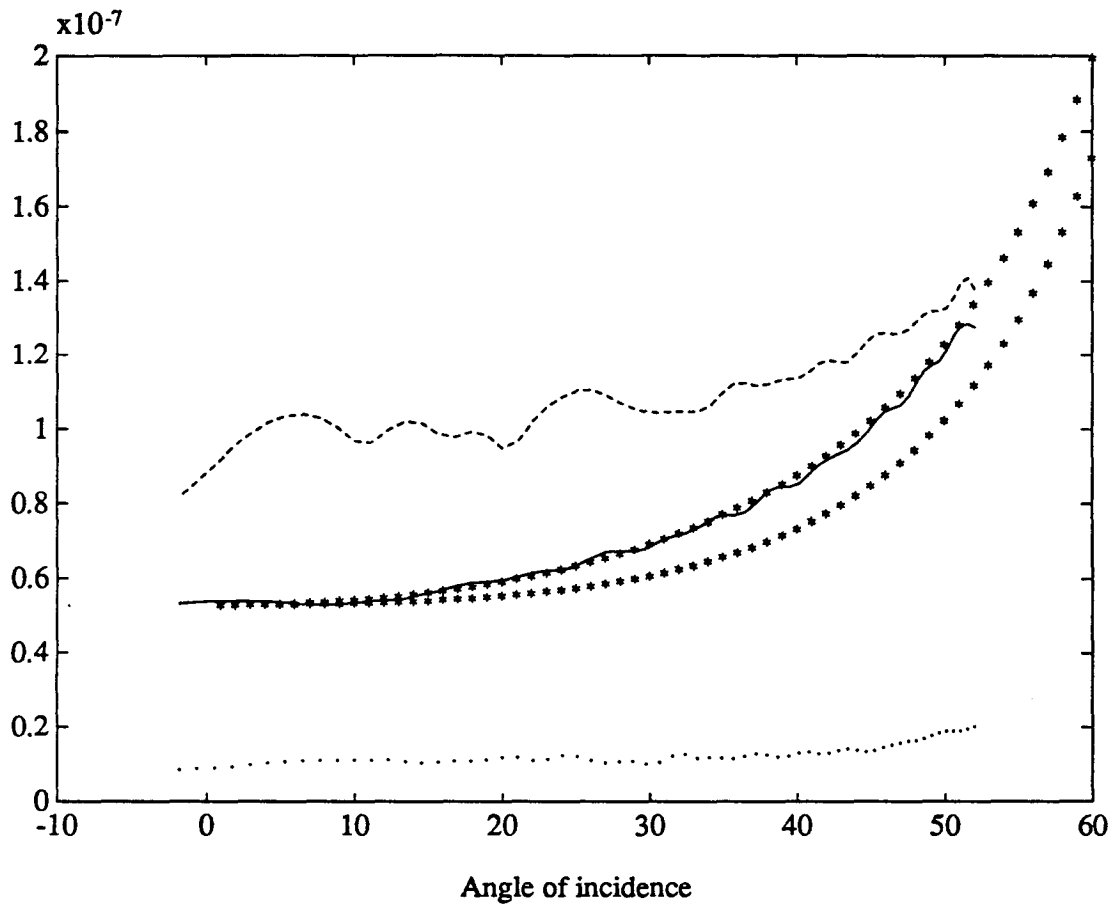
Figure 5.18 : Effect of an anisotropic upper layer on AVO measurement. The drawing convention is the same as in 5.17, and the dashed line displays the new modeling case result.
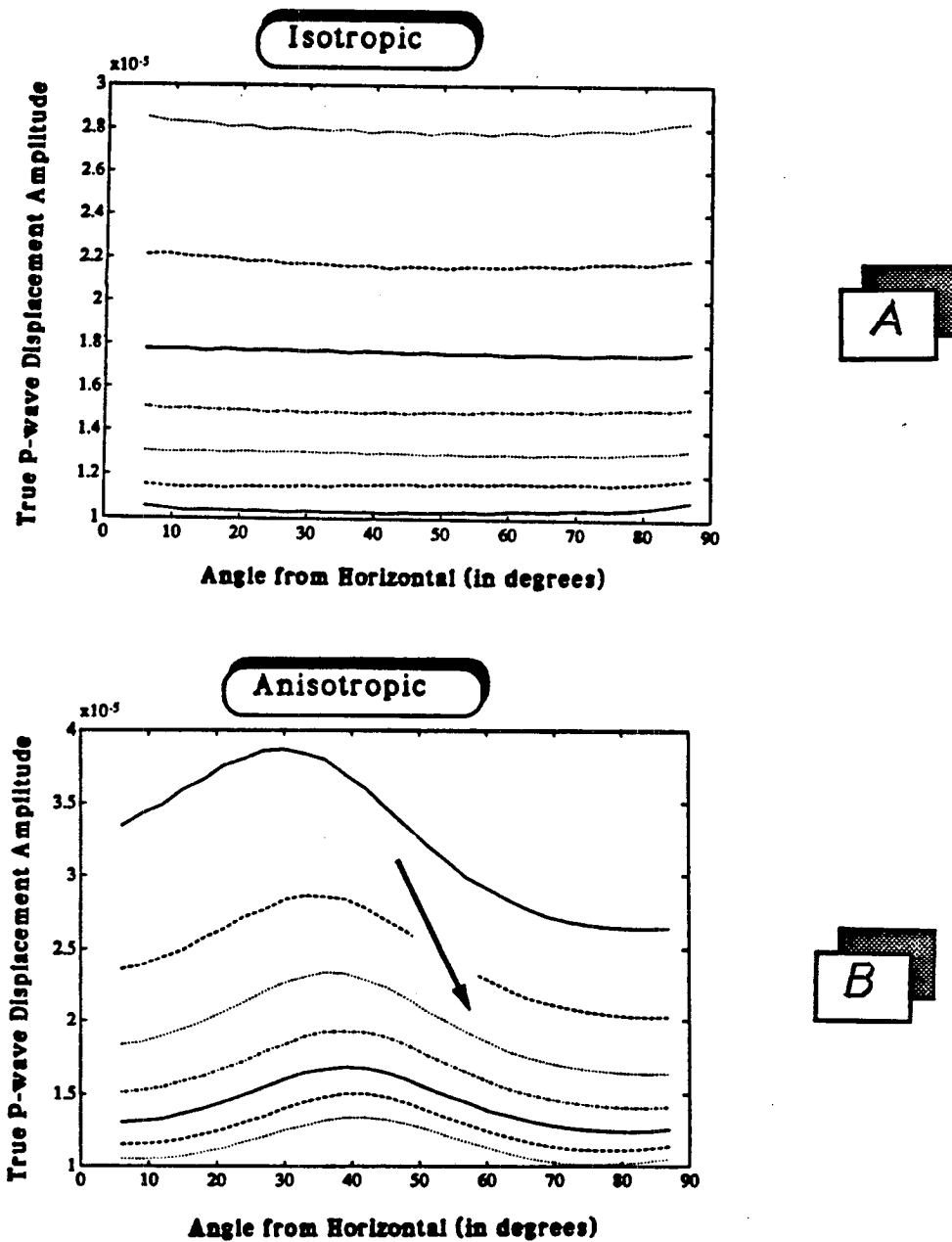
Figure 5.19 : Energy distribution along the wavefront in a) an isotropic solid, b) anisotropic solid. Each of the curve corresponds to a separate wavefront, and the arrow indicates the direction of increasing times.

References

Aki, K., and Richards, P., G., 1980, Quantitative seismology: W. H. Freeman and Co.

Banik, N., C., 1987, An effective anisotropy parameter in transversely isotropic media: Geophysics, **52**, 1654,1664.

Bourbie, T., 1982, Effect of attenuation on seismic reflections: SRB **14**

Carcione, J. M., 1987, Wave propagation in real media, Ph. D. thesis, Senate of Tel Aviv University.

Crampin S., 1984, Effective Anisotropic Elastic constants for Wave propagation through cracked solids: Geophys. J. R. Astr. Soc. , **76**, 135,145.

Daley, P., F., and Hron, F., 1977 : Reflection and transmission coefficients for transversely isotropic media: Bull., Seis. Soc. Am., **67**, 661,675.

Hosten, B., Deschamps, M., and Tittman, B.R., 1987: Inhomogeneous waves propagating in a lossy anisotropic solid. Application to the characterization of viscoelastic composite materials: J. Acoust. Soc. Am., **82**, 1763,1770.

Jones, T., 1986, Pore fluids and frequency-dependent wave propagation in rocks: Geophysics, **51**, 1939,1953.

Liu, H. P., Anderson D.L., Kanamori H., 1976, Velocity dispersion due to anelasticity ; Implication for seismology and mantle composition: Geophys. J. R. Astr. Soc. , **47**, 41,58.

Kjartanson, E., 1979, Constant Q-Wave Propagation and Attenuation: J.G.R., **84**, 4737,4748.

Kosloff, D. and Baysal, ER., 1982, Forward modeling by a Fourier method: Geophysics, **47**, 1402,1412.

Nur, A., and Simmons, G., 1969, Stress induced velocity anisotropy in rock; an experimental study: J. G. R., **74**, 6667,6674.

Thomsen, L., 1986, Weak elastic anisotropy : Geophysics, **51**, 1954,1966.

Tal-Ezer H., 1986, Spectral methods in time for hyperbolic equations: SIAM J. Numer. Anal., **23**, 11,26.

Winkler, K., and Nur, A., 1986, Pore fluids and seismic attenuation in rocks: Geophysical Research letters, v. 6, 1,4.

Wright, J., 1987, The effects of transverse isotropy on reflection amplitude versus offset: Geophysics, **52**, 564,567.

Chapter 6

Finite-difference Computation of Travel-times

Abstract

Finite-difference ray tracing (F.D.R.T.) is a numerical method designed to solve the eikonal equation on a regular grid using an upwind finite-difference-like algorithm. Because it uses a finite-difference algorithm, F.D.R.T. is between 10 and 100 times faster than classical raytracing that is used to solve two point boundary condition problems.

Expanding the scope of the method proposed by Vidale (1988) I found that :

- F.D.R.T. provides extremely accurate results for the travel times in an isotropic medium, providing the true first energy arrival for a given mode.

- extended to the anisotropic case, F.D.R.T. provides a method to incorporate to the first order the effects of anisotropy. For a material with 12% anisotropy, the maximum travel time error was 1.5% thereby smaller than the error that would have been introduced by neglecting anisotropy all together.

- extended to anelastic medium, F.D.R.T. allows for accurate modeling of dispersion, as well as attenuation, given a simple model for attenuation (constant

Q). These computations only apply if frequency dependent scattering can be neglected.

6.1 Introduction

Vidale (1988) and Van Trier (1989) have proposed a direct solution of the eikonal equation using the finite-difference technique : finite-difference ray tracing (F.D.R.T.). This method allows for an extremely rapid computation of travel times for any geophysical model that can be described on a regular mesh. It computes the arrival time of the first arriving mode, providing a continuous (C^0) curve for the first arrival independent of its type (whether it is a body wave, a refracted wave, or a scattered wave).

The speed of this algorithm (10 to 100 times faster than classical ray tracing) makes F.D.R.T. extremely useful for three-dimensional computations. F.D.R.T.'s nature makes it particularly suitable for tomography techniques since it computes the actual first arrival. Finally, it can be used to speed up full waveform finite-difference algorithms by computing the zone affected by the wave propagation phenomena and restricting the finite-difference computations to this very area.

My interest in this chapter was to try to expand the applicability of F.D.R.T. beyond its use with isotropic acoustic materials. Three directions of investigation proved to be worth pursuing:

- increasing the accuracy of the F.D.R.T. algorithm for arbitrarily located sources and receivers without changing the main algorithm

- extending the use of F.D.R.T. to anisotropic material

- extending the use of F.D.R.T. to viscoelastic materials by including the effects of dispersion and attenuation

6.2 The numerical method

This section provides a detailed description of the numerical algorithm used for F.D.R.T. by first describing interpolators related to the eikonal equation, then the upwind finite-difference algorithm. It concludes by estimating the overall accuracy of this method.

6.2.1 The eikonal equation and its numerical solutions

The propagation of two-dimensional wavefronts, and thus, the computation of travel times, is described by the eikonal equation of ray tracing:

$$\left(\frac{\partial t}{\partial x}\right)^2 + \left(\frac{\partial t}{\partial z}\right)^2 = s^2 \tag{6.1}$$

where t is the travel time. The left side the square norm of the gradient of the travel time and s is the slowness of the medium. Both partial derivatives on the left side of equation 6.1 can be evaluated numerically using a simple first order finite-difference algorithm yielding (after Vidale 1989):

$$\frac{\partial t}{\partial x} = \frac{1}{2h}(t_0 + t_2 - t_1 - t_3) \tag{6.2}$$

$$\frac{\partial t}{\partial z} = \frac{1}{2h}(t_0 + t_1 - t_2 - t_3) \tag{6.3}$$

The term h represents the grid spacing, and the location of the various indexes used in the previous equations is provided in figure 6.1a.

A combination of the three preceding equations yields the first interpolation function for the travel times in the case of a propagating plane wave. By solving equations
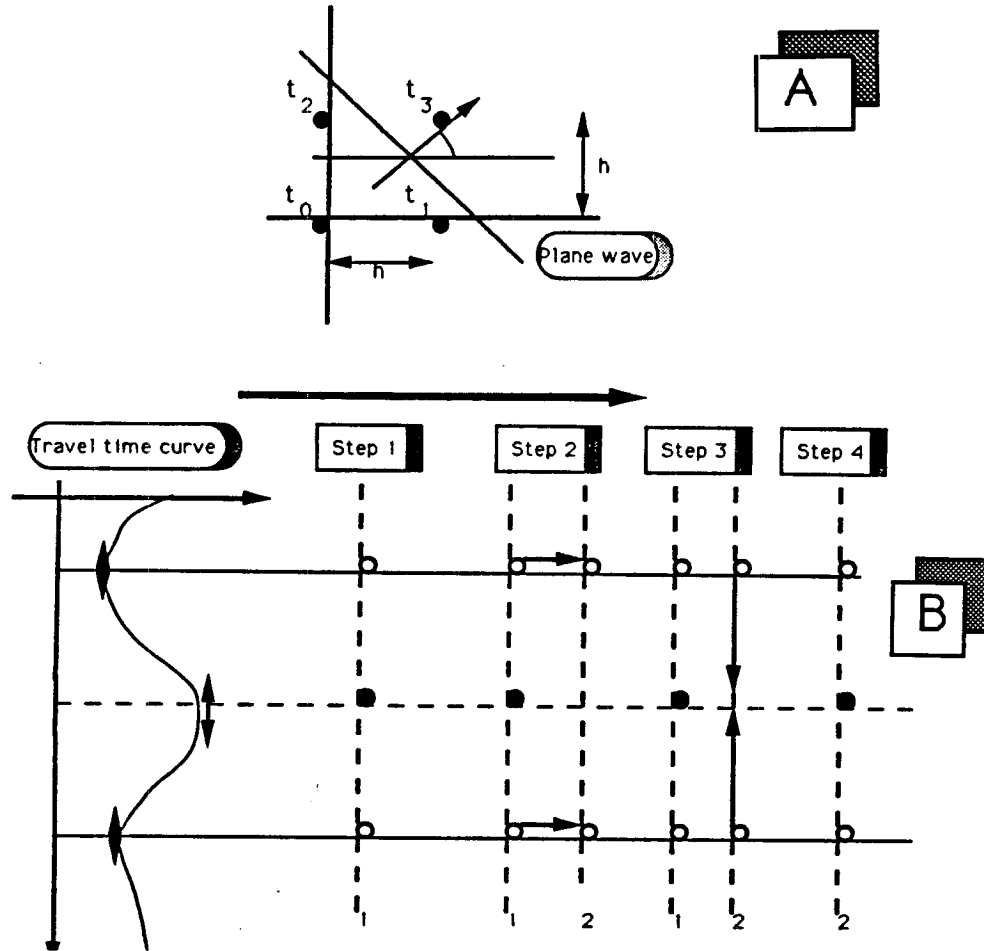
Figure 6.1: a) Indexes for the finite-difference computation of travel times: from this cell, an upwind algorithm can be devised that solves travel times for a row. b) the algorithm for travel time computations for a row (after Vidale 1989).

6.1, 6.2,and 6.3 for t_3 we obtain:

$$t_3 = t_0 + \sqrt{2(hs)^2 - (t_2 - t_1)^2}$$ (6.4)

where s is the slowness of the medium. Two other interpolators are also described by Vidale and given in Appendix 4:

- an implicit interpolator for spherical waves that computes t_3 as a function of t_1, t_2, and t_4 under the assumption of a locally spherical wave

- an explicit interpolator that computes t_3 for a new row at a minimum of the travel time curve, provided that the three other travel times are computed in the previous rows.

The accuracy achieved by these three interpolators in the source neighborhood is shown in Table 6.1. Maximum accuracy can be achieved by using the spherical interpolator in the source neighborhood and the plane wave interpolator elsewhere. Instead, as described in the next section, I preferred a center cell algorithm for optimum accuracy in cases where the source is not located on a node of the finite-difference mesh.

Algorithm	Interpolator 1	Interpolator 2	Interpolator 3
Vidale (1989)	4.8 %	0.9 %	7.6 %
Centered cell	0.2 %	N/A	0.36 %

Table 1: Maximum interpolation error in the source near field. The table entries are the maximum relative error encountered within the first five rows of points from the source for each interpolator. The first row values are provided for a straight implementation of the algorithm provided by Vidale (1989), and the second one for the centered cell algorithm developed in this paper (Interpolators 2 and 3 are described in appendix I).

6.2.2 The upwind finite-difference algorithm

This algorithm was implemented after Vidale (1989). It proceeds in four steps as shown in figure 6.1b.

- 1) For a row where travel times are known, the minimum and maximum of the travel times are computed.

- 2) Then using the third interpolator, the travel times for the next row are computed for each local minimum of the travel time curve.

- 3) Starting from each minima along a row the solution is computed using the first interpolator up the two closest local maxima.

- 4) Finally, the minimum value for both travel times computed at a local maxima is retained.

The fact that the solution is computed from the local minima, is the stability condition of the algorithm.

6.2.3 The center cell algorithm

Table 1 displays the errors associated with the use of the various interpolators described by Vidale. Though it is less computer intensive, the first interpolator yields poor results in the source neighborhood. Vidale suggests using of a hybrid algorithm using the second interpolator in the source region for optimum accuracy, and then switching to the plane wave interpolator away from the source for better numerical efficiency.

My implementation does not retain this algorithm because it requires the coding of two very different algorithms, and also because Vidale's algorithm only applies when the source is placed at a grid node. My scheme uses only the first and third interpolators in the following context:

- The travel times are computed in the source region, using a straight ray assumption, from the source to the outer edge of the center cell. This straight ray approximation is valid here because the size of the center cell is the same as the grid spacing.

- Then the solution is propagated using Vidale's algorithm with a reduced mesh resolution until it reaches a region where the true mesh resolution is achieved in the far field of the source.

- Finally, the rest of the solution is computed with the nominal mesh resolution, using the first interpolator.

This algorithm is illustrated in figure 6.2.

6.2.4 Algorithm accuracy and partial conclusion.

figure 6.3 shows the results obtained with the center cell algorithm for an isotropic homogeneous medium, where the sources and the receivers are not located at grid nodes. The accuracy of the algorithm is satisfactory: less than 0.1% error.

In the case of a layered medium (figure 6.4), the F.D.R.T. algorithm computes the true first arrival at the receivers. Below and above the low velocity layer, the first arrival is a compressional body wave. Within the low velocity layer, the V-shaped arrival time curve is generated by head waves originating at the interface between low and high velocity layers.

The results obtained in this preliminary modeling stage can be summarized as follows:
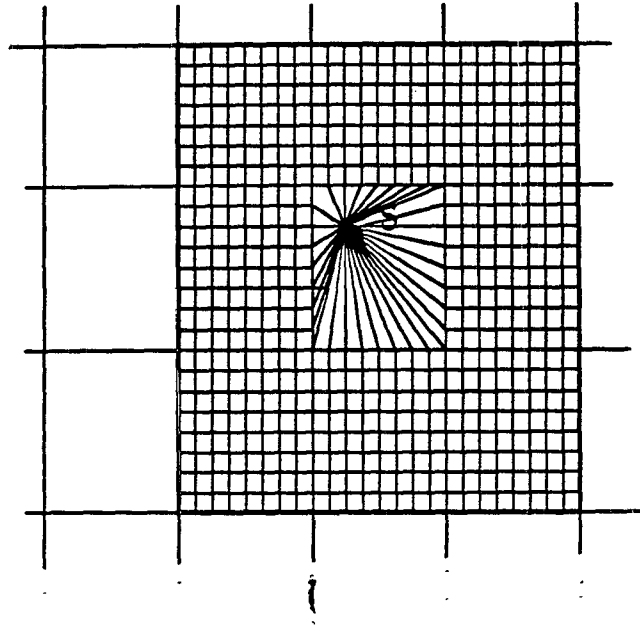
Figure 6.2: The central cell algorithm: the travel times are first computed on the outer edge of the center cell (straight rays), then in the source near field with a reduced mesh size, and finally computed in the far field, using the nominal mesh size.
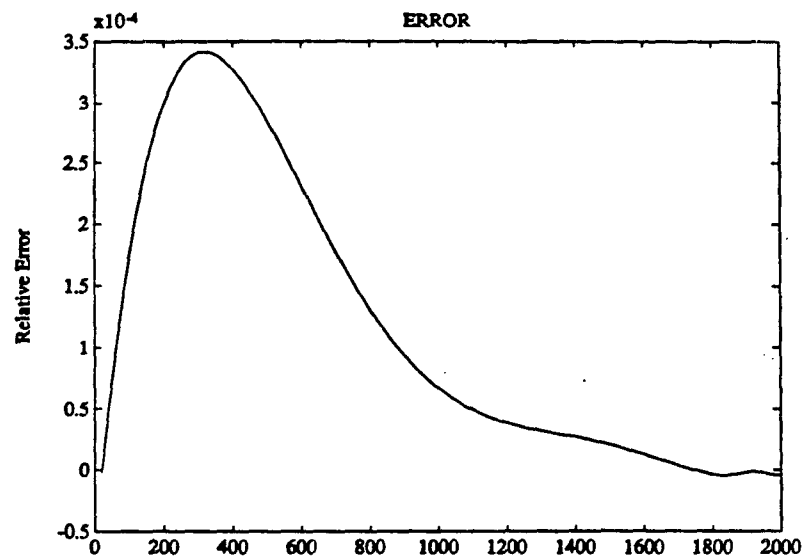
Figure 6.3:The travel time computation errors in an isotropic homogeneous solid. This graph shows the difference between the travel times computed using F.D.R.T., and those computed with an analytical solution.

- F.D.R.T. provides very accurate computations of the true first arrival travel time. This arrival can be a composite of multiple modes. Travel times are even computed in what are considered shadow zones with classical ray tracing.

- The travel time curve obtained at the receivers is continuous (C^0) which is a consequence of the search for minima and maxima in the upwind finite-difference algorithm. Nevertheless, the continuity level of these curves is not of class C^1 (their first derivative is not continuous.), or higher continuity level.

6.3 The extension of F.D.R.T. to anisotropic materials

6.3.1 The method

Since the interpolation method I have been using for the isotropic case is based on the eikonal equation (that is, the propagation of a plane wave), the algorithm developed in the first part of this paper can be easily transposed to the anisotropic case. This is done by replacing the slowness in equation 6.1 with a slowness that depends on the propagation angle of the local plane wave.

The propagation angle is defined by the notations of figure 6.1 as:

$$\theta = arctan \left(\frac{(t_2 - t_0)}{(t_1 - t_0)} \right) \tag{6.5}$$

Then, given the propagation angle, the slowness for the compressional waves, for example, can be easily computed (after Auld 1976) for a hexagonal solid as follows:

$$s = \sqrt{2\rho} \left[c_{11} sin^2\theta + c_{33} cos^2\theta + c_{44} + \sqrt{(p)} \right]^{\frac{1}{2}} \tag{6.6}$$

$$p = \sqrt{[(c_{11} - c_{44}) sin^2\theta + (c_{44} - c_{33}) cos^2\theta] + (c_{13} + c_{44})^2 sin^2 2\theta} \tag{6.7}$$
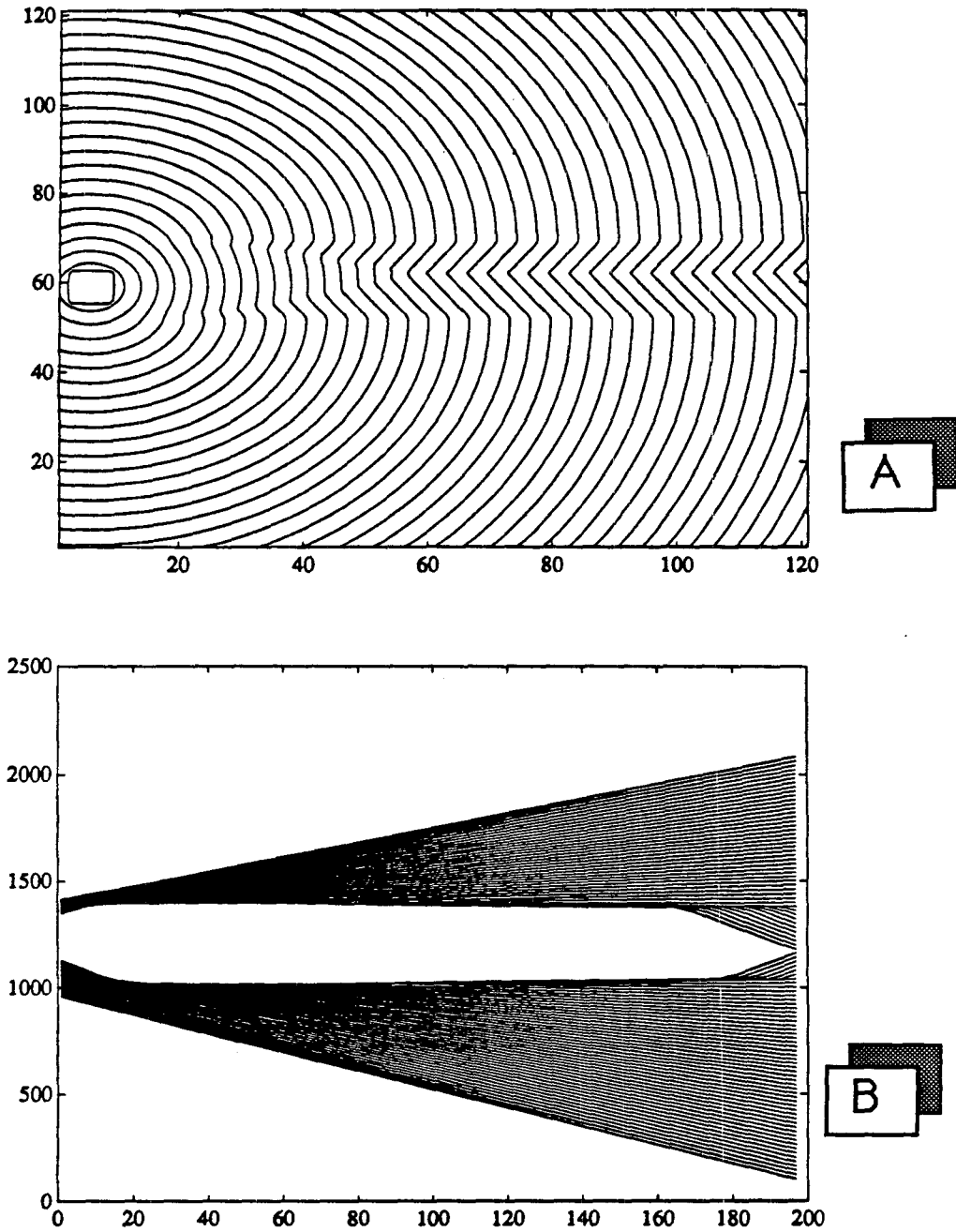
Figure 6.4: Travel time computations in an isotropic layered medium. A) Travel time map computed at each node of the grid. The source is located in the central low velocity layer. B) Raytracing using the travel time distribution displayed in figure 6.4 a.

Other approximate formulas like the one provided by Thomsen (1986) and Banik (1987) can easily be used to substantially reduce the amount of computation required to estimate the velocities.

6.3.2 The results

The results of these computations are presented in figure 6.5 for an anisotropic homogeneous medium with 12 % compressional velocity anisotropy. Figure 6.5a, shows that the error between the numerical and analytical solution is fairly high (2 %), and in any case much higher than the errors computed in the isotropic case.

Such a large error is related to the computation of θ which involves the difference of the travel times between two neighboring grid points and is thus equivalent to a differentiation. As pointed out in section 6.2, F.D.R.T. computes a C^0 travel time distribution, and the continuous computation of the propagation angles requires a C^1 distribution.

Nevertheless the error introduced by the anisotropic computation is less significant than that which would be introduced if anisotropy were neglected altogether, as figure 6.5b shows. The corollary is that if F.D.R.T. technique is used to estimate anisotropy, the error on the anisotropy percentage, or velocity ratios, would be approximately 10 %.

6.4 Extension of F.D.R.T. to viscoelastic materials

For the same reason, the results of F.D.R.T. for an anisotropic medium were not excellent, amplitude computations using F.D.R.T. yield between 10 and 25 % error. Two methods were tested, one using the energy flux conservation equation, the other using Vidale's results (1989). Both methods use the second order spatial derivative

ANALYTICAL - NUMERICAL

ERROR
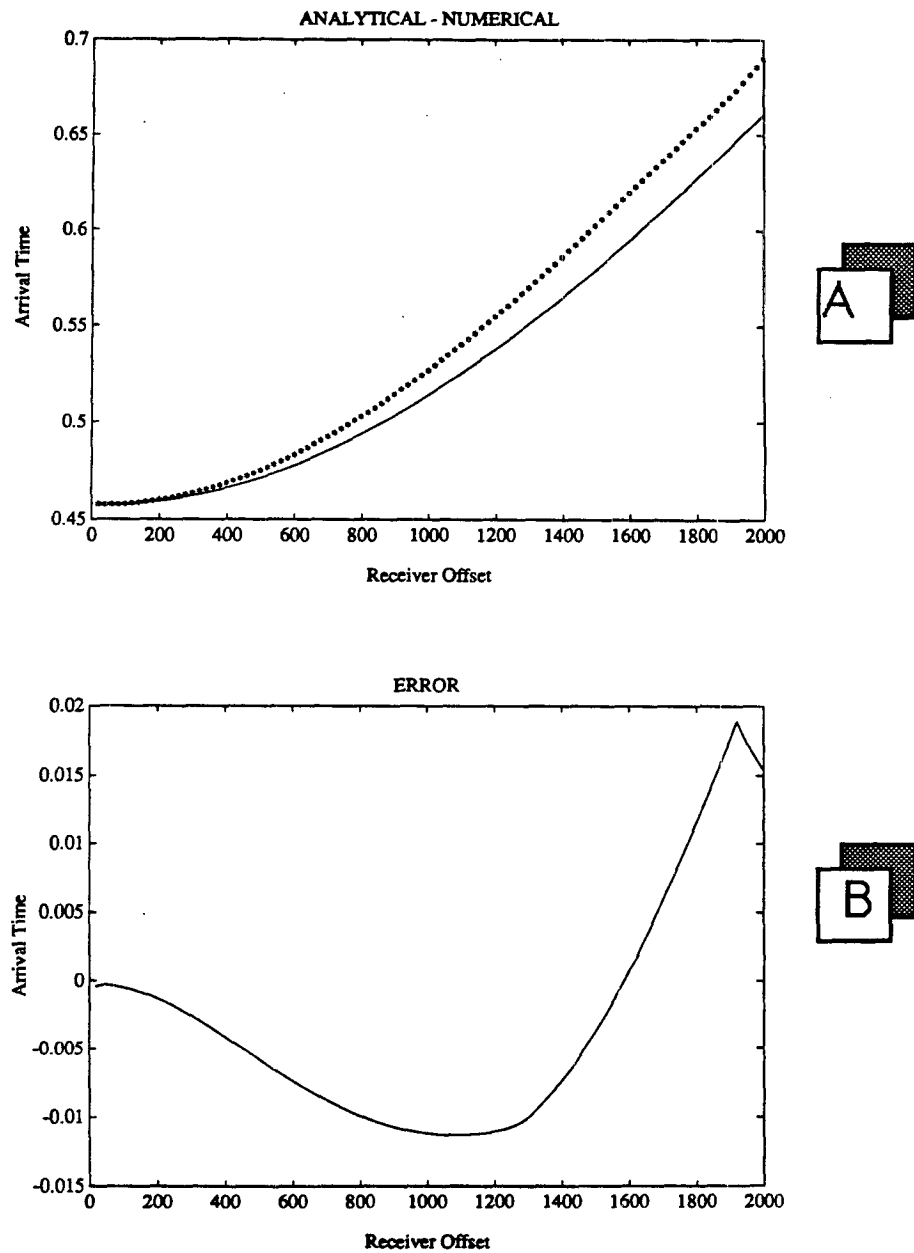
Figure 6.5: Travel time computations in an anisotropic homogeneous solid. A) The travel time difference between the F.D.R.T. computation and the analytical solution. B) The travel time curves obtained for the equivalent isotropic case (solid line) and the anisotropic case (* line).

of the travel time distribution, which is not continuous, thereby yielding a poor result for amplitude estimation.

Nevertheless, if signal signature, rather than signal true amplitude is a major concern, (which is the case for most inversion techniques), the effects of attenuation and dissipation on the initial wavelet radiated by the source can be computed with very high accuracy.

6.4.1 The method

The method is based on a first order perturbation of equation 6.1 where the slowness is a function of the signal frequency. At each node of the grid, the travel time is computed at the reference frequency (ω_0) and travel time difference ($\Delta t(\omega)$) is computed for various frequency samples in the frequency domain spanned by the source. The velocity at a given frequency for a constant Q model is provided by Aki and Richards (1976):

$$v(\omega) = v(\omega_0) \times \left[1 + \frac{1}{\pi Q} ln \left(\frac{\omega}{2\pi} \right) \right] \tag{6.8}$$

Then expanding equation 6.3 , as a function of $\Delta v(\omega)$ and the travel time difference introduced by dispersion (Δt_0, Δt_1, Δt_2), I find that:

$$\Delta t_3 = \Delta t_0 - \frac{1}{t_p} \left[\frac{2h^2}{v(\omega_0)^2} \frac{1}{\pi Q} \left(ln \frac{\omega}{2\pi} \right) + (\Delta t_1 - \Delta t_2)(t_1 - t_2) \right] \tag{6.9}$$

A similar type of equation can be written for amplitude attenuation for a given frequency (after Aki and Richards 1976) as follows:

$$a_3(\omega) = a_0(\omega) \times exp \left[-\frac{\omega l}{2c\omega Q} \right] \tag{6.10}$$

where l is the ray path length from point 0 to 3. Thus, the attenuation of the signal for a given frequency is accounted for at each grid point. The previous equations

are only valid under the assumption that all the "rays" travel along the same ray path independently of frequency. That, in turn, implies that the effects of frequency dependent scattering are neglected in this computation.

Finally, if the source time history can be written as $s(t)$, or $s(\omega)$ in the frequency domain, the history at the receivers can be reconstructed under the previous assumptions as:

$$r(\omega) = a(\omega) \times exp(i\omega t(\omega)) \qquad (6.11)$$

or after Fourier transform in the time domain as:

$$r(t) = \frac{1}{2\pi} \int a(\omega) \times exp(i\omega t(\omega)) dt \qquad (6.12)$$

therefore computing the effects of both attenuation and dispersion on the received signal.

6.4.2 The results

As illustrated in figure 6.7, this approximate computation of F.D.R.T. to model a viscoelastic medium provides accurate results. Both the effect of attenuation at high frequency, and the phase effects associated with dispersion are clearly visible when comparing figure 6.7a to figure 6.7b

6.5 Conclusions

The CPU time it takes to compute the travel times for the three cases discussed in this paper are summarized in Table 6.2. F.D.R.T. provides an extremely fast means of computing accurate travel times in a variety of medium and can therefore be applied to numerous new tasks. Chapter 7 illustrates the use of this algorithm for both cross well data interpretation purposes and non linear inversion of cross well data.
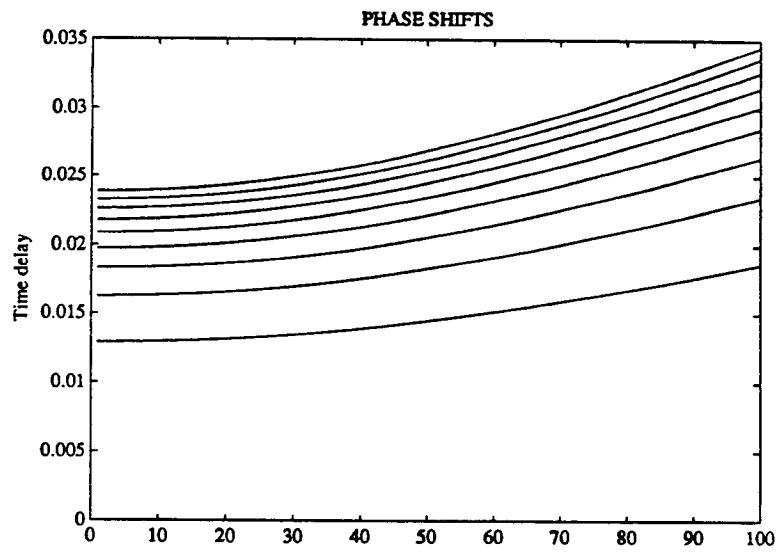
Figure 6.6: Travel time differences introduced by dispersion. Each curve is the travel time modification $\Delta t(\omega)$ introduced as a function of frequency for $Q = 100$.
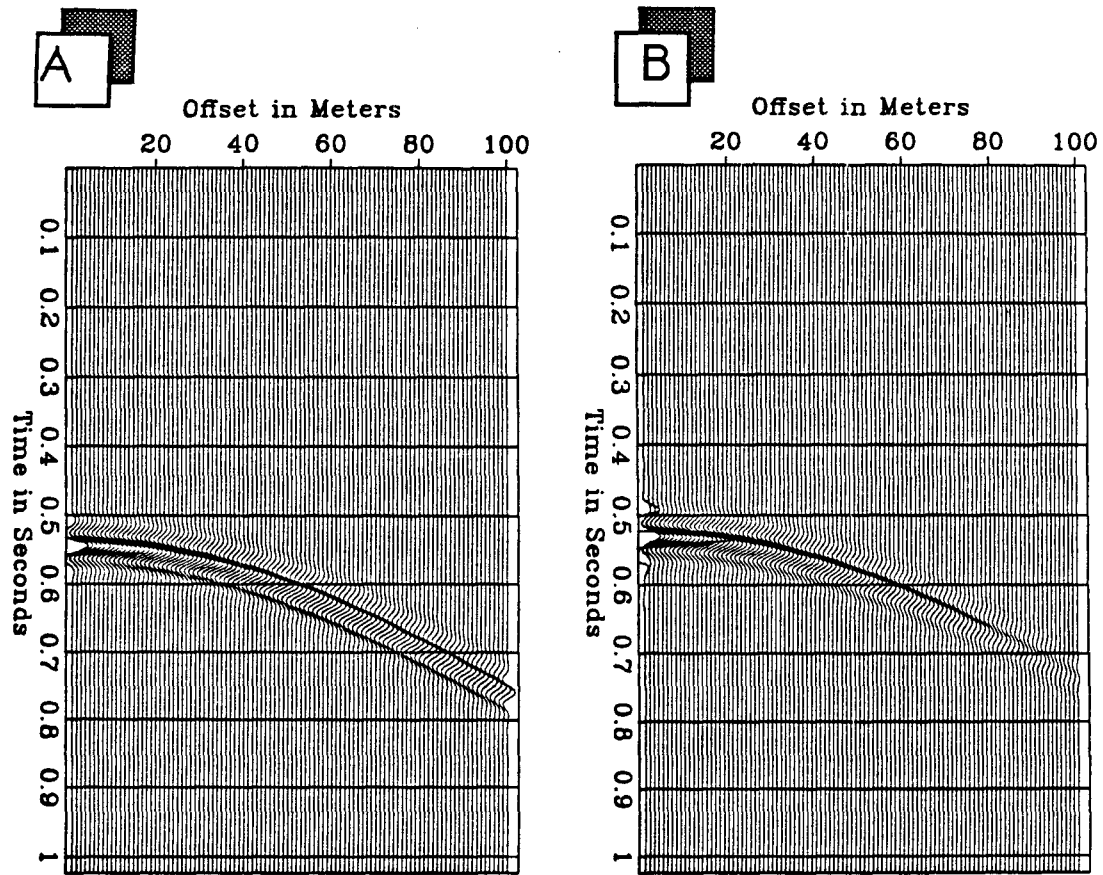
Figure 6.7: The receiver traces computed for A) $Q = 100$, B) $Q = 20$. The effects of both amplitude attenuation and dispersion (phase advance) are clearly visible on these shot gathers.

Medium:	Elastic Isotropic	Elastic anisotropic	viscoelastic
CPU time	0.3*sec*	4.6*sec*	9.1*secs*

Table 6.2: CPU time for the computations of the travel times on a 256×256 grid for the case listed in the first row.

References.

Aki, K., and Richards, P., G., 1980, Quantitative seismology: W. H. Freeman and Co.

Van Trier J., 1989, Finite-difference computation of travel times: Stanford Exploration project report, **57**, .

Vidale J., 1989, Finite-difference computation of travel times: Bulletin of the Seismological Society of America, **78**, 2062-2076.

Chapter 7

A Methodology for Cross-well Data Interpretation

Abstract

Cross-well seismic data is acquired to provide an enhanced interpretation of geo-
logical features, and to monitor EOR processes. Three specific tools were developed
to aid the interpretation of such data within its natural geological setting.

- A distributed software that handles both the data and the data flow required
  for such interpretation. The data for this study comprises 1) well logs, 2) tomo-
  graphic reconstructions of the inter-well regions, and 3) the cross-well seismic
  data itself.

- A parametrization of the earth model, in terms of both interfaces and layer
  textures that allows a thorough description of the region at any given scale.

- An automated least-square based inversion process that aids the process of
  designing the earth model in the inter-well region.

Using these capabilities, wave equation modeling as well as ray-traced modeling
was performed using an interpreted model of the inter-well region. Both modeling
methods provided a satisfactory match with the elementary attributes the actual

cross-well seismic data.

7.1 Introduction

Cross-well seismic data can be viewed as a reservoir development tool whereby the data already known about the field is enhanced through the interpretation of high frequency seismic data. The expected result of such a study is an <u>interpreted</u> and <u>integrated</u> view or image of the earth's underground. The interpretation methodology proposed in this chapter has three goals: to make use of the prior data, to define a model parametrization that will allow both classical interpretation and geophysical interpretation, and to use wave equation modeling or ray-traced modeling to tie the model designed with the actual cross-well data.

This chapter presents both the proposed methodology, and an elementary application in which the data acquired by Harris et al. (1990) is interpreted in three steps.

- First, most of the data available for the field is described. This includes a complete suite of well logs and the cross-well seismic survey, as well as the tomographic reconstructions J. Harris (1990) obtained.

- Second, an earth model is built consistently with both the log data and the tomographic data. To define this model, a geological-geophysical model parametrization is introduced that supports both interface and layer parametrizations.

- Finally after investigating an automated algorithm to reconcile the earth model with the first arrival picks of the seismic data, our model is modified to match the actual travel-time picks of the seismic data, thereby delivering an extremely simple model consistent with most of the data implemented.

7.2 Description of the data

The target of the investigation is a normal fault within the Miocene sand/shale sequence onshore in Southeast Texas. This fault was deduced from the type logs (Harris 1990), but its position was never clearly outlined.

7.2.1 The well logs

The log suite is presented in figures 7.1 and 7.2. The gamma ray and compressional velocity logs are fairly poor indicators of lithographic boundaries within this sand/shale environment. Instead, lithographic changes are perfectly recorded by the spontaneous potential and conductivity logs. These are used for this preliminary study.

On the basis of the spontaneous potential and conductivity logs, marker sand beds can easily be identified. Those annotated as $m5$ and $m10$ in figures 7.1 and 7.2 are very good examples. Both sand beds, however, have very saddle signatures in the gamma ray log, with a lower gamma ray amplitude and lower compressional velocity. Finally, the sand bed markers are also clearly visible on the density log (Harris et al. 1990). Based on the previous analysis, the sand bed annotated $m9$ in figure 7.1 is not present in figure 7.2, which indicates that this bed terminates in the inter-well region. On the basis of the field geology, and the known tectonics in this region, it is reasonable to assume that this bed is truncated by a fault. A further indication is that the stratigraphic sequence resumes normally with the $m5$ sand body. Identifying this bed truncation was one of the motivations for the acquisition of the cross-well seismic data, and is the subject of the remaining part of this chapter.

Lastly, the well deviations were measured. The deviation logs are used to estimate an optimum plane that minimizes the distance from the wells to the plane using the least-square criterion. Figure 7.3 shows the projections of the two wells considered

on this optimum plane. This plane is used in the future both for interpretation and modeling purposes because it minimizes the effects of out-of-plane wave propagation inherent in this study.

The general experiment layout shown in figure 7.3 displays both log suites and illustrates the bases of our interpretation by displaying the interpreted fault.

7.2.2 The cross-well seismic data

An example of cross-well data is displayed in figure 7.4. The data was acquired using a piezoelectric bender source constructed by Honeywell Marine Systems containing two piezoelectric bars. The source was swept from 400 to $1600Hz$ with a nominal resonant frequency of $800Hz$. The data displayed in Fig 7.4 was obtained after correlation of the received signal with the initial electrical signal (Harris, 1990).

The primary arrival is interpreted as a combination of compressional body waves, head waves, and critically refracted waves (see section 7.4). Receiver-well borehole-guided waves are clearly visible emerging mainly from the central part of the common shot gather. They are easily recognizable because of their linear moveout. In the center part of the shot gather where the travel path is minimum, the signal maximum frequency component is approximately $1000Hz$ but degrades fairly quickly with larger offsets to frequencies as low as 400 to $500Hz$. The phase of the first arrival signal seems to be fairly unstable which makes first break picking sometimes difficult without further information. The dominant causes for phase instabilities are:

- the fact that the source remains of constant length, and is swept from 400 to $1600Hz$. The sweep runs from below the source first harmonic, to the second harmonic thereby yielding a frequency dependent radiation pattern. For the first harmonic, the compressional waves are maximum along the horizontal and decay with increasing receiver offset. For the second harmonic, the compressional waves are maximum at 45^0 from the horizontal and null along the horizontal.
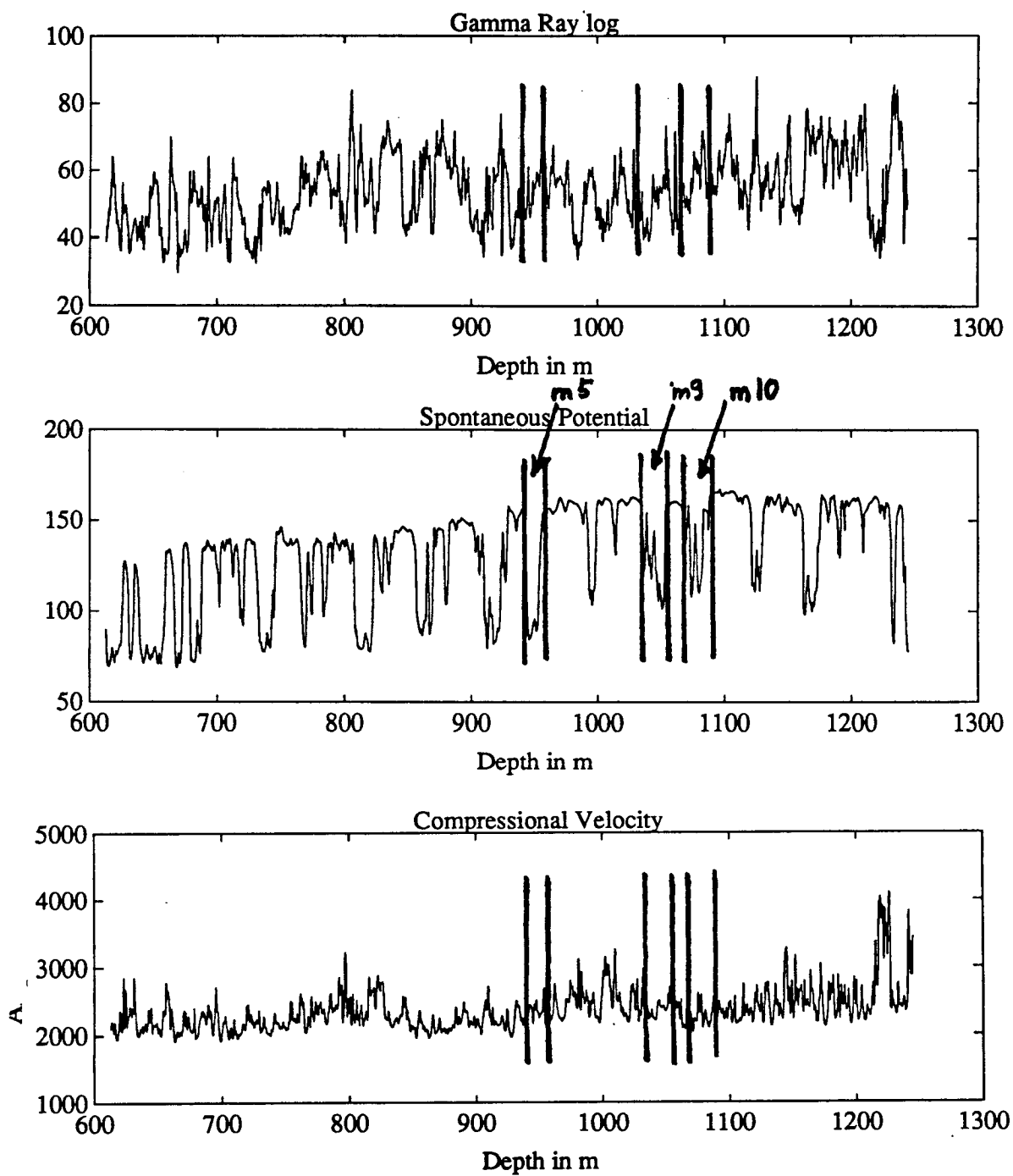
Figure 7.1: The well log suite from the 8106 well. From top to bottom: gamma-ray log, spontaneous potential log, compressional velocity log.
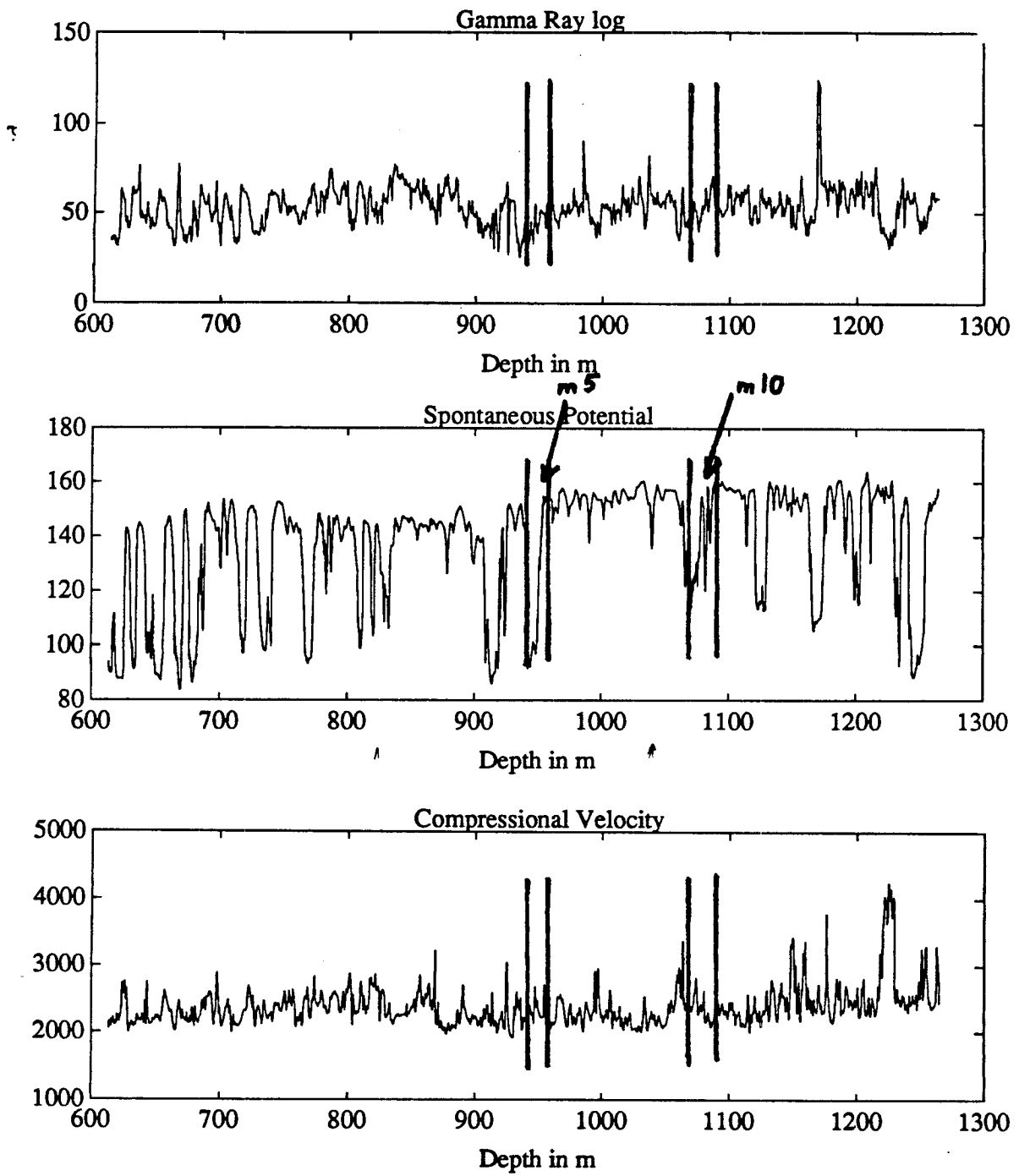
Figure 7.2: The well log suite from the 8135 well. From top to bottom: gamma-ray log, spontaneous potential log, compressional velocity log.

- because the source changes regime while sweeping, the overall electric impedance of the source changes, thereby introducing a new uncertainty: the source's electrical signal may not correspond to the mechanical output of the source. Because the electronic sweep was used for correlation, this approximation may introduce new phase variations along a single arrival.

- finally, because the receivers remain fixed for multiple source positions, the repeatability of the source radiation pattern in the borehole environment might be questionable. As Chapter 3 explains, the downhole source radiation pattern is extremely sensitive to the coupling with the borehole, and there is little guarantee that this coupling remains constant from one source location to another.

Based on the picks obtained with this data, I estimate that the first arrival picks are accurate with an average error of $4/10ms$, which corresponds to approximately half a cycle, on average, over the data.

Finally even though they are predicted by the modeling, shear waves are not seen in this data for two reasons:

- First, as Chapter 3 explains, shear waves' amplitude is maximum at 45^0 from the horizontal for the first harmonic of the source, and maximum along the horizontal for the second harmonic. Assuming that the second harmonic is attenuated along the ray path, the first harmonic shear waves' amplitude at 45^0 are subject to higher attenuation because of the smaller spatial frequency of the signal and because of the longer ray path at 45^0 than along the horizontal.

- Second, even though the conversion mechanism at the receiving borehole from elastic shear waves to borehole fluid pressure is not very well known, it is reasonable to assume that the conversion efficiency is lower for shear waves than for compressional waves (White, 1973).

Since the signal-to-noise ratio for compressional waves at 45° from the source already renders picking fairly difficult, it is reasonable to believe that most of the shear waves' amplitudes are not measured in this experiment because they are smaller than the noise amplitude.

7.2.3 The tomographic images

Two different compressional velocity tomographic images were interpretated. Even though they were not obtained using the same travel time picks and the same ray-tracing algorithm, both were computed using the string inversion algorithm proposed by Harris, et al. (1990).

The first image displayed in figure 7.5 (Lazaratos, 1990) shows numerous artifacts associated with ray paths, but the actual compressional velocities extracted from that image match well the compressional velocities obtained from the well logs especially for the low velocity sand beds. The second image (Harris et al., 1990) is displayed in figure 7.6. It does not show artifacts associated with ray paths, but provides a smoother image of the velocities. Furthermore, the velocities extracted from the latter image are 10 to 17% higher than those computed on the basis of the well logs. For both images, however, the tomographic estimation of velocities is always greater than the sonic velocity. One of the main reason that can be invoked to justify such a result is the existence of rock anisotropy, since tomography in our context essentially measures horizontal velocities, and the sonic log velocity measures a vertical velocity. Computing higher velocities along the horizontal is therefore consistent with the anisotropy hypothesis (Thomsen 1986). However, the anisotropy hypothesis is not completely justified for two reasons:

- First, even though the ray trajectories are computed in a plane, the path computation minimizes the actual path, therefore yielding a lower estimate of velocities.
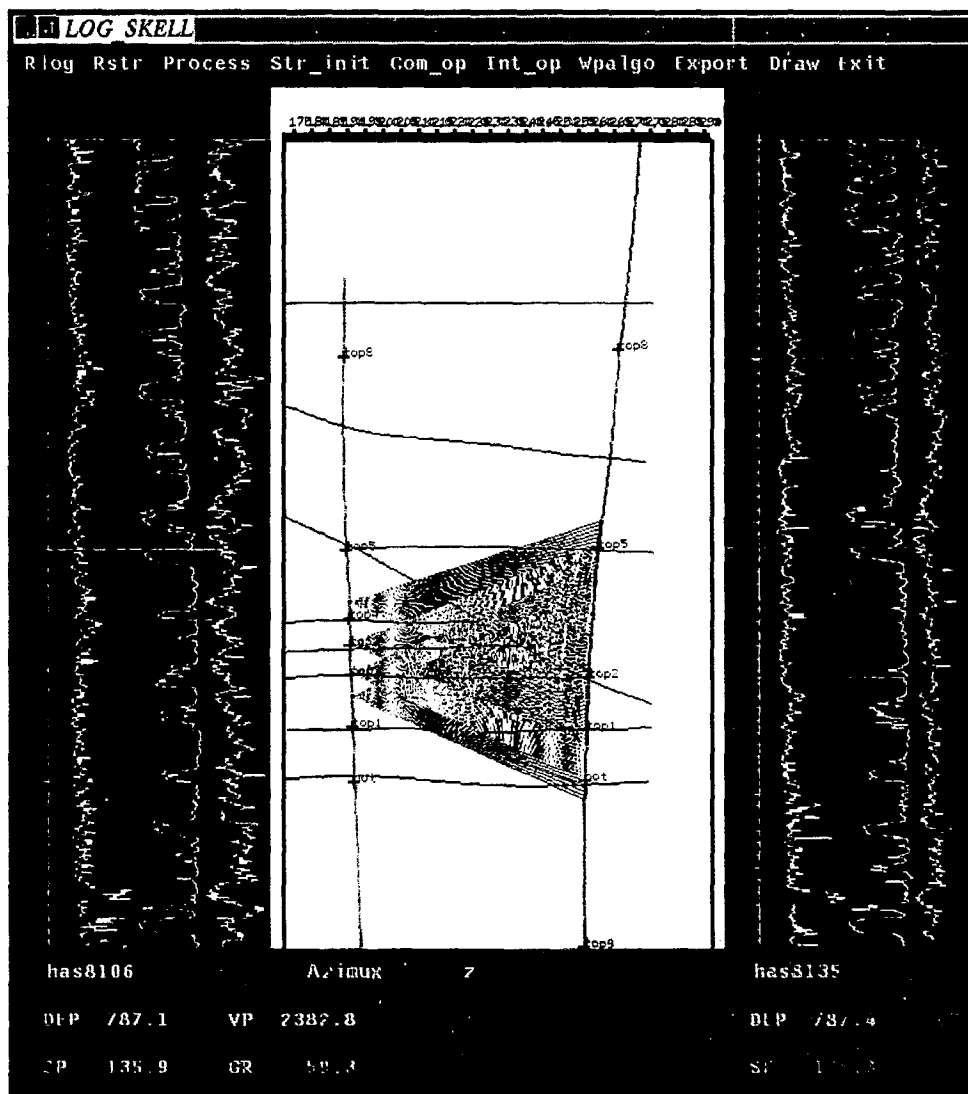
Figure 7.3: General experimental layout for cross-well seismic interpretation. The left panel displays the logs for well 8106, the right panel for well 8135. The central panel represents the well projection in the work plane (Brown lines), the two-dimensional location of the well picks, and the interpreted structure. From top to bottom shot 79, 97,117,125 are displayed.

- Second, the amount of anisotropy computed in each images differs significantly.

This last observation suggests another justification for estimating high velocities using the cross well method: the amount of anisotropy computed is a bias of the smoothing algorithm used to enhance the tomographic image as well as an artifact of the algorithm used for ray tracing. This hypothesis is investigated in the last section of this chapter.

7.3 The model parametrization

The parametrization of the interpreted model is a key ingredient in the implementation of the modeling and inversion techniques to obtain a satisfactory match between the modeled data and the cross-well seismic data. This parametrization requires both that high frequency features of our model such as interfaces be preserved, and that low frequency features such as lateral velocities variations also be preserved. Above all, the model must rely on a very small number of user controllable parameters, and must allow for the rapid implementation of prior information such as that contained in the log data.

In addition, the model parametrization must include most of the functionality of classical geological modeling, and yet preserve the capability of converting our model to a voxel-based image independently of resolution. To achieve this goal two types of parametrization were introduced: the interface parametrization, and the layers parametrization.

7.3.1 The interface parametrization

The interface parametrization is based on a classical pick and interpolate algorithm where the interpolation is performed using bicubic splines (Foley 1990). Even though this type of algorithm is not applicable to all types of interfaces, and is not overall
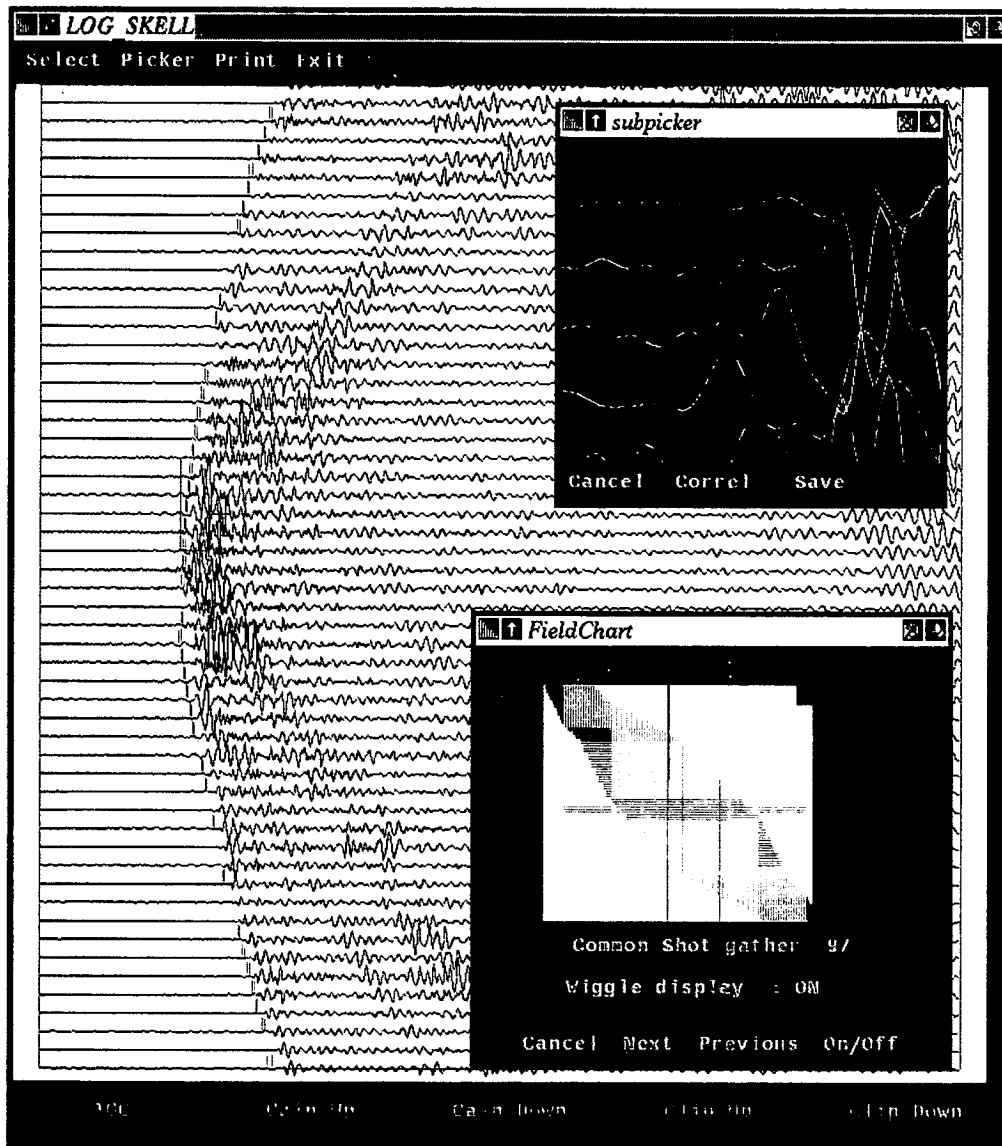
Figure 7.4: Shot gather 97: The upper right box expands the signal in the
outline box directly on the data display. The lower right box displays
the data stacking chart as well as the location of the gather currently
displayed. The red tick marks on the data are for both the computed
travel times and the manual picks. The absence of such a mark signifies
that a perfect match between the two data is obtained at the display
scale.
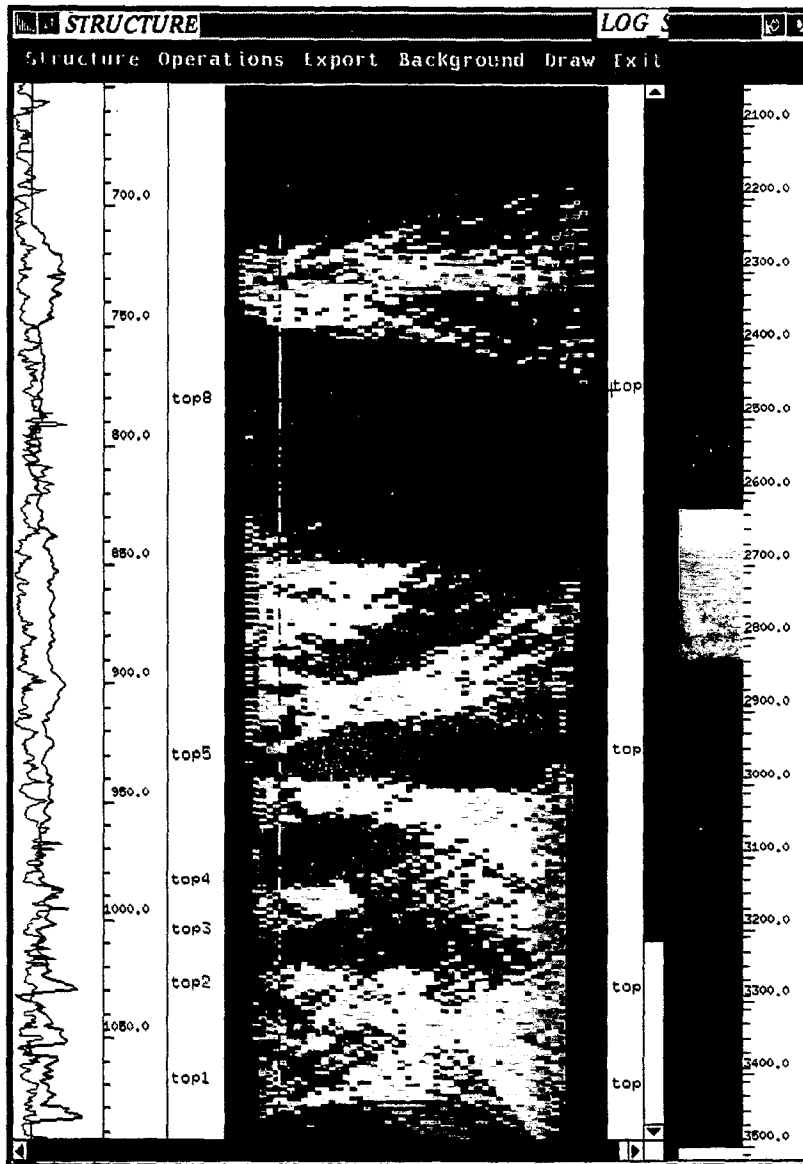
Figure 7.5: Tomographic image reconstruction in the inter-well region. The color coding of the velocities is given on the right scale. On the left is a comparison between the compressional velocity directly extracted from the image (black) and the compressional velocity from the sonic measurements at the well. Spyros Lazaratos (1990) provided the tomographic image.
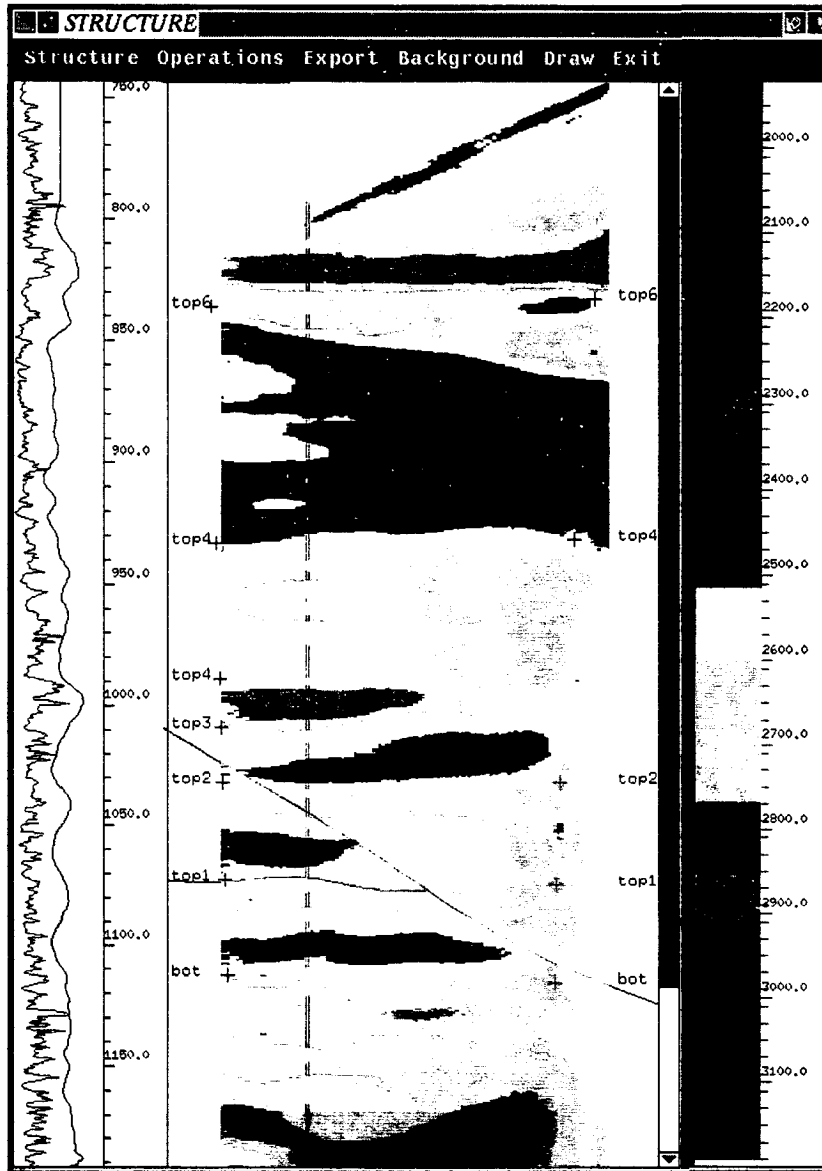
Figure 7.6: Tomographic image reconstruction in the inter-well region. The color coding of the velocities is given on the right scale. On the left is a comparison between the compressional velocity directly extracted from the image (black) and the compressional velocity from the sonic measurements at the well. Reinaldo Michelena (1990) provided the tomographic image.

very efficient compared to a pixel-based algorithm such as those used in classical geological interpretation or seismic picking, it is scale independent.

Of course, the picks' definition is not scale independent because picks are based on a choice of data sets, but the interpolated interface resulting from these picks can be computed at any scale. This flexibility is particularly important when a priori unknow resolution is required when an image is computed from the model definition.

Finally, the interface lines are also used as support domains for a variety of parameters including the upper and lower boundary velocity of the adjacent layers, reflection coefficients, boundary roughness, boundary-induced anisotropy, reflection amplitude. Sampling for each of these parameters is co-located at the pick points and can be interpolated at any point along the interface.

7.3.2 The layer parametrization

The same types of constraints that apply to the interface definition also apply to the layer parameters definition. Namely, the low frequency lateral and vertical variations within the layer must be described using a small number of user-controlled parameters.

To achieve this goal, I use a conformal mapping algorithm, similar to the one described in Chapter 2 for the finite-element method, that transforms a layer into a simple rectangle as illustrated in figure 7.7. The layer is then sampled in the transformed domain with a user-defined set of control points that are the bases for parametrization and interpolation within the layer. Computing the initial transform from the initial layer is not a numerically economical operation, but once the transform is known, the mapping of coordinates from one domain to the other is extremely fast. Computing the velocity distribution at a given point is therefore a simple matter. The real world point location is mapped in the layer transformed domain. Based on the layer parametrization, the point's attributes are computed by simple interpola-

tion in the transformed domain, and replaced directly in the real world domain. The interpolation is, of course, performed very quickly in the transform domain, because the layer sampling is regular in that domain.

7.3.3 An attempt to reconcile geology and geophysics

Based on the definitions of the previous section, any model can be designed to match the geological interpretation of the characteristics of a particular sediment body including: interface boundaries related to an abrupt variation in the depositional environment of the sediments or a change in sediment type, and layer lateral variations related to sedimentary processes or rock diagenesis.

This model can be used to sample the sediment properties at any given point by first finding the parent layer of the point considered, and then interpolating within the layer the sampled physical properties. When the modeled physical properties have to be sampled on a regular grid, which is often the case in geophysics, scanning line algorithms such as those defined by Foley et Al. (1990) are extremely efficient. Furthermore, because of descriptive structure of the model adopted, the sampling can be performed at any given scale.

7.4 Interpretation of the field data

Three major interpretation results are detailed in this last section. After defining an initial model consistent with the well log data, modeling is performed to understand the wave phenomena involved in the cross-well data and understand the history of the first arrival picked for the tomographic inversion. Finally, a simple least-square based inversion algorithm is tested on synthetic data. This inversion enhances the accuracy of our model as the final modeling results are compared to the seismic data.
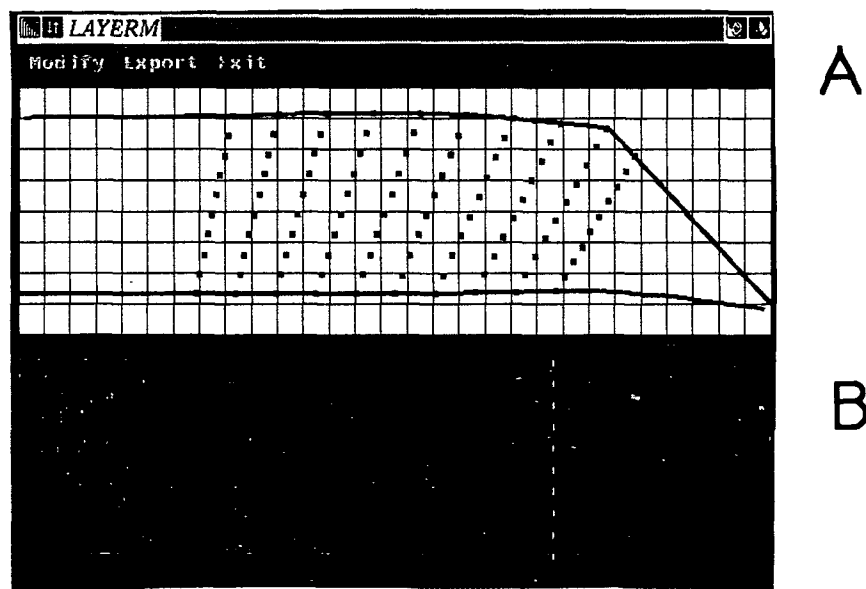
Figure 7.7:A schematic diagram of the layer parametrization. A) Real world coordinate system layer representation, B) Transformed coordinate system layer representation.

7.4.1 Ray-tracing and full-waveform modeling

Figure 7.8 displays a possible interpreted model as well as the ray coverage obtained with that model using the finite-difference ray-tracing algorithm described in Chapter 6. The ray coverage for the computed first arrivals is extremely heterogeneous and indicates that more than 80% of the rays lie within less than 2% of the image surface. As pointed out in Chapter 6, finite-difference ray-tracing computes the shortest path connecting the source to the receiver. For most of the cross-well geometry in a layered medium, these ray paths correspond to critically refracted compressional waves, also called head waves.

These head waves build up the essential part of the first arrival, as confirmed by the full-waveform finite-difference modeling. In figures 7.9, and 7.10, the arrival times computed by finite-difference ray-tracing are overlaid on the computed receiver traces. Even though the head waves are not isolated as such because of the small layer thickness, and the small velocity contrast, it is very clear that the first arrival along the horizontal direction is more complex than a single compressional wave arrival. The tie between the computed travel-times, and the actual first break of the signal clearly demonstrates that first break picks actually pick head waves along the horizontal direction and compressional waves at larger offsets.

This interpretation is one of the most consistent explanations for the discrepancy described between well logs' compressional velocities, and the velocities extracted from the tomographic images. The most attractive hypothesis investigated so far is that the rock between the two wells is anisotropic. But, anisotropy is a scale dependent property for layered media, and for the sake of clarity two types of anisotropy are distinguished:

- long wavelength anisotropy corresponds to the case where the seismic wavelength of the signal probing the material is much larger than the characteristic distance separating the layers. In this case, multiple rock models (Backus,

1962) allow the computation of an equivalent long wavelength anisotropy tensor based on the constitutive properties of the materials involved. Long wavelength anisotropy is implied in our first interpretation of the discrepancy between cross-well and log velocities.

- short wavelength anisotropy corresponds to the case where the seismic wavelength is shorter than the size of the layered heterogeneities. In this case the dominant propagation mechanism operates through head waves and layer guided waves.

Head waves are the propagation mechanism by which the first arrival is created for a wave propagating parallel to the plane of symmetry of the layered medium in a low velocity layer. Therefore velocities estimated with the short wavelength anisotropy model are the upper bound of any velocity that may be measured in the long wavelength anisotropy model since the head waves propagate essentially with the fastest possible velocity in the medium.

Let now suppose that the ray tracers used for the tomographic reconstruction do not model head waves, but rather pure body waves. In this case the ray-tracer underestimates the travel times, and the back-projection step of the reconstruction thereby overestimate the velocities to yield the correct travel time matches. This mechanism is illustrated in figure 7.5 and 7.6. For sharp velocity contrasts, the ray tracer adequately reacts providing accurate travel times and thereby eliminating the short wavelength anisotropy artifact. As the velocity distribution gets smoother, chances for the ray-tracer to recover the misinterpreted modes lessens, thereby enhancing the short wavelength anisotropy factor. Since model smoothing is inherent to the stability of the string inversion algorithm (Harris et al., 1990), as well as most tomographic algorithms (Dines 1979, McMechan et al. 1987), velocities estimated by this method will always be overestimated in comparison to the well log velocity, even if the rock investigated is only made of purely elastic isotropic layers.
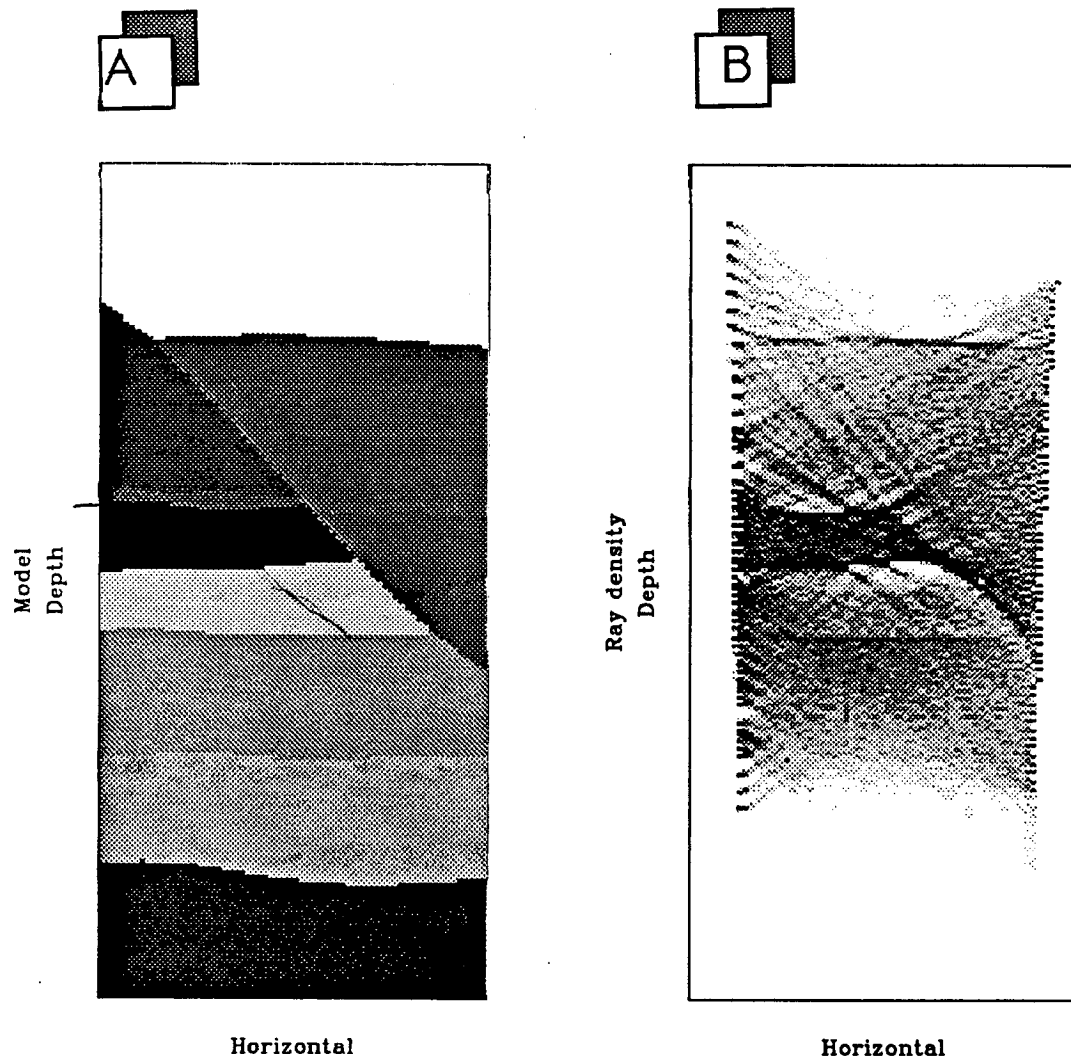
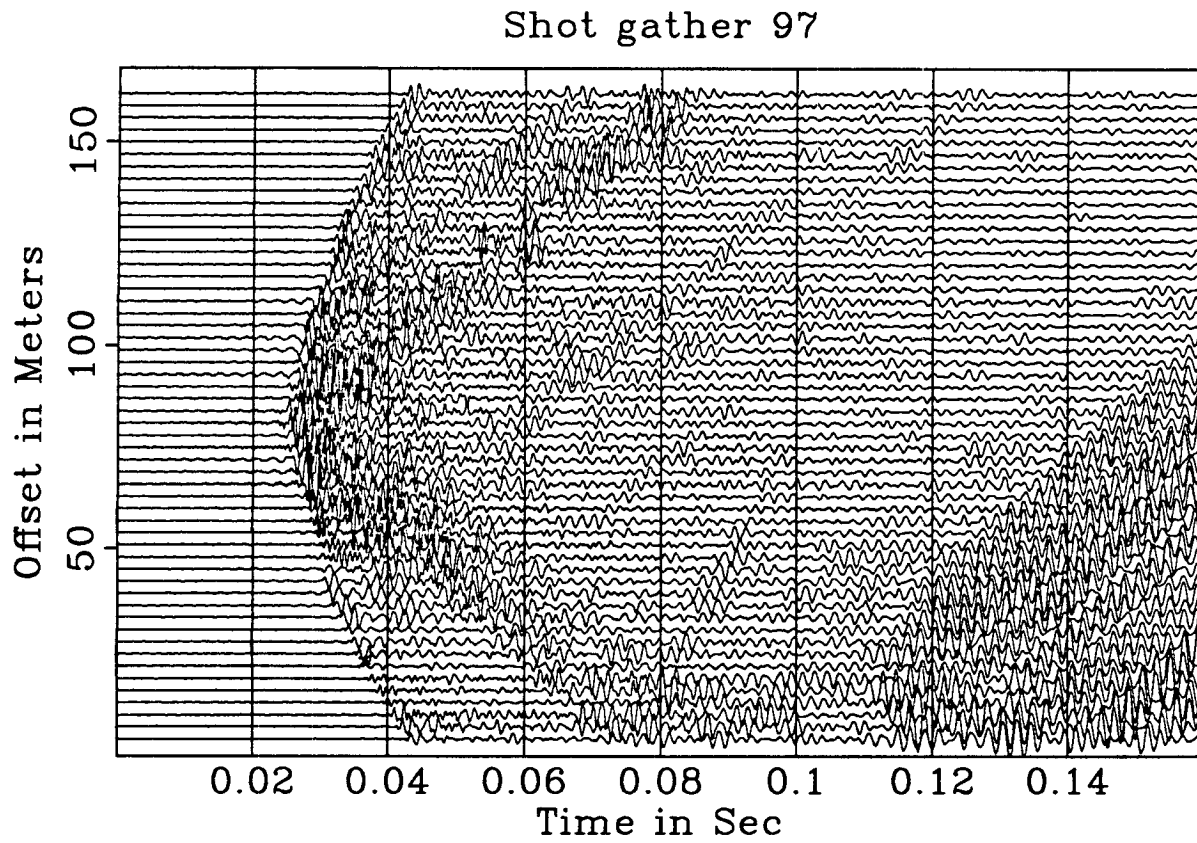**Figure 7.8:** The velocity model and ray coverage image for the cross-well data.

Figure 7.9: Common shot gather 97 from the cross-well data set.
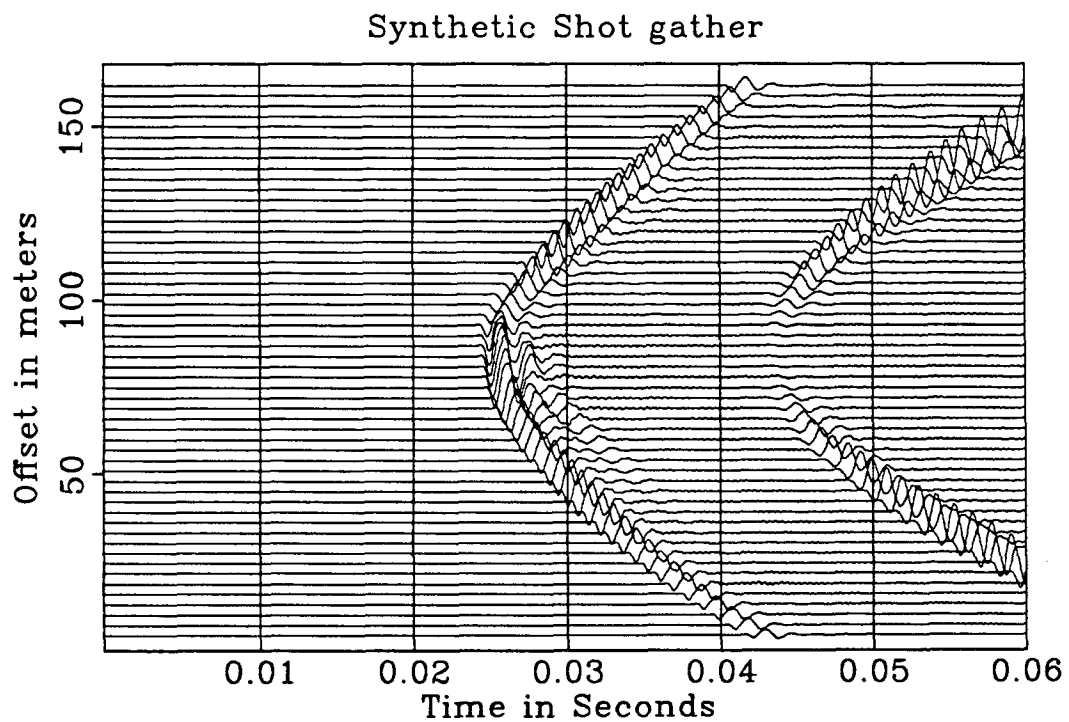
Synthetic Shot gather

Figure 7.10: A synthetic common shot gather obtained using the velocity model shown in figure 7.8.

7.4.2: Travel time inversion using finite-difference raytracing

7.4.2.1: Inversion technique

As figure 7.8 shows, the ray coverage computed with the finite-difference ray-tracing medium is extremely heterogeneous, which makes finite-difference ray-tracing a poor candidate for tomographic reconstruction. This section proposes an alternate inversion method by which the model parametrization described in section 7.3 is used as the basis function for our inversion. A vector $\vec{m}$ of the model space M is defined by:

$$\vec{m} = [m_i] = \left[x_1...x_{np}, y_1...y_{np}, M_{ij}^1...M_{ij}^{nl} \right] \tag{7.1}$$

where x_i is the horizontal coordinate of the ith interface control point, y_i is the vertical coordinate of the ith control point, M_{ij}^k is the ratio of the compressional waves moduli and the density for the ij^{th} control point of the kth layer, np is the number of interface control points, and nl is the number of layers in the model. The data space is the space of the travel time picks where a vector component d_{ij} corresponds to the picked travel time for the ith source location and j^{th} receiver component. The model and data space are related by the functional $\mathcal{F}$:

$$\vec{d} = \mathcal{F}(\vec{m}) \tag{7.2}$$

computed by finite difference ray-tracing.

Given an initial geological model $\vec{m}^0$, consistent with the prior data available, we want this inversion to provide a new model $\vec{m}^n$ that minimizes the difference $\vec{d} - \vec{d}^n$ in the least square sense. In the last expression $\vec{d}^n$ is the travel times computed based on the model $\vec{m}^n$.

One solution to the preceding problem is to use the method proposed by Beydoun (1982) after Tarantola (1982) in which the model is recurrently updated by using the

following relation:

$$\vec{m}^{n+1} - \vec{m}^n = \left[\mathcal{G}^T . \mathcal{W} . \mathcal{G} \right]^{-1} . \mathcal{G} . \mathcal{W} \left(\vec{d} - \vec{d}^n \right) \tag{7.3}$$

which is the familiar weighted least-squares solution to the linear problem:

$$\left(\vec{d} - \vec{d}^n \right) = -\mathcal{G} \left(\vec{m} - \vec{m}^n \right) \tag{7.4}$$

where $\mathcal{G}$ is defined as:

$$\mathcal{G}^T_{jk} = \frac{\partial (\mathcal{F}(m^n))_j}{\partial m_k} \tag{7.5}$$

The last operator is evaluated numerically by perturbing the model $\vec{m}^n$ to $\vec{m}^n + \delta m$ where δm is a user-defined quantity smaller than $\vec{m}^{n+1} - \vec{m}^n$. Then the corresponding perturbation $\delta \vec{d}^n$ is computed, using the finite difference ray tracer. Therefore, for one iteration, the travel times are computed first to infer the updated data vector, then as many times as there are parameters in our model. On the other hand, tomographic inversion as implemented by Harris (1990) only needs to perform one ray tracing for each iteration.

The elements of consistency of our model with the prior data are preserved through the inversion process by using the following mechanism. The components of a model space vector can only occupy one of three different states:

- 1) No constraint is applied to the point.

- 2) The value of a model vector component after an iteration is bounded by an upper and a lower limit.

- 3) The value of the component cannot be updated by the iteration process. Thus, even though it is part of the model space, it is not taken into account by the inversion.

This method allows the enforcement the users' judgement on what data is already constrained versus what data is unknown.

7.4.2.2 Synthetic inversion results and interpretation

Figure 7.11 shows the model used for our inversion test case, as well as the computed ray coverage. The initial travel times were computed by first using full-waveform finite-difference modeling, and then picking the modeled data. The agreement between the picked full-waveform data and the travel-time data computed by finite-difference ray-tracing is good. The average absolute error is lower than $0.05ms$, which is 5 % of the signal main period used in the full waveform modeling. Thirty source points were used each recorded with a receiver array of fifty geophones thereby setting the size of the data space to 1500. The model space is composed of twenty-three interface control points, and eighty moduli control points for the four central layers of our model. None of the previous model points were constrained. It clearly appears from the previous data that our problem is dramatically overdetermined, even though the numbers used to model this experiment are typical of a cross-well data acquisition.

The initial model was perturbed by modifying the interfaces locations, as well as the layer velocity distributions, which were left uniform. Figure 7.12 shows the results after ten iterations of the inversion algorithm described in section 7.4.2. The detailed results of the inversion for the interface control point location are shown in figure 7.13, and in 7.14 for the moduli inversion.

The average travel time error after the inversion is lower than $0.3ms$. As shown in figure 7.13 the inversion for interfaces' location yields an average residual error that is not greater than 18 %. On the contrary, moduli inversion yields a much higher error level as shown in figure 7.14. Furthermore, the artifacts of moduli inversion shown in figure 7.12 show that the highest errors on the moduli are strongly correlated

with zones of poor ray coverage indicated in figure 7.11. These inversion results are consistent with the interpretation of the dominant modes for the primary arrivals along the source axis. Since most of these arrivals are interpreted as head waves, the ray-coverage is very highly focussed along the interfaces, and the velocity model within the layers is not sufficiently probed to provide an adequate reconstruction of the model space in that domain.

Furthermore, the average error on the moduli after ten iterations does not seem to be biased, that is, the mean value of the error does not significantly depart from zero and therefore, the values of the velocity field do not introduce any short wavelength anisotropy. The fact that moduli errors have zero average does not demonstrate that the increased velocity field inferred from the tomographic images is caused by apparent or short wavelength anisotropy, but it certainly provides proof that the inversion proposed here does not introduce such a bias.

7.4.3 A model for the complete data set

The model presented in figure 7.15 was obtained after running the inversion algorithm described in section 7.4 from an interpreted initial model. The initial model was based on a thorough investigation of the type logs as well as on the tomograms described in section 7.2.3. The layer velocities of the initial model were based on the average log velocity in the layer intervals, and the average absolute value of the travel time errors prior to the inversion was lower than $1.1ms$.

The purpose of this investigation is to recover the fault location as well as the average layer velocity within the fault zone. The interfaces are the same as those presented in figure 7.3. and the intersection of the interfaces with the borehole projections was not allowed to be modified through the inversion process. The total number of inversion parameters was fifty-five.
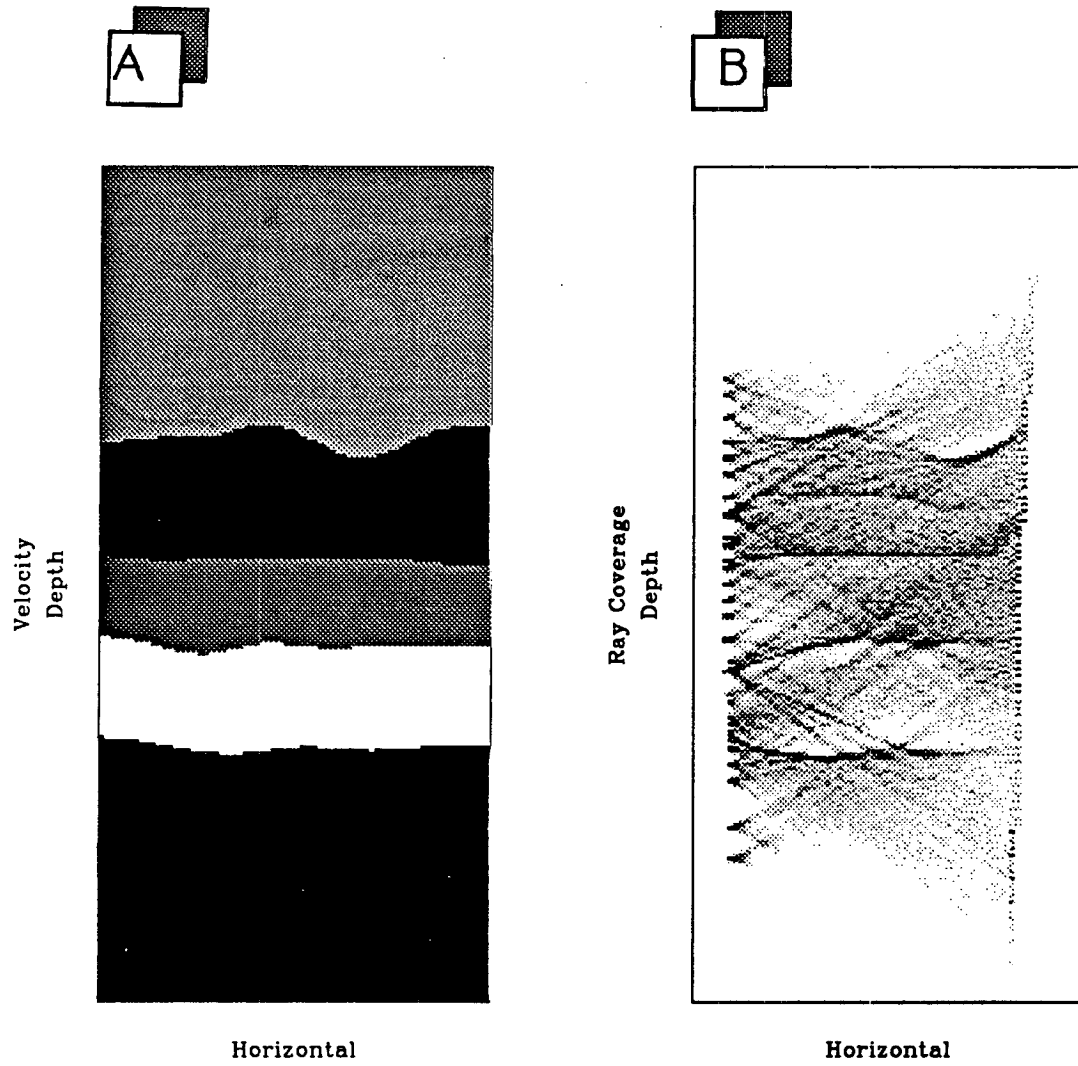
Figure 7.11: Inversion model (a) and ray-coverage image (b).
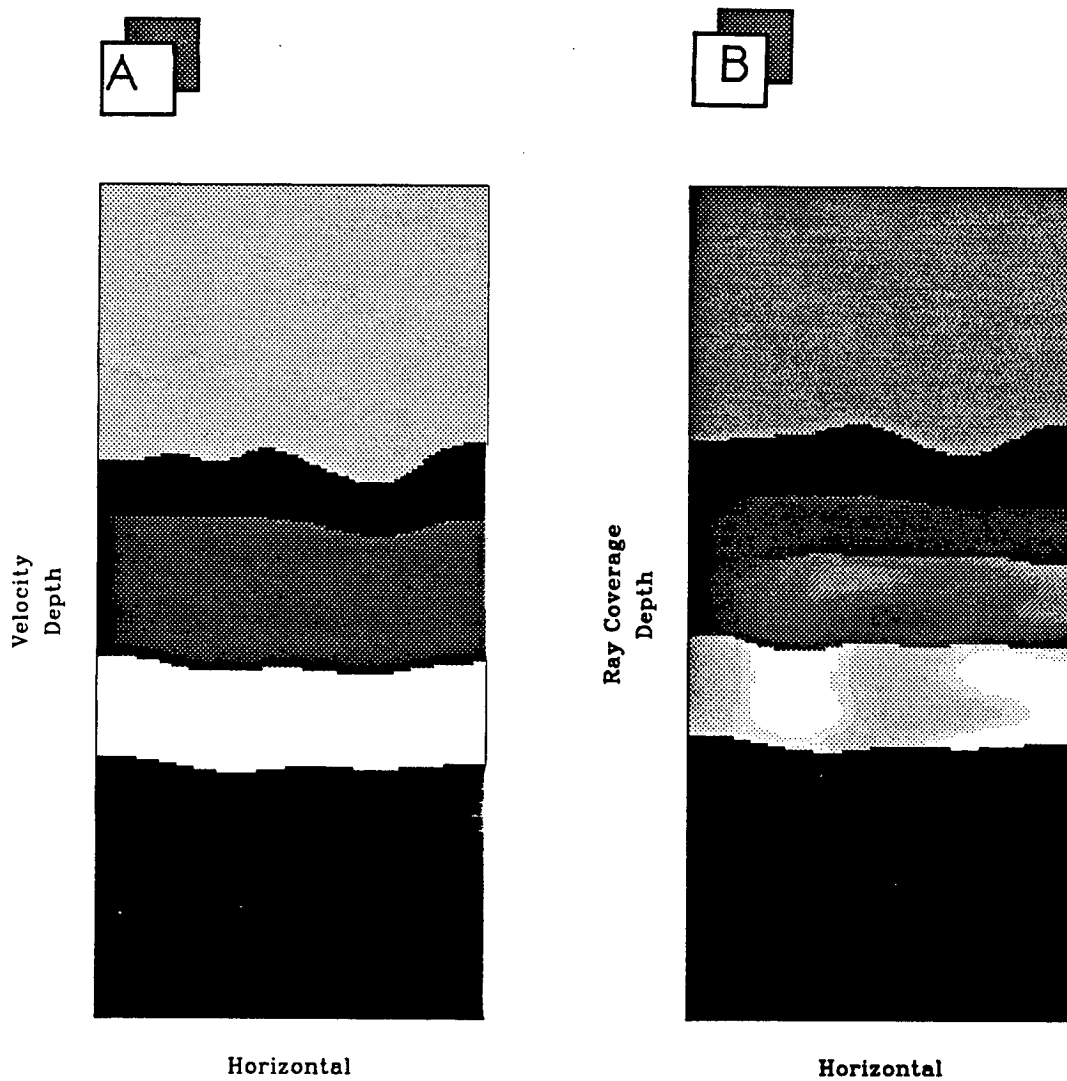
Figure 7.12: Inversion results: a) Initial model, b) Final model after 10 iterations.
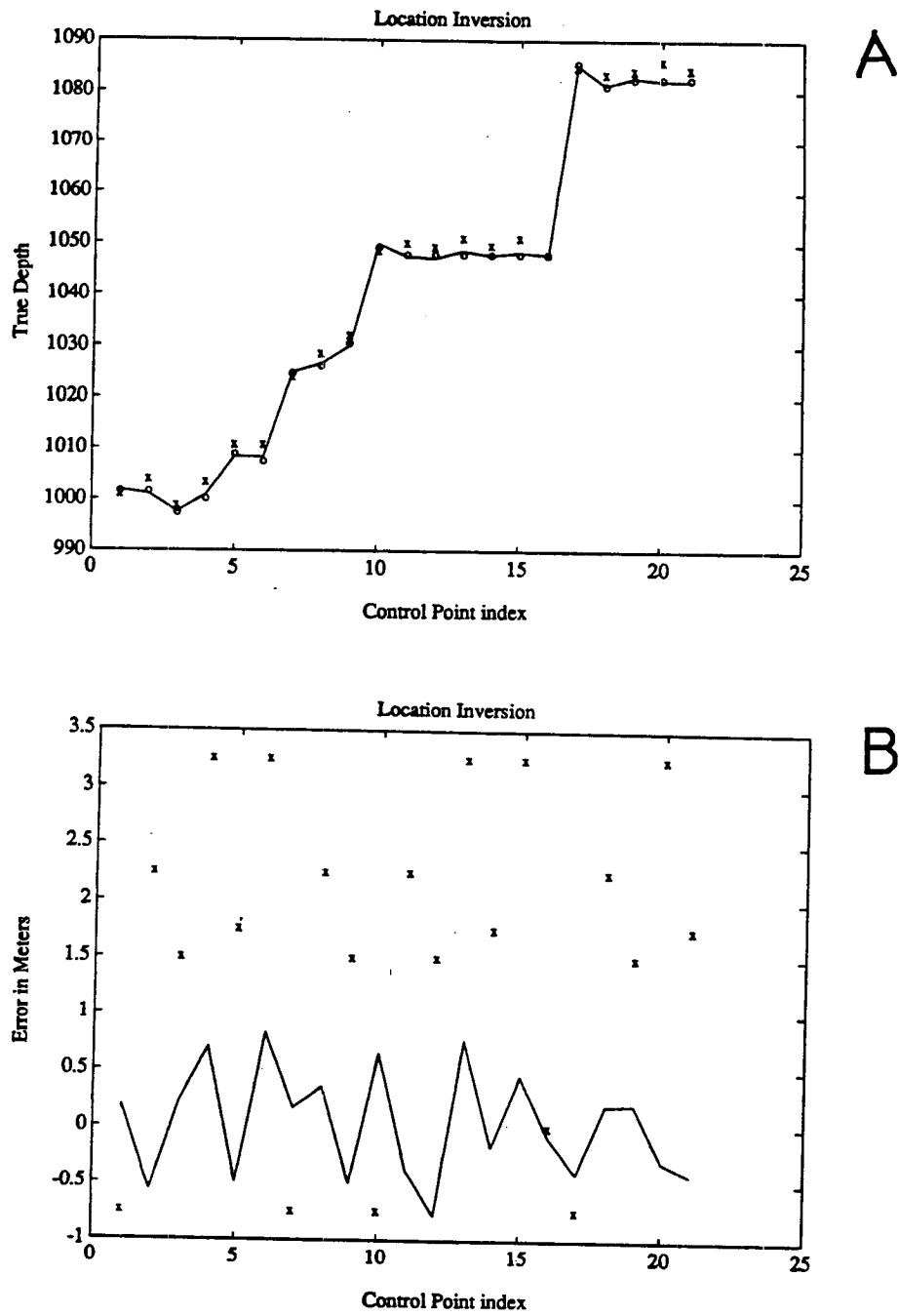
Figure 7.13: Results of the boundary location inversion: a) the x indicates the erroneous initial locations, the o indicates the true model locations and the solid line displays the inversion results. b) the x indicates the initial model location errors, and the solid line shows the final iteration errors.

Figure 7.14: Results of the moduli inversion: a) the x indicates the erroneous initial moduli, the o indicates the true model moduli, and the solid line displays the inversion results. b) the x indicates the initial model moduli errors, and the solid line shows the final iteration errors.

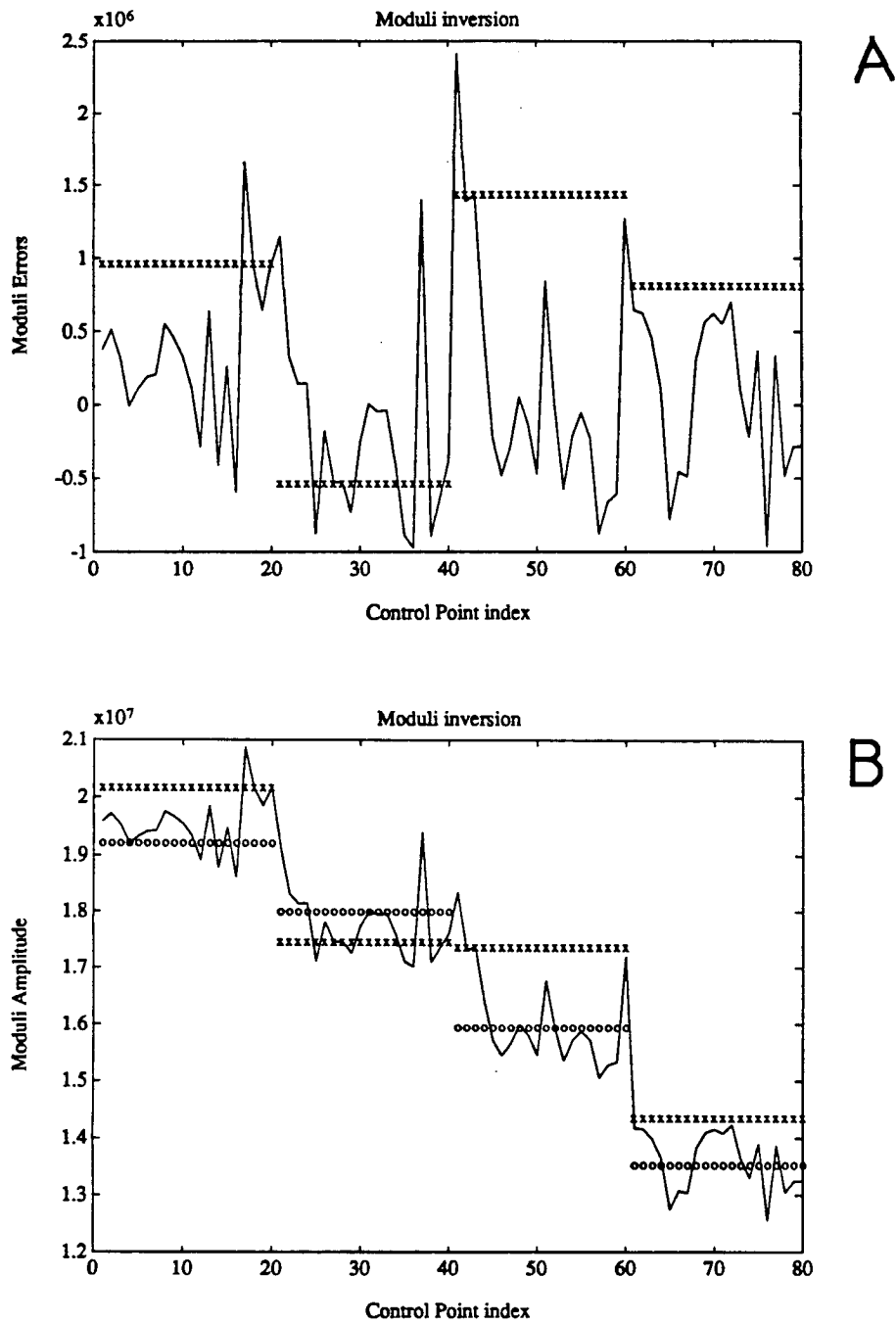Only the shot gathers probing the fault zone were retained for a total of 39 shot gathers and 1487 shot receiver pairs. The average absolute value of the travel time errors after eight iterations was lower than $0.4ms$, and the inversion was stopped at that point since this error is lower than the estimated picking error. The comparison between the computed travel times and the picked travel times is shown for three shot gathers spanning the source array that was selected. As shown in figure 7.16, the main errors come from the central area of the gathers where our model does not perform well owing to the very limited number of layers. Increasing the number of layers would probably have resulted in a more accurate description of the picks in those regions. On the other hand, including lateral velocity variations within the existing layers would not have increased the accuracy of this inversion for the following two reasons:

- These errors would have been eliminated based on rays traveling horizontally from the source to the receivers. Finite-difference ray tracing does not provide ray-coverage in the layer region for rays traveling horizontally as we have seen previously.

- The moduli variations within the layer computed by inversion would have been affected by multiple ray coverage artifacts, as the synthetic example shows. This would have resulted in an overall degradation of the interpreted image, because of which it would be almost impossible to discriminate genuine velocity variations from inversion artifacts.

Finally the average change in layer velocity during the inversion was lower than 3% which implies that our inversion algorithm does not introduce as much apparent anisotropy as is currently introduced by tomographic reconstruction.

This inversion result provides an interpreted image of the fault zone that honors the cross-well data first arrival travel times within the picking error margin. The

tomographic inversion results are compared with the inversion results previously described in figure 7.15. Most of the essential features within the fault zones are well preserved from one image to the other with a fairly regular layering of slow sand beds and slightly faster sand/clay beds. The fault location is consistent with the bed truncation clearly visible in the tomographic image. This last result illustrates that tomographic data inversion is overwhelmingly overdetermined unless the data signal-to-noise ratio allows for a complete study of the full waveform signal. Such a study, however, was neither practical (because of the amount of computer time that would have been required) nor legitimate, since the estimated error in travel time picking is well above the error that would be expected with a $1000Hz$ signal.

7.5 Conclusions

This study illustrates the impact of fast modeling capabilities on the interpretation of seismic data. The use of such modeling capability was crucial to:

- understanding the mechanisms by which the first arrival of the cross-well data is generated along the horizontal direction.

- eliminating the ambiguity raised by the evaluation of seismic waves, anisotropy in a cross-well environment.

moreover, the capability of performing extremely fast travel time modeling using a finite-difference algorithm allowed the implementation of an extremely simple inversion algorithm that assists the manual interpretation of cross-well data.

Above all the extensive use of all the geophysical data available for this study provides a simple and consistent interpretation of a specific structural feature in a fairly undifferentiated sedimentary environment where seismic velocity was not the most sensitive lithographic marker.
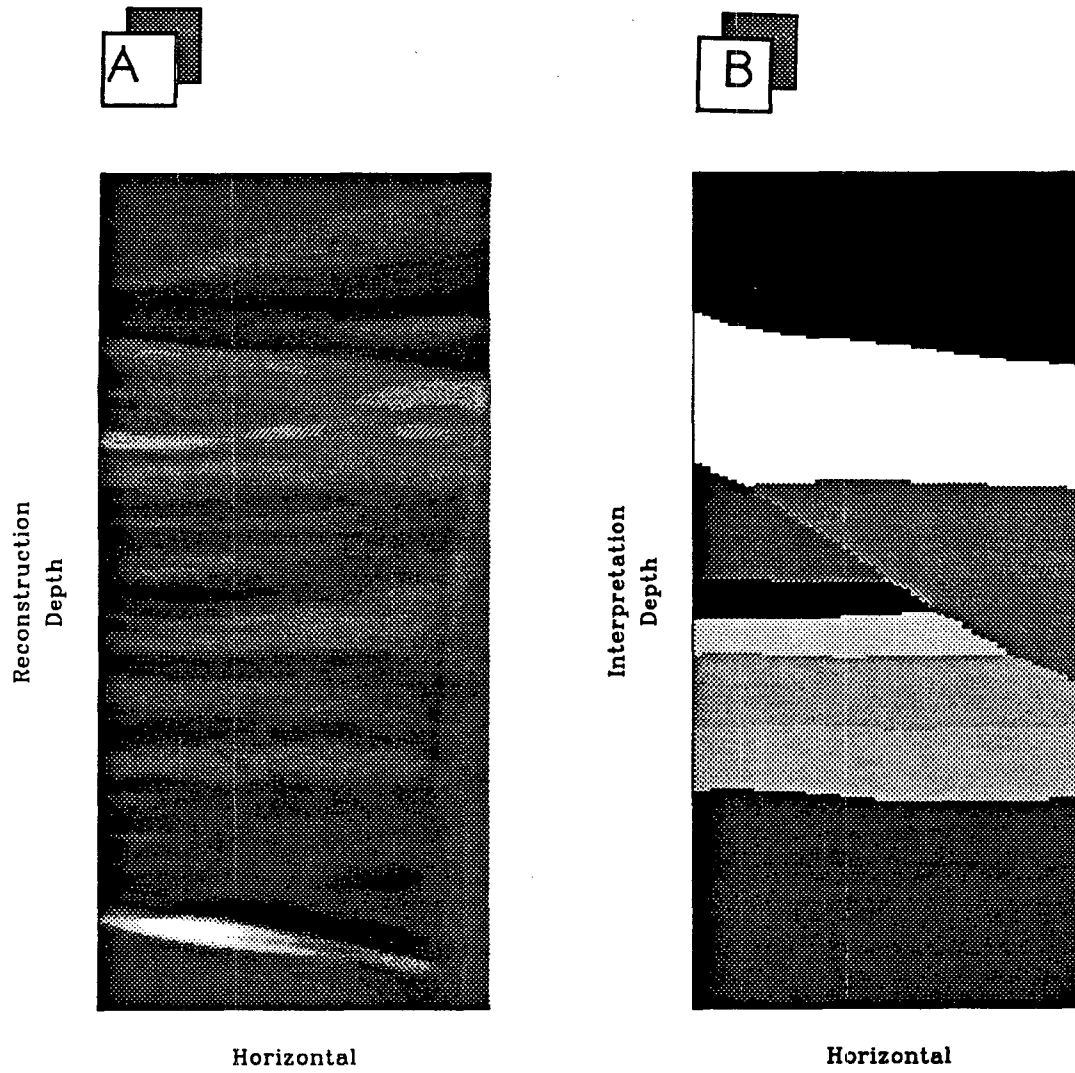
Figure 7.15: A comparison of the tomograqphic image reconstruction and the interpreted image. Both models yield similar average travel time errors in the fault neighborhood.

Appendix 1

A brief description of conventions and notations

Since most of the papers presented in this volume are related to solutions of the elastodynamic wave equation, the following notations are adopted whenever possible. Subscripts as in U_i denote the ith component of a vector field. Subscripts after a comma as in $U_{i,t}$ denote the partial derivative with respect to variable t of the ith component of the vector field U. The Einstein summation convention for repeated indexes is used whenever possible. Total derivatives are written explicitly as $\frac{du_i}{dt}$ for the total derivative of u_i with respect to t. Superscripts as in K^e are used to refer to elements in a finite-element grid.

Finally, the dependence of fields components on specific variables is left implicit in most cases where the dependence is obvious from the context, but is spelled out when necessary.

Notations in elastodynamic

c_{ijkl}	Elastic tensor.
C_{ij}	Elastic tensor in condensed notations (see A1).
ρ	Material Density.
u	Displacement field.
$\dot{u}$	Displacement field first derivative in time.
$\ddot{u}$	Displacement field second derivative in time.
σ	Stress tensor.
e_{ij}	Strain tensor $e_{ij} = \frac{1}{2}(u_{i,j} + u_{j,i})$.
δ_{ij}	Kronecker delta symbol.
k	Wave number.
f	Signal frequency.
ω	$= 2\pi f$

Notations in finite-elements

K	Impedance matrix.
M	Mass matrix
$\mathbb{A}$	Assembly operator.
Ω	Spatial domain of integration.
Γ	Surface boundary of the domain of integration.

operators

FT	Fourier transform.

∇ Divergence operator.

$\vec{\nabla}$ Gradient operator.

Curl   Rotational operator.

Appendix 2

Condensed notations for the elastic tensor

Since most of our work is limited to 2 dimensional space, with limited anisotropy levels, condensed notations for the elastic tensor have been preferred in most of this volume. The conversion from four to two index elastic tensor is performed as follows using the symmetry properties of the tensor (Auld 1973):

I	ij
1	xx
2	yy
3	zz
4	yz, zy
5	xz, zx
6	xy, yx

This tensor reduction can also be applied to other symmetric tensor like the stress or strain tensors which become vectors.

Appendix 3

Computations of the eigenvalues of the Christoffel tensor

This appendix focuses on the computation of the eigenvalues of the Christoffel tensor (equation 4.24). Expanding equation 4.24 we first have:

$$\gamma_{ik} = \left[c_{ijkl}^{(R)} + ic_{ijkl}^{(I)}\right] [Aa_l + iKk_l] [Aa_j + iKk_j] \tag{8.1}$$

Now using the assumptions stated insection 4.2.3, we have:

$$\gamma_{ik} = c_{ijkl}^{(R)} K^2 \left[1 + i\epsilon_{ijkl}\right] \left[ik_l + \frac{A}{K}a_l\right] \left[ik_j + \frac{A}{K}a_j\right] \tag{8.2}$$

where $\epsilon_{ijkl} = \frac{c_{ijkl}^{(I)}}{c_{ijkl}^{(R)}}$. Now expanding the previous equation, and neglecting all the second order terms, we find that:

$$\gamma_{ik} \simeq c_{ijkl}^{(R)} K^2 \left([-k_l k_j] + i\left[-\epsilon_{ijkl}k_l k_j + \frac{A}{K}(a_j k_l + a_l k_j)\right]\right) \tag{8.3}$$

Appendix 4

Interpolators for F.D.R.T.

Following the notation in figure 6.1a we can write a wavefield interpolator for the points 0,1,2 assuming a secondary source placed at the x_s , z_s location. Such an interpolator must therefore satisfy the following relationships:

$$t_0 = t_s + s\sqrt{x_s^2 + z_s^2} \tag{8.4}$$

$$t_1 = t_s + s\sqrt{(x_s^+ h)2 + z_s^2} \tag{8.5}$$

$$t_2 = t_s + s\sqrt{x_s^2 + (z_s + h)^2} \tag{8.6}$$

Once t_s, x_s, and z_s are computed using nonlinear regression, t_3 can be easily computed from:

$$t_3 = t_s + s\sqrt{(x_s + h)^2 + (z_s + h)^2} \tag{8.7}$$

The last four equations yield the second interpolator type.

The third interpolator, which skips from row to row (figure 6.1b) at a local minimum of the travel time curve can be written as:

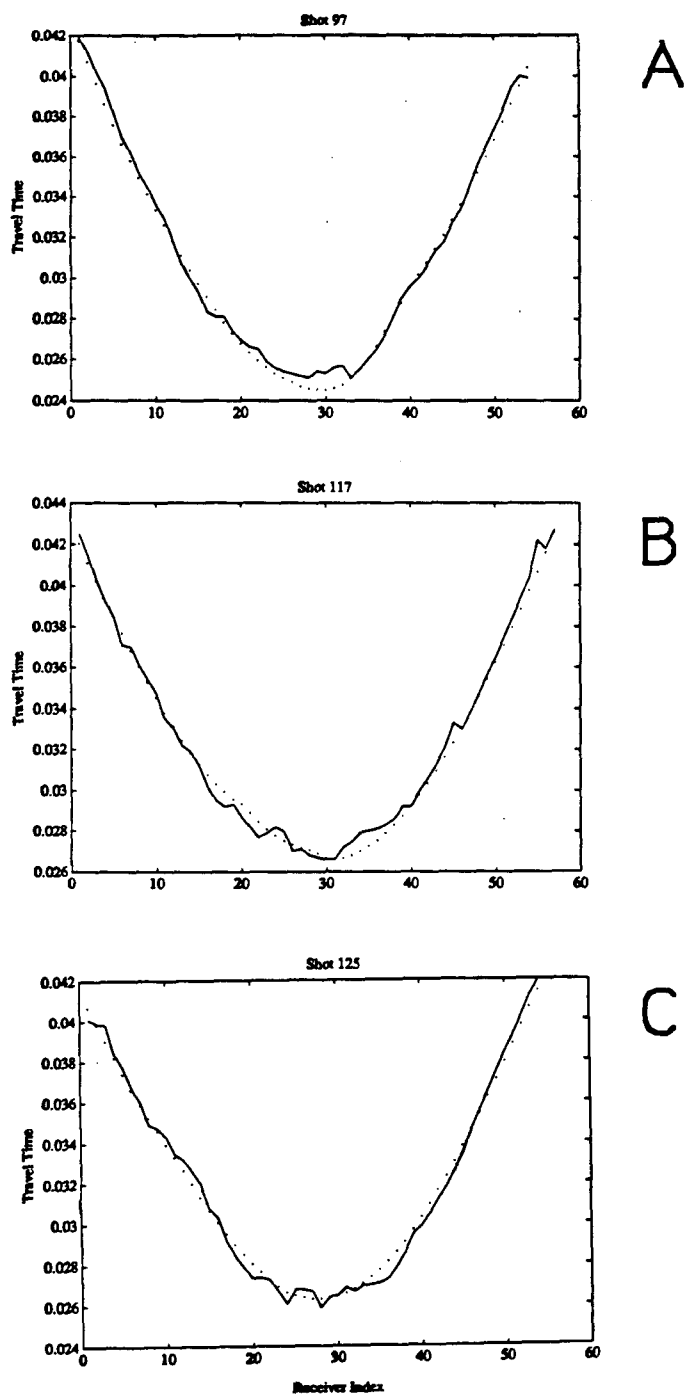$$t_3 = t_0 + s\sqrt{(hs)^2 + \frac{(t_2 - t_1)^2}{4}} \tag{8.8}$$

Figure 7.16: A comparison of the picked travel times (solid lines) and the computed travel times (dotted lines) for shot gathers a) 125, b) 117 c) 97.

References

Backus, S., 1962, Long-wave elastic anisotropy produced by horizontal layering, J. Geophys. Res., Vol. **67**, pp. 4427-4440.

Beydoun, W., 1982, Asymptotic wave methods in heterogeneous media, PhD thesis, Massachusetts Institute of Technology.

Dines, K. A., and Lytle, R. J.,1979, Computerized geophysical tomography, Proc. IEEE, 67, pp. 1065-1073.

Foley, J., Van Dam, A., Seiner S. K., Hughes, J. F., 1990, Computer graphics: Principles and practice, Addison Wesley Publishing Co, New-York.

Harris, J. M., Mavko, G., Moos, D., Nolen-Hoeksema, R., 1990, Cross-well tomographic imaging of geological structures in gulf coast sediments, Seismic Tomography Project, Stanford University.

Harris, J. M., Lazaratos, S., Michelena, R., 1990, Tomographic String inversion, Seismic Tomography Project, Stanford University.

McMechan, G. A., Harris J. M., and Anderson L., 1987, Cross-well tomography for strongly variable media with application to scale model data, Bulletin of Seismological Society of America, Vol. 77, No. 6, pp. 1945-1960.

Michelena, R., Harris, J. M., 1990, Tomographic travel-time inversion using natural pixels, to appear in Geophysics.

Tarantola, A., 1984, Inversion of seismic reflection data in the acoustic approximation, Geophysics, Vol. **49**, pp. 1259, 1266.

White, J. E., 1983, Underground sound: Elsevier, New York.